



UNIVERSIDAD DE GRANADA

ESCUELA INTERNACIONAL DE POSGRADO
PHD PROGRAM IN CIVIL ENGINEERING

SCHOOL OF BUILDING ENGINEERING

Development of engineering wood products based on poplar boards and veneers with composite material insertions for use in construction

A thesis submitted to the University of Granada for the international
degree of Doctor of Philosophy

Author

MSc. Cristian-Ioan ȚIMBOLMAȘ

Supervisors

Dr. Rafael BRAVO PAREJA
Dr. Francisco RESCALVO FERNANDEZ

Research founded by project grant reference: BIA2017-82650-R



May 2022

Editor: Universidad de Granada. Tesis Doctorales
Autor: Cristian Ioan Timbolmas
ISBN: 978-84-1117-367-4
URI: <http://hdl.handle.net/10481/75454>



UNIVERSIDAD DE GRANADA

ESCUELA INTERNACIONAL DE POSGRADO
PROGRAMA DE DOCTORADO EN INGENIERÍA CIVIL

ESCUELA DE INGENIERÍA DE LA EDIFICACIÓN

Desarrollo de productos de ingeniería elaborados a base de tablonos y chapas de chopo con inserciones de material compuesto para su uso en construcción

Tesis presentada en la Universidad de Granada para la obtención del
grado de Doctor internacional

Autor

MSc. Cristian-Ioan ȚIMBOLMAȘ

Directores

Dr. Rafael BRAVO PAREJA
Dr. Francisco RESCALVO FERNANDEZ

Investigación financiada por el proyecto con referencia: BIA2017-82650-R



Mayo 2022

Funding

Pre-doctoral contract:

This Doctoral Thesis has received financial support from the "Research Staff Training Program" (FPI) of the Ministry of Science and Innovation of the Spanish Government (grant reference: PRE2018-085447, under the research project, COMPOP, with reference: BIA2017-82650-R).

Period: September 2019 - May 2022.

Research mobility:

The period of 3 months for the research mobility at the Institute of Timber Engineering and Wood Technology (LIGNUM) from the Technical University of Graz (Austria), received funding from the "Research Staff Training Program" (FPI) of the Ministry of Science and Innovation of the Spanish Government (grant reference: PRE2018-085447, under the research project, COMPOP, with reference: BIA2017-82650-R).

Dedication

To my beloved wife, Mădălina

Abstract

Nowadays there is a wide variety of research in the field of timber engineering, for both experimental and theoretical parts, however, a close interconnection between them is still needed for a full understanding of the structural behaviour, from its origin (standing trees in forests) until the final products, as structural members (e.g.: glulam beams, solid beams, CLT panels). This thesis is a multi-disciplinary one, where the practical part is embedded with the theoretical part, through the analytical and numerical methods in order to check and validate them. The main timber species studied through this work is focused on poplar timber used in the glulam beams.

The work carried out in this thesis starts with evaluating the mechanical properties from standing trees, followed by the characterization in logs, boards, lamellas and in the last step, in the final glulam beams. As poplar is considered a timber material with low-medium quality, different solutions for the improvement of the structural behaviour have been considered through this work. These solutions were divided into environmentally friendly or eco-friendly solutions, for the case when hybrid poplar beams in combination with other timber species were used, and conventional solutions employing CFRP materials were embedded into the specimens' cross-section.

An analytical model, based on the Parallel Axis Theorem (Steiner theorem) and the transformed-section method, is developed to determine the corresponding moduli in tension and compression, based on the global modulus obtained through the bending test for mono-species and multi-species beams. In the following, this model is extended to an analytical model, valid in the linear elastic domain, which can estimate the stresses, strains, resultant forces, and corresponding moduli in tension for the combined section and section with CFRP. Through this analytical formulation, a parametric analysis for the combined beam, pine-poplar, is applied to estimate the mechanical properties of the combined glulam beam as a poplar percentage.

The digital image correlation (DIC) technique and finite element analysis (FEA) is applied in the evaluation of the mechanical properties of poplar, subject to tension force. Additionally, the CFRP bonded to poplar with different bond lengths is analyzed from two viewports in order to evaluate the longitudinal strain distribution onto CFRP (fabric and laminate) and on a poplar surface adjacent to the bond line.

Acknowledgements

After intensive research and a working period of 3-years with many challenges and difficulties, I have completed an important achievement of my life. This thesis would not have been possible without the support of many people I have met during these years, which have significantly contributed to this goal.

Foremost, I would like to express my sincere gratitude and thanks to my supervisors, Assoc. Prof. Rafael Bravo Pareja and Dr Francisco Rescalvo Fernandez for their assistance, guidance, and valuable suggestions at every stage of this research period. Special thanks from the deepest of my heart go to Assoc. Prof. Rafael Bravo Pareja for the real help with my integration into a foreign country and solving the administrative problems over these years and for his patience in our daily meetings during the pandemic.

Besides my supervisors, I would like to offer my special thanks to our head of the research group, Prof. Antolino Gallego Molina, for his contribution to obtaining the research grant, insightful remarks, and guidance during our research works. As well, I would like to address my special gratitude to my former master thesis supervisor, Assoc. Prof. Pedro Museros, from the Polytechnic University of Valencia who recommended me for this grant, without whom it would not have been possible to be here today. In addition, I would like to express my thanks, to my colleagues and laboratory staff from our research group (IDIE), for their support, especially for the experimental part carried out in these years.

My appreciation also extends to Prof. Gerhard Schickhofer, the Head of the Institute of Timber Engineering and Wood Technology (LIGNUM) from the Technical University of Graz, Austria, for giving me the opportunity to perform research in a reputable research centre, where I have extended my knowledge in the manufacturing and testing part of the glulam timber beams. Moreover, I would like to express my special thanks to Dr Andreas Ringhofer, to laboratory staff from TU Graz, and Hasslacher Norica Timber GmbH Company, represented by Mr Georg Jeitler and Mr David Obernosterer, for the supply of the pine and birch boards for the manufacturing of the GLT hybrid beams.

Last but not least, none of this could have happened without the support, encouragement and love of my wife, Mădălina, who has always been on my side over these years, to whom I extend all my sincere appreciation and warmest thanks.

Contents

Declaration	i
Abstract	vii
Acknowledgements	ix
1 Introduction and Scope of the thesis	1
2 Experimental and numerical analysis of mixed I-214 poplar/pinus Sylvestris laminated timber subjected to bending loadings	3
2.1 Introduction	3
2.2 Materials and Methods	5
2.2.1 Experimental program flow	5
2.2.2 Raw material and planks	5
2.2.3 Dynamic modulus of elasticity of planks: Acoustic Resonance Testing	6
2.2.4 Planks strength grading	7
2.2.5 Glulam timber samples	7
2.2.6 Dynamic modulus of elasticity of the glulam timber	8
2.2.7 Semi-analytical modulus of elasticity	8
2.2.8 Bending test	9
2.2.9 Strength grading of glulam timber samples	10
2.2.10 Numerical modelling	10
2.3 Results	12
2.4 Discussion	15
2.5 Conclusions	18
3 Modulus of elasticity of I-214 young poplar wood from standing trees to sawn timber: Influence of the age and stand density	21
3.1 Introduction	21
3.2 Materials and Methods	23
3.2.1 Forest and wood material description	23
3.2.2 Acoustic test on standing trees	25
3.2.3 Harvesting and logs acoustic testing	26
3.2.4 Sawing timber	27
3.2.5 Acoustic test on sawn timber samples	28
3.2.6 Bending test	29
3.2.7 Compression test	30
3.2.8 Density	31

CONTENTS

3.2.9	Statistical analysis	31
3.3	Results	31
3.3.1	Standing trees and logs: dasometric features	31
3.3.2	Features in standing trees and logs	32
3.3.3	Sawn wood in bending	32
3.3.4	Tree, logs, and sawn timber: MoE relationships	32
3.3.5	Timber in compression	35
3.4	Discussion	36
3.5	Conclusions	40
4	Improving ductility and bending features of poplar glued laminated beams by means of embedded carbon material	41
4.1	Introduction	41
4.2	Materials and Methods	43
4.2.1	Poplar planks	43
4.2.2	FRP material	43
4.2.3	Glulam timber: Layouts and manufacturing	44
4.2.4	Non-destructive resonance test (NDT)	45
4.2.5	Ductility	48
4.2.6	Bending test	49
4.2.7	Statistical analysis	49
4.3	Results and Discussion	50
4.4	Conclusions	58
5	Transformed-section method applied to multi-species glulam timber beams subjected to pure bending	61
5.1	Introduction	61
5.2	Transformed-section Theory	63
5.2.1	General formulation	63
5.2.2	Formulation for a mono-species cross-section	65
5.2.3	Formulation for a multi-species cross-section	66
5.3	Materials and Methods	69
5.3.1	Timber	69
5.3.2	Glulam beams	70
5.3.3	Bending tests	70
5.3.4	Results	71
5.4	Conclusions	76
6	Development of an analytical model to predict the bending behaviour of composite glulam beams in tension and compression	77
6.1	Introduction	77
6.2	Analytical formulation and methods	79
6.2.1	Case 1. Rectangular glulam section made up of a single timber species (Pi or Po)	80
6.2.2	Case 2. Rectangular composite glulam section made up of a single timber species and CFRP material placed at the bottom side (CLB)	82
6.2.3	Case 3. Rectangular glulam section comprising two timber species (PiPo)	83

6.2.4	Methods	85
6.3	Materials	87
6.3.1	Timber	87
6.3.2	CFRP material	87
6.3.3	Glulam samples	88
6.4	Bending Tests	88
6.5	Results and Discussions	89
6.5.1	Only-timber glulam beams	89
6.5.2	Poplar (Po) and CFRP composite beams (CLB, CLT, and CF2BT)	95
6.5.3	CLT layout	101
6.5.4	CF2BT layout	101
6.6	Conclusions	104
6.7	Appendices	107
6.7.1	Rectangular glulam section made up of a single timber species (Pi or Po)	107
6.7.2	Rectangular composite glulam section made up of a single timber species and CFRP material placed at the bottom side (CLB)	108
6.7.3	Rectangular solid section made up of a timber material and composite material at the top (CLT).	108
6.7.4	Stresses, strains and resultant forces for the CLT layout.	110
6.7.5	Rectangular solid section made up of a timber material and composite material at both sides.	110
7	Analysis of poplar timber finger joints by means of Digital Image Correlation (DIC) and Finite Element simulation subjected to tension loading	113
7.1	Introduction	113
7.2	Materials and Methods	115
7.2.1	Poplar wood and adhesive	115
7.2.2	Sample description and manufacturing	115
7.2.3	Experimental test	116
7.2.4	Digital Image Correlation	117
7.2.5	Finite element method: numerical simulations	119
7.3	Results and Discussion	121
7.3.1	Experimental results	121
7.3.2	Finite element simulation and DIC results	126
7.4	Conclusions	128
8	Multi-side Digital Image Correlation (DIC) evaluation of bonded CFRP to poplar timber	131
8.1	Introduction	131
8.2	Materials and Methods	133
8.2.1	Poplar wood and adhesive	133
8.2.2	Specimens description	133
8.2.3	Test set-up and DIC equipment	135
8.2.4	Experimental data-analysis methods	136
8.3	Results and Discussions	136
8.3.1	Results for 200 mm bond length	138
8.3.2	Results for 150 mm bond length	141

CONTENTS

8.3.3	Results for 100 mm bond length	143
8.3.4	Results for 50 mm bond length	147
8.3.5	General behaviour	149
8.4	Conclusions	154
9	Digital image correlation and numerical analysis of FRP-poplar timber interface subjected to single shear tests	157
9.1	Introduction	157
9.2	Materials and experimental set-up	159
9.2.1	Timber block, adhesive and composite material (FRPs)	159
9.2.2	Timber block, adhesive and composite material (FRPs)	160
9.2.3	Modified single shear test	160
9.3	Methods	162
9.3.1	DIC technique/instrumentation	162
9.3.2	Numerical finite simulation	162
9.4	Results and Discussions	167
9.4.1	CL specimen behaviour	169
9.4.2	CF2 specimen behaviour	172
9.4.3	CF specimen behaviour	174
9.5	Conclusions	174
10	General conclusions of the thesis	177
	Bibliography	181

List of Figures

2.1	Chart flow of the general experimental procedure. $MoE_{dyn,p}$: Dynamic modulus of elasticity of planks. $MoE_{dyn,gt}$: Dynamic modulus of elasticity of glulam timber. σ_{max} : Maximum stress in bending. $MoEst$: Static modulus of elasticity.	5
2.2	Left: Works during poplar harvesting; Right: Pine and poplar timber in the artificial dryer once the final MC=12% was achieved	6
2.3	ART layout for planks. L=Plank length.	6
2.4	Normal distribution of the dynamic modulus of elasticity of the planks.	7
2.5	Distribution of planks according with the T and C strength class.	8
2.6	Timber layers design according with planks grading and strength class GL proposed by the standard. PPI: pure pine. PPO: pure poplar. MPOPi: mixed poplar/pine. GLXc: design grading for combined. GLXh: design grading for homogeneous.	9
2.7	Four-point bending test arrangement and pure poplar sample during the bending test. Distances in mm.	10
2.8	3D-FEM model for a four-point bending test set-up and 3D-Mesh of load cells/supports.	11
2.9	Stress versus strain for the tensile strain gauge (bottom face) for all the samples.	12
2.10	General results for the tested samples. Left: Static modulus of elasticity ($MoEst$). Right: Strength grading of the samples with $MoEst$	13
2.11	Numerical and experimental load-displacement plots and their corresponding yield limits.	13
2.12	Comparison between modulus of elasticity for the tested samples. $MoE_{dyn,gt}$: dynamic modulus of elasticity. $MoEst$: static modulus of elasticity. Gray dotted line: $y=x$	15
3.1	Location of the plantation on the Iberian Peninsula. GU: plantation located at the Henares river basin, Guadalajara province, in the central area of the Iberian Peninsula. GR: two plantations located at the Genil river basin, Granada province, in the south of Spain.	24
3.2	Testing from tree to timber	25
3.3	Acoustic test on standing trees: (a) Experimental setup; (b) Picture during test. S1: Impact point sensor. S2: Receiver sensor. Distances are shown in mm.	26
3.4	Acoustic resonance test on the logs. L_L : log length.	27

LIST OF FIGURES

3.5	Theoretical cutting for obtaining the sawn timber samples for three different diameters of logs. Distances are shown in mm. GU: Guadalajara; GR_L : Granada low-stand density; GR_H : Granada high-stand density.	28
3.6	Pictures of the process from the log to timber	28
3.7	Experimental set-up of the acoustic test carried out on each particular sample. L_b : sample length, h : sample height.	29
3.8	Experimental set-up of the four points bending test of the sample. L_b : sample length, a : distance from the support to the nearest load application, L : distance between the load application points, b : sample width, F : applied force, h : sample height.	30
3.9	Experimental set-up of the compression test: (a) Parallel to grain (0°); (b) Perpendicular to grain (90°). F =applied load. Distances are shown in mm.	31
3.10	(a) Propagation velocity on standing trees versus propagation velocity on logs; (b) Elastic modulus (trees versus logs). MoE_T : modulus of elasticity in standing trees; MoE_L : modulus of elasticity in logs; C_T : propagation velocity in standing tree; C_L : propagation velocity in log; GU: Guadalajara; GR_L : Granada low-stand density; GR_H : Granada high-stand density.	33
3.11	Normal distribution of the static MoE in bending. GU: Guadalajara; GR_L : Granada low-stand density; GR_H : Granada high-stand density.	34
3.12	Experimental results. (a) MoE on trees versus static MoE in bending tests; (b) MoE on logs versus static MoE in bending tests; (c) Dynamic MoE on trees versus static MoE in bending tests. GU: Guadalajara; GR_L : Granada low-stand density; GR_H : Granada high-stand density.	35
4.1	Normal distribution of the dynamic longitudinal MoE of the sawed planks. Red line: Mean value. Green dotted line: Standard deviation limits.	43
4.2	Glulam layouts. Blue: FRP fabric. Red: FRP lamella. Distances in mm.	44
4.3	General design of glulam beams. Distances in mm.	45
4.4	General arrangement of the non-destructive resonance test.	46
4.5	N.D.T procedure for Phases 1 and 2 to obtain the $MoEdyn,c$ and $MoEdyn$	47
4.6	Procedure to determine the ductility ratio in terms of displacements. F is the applied force and δ is the vertical deflection. Left: Theoretical approach; Right: Approach considered in this study.	48
4.7	Four-point bending test set-up. Distances in mm.	50
4.8	Stress-deflection relations.	51
4.9	Variations of the ductility parameters in % compared to the control CH layout.	52
4.10	Failure patterns of the specimens.	53
4.11	Improvement of the static modulus of elasticity (left) and maximum stress (right) improvements respect to the control CH layout.	56
4.12	Dynamic modulus of elasticity vs. dynamic combined modulus for all specimens.	57
4.13	Dynamic modulus of elasticity vs. static modulus of elasticity for all specimens.	57
4.14	Mean values of dynamic modulus of elasticity against vs. static modulus of elasticity.	58

5.1	a) Section of a beam composed of a material with different behaviour in tension and compression subjected to pure bending; b) General cross-section; c) Corresponding transformed section.	64
5.2	a) Cross-section made up of a timber material with different elastic moduli in tension and compression; b) Transformed section made up of a homogeneous material, E_h	65
5.3	a) Cross-section made up of a timber material with different elastic moduli in tension and compression; b) Transformed section made up of a homogeneous material, E_h	66
5.4	a) Cross-section made up of two timber materials with different elastic moduli in tension and compression. b) Transformed section made up of a homogeneous material, E_h	68
5.5	Distribution of MoE_{dyn} of Pine and Platanus planks. Black dashed-dotted line: Mean value. Red/Green dashed line: Range of selected planks according to the standard deviation.	69
5.6	Four-point bending test set-up. Strain gauges in red colour. Distances in mm.	71
5.7	Stress-deflection relations for all the experimented specimens. b) Normal distribution of the experimental global modulus (MoE_{global}) for Pine (Pi), Platanus (Pl) and Pine-Platanus (PiPl) layouts.	71
5.8	Experimental global modulus ($MoE_{global,ex}$) and the corresponding position of the neutral axis ($Y_{n,ex}$): a) 8-Pine beams (Pi); b) 8 Pine-Platanus beams (PiPl).	73
5.9	Analytical global modulus ($MoE_{global,an}$) using Eq. 5.13. Distribution of 64 Pine-Platanus virtual specimens.	75
5.10	Global modulus of elasticity ($MoE_{global,an}$) and the corresponding moduli in tension and compression ($E_{t,an}$ and $E_{c,an}$) as a function of the Platanus percentage along the combined cross-section, employing the obtained solutions from Eqs. 5.18 and 5.14.	75
6.1	Stress-strain relations for a rectangular solid section with different behaviour in tension and compression. N.A: Neutral axis.	81
6.2	Stress-strain relations for a rectangular solid section with different behaviour in tension and compression and composite material (CFRP) at the bottom side. N.A: Neutral axis.	82
6.3	Stress-strain relations for a rectangular solid section with different behaviour in tension and compression and two different timber species: pine and poplar (PiPo).	84
6.4	Flowchart for the analytical procedure for the Po, Pi, and PiPo layouts.	86
6.5	Flowchart of the analytical procedure for the CLB, CLT, and CF2BT layouts.	87
6.6	Normal distribution of MoE_{dyn} of the sawed planks. Black vertical line: Mean value. Blue vertical dashed lines: Standard deviation limits and plank interval used.	88
6.7	Four-point bending test set-up. Distances in mm. Strain gauges in red color.	89
6.8	Stress-deflection curves for poplar (Po), pine-poplar (PiPo) and pine (Pi) beams.	90

LIST OF FIGURES

6.9	Global modulus ($MoE_{global,an,II}$) and moduli in tension ($E_{t,com,an,II}$) and compression ($E_{c,com,an,II}$). Distribution for the 64 pine poplar beams (PiPo).	94
6.10	Global modulus of elasticity ($MoE_{global,an,II}$), moduli of elasticity in tension and compression ($E_{t,com,an,II}$ and $E_{c,com,an,II}$), and density ρ as a function of the percentage of poplar.	96
6.11	Stress-deflection relations for the control beam (poplar, Po), poplar and reinforced FRP beams (CLB, CLT and CF2BT).	97
6.12	Layout density: mean and standard deviation.	98
6.13	Stress-strain relations for a rectangular solid section with different behaviour in tension and compression, and composite material (CFRP) at the top side (CLT).	109
6.14	Stress-strain relations for a rectangular solid section with different behaviour in tension and compression, and composite material (FRP) at both sides.	111
7.1	Geometry of the tensile poplar specimens with (TF) and without (TT) finger joints. Dimensions in mm.	116
7.2	Geometrical parameters of the finger joint profile and finger joint picture. Dimensions in mm.	116
7.3	Axial tensile test set-up with DIC equipment.	117
7.4	Definition of the virtual extensometer position: Ext.1, Ext.2, Ext. 3 (left), Gauge area (center); areas for strain determination (right).	118
7.5	FEM mesh: general view of the specimen (left), mesh of the fingers joint (middle and right).	120
7.6	Stress-strain relations for TT and TF specimens: (top) based on Ext. 1; (bottom-left) based on defined central area; (bottom-right) based on Ext. 3.	122
7.7	Modulus of elasticity variation of the specimens with finger joints-TF (left) and without finger joints-TT (right).	125
7.8	Modulus of elasticity variation of the specimens with finger joints-TF (left) and without finger joints-TT (right).	126
7.9	Distribution of modulus of elasticity using: extensometers - method I (left); defined areas - method II (right).	126
7.10	Experimental force-elongation curve and DIC vertical strains field at four different load steps for one representative TT (top) and TF (bottom) specimen.	127
7.11	Force-elongation of numerical and experimental relationships for TF specimen (left) and TT specimen (right).	128
7.12	Strain field distribution for TF specimen. a) Longitudinal strain (ϵ_x); b) Transversal strain (ϵ_y); c) Shear strain (ϵ_{xy}) from DIC. d) Longitudinal strain (ϵ_x); e) Transversal strain (ϵ_y); f) Shear strain (ϵ_{xy}) from FEM.	129
8.1	Schematic representation of the CFRP-timber sample, the boundary conditions, and the deformed shape of the specimen expected during testing.	134
8.2	Experimental test set-up and DIC equipment.	135
8.3	Longitudinal strain distribution in frontal view (left) and side view (right) in GOM Correlate software [171].	137
8.4	Longitudinal strain field from frontal (left) and side (right) views for the specimens with 200 mm bond length.	138

8.5	Evolution of the longitudinal strains of one representative sample with 200 mm bond length for different load levels in frontal (top) and side (bottom) views. The shaded area represents the limits of the bond length.	139
8.6	Force-slip relations for the specimens with 200 mm bond length.	140
8.7	Longitudinal strain field from frontal and side views analysis for the specimens with 150 mm bond length.	142
8.8	Evolution of the longitudinal strains of one representative sample with 150 mm bond length for different load levels in frontal (top) and side (bottom) views. The shaded area represents the limits of the bond length.	143
8.9	Force-slip relations for the specimens with 150 mm bond length.	144
8.10	Longitudinal strain field from frontal and side views analysis for the specimens with 100 mm bond length.	145
8.11	Evolution of the longitudinal strains of one representative sample with 100 mm bond length for different load levels in frontal (top) and side (bottom) views. The shaded area represents the limits of the bond length.	146
8.12	Force-slip relations for the specimens with 100 mm bond length.	146
8.13	Longitudinal strain field from frontal and side views analysis for the specimens with 50 mm bond length.	148
8.14	Evolution of the longitudinal strains of one representative sample with 50 mm bond length for different load levels in frontal (top) and side (bottom) views. The shaded area represents the limits of the bond length.	148
8.15	Force-slip relations for the specimens with 50 mm bond length.	149
8.16	Mean maximum applied force and mean interface stiffness variation. . .	150
8.17	Longitudinal strain distribution within CFRP acquired frontal view analysis (top). Longitudinal strain evolution under loading conditions (bottom).	151
8.18	Longitudinal strain distribution within timber acquired side view analysis (top). Longitudinal strain evolution under loading conditions (bottom).	153
9.1	Specimen and experimental set-up.	159
9.2	General drawing of the experimental setup and sample. Dimensions in mm.	161
9.3	Test set-up for side and frontal views.	162
9.4	Test set-up considered in the numerical simulations.	163
9.5	General damage process zone and corresponding bilinear traction-separation law [220].	164
9.6	Digital Image Correlation of the longitudinal strain field in frontal view of FRP (left) and side view of timber (right) of three representative specimens of CL (left), CF2 (middle) and CF (right), respectively prior initiation of debonding.	168
9.7	Lateral DIC view of strain flow, debonding and progression for CL (left), CF2 (central) and CF (right) specimens.	169
9.8	Experimental and FEM longitudinal strain for CL, frontal (left) and side (right).	170
9.9	Longitudinal strain distribution from the FEM model for the CL specimen corresponding to the initiation of detachment at the free end.	171
9.10	Longitudinal strain field at damage initiation (left), damage evolution (middle) and final debonding (right) of the CL specimen. FEM simulation.	171

LIST OF FIGURES

9.11	Experimental and FEM longitudinal strain for CF2, frontal (left) and side (right).	172
9.12	Longitudinal strain distribution from the FEM model for the CF2 specimen corresponding to the initiation of detachment at the free end.	173
9.13	Longitudinal strain field at damage initiation (left), damage evolution (middle) and final debonding (right) of the CF2 specimen. FEM simulation.	173
9.14	Experimental and FEM longitudinal strain for CF, frontal (left) and side (right).	174
9.15	Longitudinal strain distribution from the FEM model for the CF specimen corresponding to the initiation of detachment at the free end.	175
9.16	Longitudinal strain field at damage initiation (left), damage evolution (middle) and final debonding (right) of the CF specimen. FEM simulation.	175

List of Tables

2.1	Main mechanical properties of the tested samples. MoE_{st} : static modulus of elasticity. $MoE_{dyn,gt}$: dynamic modulus of elasticity. MoE_c : semi-analytical modulus of elasticity. $MoE_{FEM,G}$: numerical modulus of elasticity using G. σ_{max} : Maximum stress. PPI: pure pine. PPO: pure poplar. MPoPi: mixed poplar/pine. T ^o : Outer planks. T ⁱ : Inner planks	14
2.2	Strength grading for the tested samples according to the different modulus of elasticity. MoE_{st} : static modulus of elasticity. $MoE_{dyn,gt}$: dynamic modulus of elasticity. MoE_c : semi-analytical modulus of elasticity. PPI: pure pine. PPO: pure poplar. MPoPi: mixed poplar/pine. T ^o : Outer planks. T ⁱ : Inner planks.	14
2.3	Huygens-Steiner theorem results for the pure pine PPI2 and mixed poplar/pine MPoPi1 samples. T ^e : External planks. T ⁱ : Inner planks. $MoE_{dyn,p}$: dynamic modulus of elasticity of each plank. MoE_c : semi-analytical dynamic modulus of elasticity.	16
2.4	Variation in % of the elastic moduli respect to the static modulus MoE_{st} . Comparison of the numerical and experimental moduli of elasticity. MoE_{st} : static modulus of elasticity. $MoE_{FEM,G}$: calibrated modulus of elasticity using G. $MoE_{dyn,gt}$: dynamic modulus of elasticity. $MoE_{dyn,c}$: semi-analytical modulus of elasticity. PPO: pure poplar. MPoPi: mixed poplar/pine. 17	17
2.5	Comparison of experimental and numerical moduli of elasticity without considering the shear modulus and their variation in % respect to the static modulus MoE_{st} . MoE_{st} : static modulus of elasticity. $MoE_{st,g}$: global static modulus of elasticity. MoE_{FEM} : calibrated modulus of elasticity without using G.	17
2.6	Comparison of the shear moduli of elasticity. G_{ex} : experimental shear modulus. G_{FEM} : calibrated shear modulus used for numerical simulation. 18	18
2.7	Experimental and numerical stiffness used for the calibration of the FEM model. K_{ex} : experimental stiffness. $K_{FEM,G}$: calibrated numerical stiffness using G. K_{FEM} : calibrated numerical stiffness without using G. Variation in % computed respect to K_{ex}	18
3.1	Main characteristics of plantations, trees, logs and sawn timber samples. GU: Guadalajara; GR_L: Granada low-stand density; GR_H: Granada high-stand density.	23

LIST OF TABLES

3.2 Mean value±SD. DBH: diameter measured at breast height; H: tree height at a 7 cm diameter point; V: tree wood volume; ΔDBH: annual DBH growth rate; FHW: false heartwood ratio; CT: tree acoustic velocity; CL: log acoustic velocity. GU: Guadalajara; GR_L : Granada low-stand density; GR_H : Granada high-stand density. 29

3.3 Mean value±SD. MoE_T : modulus of elasticity in standing trees; MoE_L : modulus of elasticity in logs; MoE_{dyn} : dynamic modulus of elasticity in timber; $E_{0,m}$: static modulus in bending (mean value); ρ_0 : basic density in timber samples (MC=0%); $E_{c,0}$: modulus of elasticity in compression parallel to the fiber; $E_{c,90}$: modulus of elasticity in compression perpendicular to the fiber; ν : Poisson ratio. A, B, and C indicate different statistical classes among plantations within each variable. GU: Guadalajara; GR_L : Granada low-stand density; GR_H : Granada high-stand density. . . 34

4.1 Main characteristics of the used FRPs [98]. 44

4.2 General design of glulam beams. Distances in mm. 45

4.3 Mean values, covariance (%) and statistical class for: force-displacement ductility parameters (structural safety and engineering design), and moment-curvature ductility. 52

4.4 Mean values (N/mm²), covariance (%) and statistical class of: $MoE_{dyn,c}$: dynamic combined modulus; G: Shear modulus; MoE_{dyn} : dynamic modulus; MoE_s : static modulus; $MoE_{m,g}$: global modulus without shear modulus (mean); $MoE_{m,g+G}$: global modulus of elasticity with shear modulus (mean); f_m : maximum stress. 55

5.1 Glulam beams layouts 70

5.2 Experimental mean values: global modulus of elasticity (MoE_{global}), and maximum bending strength (f_m) with their corresponding mean variation. 72

5.3 Experimental (ex) global modulus of elasticity ($MoE_{global,ex}$) and the corresponding position of the neutral axis (Y_{nex}). Analytical (an) moduli in tension ($E_{t,an}$) and compression ($E_{c,an}$) using Eqs. 5.9 (Pi) and Eqs. 5.14 (PiPl). K is the ratio between moduli in tension and compression for the 8-Pine and 8-Pine-Platanus beams specimens with their corresponding mean values. 74

5.4 Experimental ($MoE_{global,ex}$) and analytical ($MoE_{global,an}$) mean value of global modulus of Pine-Platanus layout (PiPl) and the corresponding variation. 75

6.1 Description of the glulam beam layouts analyzed in this paper. 80

6.2 Stresses, strains and resultant forces for the glulam beam made of a single timber species (Pi or Po). 81

6.3 Stresses, strains and resultant forces for the CLB layout. 83

6.4 Experimental results. Mean values, covariance (%) and variation (%) of: Global modulus- $MoE_{m,global,ex}$; Static modulus - MoE_s ; Dynamic modulus - MoE_{dyn} ; Maximum stress - f_m ; Density - ρ ; for pine (Pi), Poplar (Po) and composite pine-poplar beams (PiPo). 90

6.5 Experimental (ex) and analytical (an) results for the Po specimens (top); Mean values and covariance (%) (bottom). 92

6.6	Experimental (ex) and analytical (an) results for the Pi specimens (top); Mean values and covariance (%) (bottom).	92
6.7	Experimental (ex) and analytical (an) results for the PiPo specimens (top); Mean values and covariance (%) (bottom).	93
6.8	Variation between the experimental and the analytical approaches for the PiPo layout.	93
6.9	Analytical results for composite pine-poplar specimens, mean values and covariance (%).	95
6.10	Variation between the mean analytical values for PiPo layout with respect to the mean values of Pi and Po specimens computed from the experiments.	95
6.11	Mean values (N/mm^2), covariance (%) and variation with respect to control beam (Po) (%) of: Global modulus - $MoE_{m,global,ex}$; Static modulus - MoE_s ; Dynamic modulus - MoE_{dyn} ; Maximum Stress - f_m ; Density - ρ ; for poplar-CFRP composite layouts.	96
6.12	Experimental and Analytical results for the CLB layout (top); Mean values and covariance (%) (bottom).	99
6.13	Variation between experimental and analytical approaches for CLB layout (using Working direction I).	100
6.14	Variation between experimental and analytical approaches for CLB layout using analytical data ($MoE_{m,global,ex,mean(Po)}$ represents the mean values for poplar) and Working direction II.	100
6.15	Experimental and analytical results for the CLT layout (top); Mean values and covariance (%) (bottom).	102
6.16	Variation between experimental and analytical approaches for CLT layout using experimental data and Working direction I.	103
6.17	Variation between experimental and analytical approaches for CLT layout using analytical data with Working direction II. $MoE_{m,global,ex,mean(Po)}$ represents the mean values for poplar.	103
6.18	Experimental and analytical results for the CF2BT layouts (top); Mean values and covariance (%) (bottom).	105
6.19	Variation between experimental and analytical approaches for CF2BT layout using experimental data (with work-flow I).	106
6.20	Variation between experimental and analytical approaches for CF2BT layout using analytical data (with Working direction II). $MoE_{m,global,ex,mean(Po)}$ represents the mean values for poplar.	106
6.21	Stresses, strains and resultant forces for the CF2BT layout.	112
7.1	Input elastic parameters for FEM simulations. E_1, E_2, E_3 are the moduli of elasticity in longitudinal, transversal and radial directions; G_{12}, G_{13}, G_{23} are the shear moduli in longitudinal, transversal and radial planes; $\nu_{12}, \nu_{13}, \nu_{23}$, are the Poisson's ratio.	121
7.2	Input contact parameters for FEM simulations. K_{nn}, K_{tt}, K_{ss} are the normal, tangential and radial stiffness; $\sigma_n, \tau_{nI}, \tau_{nII}$ are the maximum nominal inter-facial strength in the normal and shear direction I and II; δ_p is the effective plastic displacement.	121
7.3	Results for the TT specimens and the corresponding mean value.	123

LIST OF TABLES

7.4	Results for the TF specimens, the corresponding mean value, and the differences (Δ TF-TT %) between TT and TF specimens.	124
7.5	Mean Poisson ratio using method I (ν) with Ext. 3, and II (ν^*) with central area, mean tensile strength parallel to the grain ($f_{t,0}$), mean density and variation in (Δ TF-TT)%.	124
8.1	Mechanical properties of the CFRP materials from [98].	133
8.2	Experimental samples description and their corresponding CFRPs axial stiffness.	134
8.3	Maximum longitudinal strain applied force, interface stiffness and mean value based on load-slip relations for the specimens with 200 mm bond length.	141
8.4	Maximum longitudinal strain applied force, interface stiffness and mean value based on load-slip relations for the specimens with 150 mm bond length.	144
8.5	Maximum longitudinal strain applied force, interface stiffness and mean value based on load-slip relations for the specimens with 100 mm bond length.	147
8.6	Maximum longitudinal strain applied force, interface stiffness and mean value based on load-slip relations for the specimens with 50 mm bond length.	149
8.7	Mean maximum applied force (Δ -Force) and interface stiffness (Δ -Stiffness) differences with respect to the control specimen (CF-200) in percentage.	154
9.1	Main mechanical parameters of FRP reinforcement [98].	160
9.2	Experimental samples description and their corresponding FRPs stiffness.	161
9.3	Numerical parameters used for the CL specimen. t_n^0, t_s^0, t_t^0 are the maximum nominal interfacial strength in the normal and shear direction I and II; δ_f is the displacement at debonding; K_{nn}, K_{tt}, K_{ss} are the normal, tangential and radial stiffness.	166
9.4	Numerical parameters used for the CF2 specimen. t_n^0, t_s^0, t_t^0 are the maximum nominal interfacial strength in the normal and shear direction I and II; δ_f is the displacement at debonding; K_{nn}, K_{tt}, K_{ss} are the normal, tangential and radial stiffness.	167
9.5	Numerical parameters used for the CF specimen. t_n^0, t_s^0, t_t^0 are the maximum nominal interfacial strength in the normal and shear direction I and II; δ_f is the displacement at debonding; K_{nn}, K_{tt}, K_{ss} are the normal, tangential and radial stiffness.	167
9.6	Mean experimental and numerical failure loads, the corresponding error and standard deviation. Mean values over five specimens of each specimen typology.	167

Chapter 1

Introduction and Scope of the thesis

Wood is widely used in the construction sector for thousands of years, being one of the most environmentally friendly building materials, with excellent ecological characteristics, acting as a carbon filter. Today, timber members are continuously increasing to be used for all types of buildings, from residential buildings to public infrastructure works, and innovative and hybrid timber members are required in the market. These high demands are mainly due to its remarkable high ratio between bending strength and weight ratio, esthetical appearance, possibility to achieve high spans, and the source sustainability. Structural timber members are still facing with challenges related to defects (knots, cracks, fibre deviation, etc.) and lack of maintenance, which could lead to biological and fungal attacks. Another important point is related to their sensitivity in changes of the temperature, and humidity and its low fire resistance. For these reasons, rehabilitation, strengthening, and replacing operation of the damaged members are needed, employing different techniques.

Nowadays, the timber market is continuously looking forward to developing new structural members embedding fast-growing timber species, representing a current challenge in the wood value chains. Today, in Spain, the poplar plantation is one of the most important plantations and is a sustainable source of raw material due to its fast-growing and short cycle planted forest (from 9 years old to 18 years old). Therefore, poplar timber is becoming an interesting timber material that can be used successfully in the development of engineering products. One of the main utilization of the poplar can be associated with the production of the hybrid-combined glulam beams, by placing the poplar board in the inner part of the cross-section and using high-quality timber boards for the external parts.

The current thesis is focused on the evaluation and characterization of the poplar as a material and a structural element in combination with other timber species or CFRP solutions. The scope of the work is set to provide sufficient information about the behaviour in tension and compression, its stiffness, possibilities to improve the structural behaviour, and closed-form solution to evaluate the properties of combined hybrid glulam beams based on the acquired material properties. Based on the carried out works, this thesis is a multi-disciplinary thesis, which starts to evaluate and to characterize the poplar from standing trees, logs, boards and finally beams (pure glulam beams or combined glulam beams) and specific specimens (for tension-compression tests and bond interface behaviour). The applied testing methodologies through these works are related to the acoustic resonance method as non-destructive ones, bending, compression and tension tests as the destructive ones, in parallel with the analytical

CHAPTER 1.

INTRODUCTION AND SCOPE OF THE THESIS

models, finite element analysis (FEA), and digital image correlation technique (DIC).

The developed works for this thesis are following the current state of the art in timber engineering applied for other species, with particular emphasis on the structural behaviour in bending. In this thesis, the scope is targeted to the behaviour of poplar timber as material characterization and the mechanical performance of the poplar beams. Another scope is focused on the possibilities to improve the mechanical behaviour of poplar beams embedding other timber species with high mechanical quality or to reinforce the poplar members with CFRP materials. Then, the experimental results are compared with the results obtained through the analytical methods, which are able to determine the moduli in compression and tension based on the experimental global modulus. In addition, the methods are applied for the reinforced glulam beams, where the global modulus or corresponding moduli in tension and compression can be predicted with high accuracy. The proposed analytical models through a parametric analysis are able to determine the mechanical properties in terms of moduli, for the hybrid composite glulam beams, Pine-Poplar as the poplar percentage at the inner part of the cross-section.

The study of the poplar is extended to the tensile behaviour for specimens with and without finger joints. Therefore, the variation of the moduli in tension along the specimen is studied employing the DIC technique and finite element analysis. As well, the tensile strength and the corresponding reduction of the mechanical parameters compared with the specimens without finger joints are presented for different locations across the specimens.

To get insights about the CFRP bonded to poplar, an experimental campaign using the DIC technique and numerical modelling of the specimens has been investigated in the last two chapters of the thesis. This work is mainly focused on the longitudinal strain distribution onto CFRP and in the timber, on the surface parallel with the bond line. The specimens are subjected to shear stress, with a particular aspect related to the boundary condition of the poplar block. During the testing, the block is free to move along the applied direction of the force, which causes a notable bending of the specimens, which leads to additional strains and stresses in the timber and the bonded interface, respectively.

The thesis is structured in eight individual chapters, which are treating the works carried out during the research period, and each chapter represents an article. The first six chapters are already published in the journal mentioned at the beginning of each chapter. The works presented in the last two chapters related to the CFRP bonded to poplar are under the review process. The experimental work carried out during the mobility exchange at the Technical University of Graz will be analyzed in the future, and the results will be published in specific journals.

Chapter 2

Experimental and numerical analysis of mixed I-214 poplar/pinus *Sylvestris* laminated timber subjected to bending loadings

Title	Experimental and Numerical Analysis of Mixed I-214 Poplar/Pinus <i>Sylvestris</i> Laminated Timber Subjected to Bending Loadings
Authors	F.J. Rescalvo; C. Timbolmas; R. Bravo; A. Gallego
Journal	Materials
ISSN	1996-1944
Journal's performance	Journal impact factor (2020): 3.623 Q2 (Materials Science, Multidisciplinary: 152/334)
Details	Volume: 13 (14) – Published: July 2020; Article number: 3134
DOI	10.3390/ma13143134

2.1 Introduction

The development of Engineered Wood Products (EWP) such as glued laminated timber or Glulam [1–4] enhance the use of wood with a wider range of benefits: 1) greater dimensional stability; 2) higher design flexibility, allowing timber to be produced in a wide variety of shapes from straight beams to curved arches. This fact offers a multitude of options for large and open spaces with a reduced number of columns; 3) cover longer span lengths and cross-sections, thus being a product of a huge variety of uses, from residential constructions up to commercial buildings and timber bridges where higher structural requirements are needed; 4) higher quality of the final product due to the grading of the planks, a selection according to their stiffness and mechanical properties and the removal of knots and another undesirable defects; 5) the use of a wood species with lower diameters when compared with sawn timber; 6) the use of lower-grade timber in lower-stresses zones, resulting in a more efficient use and conservation of the timber resources. Regarding the last two benefits, poplar is one of the better candidates to be used for glulam timber. In Spain, poplar is one of the most important plantation species, covering an extension of 145,000 ha approximately

CHAPTER 2.

EXP. AND NUM. ANALYSIS OF MIXED I-214 POPLAR/PINUS

according to FAO [5,6]. Currently the use of poplar is mainly used for peeling and plywood manufacturing. The development of EWPs and its use for structural purposes is a huge opportunity to develop all the wood value chain.

Combination of different wood species has a wide range of structural advantages being introduced by [7]. In [8], authors developed a theoretical analysis and performed an evaluation by means of twenty large beams graded visually and made of Douglas-fir (*Pseudotsuga menziesii*) and lodgepole pine (*Pinus contorta*). Results demonstrate that the low-grade wood, i.e. lodgepole, with similar mechanical properties than poplar, used in the inner part of the glulam beams, had a little effect on the general mechanical properties. Previous works studied the mechanical properties of poplar glulam beams [9,10]. In particular, [10] used this grade consideration to sort the plank for every glulam beam by using the longitudinal vibration method (LVM). That work correlates the non-destructive testing with the mechanical properties of poplar glulam beams considering 4 types of adhesives. Authors also compare the results with the transform section method (TSM) calculated by using the modulus of elasticity of each plank. Results demonstrate a very good performance between TSM method and the global modulus of elasticity, with a correlation coefficient of 0.93, and a good correlation of 0.8 between LVM method and the global modulus of elasticity.

A comparison between pure glulam poplar (Neva clone, with a low density) and eucalyptus beams and mixed beams by using four types of eucalyptus clones was performed in [11]. For the grading of the planks, they performed a quasi-non-destructive static bending test applying low loads to them. Mixed beams designs consisted in five inner poplar planks and two outer eucalyptus planks. In general terms, results demonstrate that the combination of species and the use of the low-grade specie in the inner part of the glulam timber enhance the modulus of elasticity between a 9% and a 51% depending on the eucalyptus clone.

To evaluate the ductile behaviour of mixed glued laminated timber, the authors of [12] also considered poplar for the inner part of the beams, mainly due to its low density and good shear performance, using for the outer planks Norway spruce and larch wood. In addition, authors evaluated the mechanical behavior elaborating glulam timber from the same wooden species but different strength classes (as [13] proposed for poplar glulam beams). Results demonstrate that combination of species results more efficient when they have clearly different strength limits between them. Authors also remarked the high importance of an accurately grading of the planks during the design process. In [14,15], the authors also combined different species of wood with the same final conclusion of low-grade, high-grade timber distribution for inner and outer parts of the glulam timber, respectively. In [15], when a high-grade wood as Merpauh was used for the outer planks, improvements between 117% and 157% of the modulus of elasticity were achieved.

An improvement method in [16] was presented, taking into account the neutral axis shifts in bending by using the Time-of-Flight method. Authors took into account the differences between compression and tensile modulus of elasticity, improving the relationship between static and dynamic elastic modulus. Despite taking into account the neutral fiber axis shifts, results from previous works [17,18] for sawn timber, demonstrate that resonance method results in a more reliable technique to obtain the dynamic modulus of elasticity, since this method consider the whole piece of wood.

In order to qualitatively assess the behaviour of a mixed glulam timber using poplar wood for the inner part and pine for the outer layers, three layouts have been tested in

this work: 1) pure pine timber used as control specimens; 2) pure poplar timber used as control specimens; 3) mixed poplar/pine timber. To ensure a good performance and a proper sample design, all the planks were graded individually by means of the resonance acoustic testing. Subsequently, the samples were subjected to a four-point bending test following the standard [19] and the results were compared with three-non destructive methodologies: 1) numerical finite elements model (FEM); 2) Huygens-Steiner theorem; 3) acoustic resonance testing (ART). All the samples were graded and compared according the standard and an analysis of the effectiveness of the use of poplar for the inner layers has been carried out. Due to the low number of samples used for each timber layout, the results of this work should be considered only in qualitative and not in quantitative terms. In any case, since the main objective of this work is to compare the proposed numerical method with the experiments, the results make it clear that after calibration and using the shear modulus in the formulation, an excellent agreement is obtained between numerical and experimental results.

2.2 Materials and Methods

2.2.1 Experimental program flow

The experimental program followed the chart flow shown in Figure 2.1. Poplar and pine planks used for the glulam timber samples were graded according with their dynamic modulus of elasticity, $MoE_{dyn,p}$, obtained by Acoustic Resonance Testing (ART). Based on this grading, design and then manufacturing of the laminated timber were carried out. After that, timber was subjected to ART in order to obtain their dynamic modulus of elasticity, $MoE_{dyn,gt}$. Finally, they were destructively tested in bending, thus obtaining their static modulus MoE_{st} and the maximum stress in bending σ_{max} .

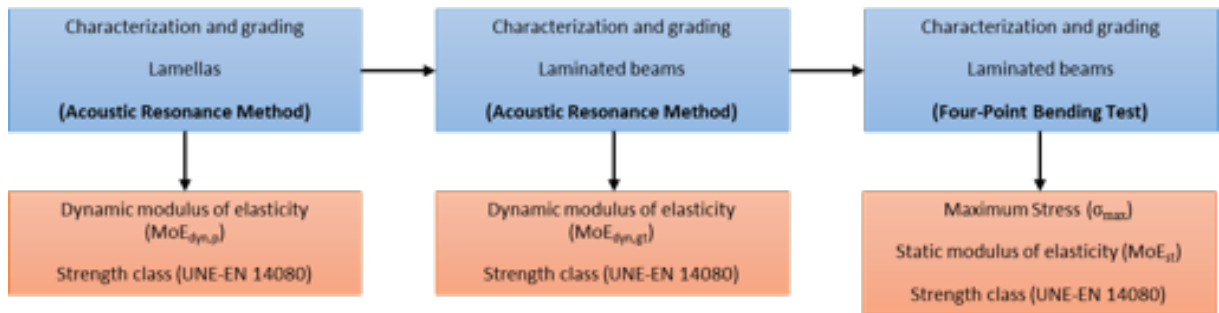


Figure 2.1: Chart flow of the general experimental procedure. $MoE_{dyn,p}$: Dynamic modulus of elasticity of planks. $MoE_{dyn,gt}$: Dynamic modulus of elasticity of glulam timber. σ_{max} : Maximum stress in bending. MoE_{st} : Static modulus of elasticity.

2.2.2 Raw material and planks

Two species were used, *Pinus sylvestris* and poplar clone I-214 (*Populus x aeuroamericana* (Dode) Guinier). Thirty four pine planks were extracted from the same sawn timber batch at 90 years old forests of Soria province (Spain), supplied by Madera Pinosoria S.L. Similarly, 14 poplar planks were extracted from the same sawn timber

CHAPTER 2.
EXP. AND NUM. ANALYSIS OF MIXED I-214 POPLAR/PINUS

batch from a 13 years old poplar plantation located at Yunquera de Henares (Guadalajara, Spain). Both pine and poplar timber were artificially dried (Figure 2.2), ensuring a final moisture content (MC) of 12%. Planks had a cross-section of 20 x 50 mm² and a total length of 1240 mm.



Figure 2.2: Left: Works during poplar harvesting; Right: Pine and poplar timber in the artificial dryer once the final MC=12% was achieved

2.2.3 Dynamic modulus of elasticity of planks: Acoustic Resonance Testing

All the planks were subjected to an ART [17, 18] in a flat-wise orientation by placing them on two elastic supports and hitting them with a hammer (2.3).

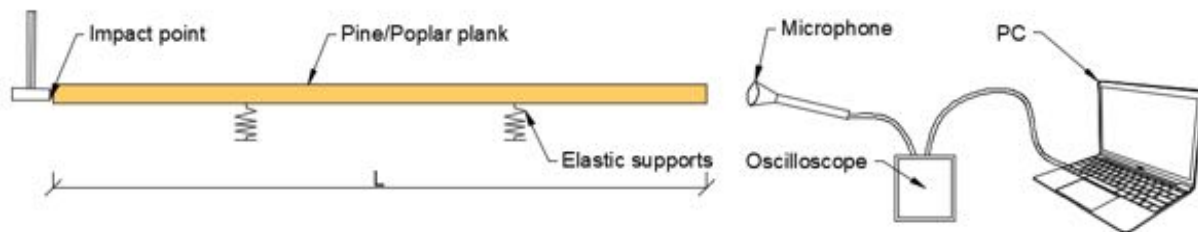


Figure 2.3: ART layout for planks. L=Plank length.

Response vibration signals along the longitudinal direction were collected with a t.bone MM-1 Thomann microphone and transducer to an electrical signal recorded with a Picoscope 4424 oscilloscope with 80 MS/s. Fundamental resonance frequency f_1 of each plank was obtained by means of spectral analysis. Using this frequency and the density of each plank (ρ_p), the dynamic elastic modulus ($MoE_{dyn,p}$) can be estimated as follows:

$$v = 2Lf_1 \tag{2.1}$$

$$MoE_{(dyn,p)}^* = \rho_p v^2 \tag{2.2}$$

where L is the plank length, and v is the propagation velocity of the stationary elastic wave. Furthermore, a correction of the dynamic elastic modulus ($MoE_{dyn,p,12}$)

from the real MC_p measured with a digital moisture meter to the $MC=12\%$ was carried out according to the standard [20] as,

$$MoE_{dyn,p} = MoE_{dyn,p}^* (1 + 0.01(MC_p - MC_{12\%})) \quad (2.3)$$

Figure 2.4 depicts the dynamic modulus of elasticity of all the planks. Results for poplar and pine follow normal distributions, with smaller values of the dynamic elastic modulus and a more reduced deviation values for the case of poplar timber compared with pine.

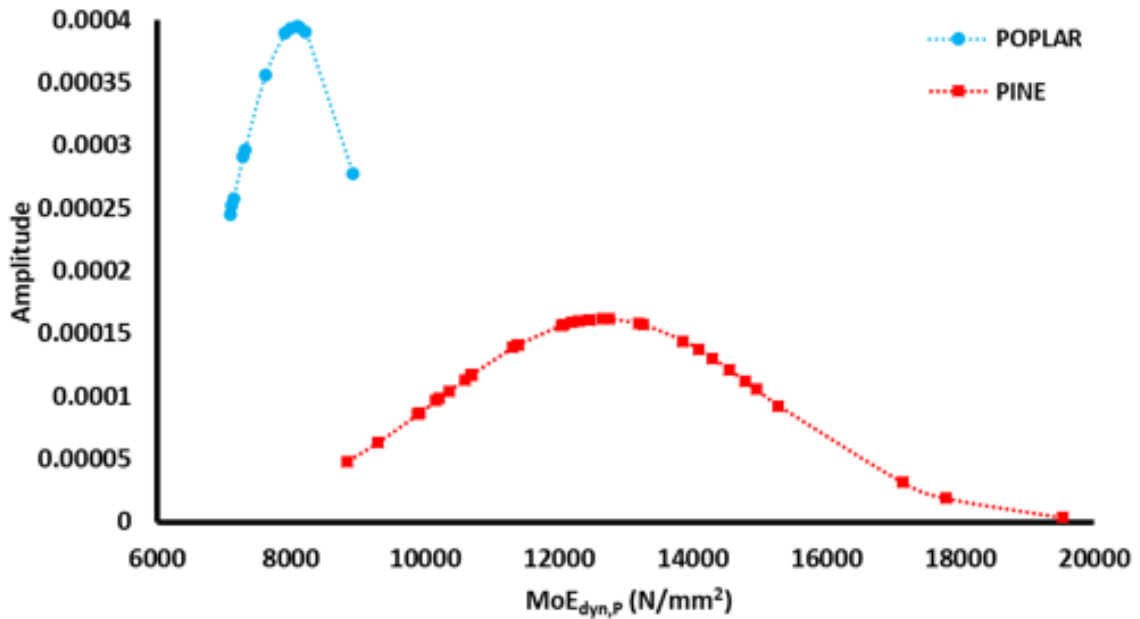


Figure 2.4: Normal distribution of the dynamic modulus of elasticity of the planks.

2.2.4 Planks strength grading

By using the $MoE_{dyn,p}$, all the planks were graded according to the standard [21] (see 2.1). That standard also associates the T strength class of the planks, which comply the minimum values of C strength class for sawn structural timber according to standard [22]. Figure 2.5 shows the distribution of planks for each particular T and C class. Within each T strength class, the planks were considered structurally equivalent and were randomly selected for glulam timber manufacturing.

2.2.5 Glulam timber samples

Three different types of 4-layers laminated timber were designed and compared; pure poplar (PPo), pure pine (PPi) and mixed poplar/pine (MPoPi) as shown in Figures 2.7. Due to the budget limitations, only two samples were manufactured for each type. Based on the T strength class of the planks and the recommendations for homogeneous timber given by the standard [21] (Table 2.2), different layouts were set up for the case of pine or poplar pure layouts used as control specimens.

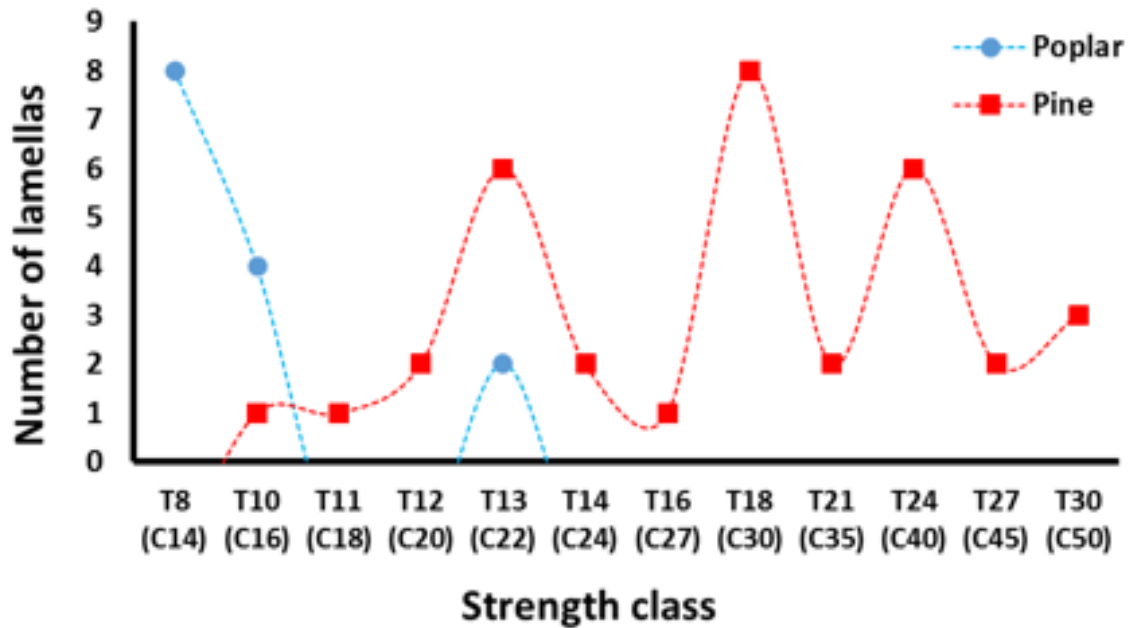


Figure 2.5: Distribution of planks according with the T and C strength class.

Figure 2.6 indicates also the GL strength class theoretically assigned by the mentioned standard (named in this paper as "design class"), except for the case of poplar/pine mixed timber because the standard does not consider multi-species layouts, and for the PPO1 sample due to the very low out-standard strength class of the poplar planks (T8).

It should be also noticed that the pine planks of the pure pine control sample PPI2 and mixed sample MPOPi1 have the same design class, T24. Thus, its mutual comparison can be used to evaluate the influence of the substitution of inner pine planks by poplar ones. The planks were glued each other by using the polyurethane resin PUR-20 from Bakar[®] with a amount of adhesive of 350 g/m^2 , applying a constant pressure during 4 hours without using any finger joints.

The elaboration process was carried out following the requirements of the standard [21](Annex I). During the elaboration process the temperature and humidity of the room (HR) was of 20°C and 40%. As indicated by the standard, the time between mechanization and gluing of the planks was lower than 24 hours. The resulting dimensions of the samples were $b=40 \text{ mm}$, $h=80 \text{ mm}$, and $L=1230 \text{ mm}$.

2.2.6 Dynamic modulus of elasticity of the glulam timber

Each particular sample was subjected to a longitudinal ART [17,18] as described in Section 2.2.3 and shown in Figure 2.3, thus obtaining the longitudinal dynamic modulus of elasticity ($MoE_{dyn,gt}$), including the MC=12% correction for each sample.

2.2.7 Semi-analytical modulus of elasticity

Since the samples are formed by planks with similar elastic properties, the parallel axis theorem or Huygens-Steiner theorem [19] can be used to semi-analytically obtain a combined modulus of elasticity, MoE_c . It was calculated by using the experimental dynamic modulus of elasticity ($MoE_{dyn,p}$) for each individual planks, as

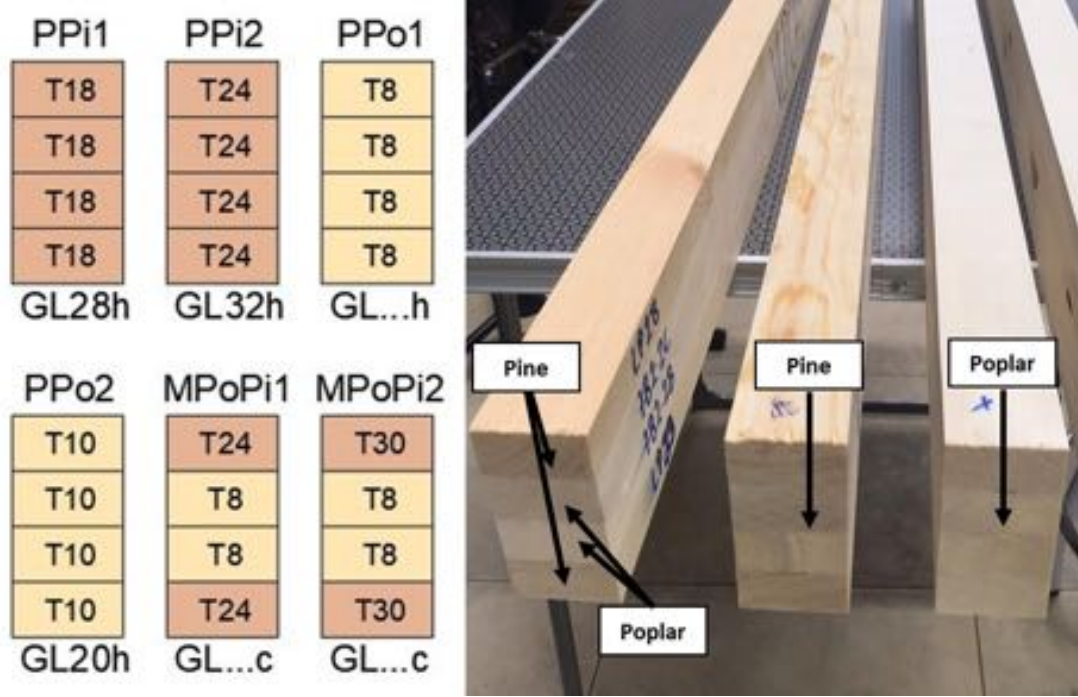


Figure 2.6: Timber layers design according with planks grading and strength class GL proposed by the standard. PPI: pure pine. PPO: pure poplar. MPOPi: mixed poplar/pine. GLXc: design grading for combined. GLXh: design grading for homogeneous.

$$MoE_c = \sum_{l=1}^N \frac{MoE_{dyn,p} \cdot I_p + A_p \cdot MoE_{dyn,p} \cdot y_p^2}{I_c} \quad (2.4)$$

where I_p is the second moment of inertia respect to sample axis, A_p is the cross-section of the sample, y_p is the distance from the combined neutral axis to the neutral axis for each particular plank p , and I_c is the combined second moment of inertia.

2.2.8 Bending test

Following the standard [19], a monotonic four-point bending test was performed for each particular sample (see Figure 2.7). Due to the plank sizes and in order to avoid torsion effects caused by a small base of the samples, a 14 h ratio was set, scaling the standard arrangement. Displacement control ratio was set at 4 mm/min, in order to fulfill the requirements of the aforementioned standard. A 100 kN-capacity testing machine was used. Two strain gauges were glued at the mid-span section of the sample on the bottom and top faces, in order to measure the maximum tensile and compression strains, respectively. The span between supports was set as 1130 mm. The maximum stress σ_{max} was calculated as:

$$\sigma_{max} = \frac{M_{max}}{W} \quad (2.5)$$

where M_{max} is the maximum bending moment and W is the section modulus. Similarly, the static modulus of elasticity MoE_{st} was calculated by using the stress-tensile strain curve, as the slope in the linear range between 20%-40% of the maximum stress.

CHAPTER 2.

EXP. AND NUM. ANALYSIS OF MIXED I-214 POPLAR/PINUS

Moreover, the global modulus of elasticity $MoE_{st,g}$ was also obtained according to the standard [19] (Section 10.3) as

$$MoE_{st,g} = \frac{3aL^2 - 3a^3}{2bh^3 \left(2 \frac{\delta_{40} - \delta_{20}}{L_{40} - L_{20}} - \frac{6a}{5Gbh} \right)} \quad (2.6)$$

by using the load-displacement ($L-\delta$) curve, in the same load range as MoE_{st} (20%-40% of the maximum load). The displacement was measured by means of a LVDT placed as shown in Figure 2.7.

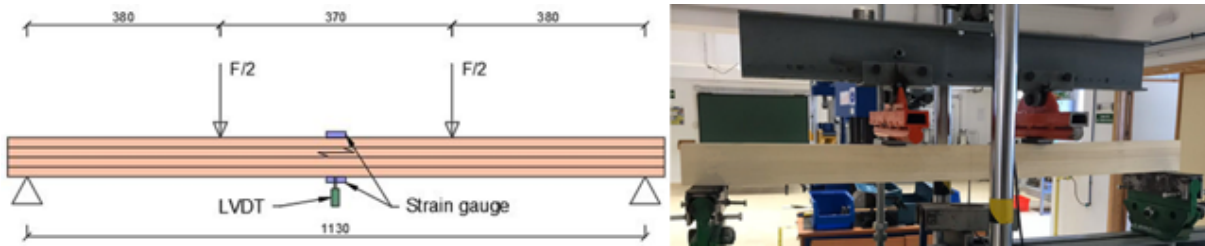


Figure 2.7: Four-point bending test arrangement and pure poplar sample during the bending test. Distances in mm.

2.2.9 Strength grading of glulam timber samples

All the mechanical properties were considered initially for the strength grading but the density and maximum stress in bending were not the critical properties for strength grading. Thus, all the samples were graded taking into account the critical property, the modulus of elasticity as follows: 1) Using the dynamic modulus $MoE_{dyn,gt}$; 2) Using the semi-analytical combined elastic modulus $MoE_{dyn,c}$; 3) Using the static modulus MoE_{st} .

2.2.10 Numerical modelling

A three-dimensional finite element model (3D-FEM) was developed into the open source finite element code Salome Meca (Code Aster)[®] [23] to evaluate the behaviour of the manufactured glulam timber subjected to four-point bending test. The samples were modelled as elasto-plastic solids and non-linear analyses were performed using a linear elasto-plastic constitutive model with hardening. The constitutive model received as input parameters the elastic modulus, shear modulus and Poisson's ratio for the linear elastic part, and the yield stresses for the plastic part with hardening. The 3D-FEM model consists of one piece with a rectangular cross-section and four simply supported solid rollers (see Figure 2.8). Bottom rollers represent the supports and top ones the points of application of the loads in the testing machine. In order to get accurate results with reasonable computational cost, an analysis of convergence of results dependent of element size was carried out. An optimum size of 8 mm was achieved and the sample was meshed into 9240 eight-node brick elements having a total number of 11935 nodes. Each roller was meshed into 1648 six-node wedge elements with a total number of 1109 of nodes, allowing a proper adaptation to the cylindrical shape. Figure

2.8-right shows in detail the defined mesh for the supports and load cells. The average radial size for each element was of 2.75 mm and outermost size of 5.85 mm was adopted, resulting in a total roller diameter of 30 mm. As a first step for the 3D-FEM model, timber was assumed to behave as an isotropic material due to the configuration of loads and boundary conditions. Rollers for the experimental test were made of steel so, in consequence, the elastic modulus of 210 GPa and the Poisson's ratio of 0.3 were considered.

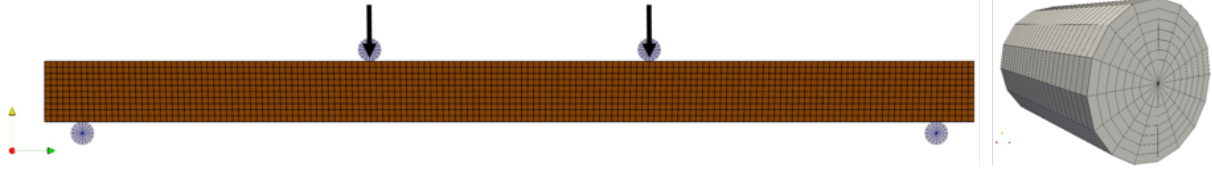


Figure 2.8: 3D-FEM model for a four-point bending test set-up and 3D-Mesh of load cells/supports.

In coherence with the experimental test, bottom rollers were restrained to move in any direction and the top rollers (points of load application) were constrained to remain horizontal, while being able to rotate and moving vertically during the simulation. Further, a contact restriction between roller and the laminated specimen surface was prescribed. Definition of contact requires the description contact candidates which comprise the slave and master surfaces [24]. The contact formulation, applied to the simulation, are normal and frictional penalties [25] due to their ability to soften the non-linearities induced by contact. Mechanical stiffness of penalty springs was calibrated to 1×10^9 kN/m according to the guidelines given in [26], while the friction coefficient was set to 0.3, which is a common value for the friction for steel surfaces. In order to simulate the whole experimental process and to improve the convergence of the contacts, the load increases linearly and is applied in the center of gravity of each top roller.

The set of non-linear equations from the finite element model was solved with a direct full Newton non-linear solver. The solution provides the displacements, elastic/plastic stresses and strains at each increment. A set of nodes located at the bottom face of the mid-span, in the same positions as LVDTs, was used to obtain the deflection during the simulation.

Moreover, in order to obtain the mechanical properties for the FEM model, a calibration process was carried out. It consisted of running the analysis using a starting value of elastic modulus, equal to the one determined through the experimental part (MoE_{st}), and then the elastic and plastic parameters as the yielding stress (σ_y) were adjusted to fit the experimental patterns. In order to compute a reasonable shear modulus (G), MoE_{st} is enforced to be equal to $MoE_{st,g}$ in Eq. 2.6. The rest of known parameters from Eq. 2.6 represent: L - span of the sample, a - distance between the supports and its nearest point of load application, b - base of the sample, h - height of the sample, L_{20} and L_{40} load at 20% and 40% of the maximum load, respectively, and δ_{20} and δ_{40} the corresponding displacement registered with de LVDT at that load values. Thus, the only unknown to be solved is the value of the shear modulus G. The Poisson's ratio (ν) was set as 0.37 by means of tests performed in [27]. Two calibration processes were carried out by considering G or not, thus obtaining the calibrated modulus of elasticity $MoE_{FEM,G}$ and MoE_{FEM} , respectively. In both cases, the calibration procedure was considered to be finished when the difference between numerical and experimental

stiffness in the elastic regime was lower than 5%. Increments of applied load, ΔL , and corresponding displacements, $\Delta \delta$, were used to compute the stiffness K applying the following relation:

$$K = \frac{\Delta L}{\Delta \delta} \quad (2.7)$$

Stiffness of the samples was computed between 15%-35% of the elastic range, based on the force-displacement relationship, for both the numerical and experimental part.

2.3 Results

Figure 2.9 shows the stress-strain curves for all the samples by using the tensile strain gauge. The samples are clearly grouped in three groups, the stress following the order $MPoPi > PPi > PPo$. Pure pine $PPi2$ sample and mixed $MPoPi1$ sample had very similar behaviour as plotted separately. It can be also observed in Figure 2.10, which compares the different static modulus of elasticity and strength class using the MoE_{st} .

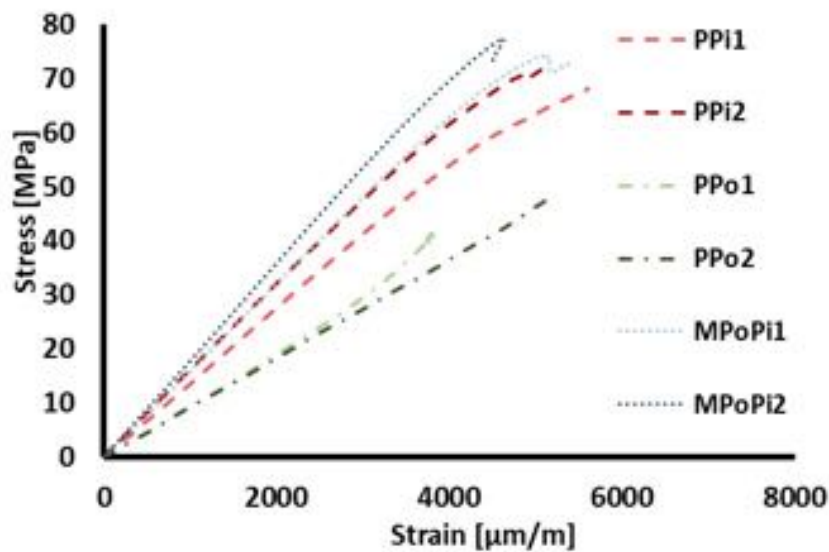


Figure 2.9: Stress versus strain for the tensile strain gauge (bottom face) for all the samples.

Figure 2.11 plots the load-displacement relations and their corresponding yield limits, comparing experimental and numerical results. An excellent agreement can be observed for all the tested samples. Table 2.2 presents the strength grading results for different elastic moduli.

Table 2.1 summarizes the results obtained for each sample, i.e. static, dynamic, semi-analytical, and numerical modulus as well as the maximum stress. The four parameters also follows the order previous mentioned, i.e. $MPoPi > PPi > PPo$.

Figure 2.12 represents the relationship between the static and dynamic moduli, in which it can be observed that the higher variations were reached by the mixed samples. Table 2.2 presents the strength grading results with the different elastic moduli.

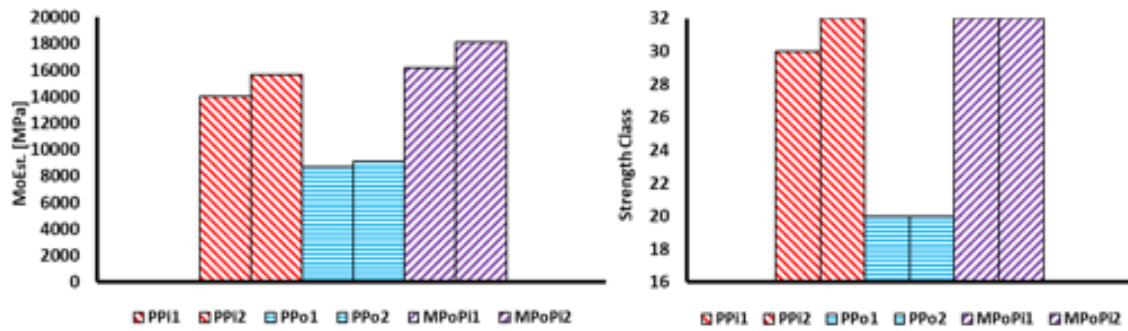


Figure 2.10: General results for the tested samples. Left: Static modulus of elasticity (MoE_{st}). Right: Strength grading of the samples with MoE_{st} .

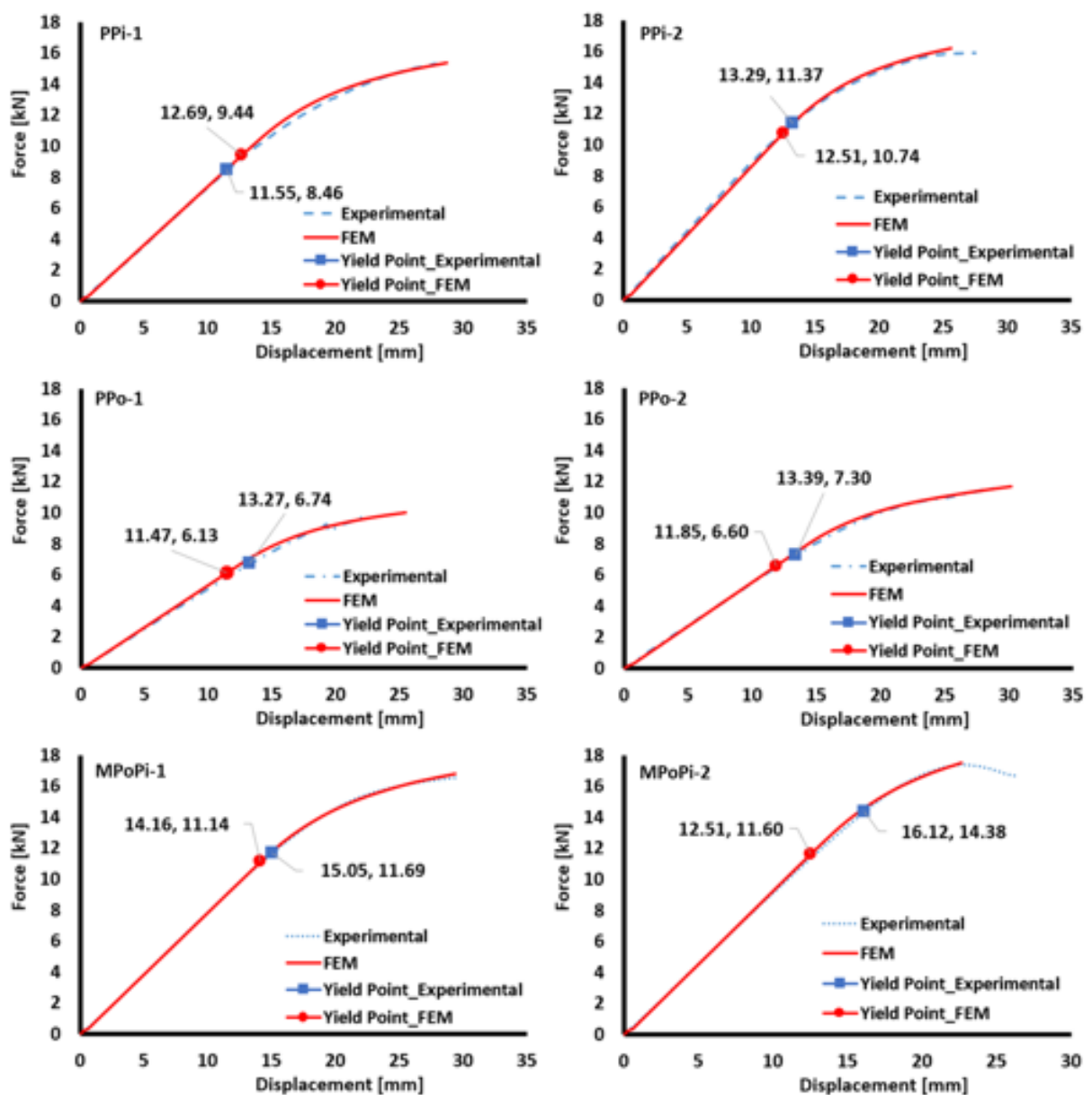


Figure 2.11: Numerical and experimental load-displacement plots and their corresponding yield limits.

Sample name	Planks SC	MoE_{st} (MPa)	$MoE_{FEM,G}$ (MPa)	$MoE_{dyn,gt}$ (MPa)	MoE_c (MPa)	σ (MPa)
PPi1	T18	14003	13030	12420	12463	62.3
PPi2	T24	15644	15544	14888	14604	65.8
PPo1	T8	8703	8603	7689	7554	39.7
PPo2	T10	9098	8908	8699	8462	49.8
MPOPi1	T ^o 24, T ⁱ 8	16162	15021	11612	13328	67.4
MPOPi2	T ^o 30, T ⁱ 8	18116	17444	12557	16332	70.6

Table 2.1: Main mechanical properties of the tested samples. MoE_{st} : static modulus of elasticity. $MoE_{dyn,gt}$: dynamic modulus of elasticity. MoE_c : semi-analytical modulus of elasticity. $MoE_{FEM,G}$: numerical modulus of elasticity using G. σ_{max} : Maximum stress. PPI: pure pine. PPO: pure poplar. MPOPi: mixed poplar/pine. T^o: Outer planks. Tⁱ: Inner planks

Sample name	SC Planks	SC Design	SC (MoE_{st})	SC ($MoE_{dyn,gt}$)	SC (MoE_c)
PPi1	T18	GL28h	GL30h	GL26h	GL26h
PPi2	T24	GL32h	GL32h	GL32h	GL32h
PPo1	T8	–	GL20h	–	–
PPo2	T10	GL20h	GL20h	GL20h	GL20h
MPOPi1	T ^o 24, T ⁱ 8	–	GL32c	GL24c	GL30c
MPOPi2	T ^o 30, T ⁱ 8	–	GL32c	GL28c	GL32c

Table 2.2: Strength grading for the tested samples according to the different modulus of elasticity. MoE_{st} : static modulus of elasticity. $MoE_{dyn,gt}$: dynamic modulus of elasticity. MoE_c : semi-analytical modulus of elasticity. PPI: pure pine. PPO: pure poplar. MPOPi: mixed poplar/pine. T^o: Outer planks. Tⁱ: Inner planks.

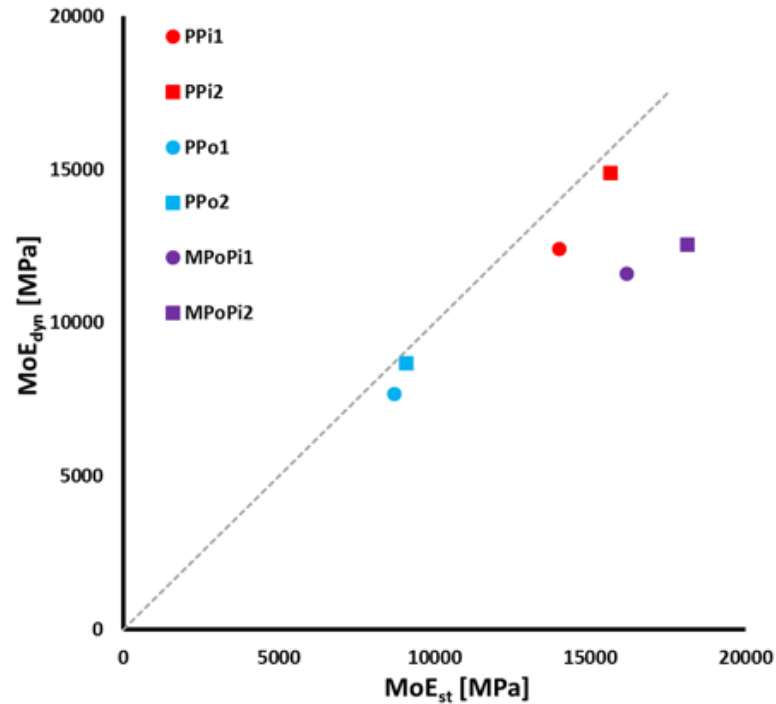


Figure 2.12: Comparison between modulus of elasticity for the tested samples. $MoE_{dyn,gt}$: dynamic modulus of elasticity. MoE_{st} : static modulus of elasticity. Gray dotted line: $y=x$.

2.4 Discussion

It can be observed that, when design strength class is available, a good agreement with the experimental and design strength is achieved. Moreover, as expected, higher mechanical properties are obtained for pure pine and mixed poplar/pine samples, compared with those for pure poplar samples, due to the lower grading of poplar timber compared with pine. However, similar values of MoE_{st} are obtained for pure pine sample PPI2 and mixed sample MPOPI1, the difference being no bigger than 3%, since they both used T24 pine planks in the outer layers. This demonstrates that the inner layers do not contribute significantly to the sample elastic modulus, allowing the use of low-grade species like poplar for these inner planks. As mentioned in [8][8], when mixing species, the outer layers of the samples provide the main stiffness contribution to the total sample. In particular, it is observed that by applying the Huygens-Steiner theorem (Eq. 2.4) and using the dynamic elastic modulus obtained for each plank, it is possible to obtain the contribution of each particular plank to the total modulus. As an example, Table 2.3 presents the results for the pure pine PPI2 and mixed poplar/pine MPOPI1 samples, with their corresponding planks strength classes and dynamic moduli of elasticity. The results clearly demonstrate that for both planks the outer planks contribute with 87% and 95% of the total stiffness for the PPI2 and MPOPI1 planks, respectively, just leaving only 13% and 7% of modulus contribution for the inner planks.

Table 2.4 shows the variations of the numerical, dynamical and semi-analytical moduli respect to the static modulus MoE_{st} . It can be observed that the variations between experimental and numerical results are very small, always below 8% for all the types of samples. In many cases, those differences are even less than 2%, demon-

CHAPTER 2.
EXP. AND NUM. ANALYSIS OF MIXED I-214 POPLAR/PINUS

Sample name	SC planks	$MoE_{dyn,p}$ (MPa)	Contribution to the total MoE_c (%)
PPi2	T ^e 24	14708	44.1
	T ⁱ 24	14932	6.4
	T ⁱ 24	14693	6.3
	T ^e 24	14441	43.3
MPoPi1	T ^e 24	14234	46.7
	T ⁱ 8	7982	3.7
	T ⁱ 8	7611	3.6
	T ^e 24	14002	46.0

Table 2.3: Huygens-Steiner theorem results for the pure pine PPi2 and mixed poplar/pine MPoPi1 samples. T^e: External planks. Tⁱ: Inner planks. $MoE_{dyn,p}$: dynamic modulus of elasticity of each plank. MoE_c : semi-analytical dynamic modulus of elasticity.

strating the effectiveness of the numerical modelling and calibration procedure using the shear modulus. More in detail, as shown in Figure 2.11, an excellent performance is achieved in the elastic range. Meanwhile, when plastification occurs, both experimental and numerical curves start to diverge, mainly due to the complex phenomenon at this load stages (cracking, debonding, etc.).

Moreover, the limit between elastic and plastic ranges is clearly separated by the definition of the yielding points for both approaches, as shown on the Figure 2.11. A big similarity is observed for this transition for both experimental and numerical methodologies.

When comparing the dynamic modulus and the semi-analytical moduli with the static modulus MoE_{st} , the variations become lower than 15% for the case of pine and poplar pure samples, demonstrating the effectiveness of these non-destructive methodologies. It can be observed how the results (elastic modulus and strength grading) are very similar each other with both non-destructive methods.

However, big variations are observed for the case of mixed samples, around 40% for the case of the dynamic modulus and 20% for the semi-analytical one. These high variations can be associated to the heterogeneity of the cross-section and the high variation of the strength class of the planks, T8 for the inner layers and T24 and T30 for the outer layers, respectively.

Considering this fact, both non-destructive methods (especially the ART carried out on the whole laminated sample) are unable to provide reliable strength grading. These results are confirmed in the Figure 2.12, in which the points corresponding to the mixed samples significantly move away from the $y=x$ straight line. However, the points corresponding the pure samples fall almost on this straight line.

It should be emphasized that the good agreement between numerical and experimental moduli is mainly due to the calibration process using the shear modulus (G). In order to discuss this issue, the influence of the shear modulus (G) is analyzed in Table 2.5, in which the experimental global modulus $MoE_{st,g}$ and the numerical modulus MoE_{FEM} , and their variations respect to the static modulus MoE_{st} , are shown. The global modulus $MoE_{st,g}$ is obtained experimentally, and it does not include the shear effect. Similarly, MoE_{FEM} is calculated without including G in the model. It is clearly observed that in both cases, very high variations are obtained (between 9%-50%). It

demonstrates the need to include G in both experimental global modulus and numerical modelling procedures. As a reference, Table 2.6 shows the value of the experimental and the calibrated shear moduli. A big similarity is obtained between them for all the tested samples.

Sample name	Variation of $MoE_{FEM,G}$ (%)	Variation of $MoE_{dyn,gt}$ (%)	Variation of $MoE_{dyn,c}$ (%)
PPi1	7.5	12.7	12.4
PPi2	0.6	5.1	6.0
PPo1	1.2	13.2	15.2
PPo2	2.1	4.6	7.5
MPOPi1	7.6	39.2	21.3
MPOPi2	3.8	44.3	10.9

Table 2.4: Variation in % of the elastic moduli respect to the static modulus MoE_{st} . Comparison of the numerical and experimental moduli of elasticity. MoE_{st} : static modulus of elasticity. $MoE_{FEM,G}$: calibrated modulus of elasticity using G. $MoE_{dyn,gt}$: dynamic modulus of elasticity. $MoE_{dyn,c}$: semi-analytical modulus of elasticity. PPO: pure poplar. MPOPi: mixed poplar/pine.

Sample name	$MoE_{st,g}$ (MPa)	Variation of $MoE_{st,g}$ (%)	MoE_{FEM} (MPa)	Variation of MoE_{FEM} (%)
PPi1	11474	22.0	11000	27.3
PPi2	12830	21.9	12544	24.7
PPo1	7976	9.1	7503	16.0
PPo2	8322	9.3	8008	13.6
MPOPi1	11955	35.2	11260	43.5
MPOPi2	13801	31.3	13444	34.7

Table 2.5: Comparison of experimental and numerical moduli of elasticity without considering the shear modulus and their variation in % respect to the static modulus MoE_{st} . MoE_{st} : static modulus of elasticity. $MoE_{st,g}$: global static modulus of elasticity. MoE_{FEM} : calibrated modulus of elasticity without using G.

Finally, Table 2.7 depicts the stiffness obtained from the numerical simulations and experimental data from Figure 2.11. As mentioned above, the elastic range is very similar for both phases, supported by a low value of error between numerical and experimental stiffness, which is below 4%. It is clear that the pure poplar samples show the lowest stiffness as confirmed by the results, while the mixed pine poplar sample MPOPi2 show the highest one, due to the existence of the T30 plank's strength class at the outer layers.

The pure pine samples show a relatively small reduction of the stiffness compared with the MPOPi-2 specimen, which demonstrates that the extreme fibers have the highest contribution to the general strength of the sample.

In particular, by comparing PPi2 and MPOPi1 samples, which are composed by the same strength class of outer planks, T24, it is clear that the insertion of poplar planks at the inner part produces a very small reduction of the stiffness. Similarly, the results

CHAPTER 2.
EXP. AND NUM. ANALYSIS OF MIXED I-214 POPLAR/PINUS

Sample name	G_{ex} (MPa)	G_{FEM} (MPa)
PPi1	300	300
PPi2	361	317
PPo1	451	401
PPo2	460	410
MPOPi1	217	229
MPOPi2	274	284

Table 2.6: Comparison of the shear moduli of elasticity. G_{ex} : experimental shear modulus. G_{FEM} : calibrated shear modulus used for numerical simulation.

Sample name	K_{ex} (N/mm)	$K_{FEM,G}$ (N/mm)	Variation of $K_{FEM,G}$ (%)	K_{FEM} (N/mm)	Variation of K_{FEM} (%)
PPi1	760	761	0.1	765	0.5
PPi2	850	880	3.4	881	3.5
PPo1	529	548	3.5	552	1.3
PPo2	551	565	2.5	564	2.2
MPOPi1	792	805	1.6	783	1.2
MPOPi2	915	949	3.6	935	2.2

Table 2.7: Experimental and numerical stiffness used for the calibration of the FEM model. K_{ex} : experimental stiffness. $K_{FEM,G}$: calibrated numerical stiffness using G. K_{FEM} : calibrated numerical stiffness without using G. Variation in % computed respect to K_{ex} .

from the Table 2.6 also show that the shear modulus does not play an important role in the computation of stiffness (K), keeping a variation below 3.5% with and without using G.

2.5 Conclusions

An experimental and numerical comparison of the mechanical behaviour and strength grading between pure pine and poplar and mixed poplar/pine laminated timber has been carried out. The main conclusions of the paper are as follows:

- Higher mechanical properties are obtained for pure pine and mixed poplar/pine laminated timber, compared with pure poplar one, due to the lower grading of poplar timber compared with pine.
- The inner planks do not contribute significantly to the whole sample elastic modulus, allowing the use of low-graded species like poplar for the inner layers of the sample.
- After calibration and using the shear modulus in the formulation, an excellent agreement is obtained between numerical and experimental results. The use of the shear modulus in the formulation must be considered in order to obtain very low variations with the experimental results. Similarly, the experimental global modulus without including the shear effect, does not provide reliable results with very high variations.

- The dynamic modulus and the semi-analytical elastic modulus obtained from the ART non-destructive grading of the whole sample or particular planks, respectively, is in good agreement with the static modulus and consequent strength grading for the case of pure samples, with relatively low variations.
- Non-destructive testing grading based on ART provide a very low grading yield for the case of mixed samples, with very high variations. Thus, this methodology should be reformulated and adapted in the future in order to get more reliable grading results.
- The insertion of low-grade poplar planks at the inner layers produces a very small reduction of the stiffness compared with the pure pine type.
- The shear modulus does not play an important role in the computation of stiffness (K), with very low variations between using and not using G.
- It should be emphasized that due to the low number of samples used for each layout, the results of this work should be considered only in qualitative and not in quantitative terms. In a future work, the elaboration of the glulam timber using the technology of the finger joints as done industrially will be considered.

Chapter 3

Modulus of elasticity of I-214 young poplar wood from standing trees to sawn timber: Influence of the age and stand density

Title	Modulus of elasticity of I-214 young poplar wood from standing trees to sawn timber: influence of the age and stand density
Authors	A. Gallego; M.A. Ripoll; C. Timbolmas; F. Rescalvo; E. Suarez I. Valverde; M. Rodríguez; F. B. Navarro; E. Merlo
Journal	European Journal of Wood and Wood Products
ISSN	0018-3768
Journal's performance	Journal impact factor (2020): 2.014 Q2 (Materials Science, Paper & Wood: 7/22)
Details	Volume: 79 (5) – Published: September 2021; Pages: 1225-1239
DOI	10.1007/s00107-021-01675-5

3.1 Introduction

The *Populus* species is one of the most important plantation species in Spain, occupying approximately 145,000 ha in 2016 according to FAO [5, 28]. The poplar groves understood as fast growing and short cycle planted forests (ranging from 9 years in the South to 18 years in the North of Spain), promote the local economic sustainable development based on the processing and use of wood resource. The silvicultural treatments of these intensive plantations and especially the plantation density together with the clonal selection, determine the growth and the technological properties of the resulting wood [29]. In particular, the stand density is the most important silvicultural factor used to control tree growth and wood quality production by altering growing conditions in utilization of nutrients, water and sunlight, which will eventually affect the wood characteristics [30, 31]. Typically, the ring width and the wood density can be affected by the site and silviculture management, and by the stand density, in particular [32].

CHAPTER 3.

MODULUS OF ELASTICITY OF I-214 YOUNG POPLAR WOOD

The mechanical properties of poplar wood at early ages have been evaluated by various authors with different destructive and non-destructive methods, showing clonal differences [33] and even comparing the results with other species [34]. The results observed by Huda [35] showed very interesting mechanical properties of some particular poplar clones for a wide range of high added value applications (e.g. plywood manufacturing and sawn timber for construction sector). The study developed by Yu [36] to better understand the variability in mechanical properties of hybrid poplar clones indicated no uniform trends relating growth rate to either higher or lower modulus of elasticity/modulus of rupture.

The *P. x euroamericana* hybrid I-214 clone is one of the most genetic materials used in poplar plantation in Spain. However, this clone has low mechanical properties as shown by various studies in France and Spain. Casado [37] showed in their research a significant influence of the width of the ring on the modulus of elasticity of the wood, and showed a moderate variability both in the width of the ring and in MOR and MoE (CoV=21%, 16.5% and 27% respectively). Based on this variability and in accordance with what was proposed by Van Acker [38] if progress is made in the correct characterization and selection of timber from poplar crops, the mechanical properties of the wood will be improved.

Non-destructive evaluation of timber as a material is widely used at different stages along the forestry and wood processing chain. By doing so, the potential quality of the timber can be evaluated without inflicting significant damage to the object evaluated [39]. These techniques are widely used for timber grading, enabling the stratification of sawn timber into quality classes defining or limiting their final use [40–42].

Although in recent years many studies have been carried out to predict the stiffness of wood by acoustic methods in different parts of the world especially in conifers [43], only some of them related the acoustic measurements in standing trees with the modulus of elasticity obtained after bending test until failure of the wood extracted from those trees (e.g. [44]). Very few studies have approached how standing tree acoustic velocity is directly linked to the mechanical properties of sawn timber in hardwood [45]. In some case as a study by Amateis and Burkhart [46] no correlation was reported between standing tree acoustic velocity and the timber mechanical properties in loblolly pine, suggesting that this was due to the small number of samples taken from each particular tree.

From tree to logs, correlations between the acoustic velocities on standing trees and logs appear to be relatively good ($R^2=0.71-0.93$), as reported in several previous studies in softwoods [47] (Moore et al. 2013) and hardwood [48]. Worse dependencies were achieved by Rais [49] for Douglas-fir wood, with a correlation of $R^2=0.35$. At the log level, the acoustic velocity was used in multiple studies for segregating logs by quality [50]. The acoustic methods for wood characterization on standing trees and logs are different (Time of Flight and Resonance).

Accuracy of the measurements can be affected by different factors such as the sensor position and distance between sensors, the type of device [51]), the signal arrival time on-set technique [33], the elastic supports in the case of logs and sawn timber [52], and the measurement of density at the time than acoustic test [53], between others. Any improvement and control of all these issues could help to optimize the results and gain accuracy. Grabianowski [54] found higher values when looking at timber sawn from outer-wood ($R^2=0.89$) than from core-wood ($R^2=0.74$). The viability of acoustic methods could be a very effective way exploring the intra-clonal variability and an

opportunity to select trees for wood quality improvement.

The current research proposes as main issue the evaluation and comparison of the bending modulus of elasticity in lumber with the dynamic modulus of elasticity obtained by acoustic non-destructive methods during three phases of the wood chain from different young plantations. Also, the second objective of this study is to evaluate the variability in the mechanical properties with the age and stand density of the plantations. Although some papers have addressed the use of acoustic methods to evaluate poplar wood [37, 55, 56] no previous studies have been identified following the methodology from tree to timber here proposed.

3.2 Materials and Methods

3.2.1 Forest and wood material description

Sixty nine trees from three private plantations, located in two different regions, were considered in this study (3.1), geographically-separated about 450 km. Genetic material was the same, Poplar clone I-214 (*Populus x euroamericana* (Dode) Guinier) in the three experimental sites. The main characteristic of the plantations are described in Table 3.1. The two GR plantations corresponded to two contiguous plots, one plot (GR_H) with higher stand density, and another (GR_L) with lower stand density. The meteorological conditions were very similar for both plantation sites, as well as the soil type. 15 trees from GU plantation, 18 trees for GR_L and 36 for GR_H were selected for the current study from the centre of each plantation. In all cases, the poplars placed at the edges of the plots were ignored for the analysis.

	GU	GR_L	GR_H
Clone	I-214	I-214	I-214
Location [DMS]	40°45'40.1"N 3°08'55.0"W	37°10'01.9"N 3°36'56.5"W	37°10'01.9"N 3°36'56.5"W
Soil	Calcaric Fluvisol	Calcaric Fluvisol	Calcaric Fluvisol
Age	13	9	9
Tree distance [m x m]	5.5 x 5.5	10 x 10	5 x 5
Stand density [stems·ha⁻¹]	330	200	400
Number of trees	15	18	36
Number of logs	29	18	36
Range of log length [m]	2.49 - 2.56	2.00 - 2.06	1.98 - 2.05
Range of log diameter [cm]	31.5 - 43.5	28.0 - 41.5	21.5 - 38.0
Number of sawn timber samples	72	55	67
Sawn timber sample section [mm²]	100 x 50	100 x 50	100 x 50

Table 3.1: Main characteristics of plantations, trees, logs and sawn timber samples. GU: Guadalajara; GR_L: Granada low-stand density; GR_H: Granada high-stand density.



Figure 3.1: Location of the plantation on the Iberian Peninsula. GU: plantation located at the Henares river basin, Guadalajara province, in the central area of the Iberian Peninsula. GR: two plantations located at the Genil river basin, Granada province, in the south of Spain.

The non destructive evaluation was carried out on the whole wood value chain, in 3 phases, as shown in Figure 3.2 Phase 1: standing trees; Phase 2: logs; Phase 3: sawn timber. After the acoustic evaluation, the sawn timber samples were subjected to four-point bending tests and compression tests parallel and perpendicular to the grain.

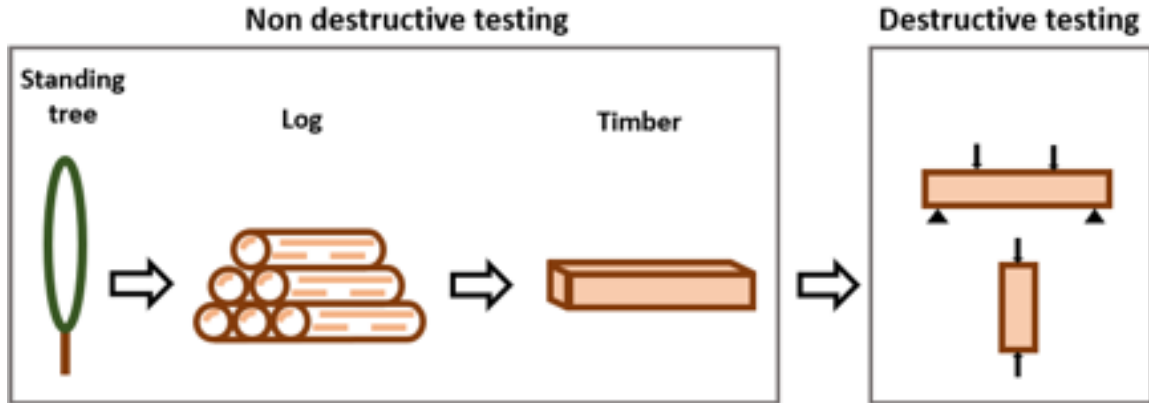


Figure 3.2: Testing from tree to timber

3.2.2 Acoustic test on standing trees

The Time-of-Flight method (ToF) was used to obtain the propagation velocity along the grain direction in standing trees. Two piezoelectric SD-02 Fakoop sensors with a resonance of about 20 kHz were nailed to the outermost part of the tree trunk (Fig. 3.3). The middle point between sensors was set at the breast height of the tree (1300 mm). Moreover, following the indications of previous works [39, 43, 57], the sensors were placed always at 600 mm from each other and the tip was inserted 25 mm into the wood. In order to ensure a good propagation of the longitudinal waves, the tips penetrated the trunk bark with an angle of 45° referring to the vertical axis of the tree.

A Picoscope[®] oscilloscope with a bandwidth of 20 MHz and a sample rate of 80 MS·s⁻¹ was used to record the signals generated by an impact hammer weighing 100 g on the upper sensor. Arrival time of the signals was calculated by means of the Akaike method as proposed in Rescalvo [33], which was used to calculate the propagation velocity shortly named as $C=d/\delta t$, d being the distance between the two transducers tips and δt being the difference arrival time of the signal to both transducers. Twelve velocity measurements per tree were carried out and the average value of the propagation velocity was used as velocity in a tree (C_T). Moreover, by means of a Trephor35 micro-corer, wood samples were extracted in order to obtain the outer wood green density (just in the tree area where the acoustic test is carried out). The cores were 4 mm diameter and had a maximum length of 35 mm without bark to calculate the green wood density by gravimetric method ($\rho_{g,T}$). Thus, the stiffness modulus in standing tree was estimated by the one-dimensional wave 3.1 approximation:

$$MoE_T = \rho_{g,t} \cdot C_T^2 \quad (3.1)$$

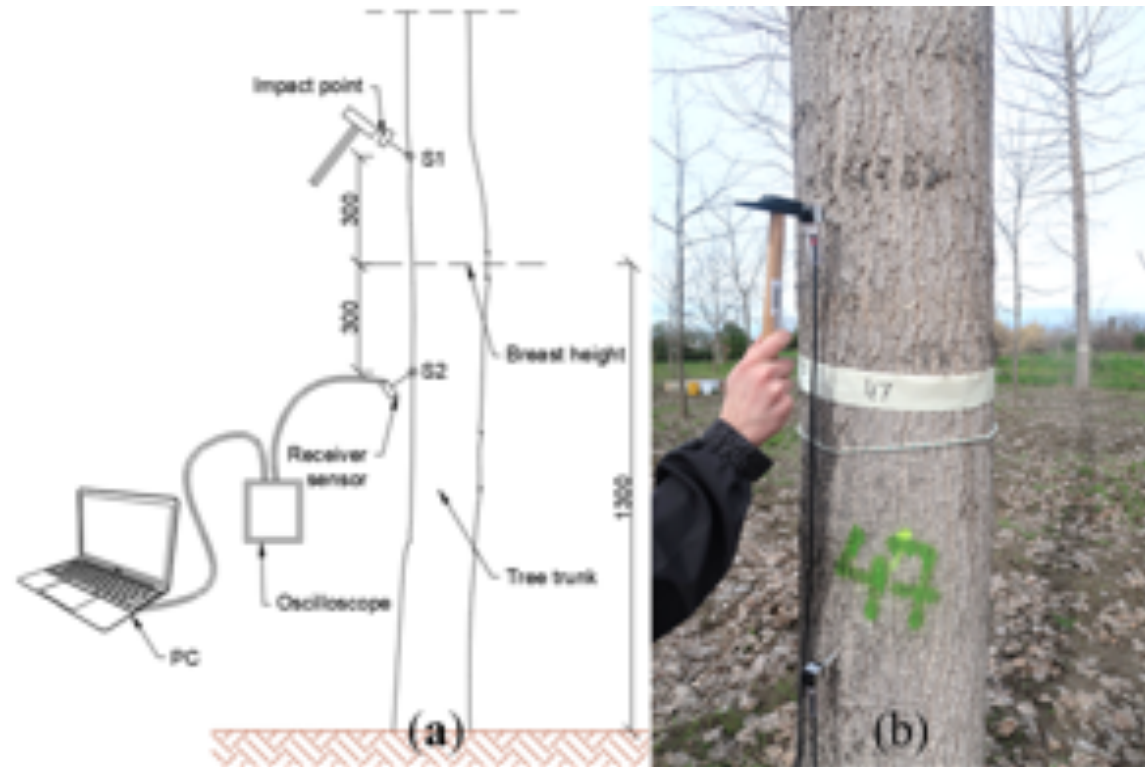


Figure 3.3: Acoustic test on standing trees: (a) Experimental setup; (b) Picture during test. S1: Impact point sensor. S2: Receiver sensor. Distances are shown in mm.

3.2.3 Harvesting and logs acoustic testing

After acoustic test on standing trees, the previously selected poplar standing trees were harvested and the diameter with bark was measured at different heights from the ground every meter until the height of 13.5 m and every two meters from 13.5 m until reaching the height (H), corresponding to a thin point diameter of 7 cm. Thus, the volume of wood of each particular portion was calculated using the Smalian formula [58],

$$V_p = \frac{(A_1 + A_2)}{2L_s} \quad (3.2)$$

where A_1 and A_2 are the area of log sections in the two heads of each particular portion and L_s is its length between two consecutive sections. Thus, the total volume of the tree, V , was obtained as the sum of the volumes of the individual portions until the height H [59].

After harvesting, one or two logs 2.0-2.5 m long were cut from each tree and used for the subsequent analysis presented in this work (see Table 3.1). Furthermore, in order to evaluate the percentage of false heartwood, which is associated with lower mechanical properties [60], for each log the false heartwood diameter and the ratio of false heartwood surface with respect to the total surface of the log head (FHW, %), were also measured [61]. The average FHW value between each of the two heads was calculated for each particular log.

Then, an acoustic resonance test was performed on each log consisting of striking with an impact hammer at one end and recording the response signal using an SD-02

sensor nailed on the opposite end (see Figure 3.4). From the response signal, the first longitudinal resonance frequency (f_1) was obtained as the first peak of the spectrum. In order to obtain the propagation velocity in the log with greater accuracy, the following actions were carried out: 1) The log was supported on elastic support at its central point, which allows reducing the damping effect of the first mode of vibration and better discrimination from other vibration modes; 2) The green density of the log, $\rho_{g,L}$ was obtained by its weight and volume, instead of obtaining a slice from one of its ends. Thus, assuming a constant section shape of the log, the elastic modulus of the log can be estimated by wave equation and the Newton-Laplace equation as follows:

$$C_L = 2L_L \cdot f_1 \quad (3.3)$$

$$MoE_L = \rho_{g,L} \cdot C_L^2 \quad (3.4)$$

where C_L is the propagation velocity of the stationary waves generated in the log at the first resonance f_1 , and L_L is the log length.

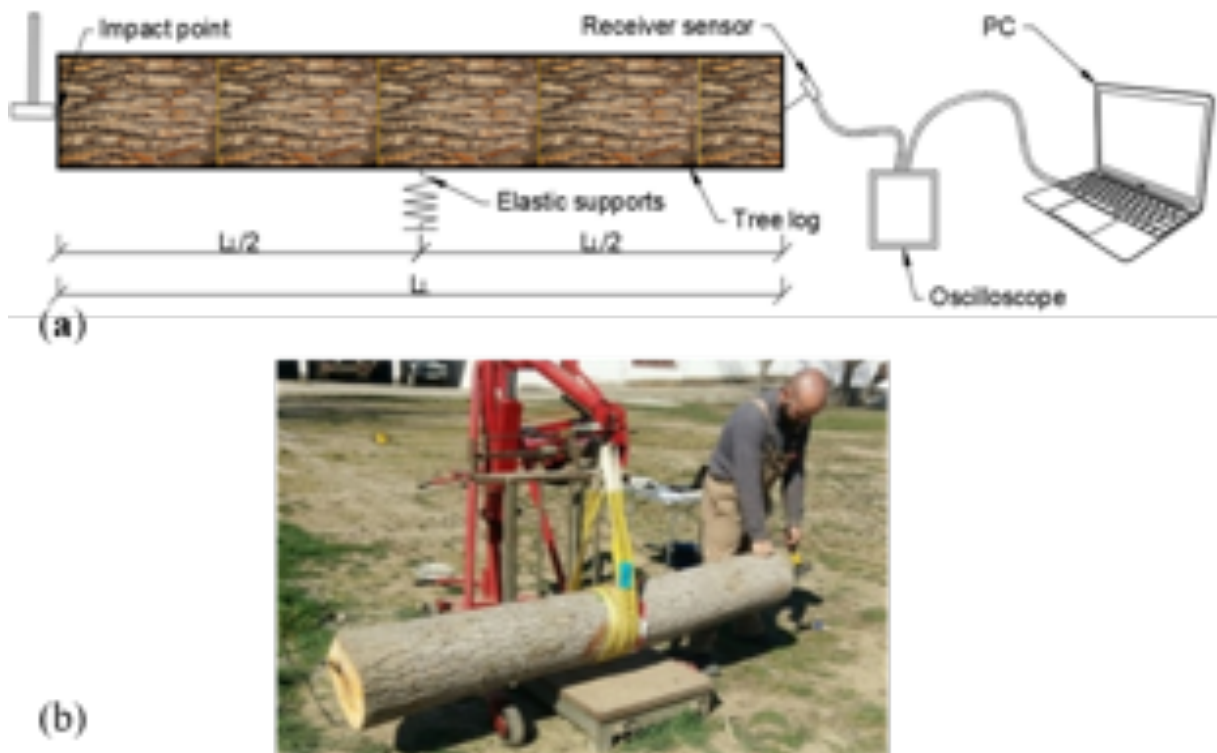


Figure 3.4: Acoustic resonance test on the logs. L_L : log length.

3.2.4 Sawing timber

The collected logs were taken to a local sawmill for each specific location. Two prismatic pieces were obtained from each log, as shown in Fig. 3.5 shows also the average cross-section of the logs of each plantation using the mean values of DBH and false heartwood ratio (FHW) for each case (Table 3.2). It was observed that due to the higher average DBH value and lower value of the FHW ratio of the logs from the GU plantation, the pieces only had sapwood. However, for the GR plantations, with a lower

CHAPTER 3.

MODULUS OF ELASTICITY OF I-214 YOUNG POPLAR WOOD

average DBH value and higher value of the FHW ratio, the sawn pieces had a certain portion of false heartwood.

Figure 3.6 shows some photographs of the sawing process. After sawing, the pieces were naturally dried in a ventilated space without direct solar radiation for 6 months, and subsequently conditioned at moisture content (MC, %) of around 12% before subsequent mechanical tests.

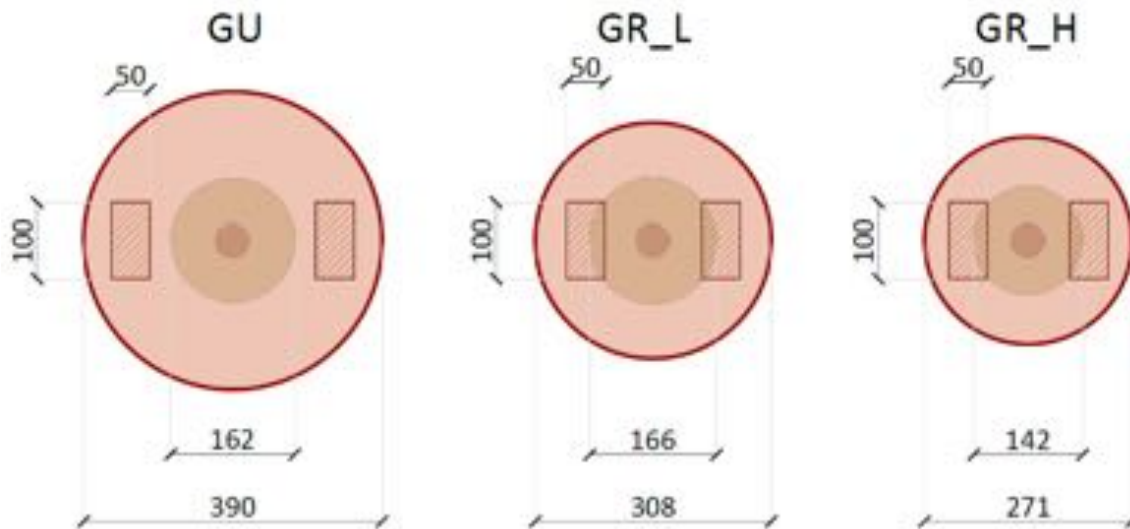


Figure 3.5: Theoretical cutting for obtaining the sawn timber samples for three different diameters of logs. Distances are shown in mm. GU: Guadalajara; GR_L: Granada low-stand density; GR_H: Granada high-stand density.



Figure 3.6: Pictures of the process from the log to timber

3.2.5 Acoustic test on sawn timber samples

Then, an acoustic resonance test was performed on each sawn timber sample consisting of striking with an impact hammer at one end and recording the response signal using a t.bonne MM-1 Thomann microphone, as shown in Figure 3.7. Assuming a constant section shape of the sample, the dynamic elastic modulus of the sample, MoE_{dyn} , was estimated by means of Equations 3.5 and 3.6. The specimens were subjected to free vibrations along the longitudinal grain direction with the sample supported in two elastics supports (Figure 3.7).

		<i>DBH</i> [cm]	<i>H</i> [m]	<i>V</i> [m ³]	Δ <i>DBH</i> [cm·yr ⁻¹]	<i>HW</i> (%)	<i>C_T</i> [km·s ⁻¹]	<i>C_L</i> [km·s ⁻¹]
GU		37.8±3.1	21.7±3.5	1.21±0.25	2.9±0.2	17.3±2.9	3.34±0.08	3.31±0.08
		A	A	A	B	B	A	A
GR	<i>L</i>	32.9±1.9	15.4±1.3	0.74±0.09	3.7±0.2	29.1±4.4	2.99±0.07	2.81±0.11
		B	B	B	A	A	C	C
	<i>H</i>	27.5±1.8	15.4±1.7	0.55±0.11	3.0±0.2	27.9±4.8	3.08±0.07	2.93±0.08
		B	B	C	B	A	B	B
Kruskal-Wallis test		F= 122 p < 0.05	F= 20.8 p < 0.05	F= 76.8 p < 0.05	F= 49.4 p < 0.05	F= 34.9 p < 0.05	F= 43.3 p < 0.05	F= 46.5 p < 0.05

Table 3.2: Mean value±SD. DBH: diameter measured at breast height; H: tree height at a 7 cm diameter point; V: tree wood volume; ΔDBH: annual DBH growth rate; FHW: false heartwood ratio; C_T: tree acoustic velocity; C_L: log acoustic velocity. GU: Guadalajara; GR_L: Granada low-stand density; GR_H: Granada high-stand density.

$$C_b = 2L_b \cdot f_1 \tag{3.5}$$

$$MoE_{dyn} = \rho_b \cdot C_b^2 \tag{3.6}$$

where C_b is the propagation velocity of the stationary waves generated in the sample at the first resonance f_1 , L_b is the sample length, and ρ_b is the sample density. The MC of each sample was measured and the MoE_{dyn} values were properly corrected to the MC=12% reference value [20,62].

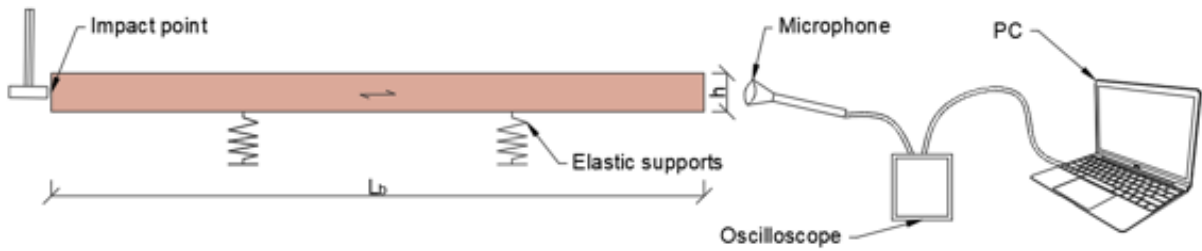


Figure 3.7: Experimental set-up of the acoustic test carried out on each particular sample. L_b : sample length, h : sample height.

3.2.6 Bending test

All the sawn timber samples were subjected to a monotonic four-point bending test following the EN 408:2010+A1:2012 [19] standard (see Figure 3.8). A constant displacement rate of $9.0 \text{ mm} \cdot \text{min}^{-1}$ was used in order to comply with the standard requirements. All the tests were performed in an S-110 CONTROLS S.A. testing machine with an electric actuator with a maximum load capacity of 100 kN. Dimensions were set up at 50 mm (b) x 100 mm (h), $a=500 \text{ mm}$, and $L=600 \text{ mm}$. The total span between supports was 1600 mm.

CHAPTER 3.

MODULUS OF ELASTICITY OF I-214 YOUNG POPLAR WOOD

All the samples were instrumented with one strain gauge placed at the bottom face (maximum tensile stress), at the mid-span of the sample as shown in Figure 3.8. Using the stress-strain curve for the tensile stress recorded by the strain gauge, the static modulus of elasticity (MoE) in bending was obtained as the slope of the curve between the 20% and 40% of the maximum bending stress, i.e., in the linear elastic zone. This modulus of elasticity differs from the global modulus proposed by the EN 408:2010+A1:2012 [19], since it is less affected by the shear effects, giving a value nearer to the modulus of elasticity in the longitudinal direction, $E_{0,m}$.

It should be emphasized that strain gauges were used instead of extensometers / displacement transducers (as indicated by the EN 408:2010+A1:2012 [19]), in order to avoid the influence of the shear stresses on the global modulus of elasticity (see [63] for more details). HBM LY series strain gauges were used for the strain measurement with a 10 mm grid length. The bonding was performed with a glue supplied by the same manufacturer and designed especially for porous materials such as wood.

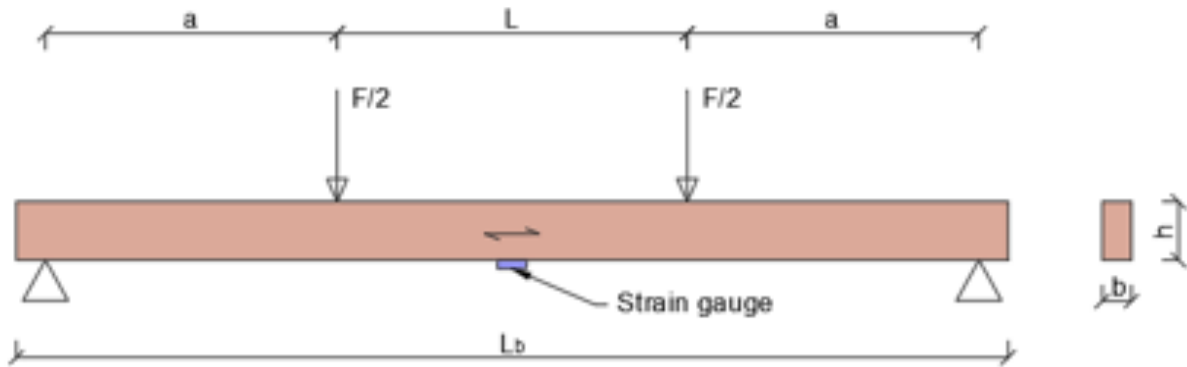


Figure 3.8: Experimental set-up of the four points bending test of the sample. L_b : sample length, a : distance from the support to the nearest load application, L : distance between the load application points, b : sample width, F : applied force, h : sample height.

3.2.7 Compression test

Compression tests parallel and perpendicular to the grain were also carried out, according to the EN 408:2010+A1:2012 standard [19]. In order to follow the requirements of the standard, two different types of samples were prepared (Figure 3.9). Since poplar is characterized for a very low fiber deviation and the modulus in compression is obtained under the 50% of the maximum compression stress, a strain gauge was placed on one face along the load direction in each case.

Distortion effect noted in EN 408:2010+A1:2012 [19] is produced in wood with high fiber deviation. Differences between the measurement according to EN 408:2010+A1:2012 standard [19] or with strain gauge are negligible since the type of test and the low fiber deviation avoids shear effects. Based on stress strain curve for the compression stress recorded by this strain gauge, the moduli of compression $E_{c,0}$ and $E_{c,90}$ were obtained as the slope of the curve between the 20% and 40% of the maximum compression stress.

Similarly, for the case of the grain direction test, a secondary strain gauge was glued perpendicular to the grain on the opposite face to the strain gauge at 0° . Thus, the Poisson's ratio (ν) was obtained also between 20% and 40% of the maximum compression stress.

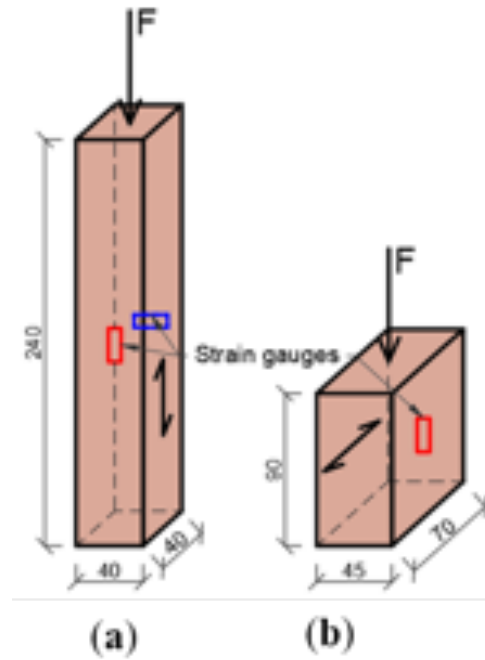


Figure 3.9: Experimental set-up of the compression test: (a) Parallel to grain (0°); (b) Perpendicular to grain (90°). F =applied load. Distances are shown in mm.

3.2.8 Density

From each particular sawn timber piece, one sample sized $50 \times 100 \times 100$ mm was extracted after bending test according EN 408:2010+A1:2012 standard [19]. From these samples, the MC and the basic density, ρ_0 (0% of MC) were obtained. The samples were dried with a constant temperature of $103 \pm 2^\circ\text{C}$ until the stabilization of two consecutive weights, according to the standard EN 13183-1:2002/AC:2003 [64].

3.2.9 Statistical analysis

Non-parametric Kruskal-Wallis tests were run by means of the package Statistix v.9[®] to know the statistical differences among plantations for all the features analyzed. Furthermore, with the aim of eliminating outliers from the data obtained, a statistical treatment based on the standard deviation (SD) has been performed. Specifically, in all simple linear regressions of the work, values outside the range $(\bar{x}-k\sigma, \bar{x}+k\sigma)$ were eliminated, \bar{x} being the average, σ the standard deviation and k is the coefficient that determines the width of the range. $k=2$ was used in this work.

3.3 Results

3.3.1 Standing trees and logs: dasometric features

The diameter measured at breast height (DBH) at GU was 27% higher than that measured at GR_H , and 13% higher in GR_L than in GR_H (Table 3.2). No differences between DBH at GU and GR_L were statistically detected, whereas both of them showed statistically higher DBH than GR_H . The annual DBH growth rate was very similar among GU

CHAPTER 3.

MODULUS OF ELASTICITY OF I-214 YOUNG POPLAR WOOD

and GR_H , and 19% higher in GR_L than in GR_H . Height measured at a 7 cm diameter point (H) was 29% higher for GU than for GR_H and GR_L , whereas no differences between the GR plantations were recorded. Tree wood volume (V) followed the sequence $GU > GR_L > GR_H$, being V at GU 55% higher than GR_H , and GR_L 26% higher than GR_H .

3.3.2 Features in standing trees and logs

The average percentage of false heartwood obtained was 39% lower for the GU plantation compared to the GR_H plantation (Table 3.2), and no statistical differences were observed between the two GR plantations with different stand density. The oldest plantation is the one with significantly higher propagation velocity. Among the youngest plantations the propagation velocity is significantly higher in the highest stand density plantation, both in trees and in logs. However, when estimating the dynamic modulus, these differences disappear, which implies the importance of considering and using the green density right when propagation velocity is measured. The propagation velocity on standing trees (C_T) and logs (C_L) were 8% and 12% higher for the oldest GU plantation compared to the GR_H plantation.

Statistical differences were observed for both velocities between the two GR plantations. Moreover, a good linear fitting was obtained between the tree and log velocities ($R^2=0.76$), although the slope was far from value 1, not included in the confidence interval at 95% (0.58,0.77) (Figure 3.10-a). Similarly, a good fitting (Figure 3.10-b) between the tree and log elastic moduli was obtained ($R^2=0.85$). In this case, the confidence interval at 95% was (0.66,0.82). These variables are 25% and 34% higher for the GU plantation compared to the GR_H plantation (Table 3.2), without detecting statistical variations between the two GR plantations.

3.3.3 Sawn wood in bending

The greater elastic modulus of timber obtained from the GU plantation (28% more in the GU plantation compared to the GR_H plantation) was obtained (Table 3.3). No statistical variations were detected between the two GR plantations. Due to the widely spread interval of the modulus of elasticity of the tested samples, a normal distribution function was used to describe how the values were distributed (Figure 3.11). It shows a greater dispersion of the values of the static modulus in bending between the different samples tested in the case of the GU plantation with respect to the two GR plantations, no visible differences between the two GR plantations.

3.3.4 Tree, logs, and sawn timber: MoE relationships

The plots in Figure 3.12 show the relationship between the static modulus obtained with the bending test ($E_{0,m}$) and the three moduli obtained by non-destructive acoustic tests (MoE_T , MoE_L and MoE_{dyn}). In general, acceptable linear regression fittings were obtained (around $R^2=0.7$ in all three cases).

In the first case (Figure 3.12-a), in which $E_{0,m}$ is plotted against the elastic modulus measured on standing tree, the slope obtained was very close to 1 and the confidence interval at 95% was (0.80, 1.15).

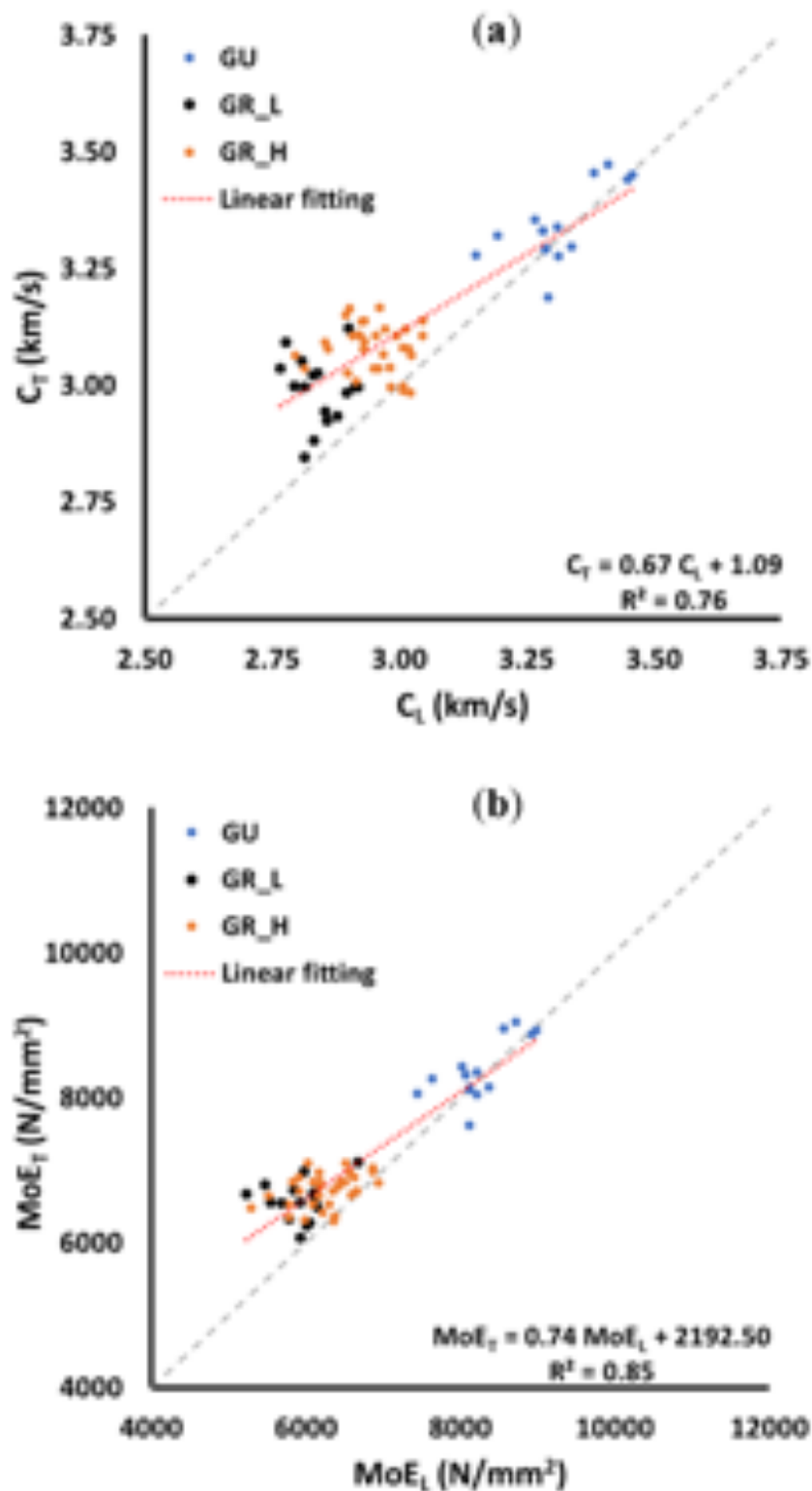


Figure 3.10: (a) Propagation velocity on standing trees versus propagation velocity on logs; (b) Elastic modulus (trees versus logs). MoE_T : modulus of elasticity in standing trees; MoE_L : modulus of elasticity in logs; C_T : propagation velocity in standing tree; C_L : propagation velocity in log; GU: Guadalajara; GR_L : Granada low-stand density; GR_H : Granada high-stand density.

CHAPTER 3.
MODULUS OF ELASTICITY OF I-214 YOUNG POPLAR WOOD

	MoE_T [kN·mm ⁻²]	MoE_L [kN·mm ⁻²]	MoE_{dyn} [kN·mm ⁻²]	$E_{0,m}$ [kN·mm ⁻²]	ρ_0 [kg·m ⁻³]	$E_{c,0}$ [kN·mm ⁻²]	$E_{c,90}$ [kN·mm ⁻²]	ν
GU	8.4±0.4 A	8.3±0.5 A	8.2±0.9 A	8.8±1.0 A	330±29 B	8.8±1.4 A	0.30±0.04 A	0.37±0.06 A
GR	L	6.6±0.3 B	5.8±0.5 B	6.7±0.6 B	7.1±0.9 B	353±18 A	6.3±0.9 A	0.21±0.04 B
		H	6.7±0.3 B	6.2±0.5 B	6.4±0.5 B	7.0±0.7 B	343±14 A	5.9±1.2 B
Kruskal-Wallis test	F= 36.9 p < 0.05		F= 59.9 p < 0.05	F= 105.2 p < 0.05	F= 88.9 p < 0.05	F= 47.8 p < 0.05	F= 44.4 p < 0.05	F= 20.2 p < 0.05

Table 3.3: Mean value±SD. MoE_T : modulus of elasticity in standing trees; MoE_L : modulus of elasticity in logs; MoE_{dyn} : dynamic modulus of elasticity in timber; $E_{0,m}$: static modulus in bending (mean value); ρ_0 : basic density in timber samples (MC=0%); $E_{c,0}$: modulus of elasticity in compression parallel to the fiber; $E_{c,90}$: modulus of elasticity in compression perpendicular to the fiber; ν : Poisson ratio. A, B, and C indicate different statistical classes among plantations within each variable. GU: Guadalajara; GR_L : Granada low-stand density; GR_H : Granada high-stand density.

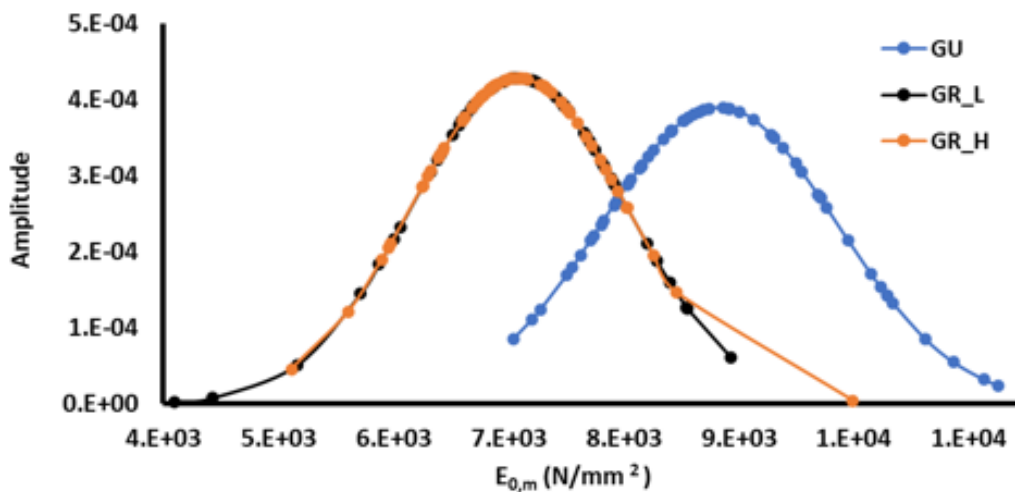


Figure 3.11: Normal distribution of the static MoE in bending. GU: Guadalajara; GR_L : Granada low-stand density; GR_H : Granada high-stand density.

In the second case (Figure 3.12-b), in which $E_{0,m}$ is plotted against the elastic modulus in logs, the slope was far away from 1 (0.78) and the value 1 was not on the confidence interval at 95% (0.64, 0.92). Finally, in the third case (Figure 3.12-c), in which $E_{0,m}$ is plotted against the dynamic elastic modulus measured in sawn timber, the slope was also very close to 1 (0.93) and the confidence interval was (0.84, 1.02).

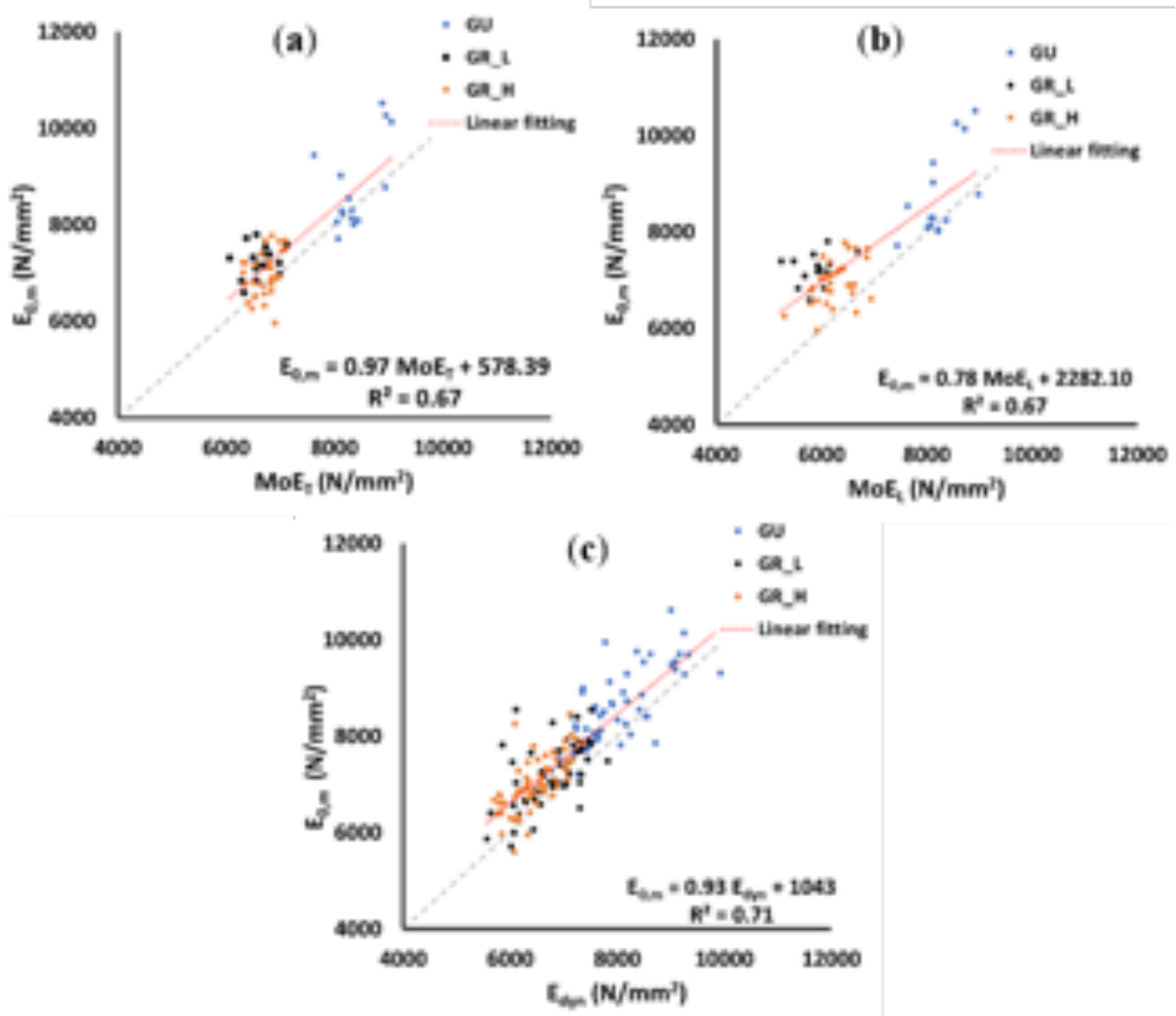


Figure 3.12: Experimental results. (a) MoE on trees versus static MoE in bending tests; (b) MoE on logs versus static MoE in bending tests; (c) Dynamic MoE on trees versus static MoE in bending tests. GU: Guadalajara; GR_L : Granada low-stand density; GR_H : Granada high-stand density.

3.3.5 Timber in compression

As for the bending elastic modulus results obtained in Section 3.3.2, higher stiffness values were obtained in both compression directions for the case of the GU plantation (Table 3.3). An increase of 51% and 57% was observed for the compression modulus along the parallel and perpendicular directions to the grain, for the GU plantation with respect to the GR_H . The elastic moduli for both directions were statistically similar for both GR plantations. A similar value of the Poisson's coefficient was obtained for the

three plantations, without detecting statistical differences between the three plantations.

3.4 Discussion

Stiffness is a very important wood quality property that predetermine the suitability of sawn timber for construction purposes. The possibility of their non-destructive assessment offers an opportunity to select trees for timber quality improvement, to optimize silvicultural practices towards higher timber quality, or to assort timber sources according to different end-use requirements in a very effective way. Destructively assessed static modulus of elasticity by using strain gauges were set as benchmarks for evaluation of the ability of non destructive methods to accurately assess stiffness and strength of the final product at different stages of wood chain, namely, on standing trees, logs and the sawn timber.

We explored the growth traits at the plantation level in order to relate them with acoustic and mechanical properties variability and to explain the stand density and age effect. Higher mean values of the height (H) and volume (V) have been observed for the GU oldest plantation, attributable to 4 more years of this plantation with respect to the two GR plantations. Likewise, between the two GR plantations significant differences in the diameter and wood volume have been observed, attributable to their different stand density. In particular, higher DBH and V values have been obtained at lower stand densities. It is also interesting to note that the lower density of plantation (GR_L) allows trees obtain diameters similar to those obtained in the older plantation (GU), but at a lower age. That is, the growth in diameter can be controlled by the stand density but the growth in height is only controlled by the age.

Regarding the mechanical properties, it has been observed that the dynamic modulus of elasticity estimated on trees and logs were greater from the oldest GU plantation. This could be associated with the onset of adult wood formation in this plantation. However, the differences in modulus of elasticity between the two GR plantations are not statistically significant, which indicates the little influence of the stand density on the stiffness of the timber at the same age. These results have also been corroborated in sawn timber samples, i.e greater stiffness of the wood obtained from the GU plantation with respect to the GR plantations, due to their older age, and null differences from a statistical point of view between the two GR plantations, indicating a low influence of the stand density. It was observed that Pearson correlation shows no significant relationship between diametric increment and the static modulus of elasticity in the trees evaluated. This is consistent with results obtained by different authors. Yu [36] observed no trend that linked the growth rate to a higher or lower modulus of elasticity. The study by Boever [65] found that the growth rate did not have a significant influence on the mechanical properties of the fast growing poplar hybrid. Pliura et al. [36] found no significant site effects on MoE and MOR for *P. deltoides*, despite large differences in DBH growth at the two sites.

Some of these results are aligned with previous published ones. In particular, Hernández et al. [66] used increment cores taken at breast height of ten *P. x euroamericana* hybrid-clones trees to estimate the mechanical properties. By using the ultrasound technique on the cores, they concluded that the radial variation of the dynamic elastic modulus had a tendency towards better mechanical properties with age. They

also observed a significant but weak correlation showing that wood density and mechanical properties decreased with increasing growth rate. Same conclusions were stated in Beaudoin [67] for some *P. x euroamericana* hybrid-clones, and in Huda [35], who found differences between clones ranging 2-13.5%. Also, Yu [36] found that the growth rate had a very low effect on the mechanical properties. They evaluated a high variability in mechanical properties caused by genetic differences in 10-years-old hybrid poplars. In Boever [65], the authors analysed the physical and mechanical properties of three *P. trichocarpa* × *deltoides* hybrids poplar clones (Beaupré, Hoogvorst and Hazendans) by means of laboratory destructive tests on timber samples. They also found that growth rate had no significant influence on the physical mechanical properties.

The impact of the growth rate of different poplar hybrids on mechanical properties is still a matter of controversy, largely because most studies include only one hybrid with a limited number of clones at a single site. Few studies have analyzed the relationships between growth rate and mechanical properties. Zhang [31] noted no significant correlations between growth rate and MOR or MoE in static bending for the diffuse porous hardwood. Diffuse porous species, such as poplar, generally display only a weak response in density to changing growth rates. In our case the results at the plot level showed a tendency to obtain a higher density of wood in the plots with a greater diameter growth rate. A significant and positive Pearson correlation between the increment diametric growth by tree and the mean wood density obtained in the lumber from the tree was also obtained.

The relationships between the mechanical properties and growth rate varied considerably by site and by hybrid [36] and also by age. Mechanical properties showed a great improvement with age as the tree progresses through juvenile wood to maturity [68]. Different results were observed on the relationships between the wood density and the width of the ring in the poplars. Ištók [69] showed a slight negative correlation between ring width and wood density in poplar clone I-214. However, according to Boever [65] no significant correlation could be found between growth and physical properties. Hernández et al. [66] pointed out significant but weak negative correlations between wood density or mechanical properties and growth rate in *P. deltoides* × *nigra*. In some cases [36] the effect of growth rate on mechanical properties was inconsistent. Sometimes, the presence of tension wood tends to increase the local density, irrespectively of growth rate. Opposite results have been observed in the principal softwood species. For the case of *Pinus radiata* D. Don, Carson [32] found that propagation velocity increased as stand density increased from 100 stems ha^{-1} up to 400 stems ha^{-1} . South African studies on locally grown softwoods support the positive influence of higher stand densities at establishment, improving the wood stiffness of *Pinus radiata* (Wessels and Froneman [70] 2015) and *Pinus elliottii* Engelm).

Different value of the dynamic modulus of elasticity was observed on trees and logs in our work. If the mean values of the modulus of elasticity between tree and log are compared each other for the same plantation, the differences are small (14% for GR_L , 8% for GR_H and only 2% for GU plantation). This result is in good agreement with the higher false heartwood percentage of the GR plantations compared to the GU plantation. Between factors indicated above that justify the difference in propagation acoustic velocity between trees and logs, it should be highlighted the low level of wood defects, the low percentage of bark, the relative uniformity of the logs in section, as well as the low percentage of false heartwood in the three plantations (Forêt Privée

CHAPTER 3.

MODULUS OF ELASTICITY OF I-214 YOUNG POPLAR WOOD

Française [71]). Hernández [66] obtained differences of more than 20% in average between dynamic and static modulus (much higher than in our study), advising caution in predicting mechanical properties of wood from density in *P. x euramericana* clones at earlier ages.

A good linear fitting has been observed between the propagation velocities of the acoustic wave on the trees and the logs, with a slope of 0.67, and between the trees and the logs elastic moduli, with a slope of 0.74. The deviation from value 1 of both slopes may be due to various factors: i) the existence of the bark and marrow in the logs, which decreases the stiffness of the whole log, and therefore affects to C_L but does not to C_T ; ii) the existence of false heartwood, which affects C_L but does not affect C_T ; iii) the existence of defects such as knots; iv) the non-constant section of the logs, which implies that equation (2) is not totally valid; v) the existence of different wave propagation modes, whose picking depends on the sensors distance and the attenuation of the material. However, in both cases, a clear separation has been observed between the three plantations, with some overlap between the two GR plantations.

Larger differences have been reported in hardwoods between dynamic and static modulus of elasticity in lumber. Smulski [72] reported differences of 22% to 32% for hardwoods of North American and Ilic [73] reported a difference of 29% for *Eucalyptus delegatensis*. In our study, the coefficient of determination (R^2) between dynamic and static MoE in lumber ($R^2=0.7$) is higher than the relationships observed in another study with the same poplar clone with a similar lumber size ([74]; $R^2=0.45-0.49$). Cheng and Hu [75] used several methods to determine the MoE for poplar wood, and the deviation comparing the MoE using longitudinal waves and static MoE was 10.4%. However, in other hardwood species, MoE_{static} was closely related to the $MoE_{dynamic}$. In eucalyptus wood, Yang [76] obtained coefficients of determination of 0.95-0.97. In other hardwood species, Chauhan and Sethy [77] obtained also a higher coefficient of determination in linear regression between dynamic and static MoE (0.85-0.96).

Linear regression fitting around $R^2=0.7$ has been obtained from the comparison between the static modulus in bending ($E_{0,m}$) and the three elastic moduli obtained by non-destructive acoustic tests (MoE_T , MoE_L , and MoE_{dyn}). The relationship between trees and logs was very similar to that reported by Wang [60] for *Pinus banksiana* Lamb. ($R^2=0.71$). This degree of concordance of the velocity correlative relationship for standing trees and derived logs across multiple species provides a measure of confirmatory support for the acoustic approach in terms of its overall consistency and agreement with expectation. More generally for conifers, Newton [78] suggests that the velocity of the dilatation wave measured on standing trees is approximately 1.22 times the velocity of the longitudinal wave measured on the derived logs. It should be noted that the relationship is better for sawn timber than for logs and trees and with values for standing trees much higher than those observed for other species in the literature [50,79].

The slope very close to 1 obtained from the regression between $E_{0,m}$ against the elastic modulus measured on standing trees, can be mainly due to different factors: 1) in our case arrival time is calculated by oscilloscope by the same algorithm and software on the tree, log and sawn timber. The application of the Akaike method for the accurate detection of the arrival time of the acoustic wave [33]2019; 2) in the use of the green density measured at the time of the measurement on standing trees [53]2019; 3) the timber has been obtained near the outer wood area with respect to the acoustic measurement on standing trees. A relatively high correlation was found by Gra-

bianowski [54] between the acoustic velocity and the mechanical properties of sawn timber from those trees. Higher values were found when looking at timber sawn from outer wood, $R^2=0.89$, than from core wood, $R^2=0.74$; 4) the low number of defects, mainly knots, due to the appropriate tree pruning carried out in the three plantations. These results are consistent with the results of Wang [51], who found that there is a good relationship between elastic modulus on standing trees and logs and the static elastic modulus in sawn timber. This finding could be very useful for predicting static MoE in bending by measuring elastic modulus in the longitudinal direction on the standing trees.

In the case of acoustic propagation velocities measured on standing trees and resonance measurements in logs, values between 7% and 36% higher were reported by several authors [54, 57, 60, 79, 80], most of them for the case of softwood. Furthermore, Wang [43] suggested that tree diameter, stand age, operating temperature and wood moisture content affect tree-log velocity relationships. Acoustic wave velocity on standing trees might be higher or lower than in logs or timber [43], depending on the species, grain direction (longitudinal or transverse), site, tree diameter, and measuring methods. According to the conclusions of Liu [81], the propagation of acoustic waves within an orthotropic tree model and with free and low reflection boundary conditions, is performed as a dilational wave between distances 0 and 1.2 m. Our measurements were made at a distance between sensors of 0.6 m. Thus, the one-dimensional model equation used in this work (Equation 3.2) should be replaced by Equation 11 of the work by Liu [81], which considers the dependence of MoE_T on green wood density, the propagation velocity and the different Poisson moduli of the tree according to the orthotropic model. This could largely justify the observed differences between MoE_T and $E_{0,m}$.

On the other hand, the slope of 0.78 obtained from the linear fitting between $E_{0,m}$ against the elastic modulus measured in logs, may be mainly due to the reasons stated above regarding the logs. It should be noted that the sawn timber samples were taken close to the outer part of the log and the measurement in logs represents the properties of whole log. More specifically, based on a simple linear regression model specification that was used to describe the relationship between standing trees and logs velocities for five coniferous species, Wang reported significant ($p \leq 0.05$) relationships with moderate to high levels of explanatory power (R^2 values of 0.93, 0.85, 0.71, 0.83, and 0.90 for *Picea sitchensis* (Bong.) Carr., *Tsuga heterophylla* (Raf.) Sarg., *P. banksiana*, *Pinus ponderosa* Douglas, and *P. radiata*, respectively).

Moreover, the slope close to 1 (0.93) obtained from the linear fitting between $E_{0,m}$ against the dynamic elastic modulus measured in the sawn timber samples, demonstrates the high fidelity of the acoustic test carried out on sawn timber in the case of poplar. In particular, Equation 8 shows the obtained linear fitting of MoE_{dyn} versus $E_{0,m}$ in the particular case of the data measured in this work:

$$MoE_{dyn} = 1.1 \cdot E_{0,m} - 1124 \quad (3.7)$$

This good result (slope close to 1) is mainly due to: 1) the homogeneity of poplar wood; 2) the high grain alignment; 3) the low content of defects indicated above; 4) the use of elastic supports to carry out the vibration test on the sawn timber samples; 5) the use of a strain gauge to measure the real strain in the grain direction at the mid-span of the sample caused by the bending, being able to obtain a static elastic modulus with less shear influence (unlike in the case of $E_{m,global}$ according to the

EN 408:2010+A1:2012 standard [19]) but taking into account the deformation of the entire element subjected to bending (unlike in the case of the E_m , local according to the EN 408:2010+A1:2012 standard [19]). The authors of Araújo [82] demonstrated that the use of a strain gauge provides more consistent readings and lowest coefficients of variations when compared with an LVDT to obtain the modulus of elasticity.

The results in compression corroborate what was observed in bending, i.e a clear influence of the age of the plantation and a null influence from the statistical point of view of the stand density on the elastic modulus at compression in the directions parallel and perpendicular to the grain. Our results are relatively different to those obtained by Aydın [34], who did not specify the variety of poplar. Finally, the Poisson's ratio of poplar timber has also been obtained, resulting values between 0.37 (for GU) and 0.40 (for GR_L and GR_H), statistically similar for the three plantations. The fact that in the two GR plantations the mean of the Poisson module is identical, suggests that it is associated with age. In the case of the GU plantation, since it is somewhat more mature wood, it is logical to think that the Poisson's coefficient is slightly lower.

3.5 Conclusions

The elastic modulus in bending and compression had a very high influence of the age of the plantation, and a null influence with the stand density. Including the three plantations, it was concluded that: 1) there is a good linear fitting between the elastic modulus measured on standing trees and the static modulus in sawn timber, with a slope very close to 1 (0.97), thus giving a high level of fidelity to the acoustic test carried out on standing trees, 2) a linear fitting between the measured elastic modulus in logs and the static modulus in bending with a slope far from 1 (0.67), thus giving a moderate level of fidelity to the acoustic test in logs, and 3) a linear fitting between the dynamic elastic modulus in sawn timber and the static modulus in bending with a slope very close to 1 (0.92), thus giving a high level of fidelity to the acoustic test in sawn timber. In all three cases, a very similar fitting coefficient was obtained, around $R^2=0.7$.

It has been concluded that the propagation velocity of acoustic waves on standing trees and logs is significantly different between the three plantations, i.e. it is influenced by the age and stand density. However, the elastic modulus obtained by acoustic non-destructive methods in trees, logs and sawn timber is only influenced by age, and does not show significant differences with the stand density. This result is totally coincident with what happens with the static modulus of elasticity obtained with the destructive bending test, which corroborates the need and interest of using the in-situ density in trees and logs to obtain the value of the elasticity modulus of the wood with acoustic methodologies.

Overall, it can be concluded that the elastic modulus of the I-214 poplar timber is more associated with the age of the plantation than with its management in terms of its stand density. This suggests that we can increase the growth without losing the technological properties of the wood, compared to a plot with worse growths of the same age. Even, a slight tendency has been detected of these technological properties of the wood to be better with lower stand density.

Chapter 4

Improving ductility and bending features of poplar glued laminated beams by means of embedded carbon material

Title	Improving ductility and bending features of poplar glued laminated beams by means of embedded carbon material
Authors	F.J. Rescalvo; C. Timbolmas; R. Bravo; I. Valverde-Palacios; A. Gallego
Journal	Construction and Building Materials
ISSN	0950-0618
Journal's performance	Journal impact factor (2020): 6.141 D1 (Civil Engineering: 7/137)
Details	Volume: 304 – Published: October 2021; Pages: 124469
DOI	10.1016/j.conbuildmat.2021.124469

4.1 Introduction

One of the first structures with glued laminated beams (glulam) still in use today was built at the end of the 19th century: the assembly room of King Edward VI College in Southampton, England. The Technological Revolution and the development of a fully water-resistant phenol-resorcinol adhesive in 1942 gave rise to the glulam industry. Nowadays, the use of automatic finger-jointing and computer-controlled fabrication machines makes it possible to build highly demanding structures with extraordinary shapes and spans, and with a high degree of precision. Glulam beams pertain to what is currently known as Engineered Wood Products (EWP) [83]. Such improvements within the manufacturing process lead to more efficient use-hence conservation-of our timber resources, as wood species with lower diameters can be used. The FAO established that by 2020, 44% of the world's forests should be cultivated forests; and by 2050 some 75% of the wood used for industrial purposes should come from fast-growing plantations.

CHAPTER 4.

IMP. DUCT. AND BEND. FEATURES OF POPLAR GLULAM BEAMS

Poplar can be seen as a very suitable source of raw material for the elaboration of glulam beams. Given the currently predominant use of poplar for plywood around Europe, the *P. x euroamericana* hybrid I-214 cultivar is the most extensive species in poplar plantations. According to FAO, in 2016 this cultivar covered about 145,000 ha, thus representing more than 50% of the total plantation area in Europe.

Mechanically, poplar timber (and particularly the clone-124) has an acceptable bending strength, yet a low modulus of elasticity. Therefore, the use of new materials such as reinforced fibre composites (FRP) serves to enhance stiffness-equalling or even surpassing engineering products based on other timber species. The notion of enhancing the mechanical properties of a glulam beam by means of FRP first appeared in the 1970s [84]. FRP reinforcement can be placed externally (Near Surface Mounted - NSM) or embedded [85]. The latter, despite requiring a more complicated elaboration process, is hidden, so that the aesthetic result is ideal for buildings where the timber is visible.

One positive aspect of embedding reinforcement in the structural element is the consequent improvement in terms of fire resistance. Martin and Tingley [86] reported that fire performance can be improved by placing the FRP internally, as the wood insulates the FRP, thus delaying the polymer matrix in reaching its glass transition temperature [87]. Williamson [87] showed by experimental testing that a one-hour fire resistance rating can be obtained with larger size FRP-reinforced glulam beams even when no sacrificial lamination is included [86].

Several authors have worked with the reinforcement of different FRP layouts and wood species in glulam beams [13, 88–90]. Ribeiro [91] strengthened glulam beams made of maritime pine wood, with a Modulus of Elasticity (MoE) similar to that of poplar. The application of a glass FRP (GFRP) pultruded lamella at the outer part of the tension side resulted in respective improvements of 46% and 41% for MoE and MoR (Module of Rupture). Other studies [92] found that the placement of two layers of GFRP fabric instead of one layer on the bottom side of a poplar glulam beam led to an improved MoE, from 7% to 13%. These works evaluated the effect of reinforcement applied near the neutral axis, where increases were slightly reduced. Nevertheless, all the fabric-reinforced beams showed ductile behaviour. Yang [93] studied several embedded reinforcement layouts by means of GFRP bars, steel bars and GFRP and CFRP (carbon FRP) plates placed at tension and compression zones in Douglas fir glulam beams. In the case of a CFRP layer placed at the tension side, they reported improvements of 1.3% and 21% for stiffness (relation between MoE and inertia) and ultimate moment, respectively. They also found that the placement of one GFRP layer at the bottom side led to a 2.3% decrease in stiffness, while its placement at the tension and compression side gave an enhancement value of up to 0.5%.

Ductility is a fundamental feature of structural elements such as bending resistance, MoR, and MoE [93–95]. Ductility can be defined as the ability to undergo significant plastic deformation before the rupture or breaking that corresponds to the failure of the element. Deformations can be understood to mean deflections, curvature or strains. Jorissen [96] evaluated plastic behaviour by means of displacement and curvature ductility. In general, ductile behaviour can be interpreted as an alarm before a catastrophic collapse.

In this work, poplar glulam beams internally reinforced with FRP were manufactured and tested so as to appraise the mechanical properties of the poplar I-214 low-grade species. Several layouts were analyzed and compared in terms of mechanical

features. The fabric or pultruded lamella of CFRP—placed at the tension, compression, or both sides of the beam—were evaluated. The paper also provides an in-depth analysis of the ductile behaviour, which is known to be a key indicator of both the engineering design and the safety of a building’s structural integrity.

4.2 Materials and Methods

4.2.1 Poplar planks

All timber was extracted from a 9-year-old poplar plantation of the cultivar I-214 (*Populus x euroamericana* [Dode] Guinier) located nearby the city of Granada, Spain. Two logs measuring 2.5 m in length of each tree were used for this work. From them, planks sized 35 x 75 x 2000 mm were sawed and dried under natural conditions of good ventilation, protected from rain and direct solar radiation, during 6 months. After drying, the average Moisture Content (MC) was $10\pm 2\%$. All the planks were subjected to longitudinal acoustic resonance tests as described in [27] to arrive at the dynamic MoE, which was corrected to MC=12% following the [20] standard, then fitted to a normal distribution (see Figure 4.1). The mean value was 7061 MPa, corresponding to class T8 class according the standard [21]. Standard deviation was 821 MPa. In order to avoid, as much as possible, heterogeneity of the manufactured glulam beams, only the planks within the standard deviation interval [6240 MPa-7882 MPa] were used (as seen between the green dotted lines in Figure 4.1).

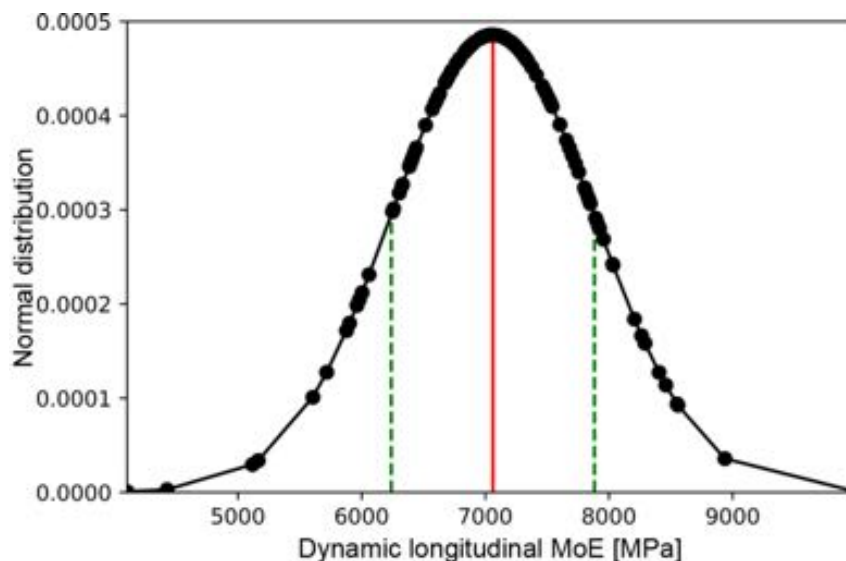


Figure 4.1: Normal distribution of the dynamic longitudinal MoE of the sawed planks. Red line: Mean value. Green dotted line: Standard deviation limits.

4.2.2 FRP material

Two types of carbon fiber reinforced materials (CFRP) were used: i) Unidirectional pultruded CFRP plate Carboplate[®] E200; and ii) Unidirectional fabric Mapewrap[®] C Uni-Ax, both from the company Mapei S.p.A. In order to improve the adhesion quality

CHAPTER 4.

IMP. DUCT. AND BEND. FEATURES OF POPLAR GLULAM BEAMS

of the FRP-timber joint [97], Mapewood[®] Primer was applied to the timber before reinforcement. To ensure an MC of $10\pm 2\%$ for the timber during the entire manufacturing process, the epoxy resin Mapewrap[®] 21 was used for FRP-wood adhesion. The main characteristics of the FRP used are summarized in Table 4.1.

	CARBOPLATE E200	MAPEWRAP C UNI-AX
Fiber orientation	Unidirectional	Unidirectional
Density (g/cm³)	1.56	-
Specific weight (g/m²)	-	300
Thickness (mm)	1.400	0.166
Resistant area per width unit (mm²/m)	1400.0	166.6
Max. tensile stress (MPa)	3300	4830
Tensile elastic modulus (GPa)	200	230
Max. elongation (%)	1.4	2.0

Table 4.1: Main characteristics of the used FRPs [98].

4.2.3 Glulam timber: Layouts and manufacturing

Once the poplar planks were selected as described in Section 4.2.1, they were randomly used for the elaboration of the glulam beams. A total of 56 beams were manufactured, divided into 7 different layouts. Layout 1 (only poplar glulam beams) was used as the control group. Table 4.2 and Figure 4.2 summarize all the layouts. Comparison of the different layouts (L) allows one to evaluate: i) The improvement provided by the FRP with respect to only-poplar beams, by comparing L2-L7 with L1; ii) The influence of the type of FRP, by comparing L3 and L2; iii) The influence of the FRP thickness by comparing L4 with L2; iv) The influence of the position of the FRP, comparing L5 with L3; and v) The influence of double reinforcement at compression and tension sides, by comparing L3, L6 and L7.

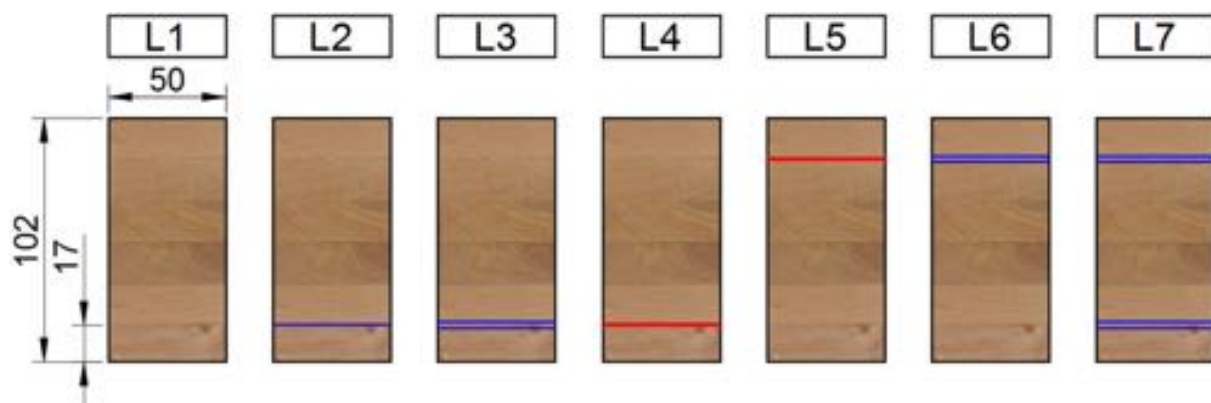


Figure 4.2: Glulam layouts. Blue: FRP fabric. Red: FRP lamella. Distances in mm.

Figure 4.2 shows the general design of 2100 mm long glulam beams used as test specimens. As seen, the design included finger joints for the connection between lamellas of the same layer elaborated according to the standard [21]– Annex I.4. For gluing,

LYT	Type of FRP	Position of FRP	Number of layers	Total THK of FRP (mm)	Cross-section ratio (%)	No. of SMP	NOMC
1	-	-	-	-	-	8	CH
2	Fabric	Bottom	1	0.166	0.16	8	CFB
3	Lamella	Bottom	1	1.400	1.37	8	CLB
4	Fabric	Bottom	2	0.322	0.32	8	CF2B
5	Lamella	Top	1	1.400	1.37	8	CLT
6	Fabric	Top	2	0.322	0.32	8	CF2T
7	Fabric	Bot.+Top	2+2	2·0.322	0.64	8	CF2BT

Table 4.2: General design of glulam beams. Distances in mm.

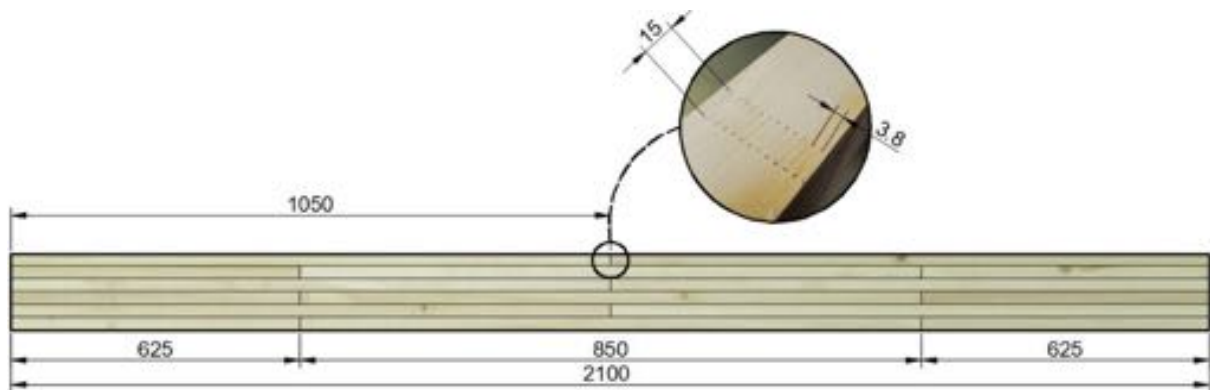


Figure 4.3: General design of glulam beams. Distances in mm.

the polyurethane resin PUR-20 Bakar[®] structural adhesive was used. A pressure of 10 N/mm² was applied, as the length of the finger was 15 mm. After curing, the lamellas were mechanized to their final thickness, 17 mm.

The gluing process between different layers was performed according to the standard [21] – Annex I.5. Since the design of the glulam beams was set for Classes 1 or 2, the pith of the lamellas was orientated to the same side (upwards). The elaboration process was divided into four phases: i) Gluing the lamellas of the main timber section using the Bakar[®] PUR-20 resin (400 g/m²); ii) Application of the primer (200 g/m²); iii) Application of the FRP reinforcement, using 320 g/m² of epoxy resin; and iv) Gluing the external lamellas. During the entire manufacturing process, the moisture content of the timber was controlled, giving an average value of 11±1%. After final curing, the beams were sawed at a final cross-section of 50 x 102 mm² and a length of 2100 mm (Figure 4.2).

4.2.4 Non-destructive resonance test (NDT)

General description of the test

Non-destructive transversal resonance tests (NDT) entailed placing the samples on two elastic supports in edgewise orientation and using a timber hammer as the impact tool (see Figure 4.4). A "t.bonne MM-1 Thomann" microphone was used to capture the elastic wave and convert it to a signal, which was recorded by a Picoscope[®] 4424 oscilloscope with 80 Ms/s of maximum sampling frequency. The BING[®] program (Beam Identification by Non Destructive Grading, [18]) was used to obtain the transversal

CHAPTER 4.

IMP. DUCT. AND BEND. FEATURES OF POPLAR GLULAM BEAMS

modulus of elasticity (MoE_{dyn}). This program is based on the theory proposed in [17] and relies on the flexural resonance frequency and the Timoshenko bending theory to determine the dynamic MoE and the shear modulus in free-free boundary conditions. Furthermore, [17] proposes the following first order solution for the motion of a resonance beam:

$$\frac{MoE_{dyn}}{\rho} = \frac{MoE_{dyn}}{KG} \cdot x_n + y_n \quad (4.1)$$

where MoE_{dyn} is the transversal dynamic MoE in edgewise position, ρ is the specimen density, K is the shear factor with a value of $K=5/6$ for a rectangular cross-section, G is the dynamic shear modulus and x_n and y_n are parameters dependant on the vibration mode. According to [17], the maximum relative errors of MoE_{dyn} and G respectively remain less than 5% and 8%, considering a length-to-depth ratio between 10 and 20 (in our case L/h was set as 20).

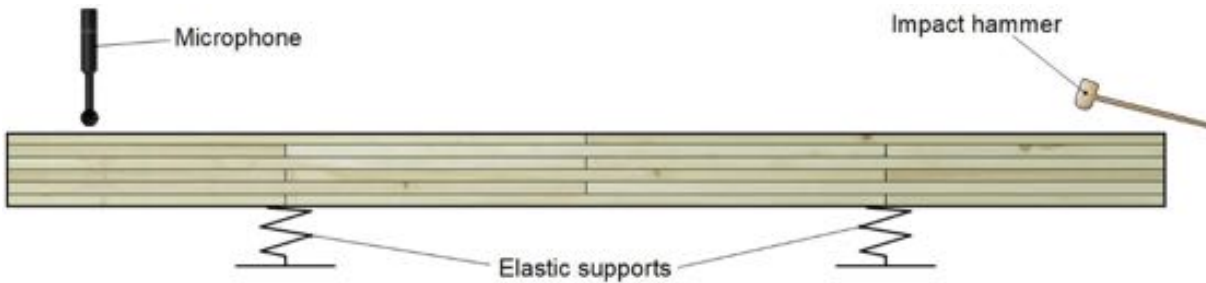


Figure 4.4: General arrangement of the non-destructive resonance test.

The elaboration process for the reinforced layouts (2-7) was divided in two phases:

-Phase 1, in which the main timber section of the beam was manufactured. After this phase, a NDT was performed separately upon the main glued section (ms) and upon the remaining non-glued lamellas (l) to obtain the $MoE_{dyn,ms}$ and $MoE_{dyn,l}$, respectively. By means of the Parallel Axes Theorem, the combined dynamic modulus for each beam without reinforcement can be obtained for each particular beam (named as $MoE_{dyn,c}$). See clarifications in Figure 4.5, more precisely,

$$MoE_{dyn,c} = \frac{(MoE_{dyn,ms} \cdot I_{ms} + A_{ms} \cdot MoE_{dyn,ms} \cdot y_{ms}^2) + (MoE_{dyn,l} \cdot I_l + A_l \cdot MoE_{dyn,l} \cdot y_l^2)}{I_c} \quad (4.2)$$

where I_{ms} and I_l are the second moments of inertia with respect to the sample axis, A_{ms} and A_l are the cross-sections, and y_{ms} and y_l are the distances from the combined neutral axis to the neutral axis of each part, respectively of the main section and the remaining lamella (s). I_c is the combined second moment of inertia.

-Phase 2, after gluing the reinforcement and the external lamella(s), a N.D.T was performed, giving the dynamic modulus of the whole beam (MoE_{dyn}).

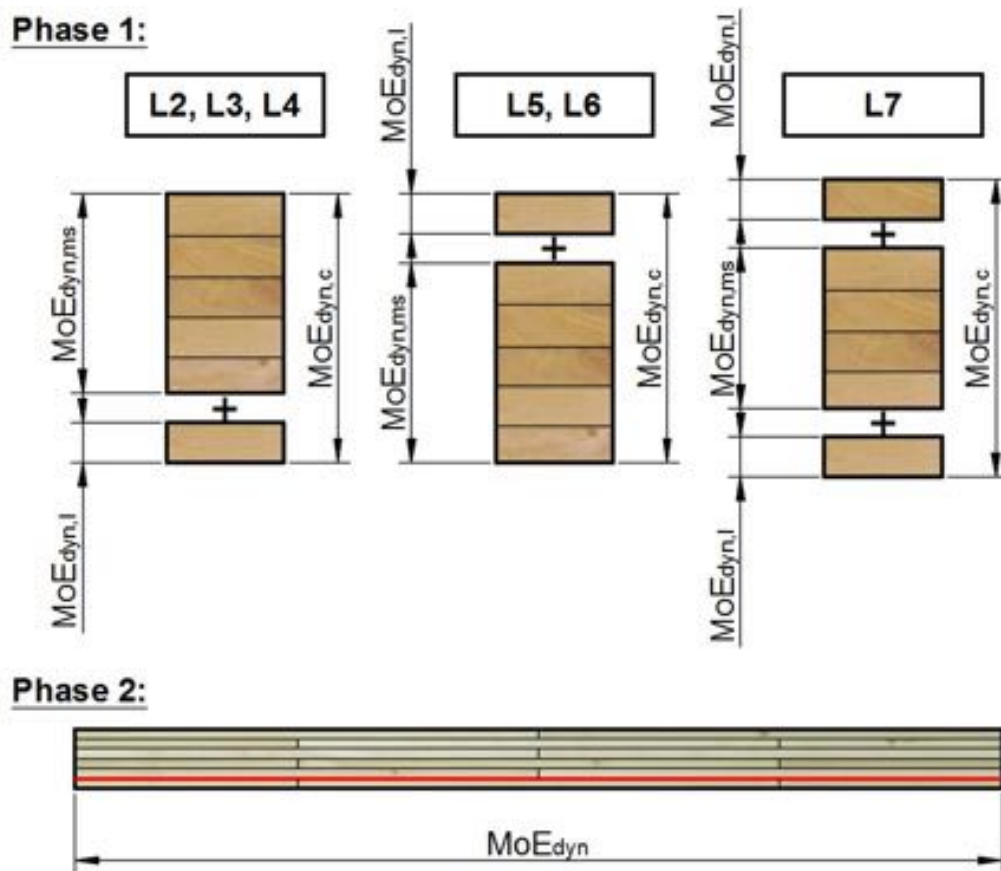


Figure 4.5: N.D.T procedure for Phases 1 and 2 to obtain the $MoE_{dyn,c}$ and MoE_{dyn} .

4.2.5 Ductility

In order to obtain the ductility ratio, the elastic and the ultimate limit were defined according to [99]. They are represented in Figure 4.6-a. This procedure can also be used to obtain the curvature ductility.

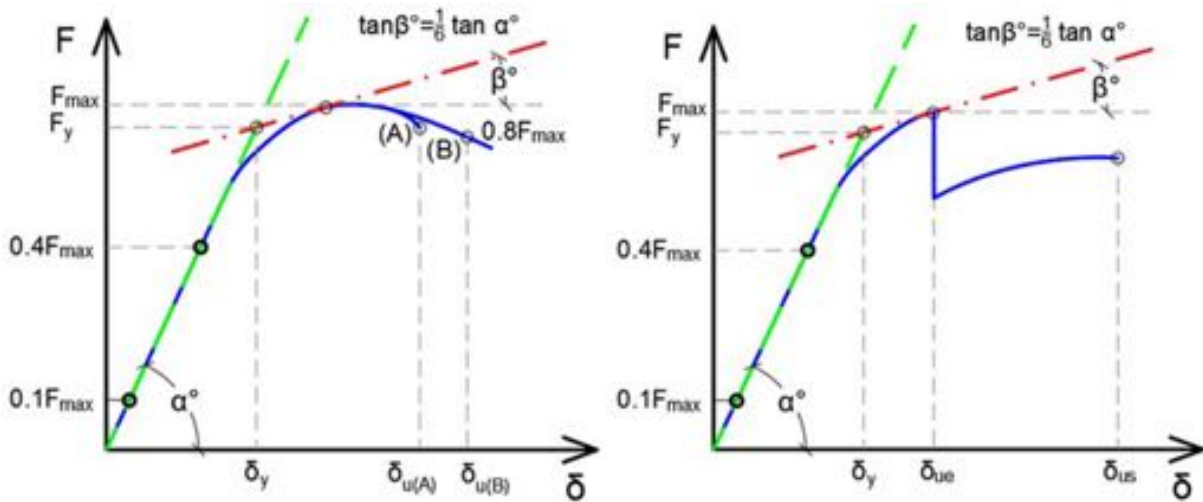


Figure 4.6: Procedure to determine the ductility ratio in terms of displacements. F is the applied force and δ is the vertical deflection. Left: Theoretical approach; Right: Approach considered in this study.

When plastification occurs, the force-displacement and moment-curvature relations become non-linear, hence essential for a proper estimation of the limits of the elastic and plastic range. As a geometric method to identify the limit between the elastic and plastic ranges, the use of two auxiliary lines is required (Figure 4.6-left): i) Green dashed line, whose slope ($\tan(\alpha)$) was obtained as between 10% and 40% of the maximum load ($0.1 \cdot F_{max}$ and $0.4 \cdot F_{max}$); and ii) Red dashed-dotted line, tangent to the force-displacement curve, where the slope is equal to $\tan \beta = (1/6 \tan \alpha)$. Hence, the geometric intersection of these two lines defines the yielding point (F_y) and its corresponding displacement (δ_y). The ultimate displacement, $\delta_{u(B)}$, was established as the displacement when the load decreases by 20% (point B) after reaching its maximum value. If this drop was not reached, this value was set as the last load value achieved ($\delta_{u(A)}$). However, due to the reinforcement, some layouts still afford bending capacity up to collapse even when the bottom layer has already failed. In other words, reinforcements lend ductility to the whole element. Taking this fact into account, two different displacement ductility ratios can be computed. The same procedure can be applied to derive the ductility ratio based on the moment-curvature relationship, bearing in mind that the ductility ratio can be evaluated until bottom layer failure, which is directly related with the drop in the force-displacement relation. In order to achieve practical applicability in line with the experimental results, two different approaches were considered (Figure 4.6-right): one corresponding to the engineering design side, the other pertaining to structural safety. Therefore, for the specimens exhibiting successive drops in the force-displacement relationship, the ultimate displacement for the engineering design considerations would correspond to the first drop in the load-displacement relation (δ_{ue}), while for safety considerations, the ultimate displacement corresponds to the ultimate load prior to total collapse (δ_{us}). As mentioned above, moment-curvature

ductility only provides an estimation of ductility corresponding to the engineering side. In order to automate this process and to provide a precise estimation of the ductility index for all the approaches, a versatile script was developed-employing Python programming language-considering the relationships of: i) displacement ductility – engineering design, $\mu_{\delta,ed}$ (Ec. 4.3); ii) displacement ductility – structural safety, $\mu_{\delta,ss}$ (Ec. 4.4); and iii) moment-curvature – engineering design, $\mu_{\chi,ed}$ (Ec. 4.5)

$$\mu_{\delta,ed} = \frac{\delta_{ue}}{\delta_y} \quad (4.3)$$

$$\mu_{\delta,ss} = \frac{\delta_{us}}{\delta_y} \quad (4.4)$$

$$\mu_{\chi,ed} = \frac{\chi_{ue}}{\chi_y} \quad (4.5)$$

where δ_{ue} and μ_{ue} are the displacement and curvature at the maximum load for the engineering design, respectively; δ_{us} is the ultimate displacement for structural safety; and δ_y and μ_y are respectively the displacement and curvature at the yielding point.

4.2.6 Bending test

All the specimens were subjected to a 4-point bending test until failure, according to the standard [19]. Loading was applied at a controlled displacement rate of 8.7 mm/min. The tests were carried out with a machine from the company CONTROLS S.A., model S-110, with one electrical actuator having a maximum capacity load of 100 kN. The distance between supports was set as 1920 mm, while the distance between points of load application was 612 mm (Figure 4.7). The strains were measured using four strain gauges (K-CLY-4 series from HBM) placed at the mid-span of the beam. The top and bottom strain gauges measured the compression and tensile strains, respectively; lateral strain gauges registered the strains at 1/4 of the total height of the beams. In order to avoid undesirable strain effects near the finger joint, top and lateral strain gauges were slightly displaced (15 mm). The objectives of the lateral gauges were: i) To determine whether the beam began to twist during the test; and ii) To obtain the experimental position of the neutral axis. By using the bottom strain gauge, the static modulus of elasticity (MoE_s) was obtained as the slope of the stress-strain relationship between 10% and 40% of the maximum stress. The maximum stress was computed with the bending theory at the mid-span, i.e.

$$f_m = \frac{3a P_{max}}{bh^2} \quad (4.6)$$

where, P_{max} is the maximum load (N), a is the distance between the load point and the nearest support (mm), b is the width of the beam (mm) and h^2 is the depth of the beam (mm). A LVDT was placed at the center of the beam to register the global modulus of elasticity ($MoE_{m,g}$) as stated by standard EN408:2011+A1:2012 [19], comparable with the MoE_s .

4.2.7 Statistical analysis

Non-parametric Kruskal-Wallis tests were run by means of the package Statistix v.9[®] to determine the statistical differences among all the beam layouts.

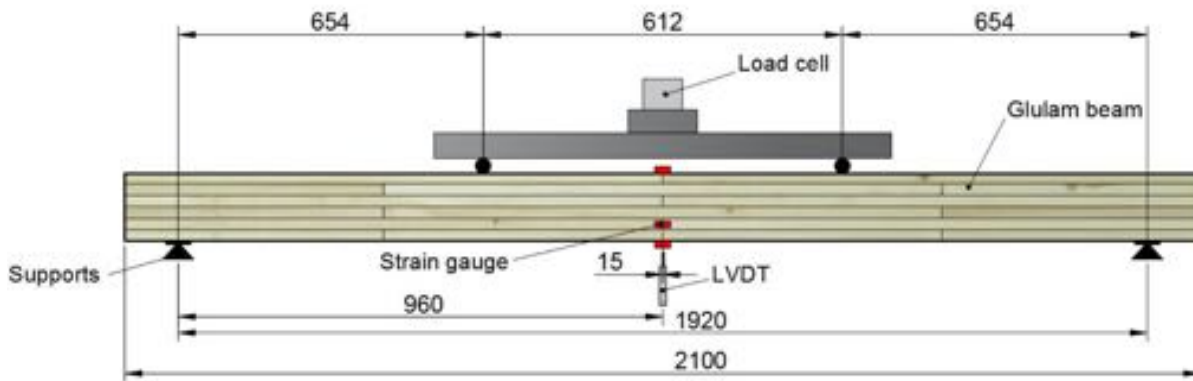


Figure 4.7: Four-point bending test set-up. Distances in mm.

4.3 Results and Discussion

Figure 4.8 shows the stress-deflection curves for all the samples of each particular layout. Two clear behaviours are identified—ductile and brittle. The ductile behaviour is observed for the layouts with reinforcement at the tension layer (L2, L3, L4, and L7), whereas brittle behaviour is seen only for the layouts having reinforcement at the compression layers (L5 and L6) or the control case without reinforcement (L1). Reinforcement at the tension layers lends the beam a high capacity to bear tensile stress. Consequently, the stress in the compression area of the timber is also increased, producing plastic deformations, introducing a non-linear behaviour at an intermediate loading rate. As the plastic deformations increase, the active area in the elastic range is reduced. Tensile stresses therefore increase until the failure of the beam under tension.

Table 4.3 summarizes the results of the three ductility parameters defined in Section 4.2.5. Figure 4.9 reflects the improvement (%) of these parameters compared with control layout L1. Figure 4.10 offers an example of the typical failure patterns for one specimen of each particular layout. The CLB layout showed the highest improvement in terms of ductility (statistical class A for all three approaches), with respective increases of 47% and 30% for engineering design and moment-curvature evaluations. Moreover, this layout provided a secondary improvement related to structural safety, around 107%. This is closely followed by the CF2B layout, giving important improvements of 26% - 115% for all three approaches (statistical class A). For the CFB layout, improvement ranges between 6% and 48% due to the thinner fabric layer, hence a statistical class between A and C. The main difference between the CFB and CF2B layouts is tied to the length of the elastic range and its corresponding slope. The CFB layout showed the shortest elastic range, with a relatively reduced slope due to the low value of the elasticity modulus. Owing to the thin fabric layer, the CFB specimens exhibited several premature failures at the bottom side (see Figure 4.10).

As the thickness of the reinforcement increased, a significant improvement in the elastic range is observed, along with a steeper slope. In such a case, the highest ductility is achieved for the structural safety side, because after failure of the bottom layer, the deflection is directly related to reinforcement stiffness. The CF2B and CLB layouts revealed a similar trend in the stress-deflection relation, yet there is a substantial difference regarding the respective yield points: the yielding range started sooner for the CF2B layout, providing the highest safety ductility, characterized by a smaller elastic

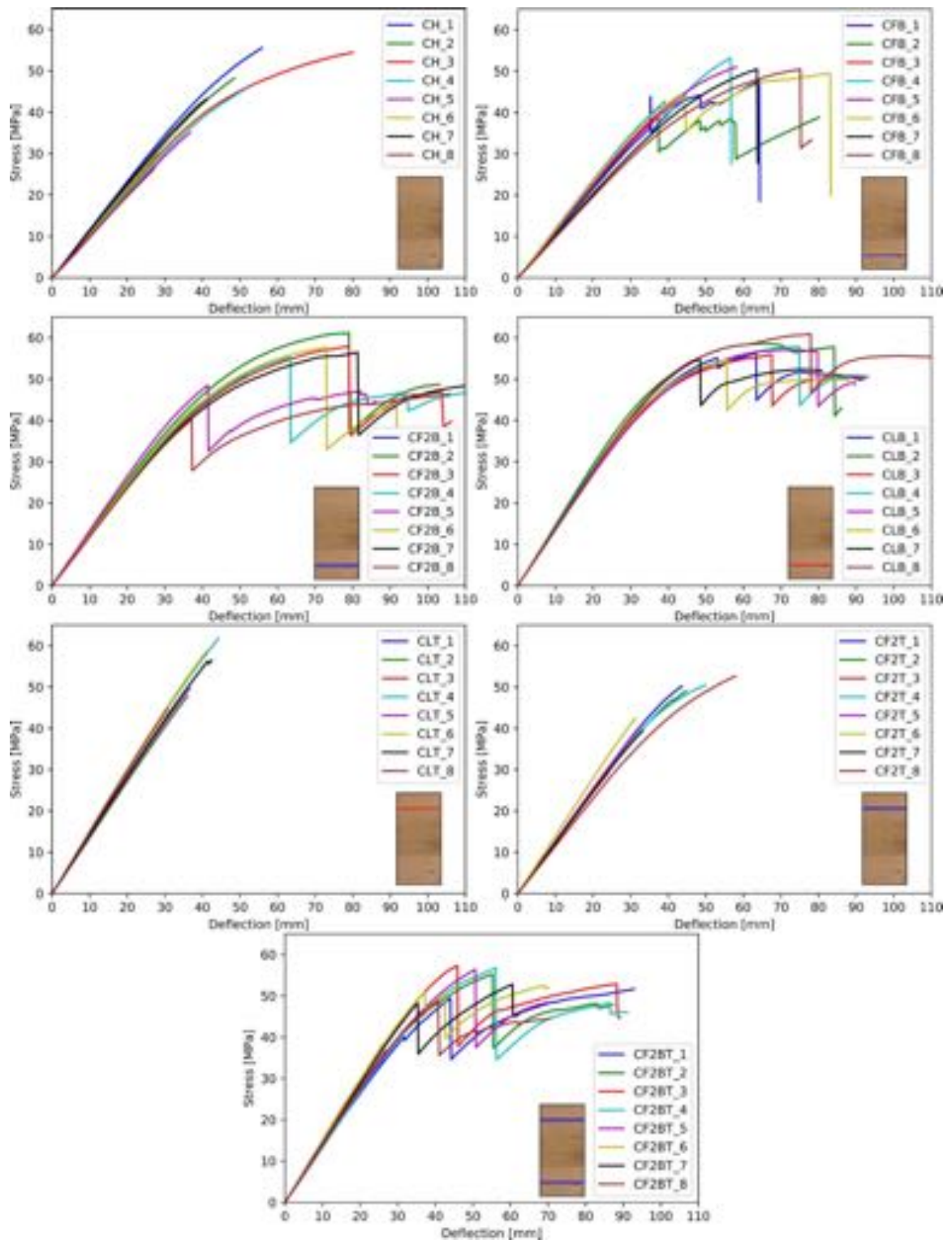


Figure 4.8: Stress-deflection relations.

CHAPTER 4.
IMP. DUCT. AND BEND. FEATURES OF POPLAR GLULAM BEAMS

Layout	Force-displacement (Structural safety)	Force-displacement (Engineering design)	Moment-curvature
CH	1.20 ± 20 BC	1.20 ± 20 BC	1.17 ± 16 AB
CFB	1.77 ± 23 ABC	1.27 ± 15 ABC	1.27 ± 17 AB
CF2B	2.58 ± 12 A	1.61 ± 19 AB	1.47 ± 16 A
CLB	2.48 ± 9 A	1.76 ± 17 A	1.53 ± 12 A
CLT	1.06 ± 2 C	1.06 ± 2 C	1.05 ± 2 B
CF2T	1.14 ± 11 BC	1.14 ± 11 BC	1.11 ± 12 B
CF2BT	2.19 ± 12.81 AB	1.26 ± 11 ABC	1.19 ± 17 AB
Kruskal-Wallis test	F = 39.6 p < 0.05	F = 11.9 p < 0.05	F = 8.81 p < 0.05

Table 4.3: Mean values, covariance (%) and statistical class for: force-displacement ductility parameters (structural safety and engineering design), and moment-curvature ductility.

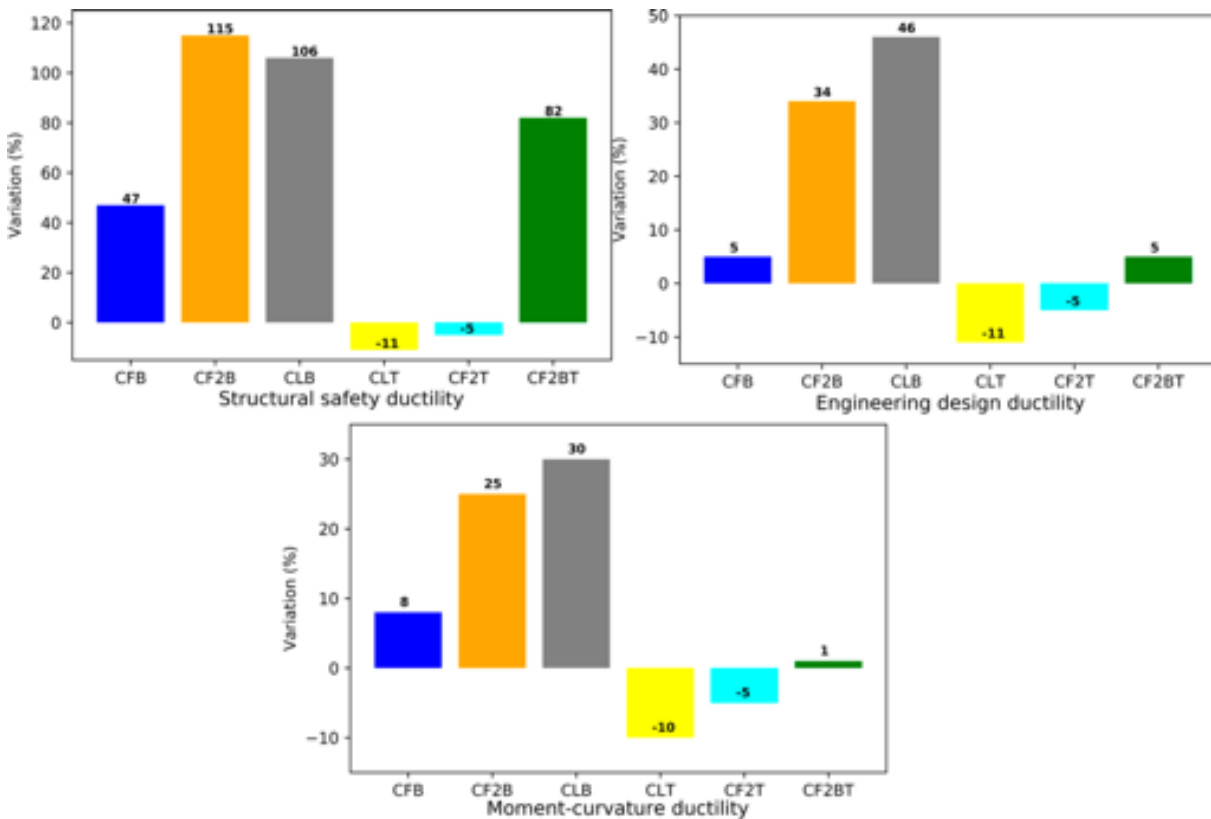


Figure 4.9: Variations of the ductility parameters in % compared to the control CH layout.



Figure 4.10: Failure patterns of the specimens.

CHAPTER 4.

IMP. DUCT. AND BEND. FEATURES OF POPLAR GLULAM BEAMS

range than that of the CLB layout. As seen in the fracture patterns (Figure 4.10), these specimens have a deformed shape, the significant plastic deformation at the compression area being a consequence of the specimen's high ductility.

For the CLT and CF2T layouts, decreasing ductility is clearly observed, identified through a straight linear variation of the stress-deflection relation; meanwhile, a clearly elasto-plastic behaviour is seen for layouts with reinforcement at the tension layers. Thus, the elastic range is shared by the layouts with brittle and ductile behaviour. The most representative elastic range is that of the CLT specimen, exhibiting a steep slope and a wide elastic range without plastic deformation. The fracture patterns (Figure 4.10) offer no evidence of plastic deformation for either the CLT or the CF2T layout. Such behaviour can be attributed to the reinforcement at the compression layers, which impedes plastic behaviour. The behaviour becomes brittle because the tensile stress is only withstood by the poplar lamellas.

The CF2BT layout exhibited optimal behaviour in both elastic and plastic terms, standing as reasonable improvement. In this case, the yield point is similar to cases CF2B and CLB, due to high stress concentration at the compression zone. One important feature observed in the experimental tests resides in the specimens' behaviour during the second loading phase, after appearance of the first drop. The CF2B and CLB specimens exhibited excessive plastic deformation because the top area was plasticized, with high-stress concentrations being undergone only by the poplar lamella. The CF2BT layout behaved differently in the second phase, where a short elastic range is observed prior to the ultimate plasticization of the sections. As noted during the experiments, the high plasticizations can be traced to progressive debonding between poplar layers, and to cracks propagating along the beam (see Figure 4.10).

Table 4.4 summarizes the results for the seven layouts regarding elastic moduli and maximum stress, including covariance and statistical results. Figure 11 shows the improvement (%) of the static modulus and maximum stress when compared with control layout L1.

The selected poplar lamellas occupied a range of 6240-7882 N/mm². The range of mean values for the combined modulus $MoE_{dyn,c}$ was found to be 7286-8549 N/mm². These values are about 1000 N/mm² higher than those of the dynamic moduli of the single lamellas before gluing. In other words, the improvement can essentially be attributed to the gluing process (glue contribution), with a lesser influence of defects due to the finger joint manufacturing. The shear modulus of the specimens shows little variation, meaning that the reinforcement and gluing process hardly influence this mechanical parameter.

Regarding the MoE_{dyn} , the reinforcement improves stiffness, especially for the cases in which pultruded laminated is used (CLT and CLB) and two fabric layers are placed in the areas of tension and compression (CF2BT). Among these three layouts, no statistical differences were observed. Similarly, no statistically significant improvement was afforded by the fabric (one or two layers) placed only at the compression or the tension side, with respect to the control layouts CH.

The static modulus of elasticity (MoE_s) showed most noteworthy improvement when about 44% of pultruded laminate is placed at the tension side (CLB), with a clearly independent statistical class A as compared to the other layouts. This result is followed by an improvement of around 29% provided by the 2-layer carbon fabric at both compression and tension zones (CF2BT), characterized by the AB statistical class. The sections having reinforcement at the tensile zones bear the highest tensile stress,

Layout	MoEdyn,c	MoEdyn	G	MoEs	MoEm,g	MoEm,g+G	fm
CH	7586 ± 4	7586 ± 4	866 ± 8	8146 ± 9	7615 ± 18	8033 ± 19	43 ± 26
	AB	B	A	C	B	B	B
CFB	7570 ± 5	7926 ± 4	834 ± 9	8567 ± 14	7865 ± 12	8300 ± 12	48 ± 10
	AB	B	A	BC	B	B	AB
CF2B	7283 ± 4	8546 ± 5	861 ± 7	9326 ± 9	8777 ± 11	9317 ± 11	55 ± 13
	B	AB	A	ABC	AB	AB	AB
CLB	761 ± 3	9656 ± 4	797 ± 8	11758 ± 8	10335 ± 8	11195 ± 8	57 ± 34
	B	A	A	A	A	A	A
CLT	7901 ± 3	10086 ± 5	847 ± 10	9535 ± 5	10885 ± 9	11805 ± 10	52 ± 12
	AB	A	A	ABC	A	A	AB
CF2T	7428 ± 3	8500 ± 7	885 ± 7	9058 ± 14	9140 ± 11	9733 ± 13	47 ± 17
	B	AB	A	BC	AB	AB	B
CF2BT	8025 ± 5	9419 ± 5	864 ± 12	10525 ± 8	1036 ± 19	11200 ± 21	54 ± 5
	A	A	A	AB	AB	AB	AB
Kruskal	F = 8.77	F = 42.9	F = 1.06	F = 10.8	F = 9.18	F = 10.1	F = 6.08
Wallis test	p < 0.05	p < 0.05	p = 0.40	p < 0.05	p < 0.05	p < 0.05	p < 0.05

Table 4.4: Mean values (N/mm²), covariance (%) and statistical class of: $MoE_{dyn,c}$: dynamic combined modulus; G: Shear modulus; MoE_{dyn} : dynamic modulus; MoE_s : static modulus; $MoE_{m,g}$: global modulus without shear modulus (mean); $MoE_{m,g+G}$: global modulus of elasticity with shear modulus (mean); f_m : maximum stress.

giving the highest improvement of the MoE_s , compared with the control section CH (C class), since the presence of the reinforcement increases stiffness in tension. It is worth mentioning that, due to the different behaviour of timber under tension and compression, the maximum tension layer of the beam undergoes high tensile stress, meaning stress concentration in the reinforcement. Intermediate improvement is obtained for the CFB and CF2B, even when differences are not statistically relevant compared with the control layout (BC and ABC classes, respectively). Statistical tests also reveal some differences owing to increased carbon fabric thickness. Layouts CF2B and CLB showed relevant differences from a statistical viewpoint (ABC and A classes, respectively). A medium-high improvement is also obtained for some CLT and CF2T specimens, even though the reinforcement was at the compressive zone (11%-17%). The existence of the reinforcement would have increased the total stiffness of the specimen, and especially the modulus of elasticity at compression. Thus, the ratio between the modulus of elasticity in tension and the compression is reduced, acting as a homogeneous section (similar modulus at tension and compression). The reinforcement keeps the wood from developing plastic deformations at the compression area. Still, its behaviour is perfectly linear, without a yielding range, due to the brittle behaviour of the timber at tension. Finally, the CF2BT layout displayed a clear improvement in terms of the static modulus of elasticity (around 29%). It was observed that this layout reduces plastic deformation at the compression area, showing a proper behaviour of the whole section up to failure, sustained by the stress-deflection relation and the failure pattern shown in Figure 4.10.

Nearly the same tendency can be observed for the $MoE_{m,g}$ and $MoE_{m,g+G}$ elastic moduli. Moreover, differences are seen for the static and global moduli. This is mainly because the static modulus, MoE_s , was obtained by means of the strain gauge, taking the real strain at the mid-span of the beam. In turn, the global modulus was calculated according to the standard [19][22], in which the shear modulus is omitted. Yet

CHAPTER 4.

IMP. DUCT. AND BEND. FEATURES OF POPLAR GLULAM BEAMS

the global modulus $MoE_{m,g}$ is highly influenced by the shear stresses, as opposed to the MoE_s , which is scarcely influenced by the shear but serves to measure the global deformation. The standard also gives a $MoE_{m,g}/G$ ratio equal to 16, which is far from the value of 9 obtained for the control layout. A direct application of the standard ratio is therefore not valid for all species. For CH beams, results demonstrate that when an appropriate value of G is considered ($MoE_{m,g+G}$), the difference between the static and global moduli decreases from 7% to just 1%. For the beams reinforced at compression with a pultruded laminate (CLT), the differences -even when G is applied- can be associated with the fact that measurement of G by NDT methods ignores the position of the reinforcement in the destructive test.

In terms of the maximum stress (f_m), the highest improvement (around 33%) is also achieved when the pultruded laminate reinforcement is placed at the tensile zone. The influence of the reinforcement thickness is evident, meaning respective improvements from 12% to 28% for the CFB and CF2B layouts. Statistically, no differences are observed between the CF2B and CF2BT layouts, since the reinforcement has high performance under tensile stresses. Therefore, the reinforcement placed at the bottom side of the cross-section is the one that mostly contributes on the improvement of the maximum stress. Thus, for the same load level, in both cases the reinforcement in tensile area considerably reduces the stress in the bottom poplar lamella (maximum tensile) while the top reinforcement lightly reduces the tensile stresses at the bottom. The latter behaviour is evidenced by the CF2T layout (10% of improvement), where the reinforcement is only placed in compression, while the lower mid cross-section of the beam undergoes tensile stresses through the poplar lamellas. The CLT, with the pultruded laminate reinforcement placed at compression, achieves a significant improvement of roughly 22%, showing that even at compression, the thickness of reinforcement proves very relevant in terms of the maximum tensile stress.

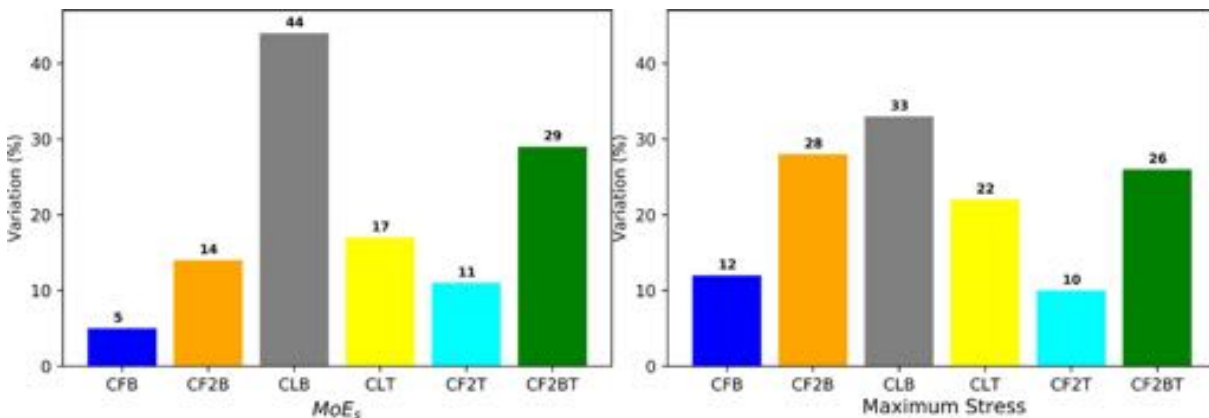


Figure 4.11: Improvement of the static modulus of elasticity (left) and maximum stress (right) improvements respect to the control CH layout.

A comparison of the dynamic moduli ($MoE_{dyn,c}$ and MoE_{dyn}) and the static modulus (MoE_s) is depicted in Figures 4.12, 4.13, and 4.14 representing all the samples of each layout (Figures 4.12 and 4.13) or only the mean value for each particular layout. Figures 4.12 and 4.13 show that the experimental points are basically grouped in clusters, each one associated with a particular layout.

In greater detail, Figure 4.12 clearly shows that all the points are distributed around a horizontal line, as $MoE_{dyn,c}$ represents the contribution of the poplar lamellas alone.

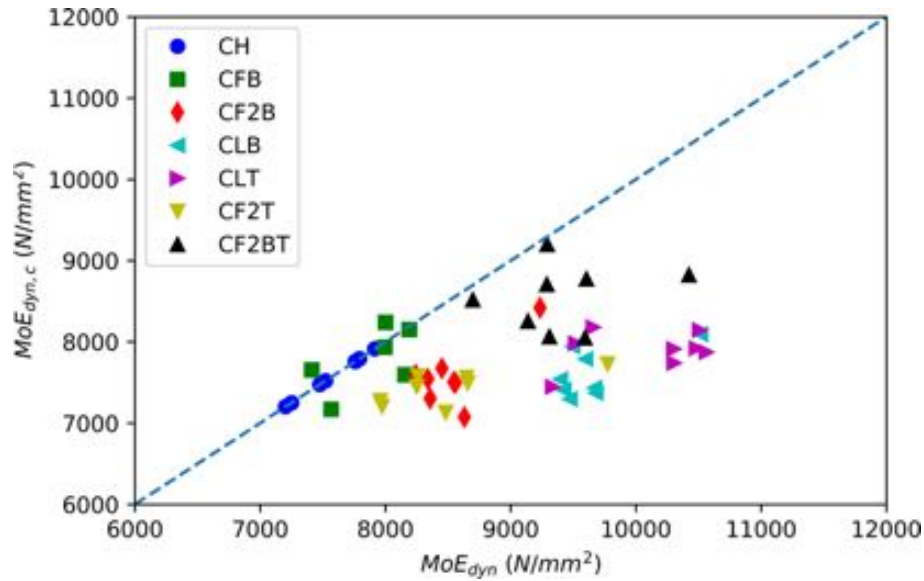


Figure 4.12: Dynamic modulus of elasticity vs. dynamic combined modulus for all specimens.

It is clear that all the clusters corresponding to reinforcement layouts provide MoE_{dyn} values that are higher than the corresponding $MoE_{dyn,c}$, demonstrating the improvement provided by reinforcement. Given the reasons expounded above, the clusters corresponding to CFB, CF2B and CF2T are very close to each other and very close to the CH control one, demonstrating non-significant improvements from a statistical point of view. A pertinent example is the CF2B layout, where the $MoE_{dyn,c}$ of the section without reinforcement is 4.0% below the control CH layout.

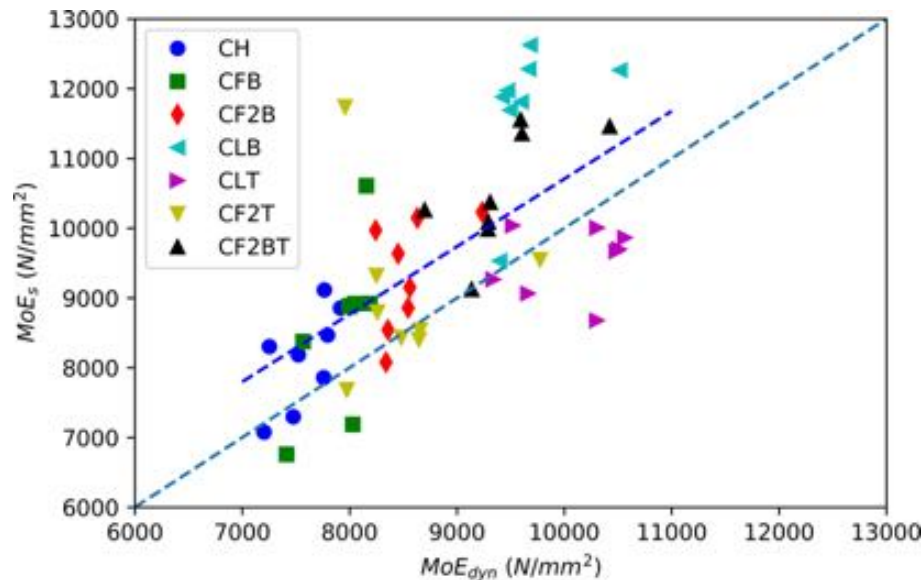


Figure 4.13: Dynamic modulus of elasticity vs. static modulus of elasticity for all specimens.

Figure 4.12 displays a sample-by-sample comparison of the static and dynamic moduli. Once again, a clear difference can be seen between the CFB, CF2B and CF2T clusters, which are statistically very close to the control CH cluster, meaning no rel-

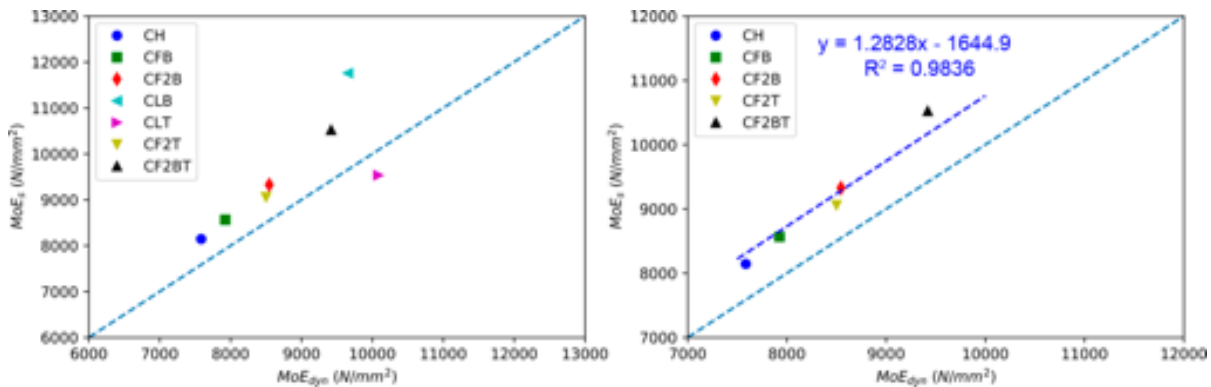


Figure 4.14: Mean values of dynamic modulus of elasticity against vs. static modulus of elasticity.

evant improvements in stiffness; in contrast, the CLB, CLT and CF2BT clusters provide substantial improvement with respect to the control. Such behaviour is likewise reflected in Figure 4.14-left, where only the mean value of each particular layout is represented.

In this case, though almost all the points are straightly aligned close to the 45° line-which would represent the optimum situation in which static and dynamic moduli are similar; that is, NDT and destructive tests providing the same results- the points for the layouts with pultruded carbon laminated lie beyond the linear behaviour, demonstrating a clear influence of the type of reinforcement on the dispersion of results between the NDT and the destructive test. The difference is also highly conditioned by the position of the pultruded laminate, which would clearly influence the vibration patterns of the composite beam.

4.4 Conclusions

This paper demonstrates a clear influence of the position and the precise type of reinforcement along the timber cross-section upon the mechanical behaviour of the whole element.

When one or two layers of carbon fabric are used (0.166 mm thickness each), either in the compression or the tension layer, only minor improvements in stiffness are obtained -no higher than 15%, and not significantly different from the control non-reinforced beams. The influence of fabric thickness on stiffness is limited, proving more relevant in the case of the maximum load, for which significant improvement is achieved when two fabric layers are used (around 28%).

For the case in which pultruded carbon laminate is used together with two layers of carbon fabric on both the compression and tension sides, significant improvements are obtained in terms of stiffness and strength (up to 44% and 33%, respectively, when reinforcement exists at the tension side). Improvement is lower when the reinforcement is used only on the compression side (17% and 22%, respectively).

A good correlation is observed between the dynamic and static moduli (non-destructive and destructive procedures), except when pultruded laminated carbon is used for reinforcement, in which case its position is clearly influential. This may be due to the higher mass ratio provided by the pultruded laminated as compared to the carbon fabric, conditioning the vibration pattern of the entire element. Nevertheless, this issue

will be more deeply addressed in future work by using numerical simulations.

High values of ductility are obtained when the reinforcement is placed at the tension area (ductility values up 2.60). When reinforcement is placed only at the compression zone, a brittle behaviour is observed, similar to that corresponding to the control case without reinforcement.

With the aim of taking this concept to a higher Technology Readiness Levels (TRL), two objectives will be addressed in future research: I) To elaborate and test specimens obtained from different plantations in the north and south of Spain; II) Employing finite element models (FEM), optimization and reliability techniques, high performance samples can be designed taking into account the statistical nature of the mechanical properties of the poplar timber materials.

Chapter 5

Transformed-section method applied to multi-species glulam timber beams subjected to pure bending

Title	Transformed-section method applied to multispecies glulam timber beams subjected to pure bending
Authors	C. Timbolmas; R. Bravo; F. J. Rescalvo; M. Portela
Journal	Mechanics of Advanced Materials and Structures
ISSN	1537-6494
Journal's performance	Journal impact factor (2020): 4.030 Q1 (Mechanics: 28/135)
Details	Published: October 2021; Pages: 1-10
DOI	10.1080/15376494.2021.1985665

5.1 Introduction

Wood has been used in the construction sector for thousands of years, mainly due to its nature, which ensures its noticeable bending performance, since it can withstand both tension and compression. Moreover, the high strength to weight ratio, aesthetic appearance and the potential sustainability of the source, make it more attractive for different construction sectors, such as residential buildings, industrial buildings and footbridges [100, 101].

Structural glued-laminated timber (glulam) is one of the oldest Engineered Wood Products (EWP) [102] and the development of EWP starts to represent an attractive alternative for the construction to gain healthy environments [103]. Wood by its nature is a material with anisotropic behaviour in longitudinal, radial, tangential directions, and besides these, timber behaves differently in tension and compression. The numerical and analytical models become challenging and many authors proposed different models which take into account the different behaviour in tension and compression, respectively [104, 105].

By definition, composite structural members are composed of two materials with different mechanical properties. In order to analyse these members using the standard formulations of the strength of materials theory, the composite cross-section is

CHAPTER 5.

TRANSF.-SECT. METHOD APPLIED TO MULTI-SPECIES

transformed into a homogeneous one using the transformation method in combination with the Parallel axis theorem [106]. One of the most important parameters for an analytical model, based on the Parallel axis theorem, is represented by the modulus of elasticity (MoE) and geometric dimensions of each assembly part. Since timber is a material characterized by a different behaviour in tension and compression, the well-known transformed-section method can be applied. A multitude of research works are developed using the transformed-section method, especially in reinforced and/or prestressed beams, and composite steel-concrete structures [107–110]. Moreover, this technique starts to be widely used also for the composite timber section, especially in timber-concrete cross-sections. An experimental and theoretical investigation employing the transformed-section method was used in a recent research work related to timber beam and concrete slab connected with coach screw [111].

In general, when a cross-section is composed of at least two timber materials or one timber material defined by different behaviour in tension and compression, the utilization of the transformed-section method needs to be involved. This method is widely applicable in composite timber members or multi-layered timber sections, analyzed in a comparative way with the experimental and FEM technique [112, 113]. Fossetti [114], developed an analytical model based on homogenization, able to predict the stresses and the ultimate bending capacity of multilayer large-scale glulam beams, taking into account the effect of the reinforcement. The same approach has been used to characterize the global elastic and bending parameters where several sections with different properties were converted into equivalent transformed sections with the same properties [115]. Many practical research work [116–124] were carried out by several authors employing different glulam beam layouts, being compared with analytical models developed based on beam theory.

The modulus of elasticity has a strong correlation with the strength parameters, in view of the fact that is a key parameter for wood products. Mainly, the MoE of a glulam section is predicted employing the transformed section method based on the dynamic MoE of the timber layer [16, 125]. Other advanced techniques, such as the lamination surface scanning, can be applied to measure the fibre direction fields of the timber layers, thus obtaining a mapping of the longitudinal distribution of MoE in a glulam beam [126, 127].

To compute the elastic moduli of the timber, an analytical model is formulated, based on the transformed-section method and parallel axes theorem for pure and combined sections. These solutions provide relations for the mechanical behaviour in tension and compression, the global modulus of elasticity and the neutral axis position. Static bending tests were performed according to the EN 408:2010+A1:2012 [19], standard, which provided the data required by the developed model. The work also describes and discusses the obtained analytical results based on the experimental results as input data. Finally, a parametric analysis is carried out for the combined section as a function of a particular-species timber percentage. The parametric analysis is focused on the global modulus of the whole cross-section and the ones in tension and compression.

5.2 Transformed-section Theory

5.2.1 General formulation

Timber is an anisotropic linear elasto-plastic material with a different behaviour at tension and compression [105]. For structural members subjected to bending, it is considered that timber behaves in the longitudinal direction as a linear elasto-plastic material. Therefore, the longitudinal elastic behaviour must be defined by two different elastic moduli: modulus in tension (E_t) and modulus in compression (E_c), separated by the position of the neutral axis (Y_n). Usually, in order to define the global elastic longitudinal behaviour of a beam, the global modulus of elasticity is used (MoE_{global}), which comprises a value that lies between tension and compression moduli and consequently represents the homogeneous elastic behaviour of the whole section of a beam [75].

The different behaviour in tension and compression allows the cross-section to be considered as a composite section, composed of two materials with different elastic moduli. The transformed section method permits to analyze the behaviour of a composite cross-section as a section made up of an equivalent material [16]. Figure 5.1 shows a general section of a beam subjected to pure bending, where the position of the neutral axis (Y_n) defines the limit between the area of the section in tension (E_t - bottom part) and the area in compression (E_c - top part). The Navier-Bernoulli hypothesis considers that the cross-section remains plane during bending (see Figure 5.1-a), consequently the condition of geometric compatibility of deformation is satisfied. This hypothesis allows to geometrically transform the section into an equivalent one, multiplying the width of each material $b(y)$ by its corresponding modular ratio (n). Figure 5.1-b shows a general composite section and the corresponding transformed section (Figure 5.1-c) as an equivalent material with elastic modulus E_h , using two different modular ratios, one related with the moduli in compression (n_ch) and the other one in tension (n_th).

The curvature (ρ) of a whole cross-section and a homogeneous one is given by the following expression,

$$\rho = \frac{M}{MoE_{global}I_{global}} = \frac{M}{E_h I_h} \quad (5.1)$$

Since the acting moment on the entire cross-section and the homogeneous section is the same, the following relation between the moduli of the entire cross-section (MoE_{global}) and homogeneous one (E_h) are obtained,

$$MoE_{global} = \frac{E_h I_h}{I_{global}} \quad (5.2)$$

where I_{global} is the inertia of the entire cross-section (Figure 5.1-b) and I_h is the inertia of the homogeneous section (Figure 5.1-c). The computation of homogeneous inertia (I_h) follows the Steiner theorem (Parallel axes theorem) as,

$$I_h = I_{Ath} + A_{th}(Y_{th} + Y_{CG})^2 + I_{Ach} + A_{ch}(Y_{ch} - Y_{CG})^2 \quad (5.3)$$

where I_{Ath} , I_{Ach} are the inertia of the homogenised tensile and compression areas with respect to their own centre of gravity (Y_{th} and Y_{ch} , respectively, Figure 5.1-c). The $A_{th} = n_{th} A_t$ is the area of the transformed section in tension and $A_{ch} = n_{ch} A_c$ is the area of the transformed section in compression. The $n_{th} = E_t/E_h$ and $n_{ch} = E_c/E_h$ are

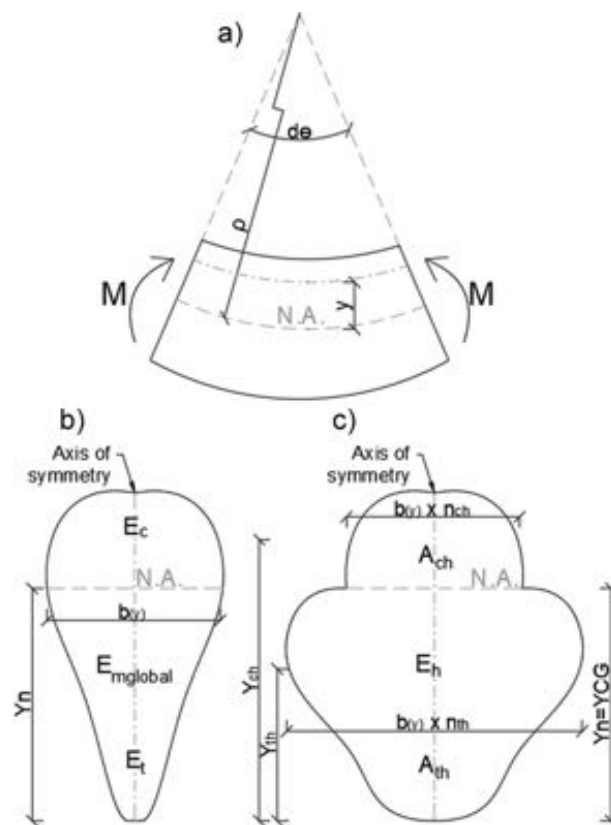


Figure 5.1: a)Section of a beam composed of a material with different behaviour in tension and compression subjected to pure bending; b) General cross-section; c) Corresponding transformed section.

modular ratios for compression and tension of homogeneous material; Y_{CG} is the centre of gravity of the transformed section computed as,

$$Y_{CG} = \frac{A_{th} + Y_{th} + A_{ch}Y_{ch}}{A_{th} + A_{ch}} \quad (5.4)$$

For a homogeneous section subjected to pure bending, the position of the centre of gravity (Y_{CG}) coincides with the position of the neutral axis (Y_n) [128]. The position of the neutral axis defines the limit between the tension and compression areas in the entire cross-section, consequently, this limit must be in the same position as in the transformed section, in order to achieve the same compression-tensile resultant forces and moment. Therefore, the computation of the position of Y_n coincides with the position of the centre of gravity (Y_{CG}) of the transformed section.

In view of these experimental data, several assumptions are considered in this work: a) timber behaves purely linear elastic in tension and compression; b) the connection of the bond-line between layers or between finger joints is rigid; c) no debonding between layers occurs. The linear elastic assumption is valid for the usual applied loads in service. Rigid joints are commonly assumed by many authors (see e.g.: [113, 128] among others) when high stiffness resin is applied. However, this assumption must be studied carefully if a low stiffness polyurethane (PUR) resin is used since it implies a reduction in MoE. In a similar way, no debonding between layers is assumed if a high stiffness resin is applied and service loads do not produce stresses higher than the tensile strength of the resin.

5.2.2 Formulation for a mono-species cross-section

The aforementioned theory is applied here to the pure rectangular section depicted in Figure 5.2-a.

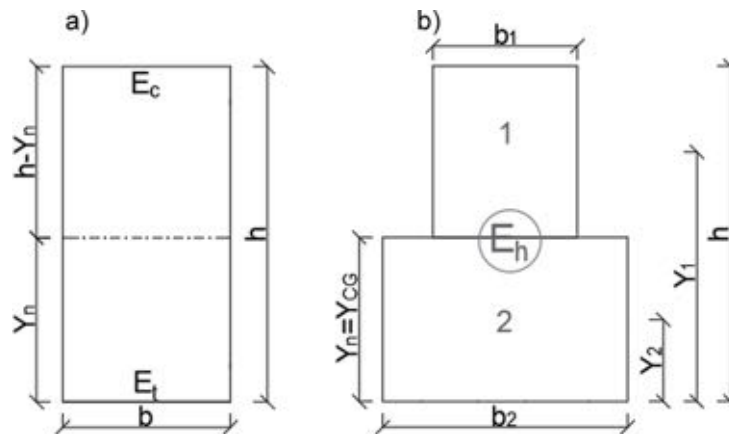


Figure 5.2: a) Cross-section made up of a timber material with different elastic moduli in tension and compression; b) Transformed section made up of a homogeneous material, E_h .

The transformed section is shown in Figure 5.2-b, using the following modular ratios:

$$n_{ch} = \frac{E_c}{E_h}, n_{th} = \frac{E_t}{E_h} \quad (5.5)$$

CHAPTER 5.
TRANSF.-SECT. METHOD APPLIED TO MULTI-SPECIES

The position of the centre of gravity is given as:

$$Y_{CG} = \frac{A_1 Y_1 + A_2 Y_2}{A_1 + A_2} \quad (5.6)$$

where $A_1=b_1(h-Y_n)$, $A_2=b_2 Y_n$, $Y_1=(h+Y_n)/2$, $Y_2=Y_n/2$, $b_1=bn_{ch}$, $b_2=bn_{th}$. By using the condition $Y_n=Y_{CG}$ to equation (5.6), the position of the neutral axis is computed as follows:

$$Y_n = \frac{\sqrt{E_c} h}{\sqrt{E_c} + \sqrt{E_t}} \quad (5.7)$$

The global modulus is computed as $MoE_{global} I_G=E_h I_h$, where $I_G=\frac{bh^3}{12}$ is the inertia of the whole section and I_h is the inertia of the homogeneous section with respect to its centre of gravity (Y_{CG}). Steiner theory (Parallel axes theorem) further can be applied as $I_h=I_1+A_1(Y_1-Y_{CG})^2 + I_2+A_2(Y_2-Y_{CG})^2$, where $I_1=\frac{b_1(h-Y_n)^3}{12}$ and $I_2=\frac{(b_2 Y_n^3)}{12}$. Applying the above relations, the global modulus as a function of the moduli in tension and compression is expressed as follows:

$$MoE_{global} = \frac{4E_c E_t}{(\sqrt{E_c} + \sqrt{E_t})^2} \quad (5.8)$$

Additionally, the relations between E_c or E_t , MoE_{global} , and Y_n can be computed by solving the system of equations (Eqs. 5.7, 5.8), and the solutions are:

$$E_c = \frac{MoE_{global} h^2}{4(h - Y_n)^2}, E_t = \frac{MoE_{global} h^2}{4Y_n^2} \quad (5.9)$$

5.2.3 Formulation for a multi-species cross-section

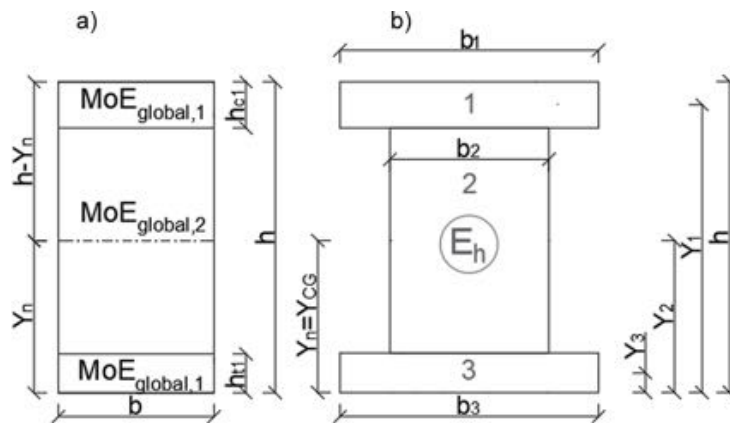


Figure 5.3: a) Cross-section made up of a timber material with different elastic moduli in tension and compression; b) Transformed section made up of a homogeneous material, E_h .

Figure 5.3-b shows the transformed section from material 1 ($MoE_{global,1}$) and material 2 ($MoE_{global,2}$), into an equivalent material (E_h), using the modular ratios defined as:

$$n_{1gl} = \frac{MoE_{global,1}}{E_h}, n_{2gl} = \frac{MoE_{global,1}}{E_h} \quad (5.10)$$

The position of the centre of gravity of the transformed section is:

$$Y_{CG} = \frac{A_1Y_1 + A_2Y_2 + A_3Y_3}{A_1 + A_2 + A_3} \quad (5.11)$$

where $A_1=b_1 h_{c1}$, $A_2=b_2(h-h_{c1}-h_{t1})$, $A_3=b_3 h_{t1}$, $Y_1=h-\frac{h_{c1}}{2}$, $Y_2=h-\frac{(h_{c1}+h_{t1})}{2}+h_{t1}$, $Y_3=\frac{h_{t1}}{2}$, $b_1=bn_{1gl}$, $b_2=bn_{2gl}$, $b_3=bn_{1gl}$. Applying the condition, $Y_n=Y_{CG}$ to Eq. 11, the position of the neutral axis Y_n is computed as follows:

$$Y_n = \frac{MoE_{global,1}((h-h_{c1})^2 - ht1^2 + MoE_{global,1}(2hh_{c1} - hc1^2 + ht1^2))}{2(MoE_{global,2}(h-h_{c1}-ht1) + MoE_{global,1}(hc1 + ht1))} \quad (5.12)$$

where h , h_{c1} , h_{t1} is defined in Figure 5.3-a. The global modulus of the combined section is computed with the relation, $MoE_{global} I_G=E_h I_h$, where $I_G=\frac{(bh^3)}{12}$ is the inertia of the entire cross-section, I_h is the inertia of the homogeneous section with respect to its centre of gravity (Y_{CG}). Steiner theory (Parallel axes theorem) further can be applied as $I_h=I_1+A_1(Y_1 - Y_{CG})^2+I_2+A_2(Y_2 - Y_{CG})^2+I_3+A_3(Y_3 - Y_{CG})^2$, where $I_1=\frac{(b_1hc1^3)}{12}$, $I_2=\frac{(b_2(h-hc1-ht1)^3)}{12}$, and $I_3=\frac{(b_3ht1^3)}{12}$. Applying the above relations, the global modulus of the combined section, as a function of the global modulus of each material, can be expressed as:

$$\begin{aligned} MoE_{global} = & \frac{1}{h^3} \cdot 4(MoE_{global,2}(h-h_{c1}-h_{t1})(h^2 + h_{c1}^2 - h_{c1}h_{t1} + h_{t1}^2 \\ & + h(-2h_{c1} + h_{t1} - 3Y_n) + 3h_{c1}Y_n - 3h_{t1}Y_n + 3Y_n^2) + \\ & MoE_{global,1}(3h^2h_{c1} - 3hh_{c1}h_{c1} + 2Y_n + (h_{c1} + h_{t1}) \\ & (h_{c1}^2 - h_{c1}h_{t1} + h_{t1}^2 + 3h_{c1}Y_n - 3h_{t1}Y_n + 3Y_n^3))) \end{aligned} \quad (5.13)$$

It can be observed that the global modulus depends on the moduli and the depth of each material (h , h_{c1} , h_{t1}), consequently, the geometry of the specimens influences the global modulus. Eqs. 5.9 and 5.13 allow computing the influence of the global modulus of both materials of the moduli in tension and compression of the combined beam, considering that the global modulus takes into account the behaviour of a beam as it was composed of one material. Consequently, these moduli will be defined as combined moduli $E_{c,comb}$ and $E_{t,comb}$, which can be calculated as:

$$E_{c,comb} = \frac{MoE_{global}h^2}{4(h - Y_n)^2}, E_{t,comb} = \frac{MoE_{global}h^2}{4Y_n^2} \quad (5.14)$$

On the other hand, the combined rectangular section depicted in Figure 5.4-a is transformed into a homogeneous section, taking into account the elastic moduli in tension and compression of each material

Hence, for this case, the following modular ratios are applied:

$$n_{ch1} = \frac{E_{c1}}{E_h}, n_{ch2} = \frac{E_{c2}}{E_h}, n_{th1} = \frac{E_{t1}}{E_h}, n_{th2} = \frac{E_{t2}}{E_h} \quad (5.15)$$

CHAPTER 5.
TRANSF.-SECT. METHOD APPLIED TO MULTI-SPECIES

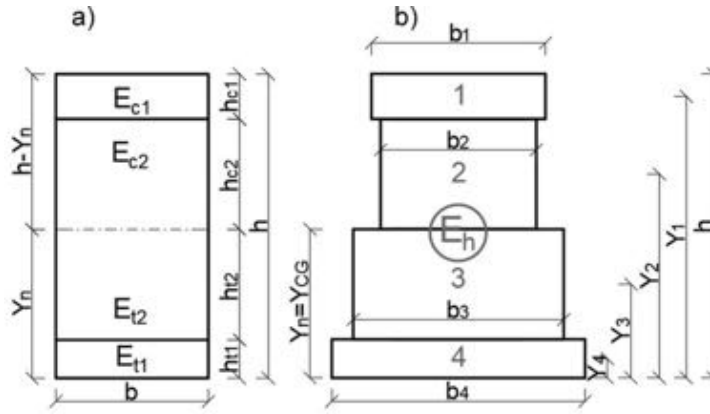


Figure 5.4: a) Cross-section made up of two timber materials with different elastic moduli in tension and compression. b) Transformed section made up of a homogeneous material, E_h .

Based on the geometry of the combined section, the MoE_{global} and Y_n , as a function of E_c and E_s of each material, are obtained. The position of the centre of gravity corresponding to the transformed section in Figure 5.4-b is:

$$Y_{CG} = \frac{A_1 Y_1 + A_2 Y_2 + A_3 Y_3 + A_4 Y_4}{A_1 + A_2 + A_3 + A_4} \quad (5.16)$$

where $A_1 = b_1 h_{c1}$, $A_2 = b_2 (h - Y_n - h_{c1})$, $A_3 = b_3 (Y_n - h_{t1})$, $A_4 = b_4 h_{t1}$, $Y_1 = h - \frac{h_{c1}}{2}$, $Y_2 = \frac{(h + Y_n - h_{c1})}{2}$, $Y_3 = \frac{(Y_n + h_{t1})}{2}$, $Y_4 = \frac{h_{t1}}{2}$, $b_1 = b n_{ch1}$, $b_2 = b n_{ch2}$, $b_3 = b n_{th2}$, $b_4 = b n_{th1}$. By using the condition $Y_n = Y_{CG}$ into the Eq. 5.16, the position of the neutral axis is computed as follows:

$$Y_n = \frac{1}{E_{c2} - E_{t2}} \cdot (E_{c2} h + E_{c1} h_{c1} - E_{c2} h_{c1} + E_{t1} h_{t1} - E_{t2} h_{t1} - 0.5 \sqrt{4(E_{c2}(h - h_{c1})) + E_{c1} h_{c1} + (E_{t1} - E_{t2}) h_{t1}^2} - 4(E_{c2} - E_{t2})(E_{c2}(h - h_{c1}))^2 + E_{c1}(2h - h_{c1})h_{c1} + (E_{t1} - E_{t2})h_{t1}^2) \quad (5.17)$$

where h , h_{c1} , h_{t1} , h_{c2} and h_{t2} are defined in Figure 5.4-a. The global modulus of elasticity is computed with the relation, $MoE_{global} I_G = E_h I_h$, where $I_G = \frac{bh^3}{12}$ is the inertia of the cross-section, I_h is the inertia of the homogeneous section with respect to its centre of gravity (Y_{CG}). Steiner Theory (Parallel Axes Theorem) further is applied $I_h = I_1 + A_1 (Y_1 - Y_{CG})^2 + I_2 + A_2 (Y_2 - Y_{CG})^2 + I_3 + A_3 (Y_3 - Y_{CG})^2 + I_4 + A_4 (Y_4 - Y_{CG})^2$, where $I_1 = \frac{(b_1 h_{c1}^3)}{12}$, $I_2 = \frac{b_2 (h - Y_n - h_{c1})^3}{12}$, $I_3 = \frac{(b_3 (Y_n - h_{t1})^3)}{12}$, and $I_4 = \frac{(b_4 h_{t1}^3)}{12}$. Hence, the global modulus as a function of E_t and E_c of each material is:

$$MoE_{global} = \frac{1}{h^3} \cdot 4(E_{t1} h_{t1}^3 - E_{t2} h_{t1}^3 + E_{c2}(h - h_{c1} - Y_n)^3 - 3E_{t1} h_{t1}^2 Y_n + 3E_{t2} h_{t1}^2 Y_n + 3E_{t1} h_{t1} Y_n^2 - 3E_{t2} h_{t1} Y_n^2 + E_{t2} Y_n^3 + E_{c1} h_{c1}(3h^2 + h_{c1}^2 + 3h_{c1} Y_n + 3Y_n^2 - 3h(h_{c1} + 2Y_n))) \quad (5.18)$$

Similarly, the equivalent moduli in tension and compression can also be calculated using Eq. 5.14, applying the obtained MoE_{global} from the Eq. 5.18.

5.3 Materials and Methods

5.3.1 Timber

In this study, two wood species were used, *Pinus Sylvester* and *Platanus* (*Platanus hispanica* Mill.ex Muenchh). The *Platanus* wood was extracted from a 16 year old plantation belonging to IFAPA (Instituto de Investigación y Formación Agraria y Pesquera) located at the Vega de Granada, Spain. After harvesting and sawning, timber planks were dried naturally for at least 7 months, ensuring that a moisture content (MC) below 12% was achieved. The Pine wood was supplied by the company Madera Pinosoria S.L. located at Soria, Spain. In this case, the wood was dried by the same company in an industrial wood kiln. In both cases, planks of 35 x 75 x 2000 mm were extracted, which after drying were subjected to an acoustic resonance NDT test in the longitudinal direction (grain direction). By means of the plank density and the propagation velocity obtained from the natural resonances, the dynamic elastic modulus (MoE_{dyn}) was obtained 27, which was adjusted to 12% according to the standard EN 384:2016+A1:2018 [20] by measuring the moisture content of each board by means of a protimeter model surveymaster SM from the company Neurtek S.L. Figure 5.5 shows the distribution of MoE_{dyn} for the planks of both species with a total of 300 and 80 planks for Pine and *Platanus* and a mean value of 12290 MPa and 9989 MPa, respectively. In order to objectively discard the planks with the highest deviation, the standard deviation was calculated, with a value of 1123 MPa for *Platanus* and 2169 MPa for Pine. Then, the planks included in the range of the standard deviation, i.e. [11167-12290] and [8866-11112] MPa for Pine and *Platanus*, respectively, were used for the manufacturing process. Meanwhile the planks outside this range were discarded in order to avoid as much as possible the heterogeneity factor of the modulus of elasticity during the elaboration process.

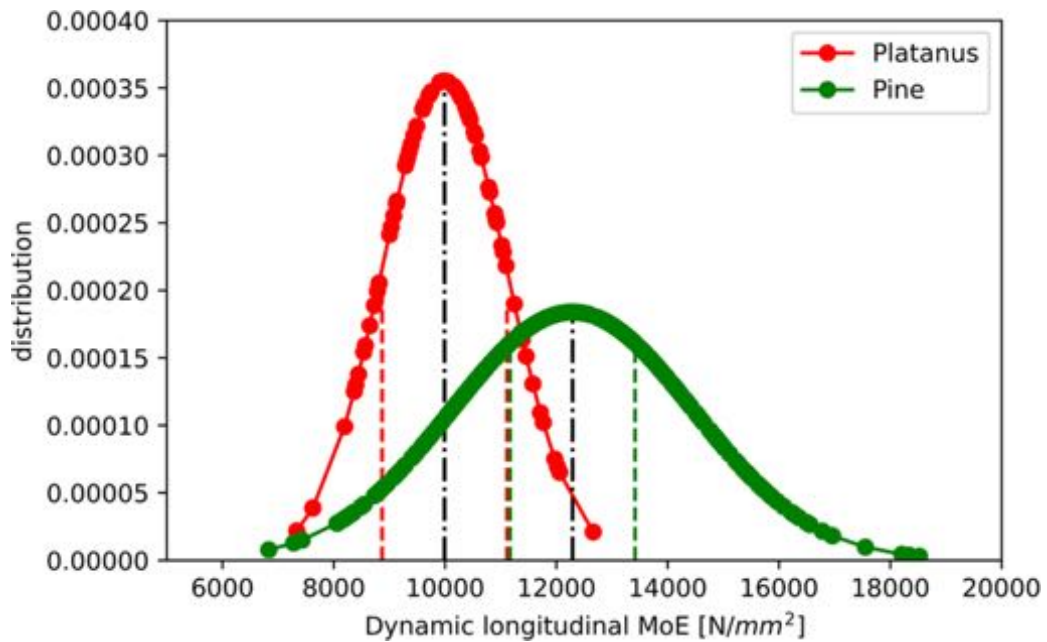


Figure 5.5: Distribution of MoE_{dyn} of Pine and *Platanus* planks. Black dashed-dotted line: Mean value. Red/Green dashed line: Range of selected planks according to the standard deviation.

5.3.2 Glulam beams

Three different layouts were tested, as shown in Table 5.1. Two layouts were made of pure monospecies Pine and Platanus wood, respectively (Pi and Pl). A third layout was a composite multi-species one, manufactured by placing the Pine planks at the outer portions (compression and tensile) and the Platanus in the inner part of the beam, due to the lower mechanical properties of Planatus compared with pine. All the specimens were elaborated by assembling 6 layers of planks with a thicnekss of 17 mm, resulting in a final cross-section of $105 \times 50 \text{ mm}^2$ and a total length of 2100 mm. The manufacturing process included the finger-joint technology, according to the specifications of the standard EN 14080:2013 [21] (Annex I.4 and I.5). A polyurethane resin was used as structural adhesive. In order to ensure a correct adhesive application, the moisture content of the wood was controlled during the whole process, with an average value of $10.8 \pm 1\%$. Once the beams were manufactured, they were conditioned in a climate chamber at $20 \pm 1^\circ\text{C}$ and $65 \pm 5\%$ of relative humidity.




Nomenclature	Pi	Pl	PiPl
Description	Pine	Platanus	Pine (outer layers) + Platanus (inner layers)
Cross-section			

Table 5.1: Glulam beams layouts

5.3.3 Bending tests

Static four-point bending tests were carried out by using a multi-testing machine, with a bending device and a load cell with a maximum capacity of 200 kN, model PB2-F/200. The tests were performed according to the requirements of the EN 408:2010+A1:2012 standard [19], with a displacement control rate of 8.7 mm/min, so that the rupture would occur in 300 ± 120 s, at least for the beams without reinforcement. As indicated in the EN 408:2010+A1:2012 standard [19], a distance between upper supports of 612 mm and a distance of 1920 mm between the lower supports were established to avoid the shear failure (Figure 5.6). The strain measurement was carried out with four strain gauges placed on the mid-span of each beam, two on the faces of maximum tension and compression and two on the lateral faces at 1/4 of the height. For the case of Platanus beams only a strain gauge was placed at the bottom due to lack of sensors. For that reason, the neutral axis could not be measured in the tests. Using the strain gauge located at the bottom face (maximum tensile) present for all tests, the static elastic modulus (MoE_s) was calculated. For that, the stress-strain relationship in the range 10%-40% of the maximum ultimate stress f_m was used, where

$$f_m = \frac{3aP_{max}}{bh^2} \quad (5.19)$$

P_{max} is the maximum load, b the base of the beam, h the height of the beam and a the distance between the application points of the load. By means of a LVDT placed at the mid-span of the specimens, the global elastic modulus (MoE_{global}) was calculated according to the standard EN 408:2010+A1:2012 [19].

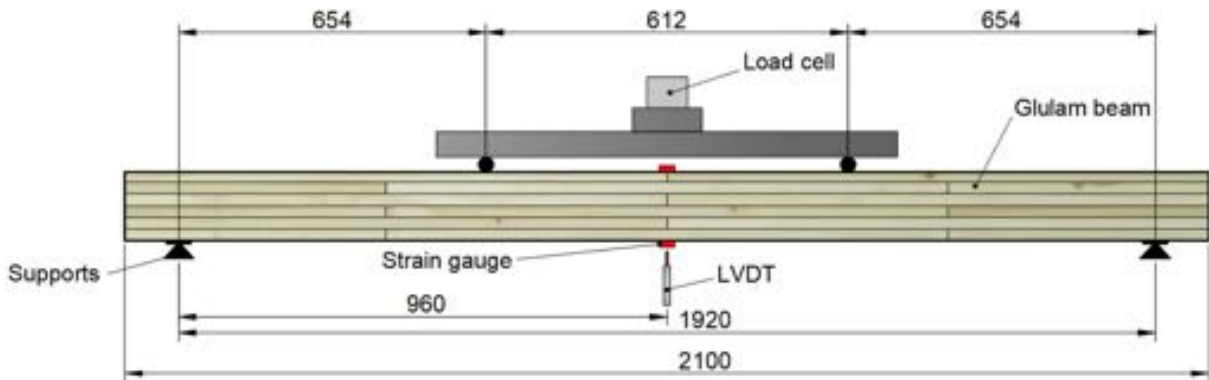


Figure 5.6: Four-point bending test set-up. Strain gauges in red colour. Distances in mm.

5.3.4 Results

Experimental results

The stress-deflection curves, the normal statistical distribution of the modulus of elasticity and the main mechanical features for all specimens obtained through the four-point bending tests are showed in Figure 5.7 and Table 5.2, respectively. Table 5.2 shows the mean values of global modulus (MoE_{global}) based on the recorded displacements using the LVDT, and the maximum bending strength (f_m). Using the Pine layout (Pi), as control specimen (the layout with the higher mechanical properties), the variations of the mean properties between (Pi) and Platanus (Pl), (Pi) and Pine-Platanus (PiPl) are computed respectively.

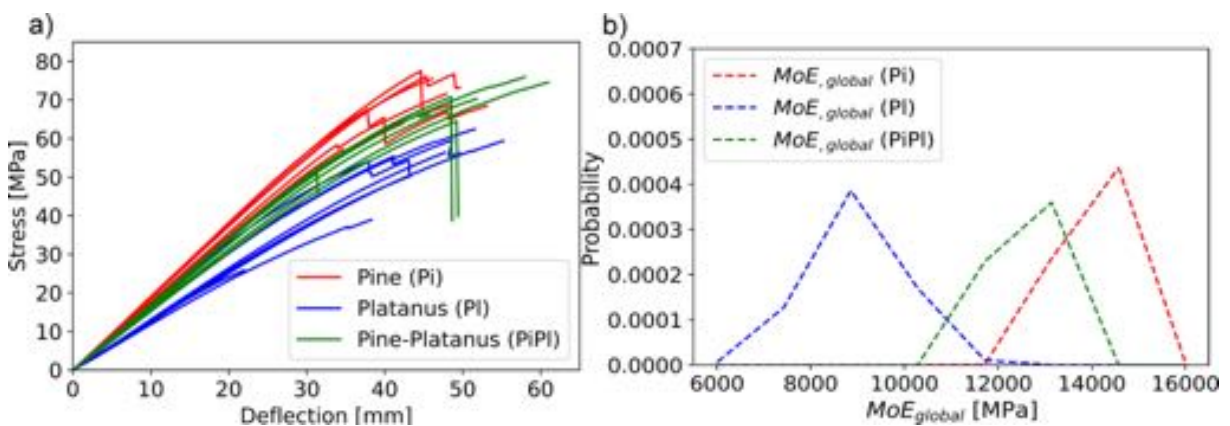


Figure 5.7: Stress-deflection relations for all the experimented specimens. b) Normal distribution of the experimental global modulus (MoE_{global}) for Pine (Pi), Platanus (Pl) and Pine-Platanus (PiPl) layouts.

The stress-deflection curves depicted in Figure 5.7-a show that all specimens have a linear elastoplastic behaviour with a clear limit between the elastic and plastic range.

Specimen Name / Variation	Global modulus (MoE_{global}) (MPa)	Maximum bending strength (f_m) (MPa)
Pine (Pi)	14027	72
Platanus (Pl)	8962	51
Pine-Platanus (PiPl)	12510	66
Variation Pl to Pi (%)	-36	-30
Variation PiPl to Pi (%)	-11	-8

Table 5.2: Experimental mean values: global modulus of elasticity (MoE_{global}), and maximum bending strength (f_m) with their corresponding mean variation.

The maximum and minimum slopes of the relations correspond to Pine (Pi) and Platanus (Pl), with a mean MoE_{global} of 14027 MPa and 8962 MPa, respectively.

The composite multi-species Pine-Platanus layout (PiPl) reveals a behaviour closer to the one of the Pine with a mean decrease of 11% with respect to the control layout (Pi), while the decrease of the Platanus is 36%. Hence, the combination of both species provides a specimen with agreeable properties. Figure 5.7-a evidences that the plastic range for Platanus is higher than the one for the Pine, while the Pine-Platanus beam provides high MoE_{global} and relatively acceptable plasticity (Figure 5.7-b). For Pine layout, the maximum bending strength is clearly higher than for Platanus one with mean values of 72 MPa and 51 MPa, respectively.

As stress-deflection relation and experimental data state, the maximum bending strength of the Pine-Platanus specimens exhibited a mean value of 66 MPa and a corresponding decrease of 8% with respect to control layout (Pi). It is worth mentioning that the Platanus layouts are characterized by a mean decrease of 30% in terms of maximum bending strength compared with the Pine layout (Pi).

Analytical results

- Application 1: Calculation of elastic moduli in tension and compression.

The analytical formulations previously developed provides the relations between MoE_{global} , E_c and E_t for pure specimens, and the equivalent $E_{c,comb}$ and $E_{t,comb}$ for combined multi-species specimens. Given the experimental data of MoE_{global} and the position of the neutral axis (Y_n) for Pine (Pi) and the composite Pine-Platanus beam (PiPl), it is possible to compute analytically the moduli in tension and compression applying the equations Eqs. 5.9 for mono-species and Eqs. 5.14 for multi-species beams, respectively.

Figure 5.8 shows the experimental global modulus and the corresponding position of the neutral axis for 8 specimens for Pine and Pine-Platanus layouts.

The left part of Table 5.3 shows the experimental input data ($MoE_{global,ex}$ and Y_{nex}). The right part shows the corresponding analytical results, i.e. moduli in tension and compression for Pine (Pi) and Pine-Platanus (PiPl), where "K" is the ratio between the tension and compression moduli. Table 5.3 shows a clear tendency for the computed analytical values, since the modulus in tension is higher than the modulus in compression for each specimen. Notice that Table 5.3 and Figure 5.8 only show the data for the specimens for which the neutral axis could be computed with strain gauges located at

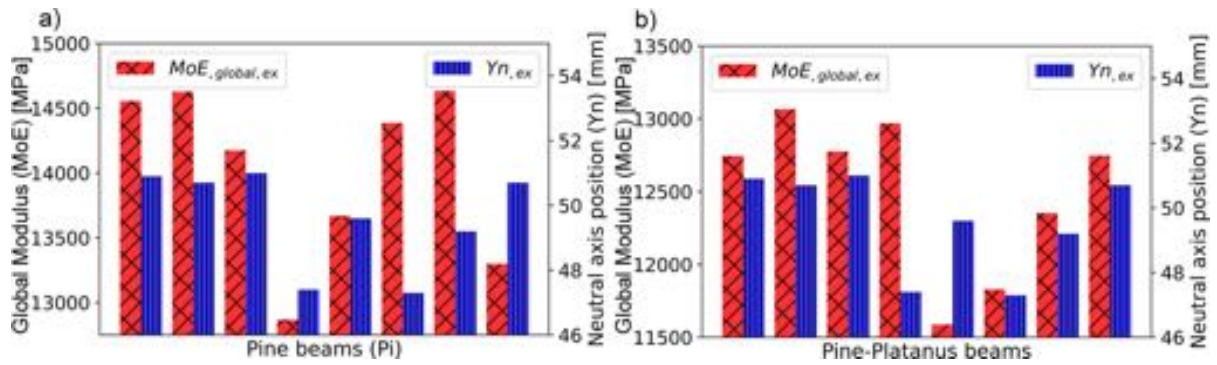


Figure 5.8: Experimental global modulus ($MoE_{global,ex}$) and the corresponding position of the neutral axis ($Y_{n,ex}$): a) 8-Pine beams (Pi); b) 8 Pine-Platanus beams (PiPl).

the top and bottom mid-sides.

Table 5.3 also summarizes the variations of the analytical moduli of elasticity in tension, compression and experimental global moduli for the Pine-Platanus beams (PiPl), with respect to the mean value of moduli of the control layout (Pi). It is shown that the decrease of the moduli is relatively low, defined by a mean decrease in compression and tension, around 10.1% and 11.2%, respectively. The same reduction range is observed for the experimental global modulus, whereas the mean decrease of the Pine-Platanus (PiPl) layout with respect to the Pine (Pi) layout is around 10.8%.

- *Application 2: Calculation of the global modulus.*

Based on the experimental values of the global modulus of Pine (Pi) and Platanus (Pl) glulam beams depicted in Figure 5.7, it is possible to assess the global modulus (MoE_{global}) of the combined beam (PiPl). Applying Eq. 5.13, it is possible to compute the MoE_{global} of 64 virtual Pine-Platanus specimens since there are 8 available experimental data of each timber material. Figure 5.9 shows the distribution and the corresponding histogram of the computed MoE_{global} for these 64 virtual specimens. Table 5.4 summarizes the mean value of computed global modulus (12526 MPa), compared with a mean value of the experimental global modulus (12510 MPa) and its corresponding variation. The difference between analytical and experimental value shows a subtle variation, being extremely low, around 0.13%.

- *Application 3: Parametric analysis of multi-species Pine-Platanus glulam beams.*

The combination of Pine and Platanus provides a multi-species beam (PiPl) with a global modulus closer to the one of the Pine (Pi), as seen in Figure 5.7. In order to analyse the influence of the percentage of both species that compose the cross-section in the moduli of elasticity, the Eq. 5.18 can be applied.

Figure 5.10 shows the MoE_{global} and the corresponding equivalent moduli of elasticity in tension and compression of the combined beam (PiPl), using the Eqs. 5.18 and 5.14. As expected, the global modulus lies around the mid-range defined by the tension and compression moduli. The three curves (Figure 5.10) show that the influence of the Platanus layers is negligible for a percentage up to 35%, while a decrease of the slope starts to be visible after 40%.

CHAPTER 5.

TRANSF.-SECT. METHOD APPLIED TO MULTI-SPECIES

Methodology	Experimental		Analytical – Eqs. 5.9 (Pi) and Eqs. 5.14 (PiPl)		
	$MoE_{global,ex}$ (MPa)	Y_{nex} (mm)	$E_{c,an}$ (MPa)	$E_{t,an}$ (MPa)	K
Pine (Pi)	14556	51.0	14556	14556	1.00
	14628	48.7	13393	16042	1.20
	14175	50.8	14065	14287	1.02
	12868	48.6	11737	14170	1.21
	13669	48.5	12421	15115	1.22
	14386	47.5	12598	16584	1.32
	14634	49.9	14023	15286	1.09
	13299	50.3	12941	13672	1.06
	$MoE_{global,ex,mean}$ (MPa)	$Y_{nex,mean}$ (mm)	$E_{c,an,mean}$ (MPa)	$E_{t,an,mean}$ (MPa)	K_{mean}
	14027	49.4	13217	14964	1.14
Pine-Platanus (PiPl)	$MoE_{global,ex}$ (MPa)	Y_{nex} (mm)	$E_{c,an}$ (MPa)	$E_{t,an}$ (MPa)	K
	12747	50.9	12697	12797	1.01
	13066	50.7	12914	13221	1.02
	12776	51.0	12776	12776	1.00
	12969	47.4	11315	15014	1.33
	11588	49.6	10977	12251	1.12
	11829	47.3	10283	13752	1.34
	12353	49.2	11525	13273	1.15
12748	50.7	12599	13273	1.05	
	$MoE_{global,ex,mean}$ (MPa)	$Y_{nex,mean}$ (mm)	$E_{c,an,mean}$ (MPa)	$E_{t,an,mean}$ (MPa)	K_{mean}
	12510	49.6	11886	13295	1.13
Variation of mean values of PiPl with respect to Pi layout (%)	-10.8	0.4	-10.1	-11.2	-0.9

Table 5.3: Experimental (ex) global modulus of elasticity ($MoE_{global,ex}$) and the corresponding position of the neutral axis (Y_{nex}). Analytical (an) moduli in tension ($E_{t,an}$) and compression ($E_{c,an}$) using Eqs. 5.9 (Pi) and Eqs. 5.14 (PiPl). K is the ratio between moduli in tension and compression for the 8-Pine and 8-Pine-Platanus beams specimens with their corresponding mean values.

For this study, the combined manufactured specimen is composed of six layers with a thickness of 17 mm, two external Pine layers and four inner Platanus layers. Thus, the Platanus percentage for the experimental specimens corresponds to 66%. Hence, the analytical variation of the curves at 66% (see dash-dotted line in Figure 5.10) provides similar values as the ones determined based on the experiments (Table 5.4).

As seen in Table 5.4, the analytical results related to the global modulus, provided by the parametric analysis and the results corresponding for a Platanus percentage of 66%, are comparable with the results acquired from the experimental part. In addition,

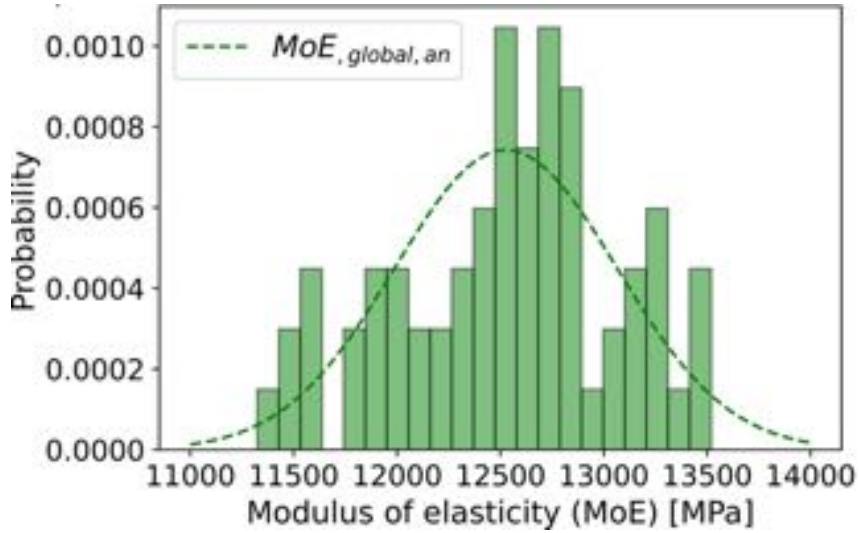


Figure 5.9: Analytical global modulus ($MoE_{global,an}$) using Eq. 5.13. Distribution of 64 Pine-Platanus virtual specimens.

Layout	$MoE_{global,ex}$ (MPa)	$MoE_{global,an}$ (MPa)	Variation (%)
PiPl	12510	12526	0.13

Table 5.4: Experimental ($MoE_{global,ex}$) and analytical ($MoE_{global,an}$) mean value of global modulus of Pine-Platanus layout (PiPl) and the corresponding variation.

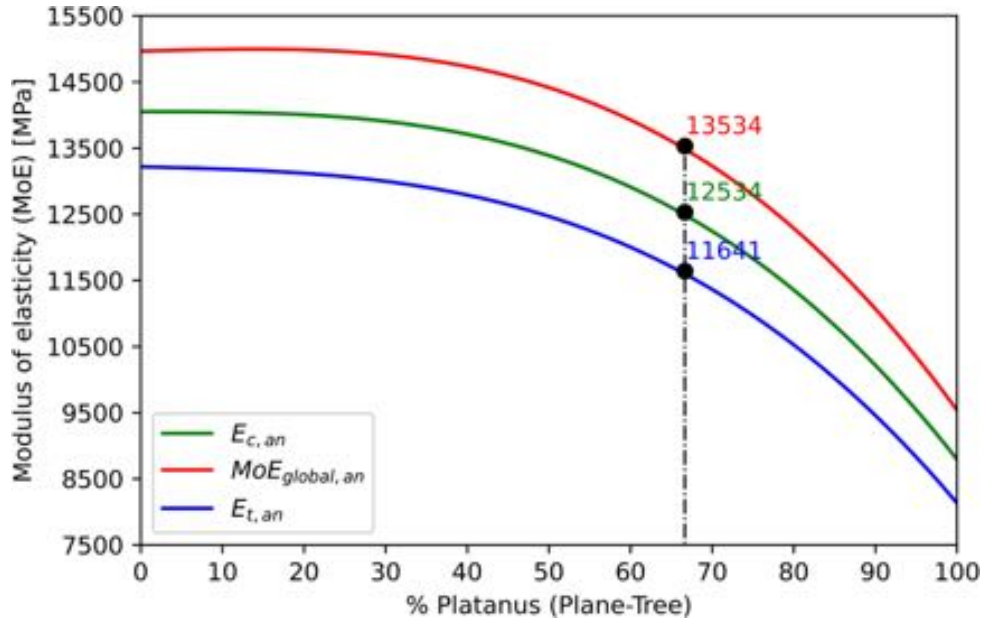


Figure 5.10: Global modulus of elasticity ($MoE_{global,an}$) and the corresponding moduli in tension and compression ($E_{t,an}$ and $E_{c,an}$) as a function of the Platanus percentage along the combined cross-section, employing the obtained solutions from Eqs. 5.18 and 5.14.

the analytical moduli in tension and compression obtained from the Eqs. 5.14, are very close to the moduli obtained employing parametric analysis.

5.4 Conclusions

In this paper, an analytical model based on the transformed method of composite sections, is developed to compute the global modulus of elasticity and the corresponding moduli, in tension and compression, for glulam beams. The combination of a relatively low-quality timber (Platanus) and a high-quality one (Pine) has been studied. The main aim is to substitute the inner part of a pure Pine beam by Platanus, to obtain a more economical and sustainable cross-section. The experimental tests have revealed that the combined layouts are characterized by a high global modulus of elasticity closer to Pine layouts.

The developed analytical procedure can assess the global modulus and the corresponding moduli in tension and compression, estimating also the variation between analytical and experimental results with an accuracy less than 1%.

The analytical results demonstrate that this model is a powerful technique to characterize the behaviour of a cross-section subjected to pure bending, expanding the analyses proposed in current standards. The proposed model allows to establish the Platanus influence within the combined section and to estimate the main mechanical properties for a future manufactured specimen.

Finally, in view of the obtained results, the developed model represents an adequate starting point for the optimization process. Although experimental tests for the characterization of the timber in tension and compression have not been carried out, the analytical model provides results that are in accordance with the experimental trends, where the modulus in tension is greater than the one in compression. Additionally, it is worth to remark that the developed analytical model in this study is a versatile one and it can be extrapolated to any combined timber beam made up by different wood species or reinforced timber beams.

Chapter 6

Development of an analytical model to predict the bending behaviour of composite glulam beams in tension and compression

Title	Development of an analytical model to predict the bending behavior of composite glulam beams in tension and compression
Authors	C. Timbolmas; R. Bravo; F.J. Rescalvo; A. Gallego
Journal	Journal of Building Engineering
ISSN	2352-7102
Journal's performance	Journal impact factor (2020): 5.318 D1 (Civil Engineering: 13/137)
Details	Volume: 45 – Published: January 2022; Pages: 103471
DOI	10.1016/j.jobe.2021.103471

6.1 Introduction

Structural timber members and the development of Engineered Wood Products (EWP) are emerging as highly demanded products in building and civil engineering sectors, offering outstanding structures and a healthy environment for residential buildings, sports halls, industrial buildings, and even bridges [83, 129].

Wood is a natural material of heterogeneous behaviour. Nowadays, for general design purposes, timber is characterized by a global modulus value as the standard state. Being an anisotropic material, the theoretical models applied to simulate wood's different behaviour in tension and compression are challenging [104, 105].

The most important mechanical parameters specific to timber elements are the modulus of elasticity (MoE), the maximum bending strength, and density [130]. Different timber members and structural design solutions have been studied for decades. Many authors address timber properties in terms of local and global behaviour, respectively defined by the local modulus of elasticity (MoE_s) and the global modulus of elasticity ($MoE_{m,global}$) [131]. The ratio between the local and global modulus in bending for pine

CHAPTER 6.

DEVELOPMENT OF AN. MODEL TO PREDICT BENDING BEHAVIOUR

and spruce have been studied by Bacher in his work [132]. A main objective of this paper is to develop an analytical model that can be applied using the experimental results of static bending tests (EN 408:2010+A1:2012 [19]) to obtain the relation between global MoE and elastic moduli in tension and compression.

The use of composite materials to reinforce timber elements [84, 85, 125, 133] introduces a new variable and added complexity to the challenge of understanding timber's global behaviour. Several approaches have been applied to analyse the behaviour of these elements. The so-called rule of mixtures provides an estimation of the global MoE of the composite timber as a homogeneous material. This rule has traditionally been applied to study the micro-mechanics of FRP materials and then extended to timber by [134], taking into account the different behaviour under tension and compression. Similarly, the combination of homogenization techniques and the parallel axis theorem (Steiner theorem) allow one to derive the global MoE of sections composed by multiple layers through the MoE of each layer [135]. Detailed analytical investigations of the elastic and plastic behaviour along with different failure mechanisms for reinforced beams have been undertaken by several models based on the equilibrium, compatibility and constitutive equations of the reinforced timber section. These models range from linear elastic approaches with the same behaviour in tension and compression [13], to elasto-plastic ones with different behaviours in the plastic range in tension and compression by [97] and [116, 136], or linear elasto-plastic models that statistically account for the influence of timber knots [137]. Non-linear elastic and plastic behaviours in compression are proposed by [90, 138], models suitable for the study of reinforced beams behaviour until collapse. Complex constitutive models that take into account the anisotropy of timber and different behaviour in tension and compression can be applied in the context of the finite element method (see [105, 139, 140]), standing as a valuable tool to predict the behaviour and mode of failure of a timber element.

In an analytical model based on the elastic beam theory, determining the position of the neutral axis is a key aspect for assessing the elastic modulus. An improved method of predicting the global modulus in view of the neutral axis position under bending stress has been proposed by Shim [16] and Yang [93], who developed a consistent analytical model for glulam section with reinforcement, employing an elasto-plastic model defined by an identical elastic modulus in tension and compression. In their research paper, the flexural capacity and flexural stiffness were calculated and compared with experimental results. The results based on the proposed analytical model agreed well with the experimental mean value.

The present contribution develops an extensive analytical model to estimate the main strength and elastic parameters of a glulam timber element having different layouts. The developed analytical model takes into account the different elastic behaviour in tension and compression. Previous research efforts [141, 142] approach the determination of moduli in tension and compression for glulam beams by employing specific pure tensile tests and compression tests. Under the assumption of the different scenarios, this analytical model makes it possible to obtain -through a single bending test-significant information about the mechanical behaviour of the element, beyond the direct parameters (maximum stress, global elastic modulus, etc.). Parameters such as tensile and compressive elastic moduli prove highly valuable when analyzing timber elements reinforced with composite materials. They provide for a better assessment of the elastic part than previously published models, yielding the influence and relation of the tension and compression elastic moduli in global MoE, stresses and strains.

Based on equilibrium, constitutive and compatibility equations, for pure and composite sections, the analytical model is formulated in Section 6.2. The fundamental equations for all of the reinforced cases are presented in the Appendices. Solutions are given in each subsection of Section 6.2, providing relations for the mechanical behaviour in tension and compression, the global modulus of elasticity, and the neutral axis position. Although from a practical standpoint the global modulus of elasticity is used to evaluate deflections and stresses, computation of the corresponding moduli of elasticity in tension and compression gives further information on the influence of tension and compression in the global modulus of bending. Consequently, the global behaviour in terms of deflections and normal stresses can be efficiently controlled/optimized by inserting adequate reinforcements (timber species or FRP).

The proposed analytical model is applied for different beam layouts, as described in Section 6.3. Static bending tests were performed according to the EN 408:2010+A1:2012 [19] standard, as described in Section 6.4, which provided the data required for the analytical model. Section 6.5 expounds and discusses the results of the experimental tests along with the results obtained by means of the analytical formulations. Finally, the last section summarizes the main features of the analytical method and highlights improvements seen for the composite beam layouts studied.

6.2 Analytical formulation and methods

An analytical model is proposed to compute the elastic behaviour of composite timber beams subjected to pure bending. Timber is an anisotropic material presenting different behaviour under tension and compression (i.e., E_t and E_c are different). The limit between compression and tension areas is defined by the position of the neutral axis (y_n) [118, 124]. For practical purposes, the timber section is characterized by a global modulus of elasticity, representing the general flexural behaviour of the material.

In order to derive the relationships between the moduli in tension and compression, and the global modulus, the application of stress-strain relations, force-moment equilibrium equations and the curvature relation are considered. In all cases, the Euler-Bernoulli beam theory served to develop the analytical procedure [143].

The proposed analytical procedure provides the moduli in tension and compression based on the global modulus, and the position of the neutral axis determined employing the experimental data. That is, once the mechanical properties of each individual material are known, the procedure allows for calculation of the global modulus of elasticity and the position of the neutral axis. An equivalent modulus of elasticity in tension and compression for an equivalent beam can therefore be calculated for composite beam layouts. Subsequently, an improvement in the configuration of those layouts can be estimated and studied by means of parametric analysis.

In view of the experimental data, several assumptions are considered: a) the timber behaviour is linear elastic in tension and compression; b) full interaction between timber layers, finger joints, and carbon fiber reinforced material (CFRP) is possible; c) no de-bonding between timber layers and the CFRP material occurs. The following cases are studied (see Table 6.1): 1) rectangular glulam section made up of a single timber species (Poplar (Po) or Pine (Pi)); 2) rectangular composite glulam section composed by a single timber species and CFRP material placed at the bottom (CLB), top (CLT), or both sides of the beam (CF2BT); 3) rectangular composite glulam section comprising

CHAPTER 6.

DEVELOPMENT OF AN. MODEL TO PREDICT BENDING BEHAVIOUR

two different timber species (Pine and Poplar (PiPo)).

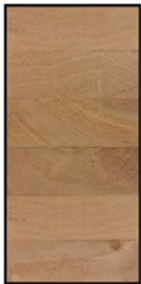




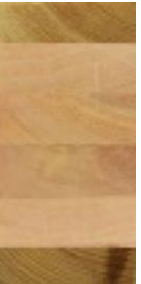
Nomenc.	Po	CLB	CLT	CF2BT	Pi	PiPo
CFRP and thickness	No CFRP	Pultruted laminated sheet (1.4 mm)	Pultruted laminated sheet (1.4 mm)	Fabric e (0.332 mm)	No CFRP	No CFRP
Description	Poplar	Poplar + CFRP at bottom	Poplar + CFRP at top	Poplar + 2 layers CFRP at both sides	Pine	Pine (outer layers) + Poplar (inner layers)
Cross-section						

Table 6.1: Description of the glulam beam layouts analyzed in this paper.

This work is limited to experimental analysis and application of the analytical model to the layouts presented in Table 6.1, composed by a single timber species, two timber species, or beams of timber with CFRP. Linear elastic behaviour is always assumed, for which reason elasto-plastic or non-linear elastic constitutive models remain beyond the scope of the paper. The focus is on the computation of elasticity moduli, practical parameters needed to estimate the behaviour of a structural timber element.

6.2.1 Case 1. Rectangular glulam section made up of a single timber species (Pi or Po)

For this case, the stress-strain distribution and geometric quantities are depicted in Figure 6.11.

The equilibrium of the section, force-stress relationships, stress-strain relationships, compatibility equation and geometric relations for the section in Figure 6.1 are presented in Appendix 6.7.1. Solving the system of equations from Appendix 6.7.1, the expressions of Table 6.2 can be obtained:

where F_c and F_t are the resultant compressive and tensile forces, respectively, M_{bend} is the applied bending moment, σ_c and σ_t are the maximum compressive and tensile stress respectively, ε_c and ε_t are the maximum compressive and tensile strains, respectively, E_c and E_t are the moduli of elasticity in compression and tension, respectively, y_n is the position of the neutral axis (measured from the bottom side), and h , b are the depth and width of the cross-section.

The position of the neutral axis can be obtained as a function of the modulus of elasticity in tension and compression, i.e.,

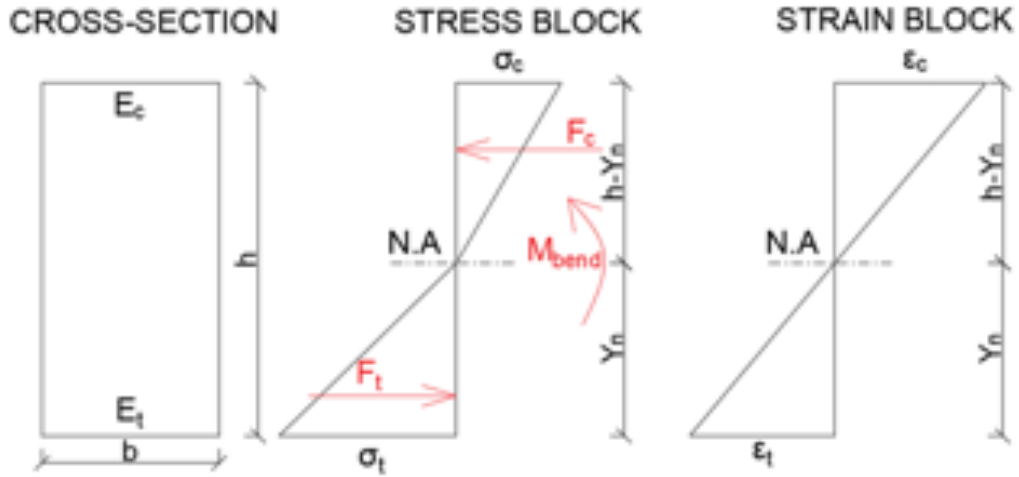


Figure 6.1: Stress-strain relations for a rectangular solid section with different behaviour in tension and compression. N.A: Neutral axis.

C/T	Stresses	Strains	Resultant forces
Top (Compression)	$\sigma_c = \frac{3(1+\sqrt{E_c}\sqrt{E_t})M_{bend}}{bh^2}$	$\epsilon_c = \frac{3(1+\sqrt{E_c}/\sqrt{E_t})M_{bend}}{bE_ch^2}$	$F_c = \frac{3M_{bend}}{2h}$
Bottom (Tension)	$\sigma_t = \frac{3(1+\sqrt{E_t}\sqrt{E_c})M_{bend}}{bh^2}$	$\epsilon_t = \frac{3(1+\sqrt{E_t}/\sqrt{E_c})M_{bend}}{bE_th^2}$	$F_t = \frac{3M_{bend}}{2h}$

Table 6.2: Stresses, strains and resultant forces for the glulam beam made of a single timber species (Pi or Po).

$$y_n = \sqrt{E_c}h / (\sqrt{E_c} + \sqrt{E_t}) \quad (6.1)$$

Taking into account the relationship between the curvature of the cross-section composed by a homogeneous material and the applied bending moment, the relationship between them can be expressed as

$$M_{bend} = MoE_{global} \times I/Rc \quad (6.2)$$

where I is the inertia of the section, MoE_{global} is the global modulus of elasticity, and Rc is the radius of curvature of the cross-section.

In addition, the maximum compressive strain can be expressed as a function of the radius of curvature, i.e.,

$$\frac{h - y_n}{Rc} = \epsilon_c \quad (6.3)$$

Combining Eqs. 6.2 and 6.3, the external bending moment can be expressed as a function of the modulus of elasticity in tension and compression, i.e.,

$$M_{bend} = \left(\frac{4E_cE_t}{(\sqrt{E_c} + \sqrt{E_t})^2} \right) \frac{I}{Rc} \quad (6.4)$$

Replacing the obtained expression of the external bending moment (Eq. 6.4) in Eq. 6.2, the global modulus of elasticity can be calculated as:

$$MoE_{global} = \left(\frac{4E_cE_t}{(\sqrt{E_c} + \sqrt{E_t})^2} \right) \quad (6.5)$$

CHAPTER 6.

DEVELOPMENT OF AN. MODEL TO PREDICT BENDING BEHAVIOUR

Furthermore, combining the obtained expression for the position of the neutral axis (Eq. 6.1) with the global modulus expression (Eq. 6.5), E_t and E_c can be expressed as a function of the global modulus and the position of the neutral axis, i.e.,

$$E_c = \frac{MoE_{global}h^2}{4(h - y_n)^2}; E_t = \frac{MoE_{global}h^2}{4y_n^2} \tag{6.6}$$

The obtained relationship (Eq. 6.6) provides a precise and valid way to characterize the timber behaviour in tension and compression, by working directly with the experimental data obtained from the bending tests.

6.2.2 Case 2. Rectangular composite glulam section made up of a single timber species and CFRP material placed at the bottom side (CLB)

The stress-strain distribution and geometry for this case are depicted in Figure 6.2.

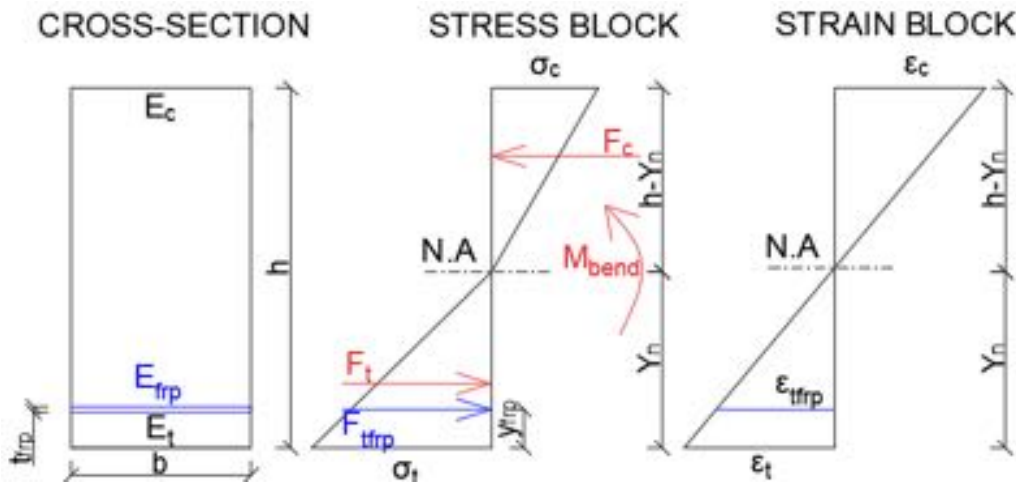


Figure 6.2: Stress-strain relations for a rectangular solid section with different behaviour in tension and compression and composite material (CFRP) at the bottom side. N.A: Neutral axis.

The aforementioned approaches are applied to the section in Figure 6.2, the equilibrium, compatibility, constitutive and geometrical relations being summarised in Appendix 6.7.2. Solving the system of equations, the expressions of Table 6.3 can be obtained.

Here F_{tfrp} is the resultant tensile force at the CFRP, σ_{tfrp} and ϵ_{tfrp} are the tensile stress and strain at the CFRP, E_{frp} is the modulus of elasticity of the CFRP, and t_{frp} and y_{frp} are the CFRP thickness and position (measured from the bottom face). The symbol Γ_0 is defined as:

$$\Gamma_0 = E_t (3y_{frp} - y_n) y_n^2 + E_c (h - y_n)^2 (2h - 3y_{frp} + y_n) \tag{6.7}$$

For this case, the position of the neutral axis can be expressed as a function of the modulus of elasticity in tension-compression and the composite material characteristics:

$$y_n = \frac{1}{E_c - E_t} (E_c h + E_{frp} t_{frp} - A) \tag{6.8}$$

C/T	Stresses	Strains	Resultant forces
Top (Compression)	$\sigma_c = \frac{6E_c M_{bend}(h-y_n)}{b \cdot \blacksquare_0}$	$\varepsilon_c = \frac{\sigma_c}{E_c}$	$F_c = \frac{3E_c M_{bend}(h-y_n)^2}{\blacksquare_0}$
Bottom (Tension)	$\sigma_t = \frac{6E_c M_{bend} y_n}{b \cdot \blacksquare_0}$	$\varepsilon_t = \frac{\sigma_t}{E_t}$	$F_t = \frac{3E_t M_{bend} y_n^2}{\blacksquare_0}$
CFRP (Tension)	$\sigma_{tfrp} = \frac{3M_{bend}(E_c(h-y_n)^2 - E_t y_n^2)}{b t_{frp} \blacksquare_0}$	$\varepsilon_{tfrp} = \frac{\sigma_{tfrp}}{E_{frp}}$	$F_{tfrp} = \frac{3M_{bend}(E_c(h-y_n)^2 - E_t y_n^2)}{\blacksquare_0}$

Table 6.3: Stresses, strains and resultant forces for the CLB layout.

where,

$$A = \sqrt{E_c E_t h^2 + 2E_c E_{frp} t_{frp} (h - y_{frp}) + E_{frp} t_{frp} (E_{frp} t_{frp} + 2E_t y_{frp})} \quad (6.9)$$

Following the same principles as described in Case 1, combining the expression of the bending moment expressed by the global modulus of elasticity (Eq. 6.5) with the expression of the bending moment considering different behaviours of the material (Eq. 6.4), the global modulus of an equivalent section can be expressed as:

$$M o E_{global} = \frac{2\Gamma_0}{h^3} \quad (6.10)$$

Replacing the expression of the global modulus of elasticity obtained for this case (Eq. 6.10) in the relationship obtained for Case 1 (Eq. 6.6), the equivalent moduli in tension and compression for an equivalent section can be determined. Given this situation, there are two possibilities for their estimation: i) Using the experimental data as input data and following the procedure described for Case 1 (Eq. 6.6); ii) Using the moduli of elasticity of timber (E_t and E_c) and composite material modulus as input data.

6.2.3 Case 3. Rectangular glulam section comprising two timber species (PiPo)

Figure 6.3 shows the stress-strain distribution and geometric quantities for the rectangular section of this particular case, in which two different timber species are combined (pine and poplar).

Considering the aforementioned approaches, the following relations are applied:

1. equilibrium of the section (moment and axial forces):

$$F_{cpine} + F_{cpop} - F_{tpop} - F_{tpine} = 0 \quad (6.11)$$

$$F_{cpine} dF_{cpine} + F_{cpop} dF_{cpop} + F_{tpop} dF_{tpop} + F_{tpine} dF_{tpine} - M_{bend,c} = 0 \quad (6.12)$$

CHAPTER 6.

DEVELOPMENT OF AN. MODEL TO PREDICT BENDING BEHAVIOUR

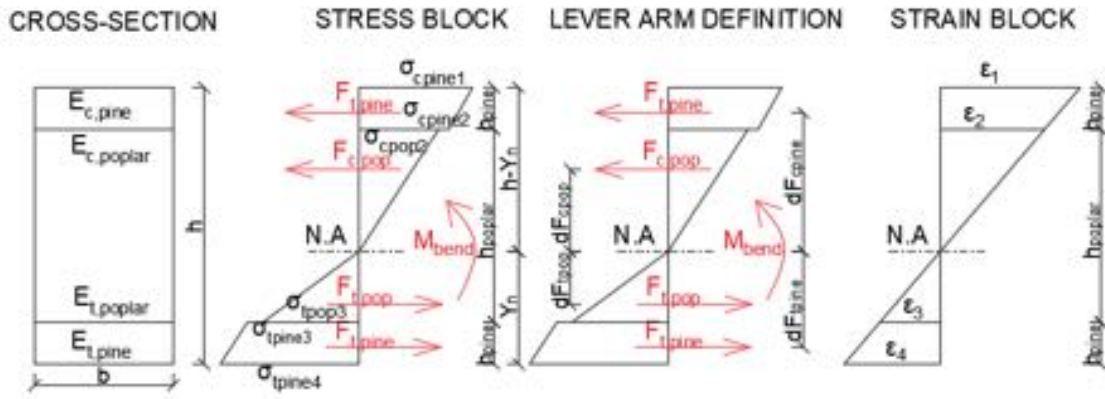


Figure 6.3: Stress-strain relations for a rectangular solid section with different behaviour in tension and compression and two different timber species: pine and poplar (PiPo).

2. lever arm definition:

$$dF_{cpine} = \left(\sigma_{cpine2} \frac{h_{pine}^2}{2} + \frac{\sigma_{cpine1} - \sigma_{cpine2}}{2} 2h_{pine} \frac{2}{3} h_{pine} \right) / \left(\frac{1}{2} (\sigma_{cpine1} + \sigma_{cpine2}) h_{pine} \right) + h_{cpop} \quad (6.13)$$

$$dF_{cpop} = \frac{2}{3} h_{cpop}; dF_{tpop} = \frac{2}{3} h_{tpop} \quad (6.14)$$

$$dF_{tpine} = \left(\sigma_{tpine3} \frac{h_{pine}^2}{2} + \frac{\sigma_{tpine4} - \sigma_{tpine3}}{2} 2h_{pine} \frac{2}{3} h_{pine} \right) / \left(\frac{1}{2} (\sigma_{tpine4} + \sigma_{tpine3}) h_{pine} \right) + h_{tpop} \quad (6.15)$$

3. force-stress relationships:

$$0.5 \times h_{pine} \times b \times (\sigma_{cpine1} + \sigma_{cpine2}) = F_{cpine} \quad (6.16)$$

$$0.5 \times h_{cpop} \times b \times \sigma_{cpop2} = F_{cpop} \quad (6.17)$$

$$0.5 \times h_{tpop} \times b \times \sigma_{tpop3} = F_{tpop} \quad (6.18)$$

$$0.5 \times h_{pine} \times b \times (\sigma_{tpine3} + \sigma_{tpine4}) = F_{tpine} \quad (6.19)$$

4. stress-strain relationships:

$$E_{cpine} \times \epsilon_1 = \sigma_{cpine1}; E_{cpine} \times \epsilon_2 = \sigma_{cpine2} \quad (6.20)$$

$$E_{cpop} \times \epsilon_2 = \sigma_{cpop2}; E_{tpop} \times \epsilon_3 = \sigma_{tpop3} \quad (6.21)$$

$$E_{tpine} \times \epsilon_3 = \sigma_{tpine3}; E_{tpine} \times \epsilon_4 = \sigma_{tpine4} \quad (6.22)$$

5. compatibility equations:

$$\varepsilon_1 \frac{h - y_n - h_{pine}}{h - y_n} = \varepsilon_2; \varepsilon_1 \frac{y_n - h_{pine}}{h - y_n} = \varepsilon_3; \varepsilon_1 \frac{y_n}{h - y_n} = \varepsilon_4 \quad (6.23)$$

6. geometric definitions:

$$y_n + (h - y_n) = h; 2h_{pine} + h_{tpop} + h_{cpop} = h \quad (6.24)$$

$$h_{pine} + h_{tpop} = y_n; h_{pine} + h_{cpop} = h - y_n \quad (6.25)$$

where, F_{tpine} and F_{cpine} are the resultant tensile and compressive forces in the pine layer, F_{tpop} and F_{cpop} are the resultant tensile and compressive forces in the poplar layer, dF_{tpine} and dF_{cpine} are the lever arm of the pine layer in tension/compression, dF_{tpop} and dF_{cpop} are the lever arm of the poplar layer in tension and compression, σ_{cpine1} and σ_{cpine2} are the maximum and minimum compressive stresses in the pine layer, σ_{cpop2} and σ_{tpop3} are the maximum compressive and tensile stresses in the poplar layer, σ_{tpine3} and σ_{tpine4} are the minimum and maximum tensile stresses in the pine layer, E_{cpop} and E_{tpop} are the moduli of elasticity of poplar in compression and tension, E_{cpine} and E_{tpine} are the moduli of elasticity of pine in compression and tension, ε_1 and ε_4 are the maximum compressive and tensile strains, ε_2 and ε_3 are the compressive and tensile strains in the interface between the poplar and pine layers, h_{pine} is pine thickness (external layers) and h_{cpop} and h_{tpop} are the poplar thickness in compression and tension.

For this case, the stresses, strains, position of the neutral axis, and resultant forces can only be obtained numerically, owing to the complexity of solutions derived from the system of equations. Nevertheless, the global modulus of elasticity and moduli in tension and compression can be expressed as a function of the modulus of elasticity in tension and compression of each timber species, as in the previous cases.

6.2.4 Methods

Based on the developed formulations, two separate working directions are discerned:

1. Once the global modulus of elasticity and the position of the neutral axis are derived from the experiments, the moduli in tension and compression of real pure and combined beams can be computed.
2. If the moduli in tension and compression of each timber material are known, then the MoE_{global} and the corresponding values in tension and compression for future manufactured combined beams can be predicted.

Consequently, this work-flow is adequate for application to unreinforced and reinforced beams.

CHAPTER 6.

DEVELOPMENT OF AN. MODEL TO PREDICT BENDING BEHAVIOUR

Unreinforced beams (without CFRP)

The work-flow for unreinforced beams is depicted in Figure 6.4. Every specimen of each layout is characterized by two experimental data: i) global modulus ($MoE_{m,global,ex}$); ii) position of the neutral axis (Yn_{ex}). These experimental values are used to compute the moduli in tension and compression of each layout (left part of Figure 6.4, $E_{c,pop}$ and $E_{t,pop}$ for poplar, $E_{c,pine}$ and $E_{t,pine}$ for pine, and $E_{c,comb,I}$ and $E_{t,comb,I}$ for combined beams) using the equation from Case 1 (Eq. 6.6).

Employing the computed data of the pure beams, the global modulus (MoE_{global}) and moduli in tension and compression (E_t and E_c) for manufactured combined beams are computed. In this case, 8 specimens of each pure timber species were experimentally used. Consequently, using equations 6.11 to 6.25, it is possible to predict the moduli of up to 64 manufactured beams (right part of Figure 6.4).

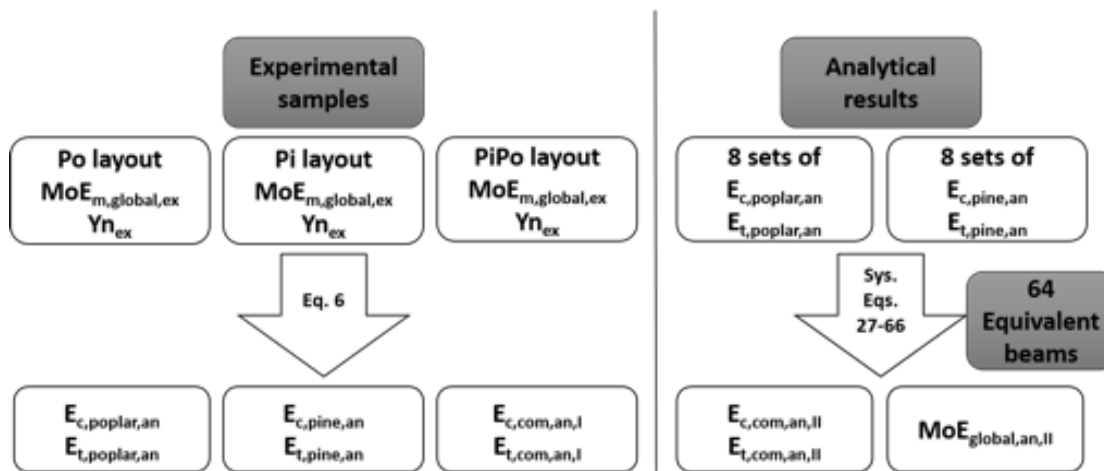


Figure 6.4: Flowchart for the analytical procedure for the Po, Pi, and PiPo layouts.

Reinforced beams (with CFRP)

For reinforced beams (i.e., timber beams with CFRP layers), a different work-flow is depicted in Figure 6.5. Similarly, every specimen of each layout is characterized by two experimental data: i) global modulus ($MoE_{m,global,ex}$); ii) position of the neutral axis (Yn_{ex}). These experimental values are used to compute the moduli in tension and compression ($E_{t,com,an,I}$ and $E_{c,com,an,I}$) of each reinforced layout (left part of Figure 6.5), by means of the equation from Case 1 (i.e. Eq. 6.6).

Using the data computed from the pure poplar beams and the properties of the CFRP material provided by the supplier, the MoE_{global} and E_t and E_c for manufactured composite beams of each layout can be obtained. In this case, 8 specimens of pure poplar timber and the properties of the CFRP material are used to compute the behaviour in tension and compression for a reinforced section ($E_{c,com,an,II}$ and $E_{t,com,an,II}$) using the corresponding analytical formulation (Eq. 6.10 for CLB layout; Eq. 6.52 for CLT layout; Eq. 6.66 for CF2BT layout).

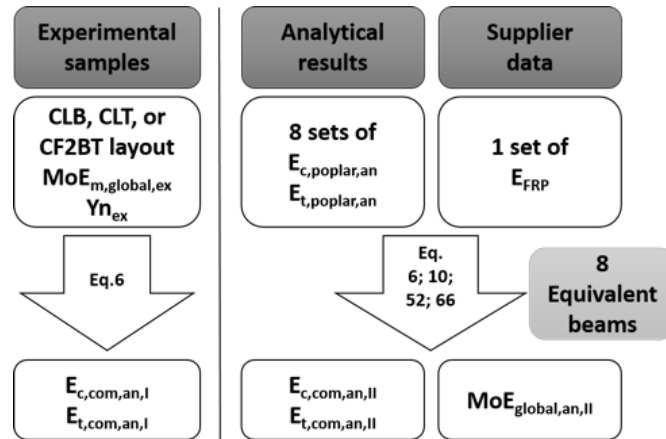


Figure 6.5: Flowchart of the analytical procedure for the CLB, CLT, and CF2BT layouts.

6.3 Materials

6.3.1 Timber

Two timber species were used in this work, *Pinus Sylvester* and poplar clone I-214 (*Populus x euroamericana* [Dode] Guinier). The pine wood was supplied by the company Madera Pinosoria S.L. (Soria, Spain), while the poplar wood was extracted from a 9-year-old poplar plantation located on the Vega de Granada, Spain. In both cases, planks sized 35 x 75 x 2000 mm were extracted. The pine wood was dried in an industrial unit until achieving a final moisture content (MC) of 9.5%, while the poplar wood was dried naturally for 6 months until reaching an MC of 10±2%. As detailed in [27], all the planks were subjected to an acoustic resonance non-destructive test (NDT) longitudinal to the fiber direction, thus obtaining the dynamic elastic modulus (MoE_{dyn}), adjusted to MC=12% as stated in the standard (EN 384:2016+A1:2018 [20]). Figure 6.6 indicates the normal distribution of the planks for each particular timber species. It clearly shows a higher homogeneity for the case of poplar, extracted from the planted forest, as compared with the pine from natural forests. The mean values were 7061 MPa and 12290 MPa for poplar and pine, respectively. The standard deviation of the poplar samples was 821 MPa, so that the planks outside the range [6240-7882] MPa were discarded and not used for this experiment. Moreover, in order to achieve consistency in the manufacturing process, especially in the elaboration of glulam beams with mixed species, the same standard deviation was considered for the case of pine, taking only the planks graded within the range [11469-13111] MPa.

6.3.2 CFRP material

Two types of CFRP materials were used, pultruded laminate and fabric. The pultruded laminate is a unidirectional pultruded plate, while the fabric consists of dry-braided yarns that can be arranged in one or more directions. In this work, commercial unidirectional Carboplate® E200 laminate and Mapewrap® C Uni-Ax fabric, both from Mapei S.p.A., were used. The epoxy resin Mapewrap® 21 was used for wood-CFRP gluing. In order to improve the adherence between the two materials [97], Mapewood® Primer was used. The Young modulus provided by the manufacturer for the unidirectional pultruded plate is 170 GPa, and 230 GPa for the fabric layer.

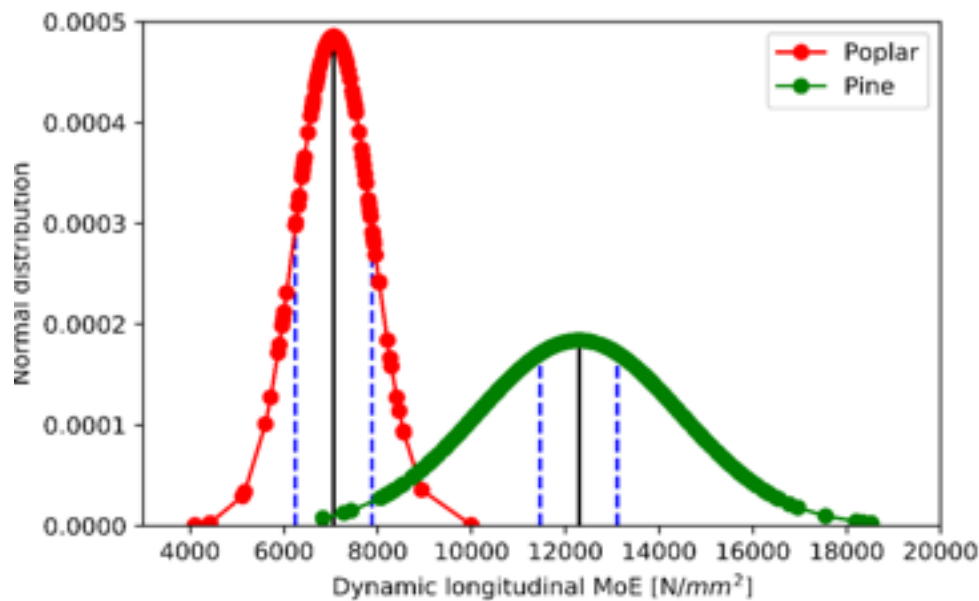


Figure 6.6: Normal distribution of MoE_{dyn} of the sawed planks. Black vertical line: Mean value. Blue vertical dashed lines: Standard deviation limits and plank interval used.

6.3.3 Glulam samples

As shown in Table 6.1, 6 different layouts were manufactured and tested, with a cross-section of $102 \times 50 \text{ mm}^2$ and a length of 2100 mm. For each layout, 8 beams were elaborated. They were composed by assembling 6 layers of planks 17 mm thick. The elaboration process was carried out according to the standard EN 14080 [21] (Annex I.4 and I.5), using finger joint technology. The polyurethane structural resin PUR-20 from Bakar – Adhesivos Plásticos Reunidos S.L. company was used as the adhesive.

6.4 Bending Tests

Using a multi-testing machine with a maximum capacity of 100 kN, four-point bending tests were carried out. The tests were performed according to the requirements of the [EN 408:2010+A1:2012] [19] standard, with a displacement control rate of 8.7 mm/min, so that the rupture would occur in $300 \pm 120 \text{ s}$, at least for the beams without CFRP material. As indicated in the [EN 408:2010+A1:2012] [19] standard, distances between upper supports of 612 mm and of 1920 mm between the lower supports were established to avoid shear failure (Figure 6.7). The strain measurement was carried out with commercial strain equipment. Four strain gauges were placed on the mid-span of each beam, two on the faces of maximum tension and compression and two on the lateral faces at $1/4$ of the height. The static elastic modulus (MoE_s) was calculated with the strain gauge located at the bottom face (maximum tensile). To this end, the stress-strain relationship in the range 10%-40% of the maximum ultimate stress f_m was used, where

$$f_m = \frac{3a P_{max}}{bh^2} \quad (6.26)$$

P_{max} being the maximum load, b the base of the beam, h the height of the beam, and a the distance between the application point of the load and the nearest support. By means of an LVDT placed at the mid-span of the specimens, the global elastic modulus ($MoE_{m,global,ex}$) was calculated, following the standard [EN 408:2010 + A1:2012] [19].

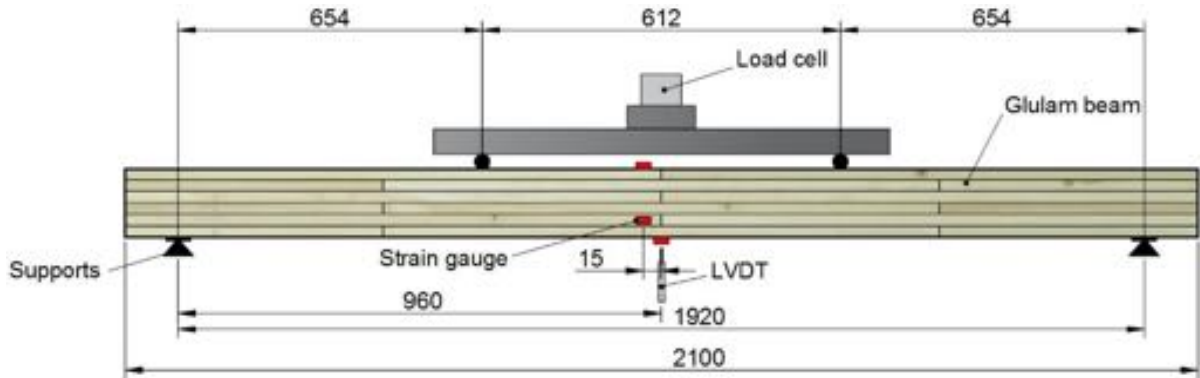


Figure 6.7: Four-point bending test set-up. Distances in mm. Strain gauges in red color.

6.5 Results and Discussions

Results are divided in two sections, the first one corresponding to the only-timber beams (single species or two-species composite) and the second corresponding to the composite timber-CFRP beams.

6.5.1 Only-timber glulam beams

Experimental results

Table 6.4 shows the computed moduli of elasticity based on the displacements ($MoE_{m,global,ex}$)¹ and strains (MoE_s) recorded by the LVDTs and strain gauges, respectively. In addition, the dynamic modulus (MoE_{dyn}) obtained through the acoustic NDT test is presented for all of the layouts. The maximum bending strength (f_m) and the density (ρ) of the specimens are illustrated in Table 6.4 for the three timber glulam layouts: pure pine (Pi), pure poplar (Po) and pine and poplar composite (PiPo). Figure 6.8 shows the stress-deflection curves obtained for all the samples of each particular layout.

The strain-deflection curves (Figure 6.8) and the three first columns of the table (i.e. MoE values) show that the pine beams are stiffer than those of the poplar due to different strength classes. In terms of global modulus ($MoE_{m,global,ex}$), the variation between these two layouts is around 79%; in terms of static modulus (MoE_s) the variation is around 77%; and the variation based on the non-destructive tests (MoE_{dyn}) is 75%. Note that the superior mechanical properties of pine make it more suitable as structural timber, as expected.

¹Note that $MoE_{m,global,ex}$ from experiments contains subscript "ex" in order to differentiate the MoE_{global} , computed with the analytical formulations presented in this paper.

CHAPTER 6.
DEVELOPMENT OF AN. MODEL TO PREDICT BENDING BEHAVIOUR

Layout and Variation	$MoE_{m,global,ex}$ (N/mm ²)	MoE_s (N/mm ²)	MoE_{dyn} (N/mm ²)	f_m (N/mm ²)	ρ (kg/m ³)
Poplar (Po)	8478 ± 7.9	7615 ± 17.8	7586 ± 3.5	42.9 ± 25.8	391 ± 2.8
Pine (Pi)	15206 ± 5.6	13476 ± 4.8	13304 ± 5.4	72.4 ± 6.2	553 ± 2.4
Pine-Poplar (PiPo)	13057 ± 4.8	11725 ± 4.1	11346 ± 4.8	56.0 ± 10.8	457 ± 1.3
Variation Pi-Po (%)	79	77	75	69	41
Variation PiPo-Po (%)	54	54	50	31	17
Variation PiPo-Pi (%)	-14	-13	-15	-23	-17

Table 6.4: Experimental results. Mean values, covariance (%) and variation (%) of: Global modulus- $MoE_{m,global,ex}$; Static modulus - MoE_s ; Dynamic modulus - MoE_{dyn} ; Maximum stress – f_m ; Density – ρ ; for pine (Pi), Poplar (Po) and composite pine-poplar beams (PiPo).

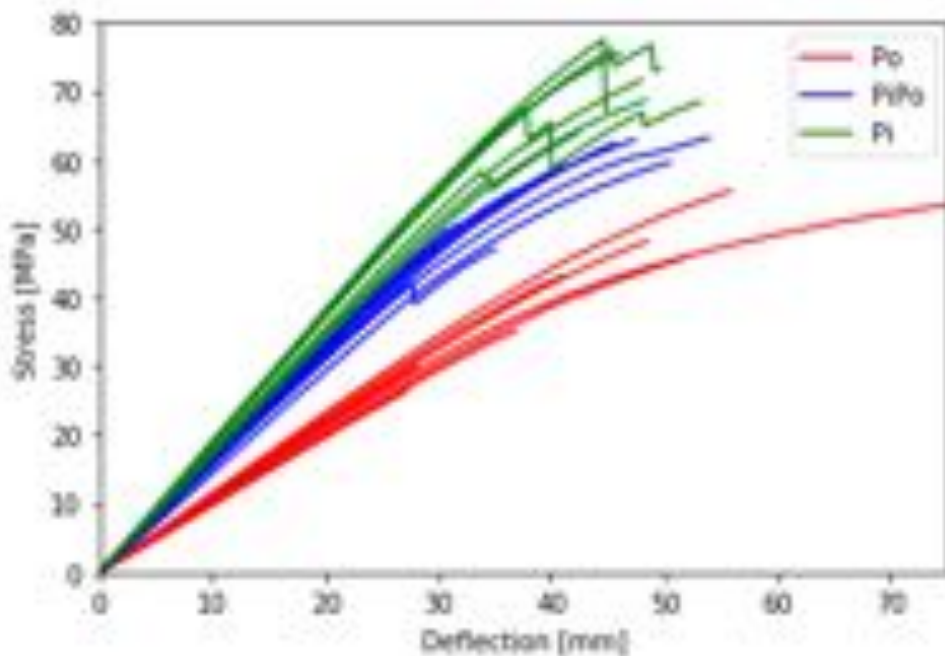


Figure 6.8: Stress-deflection curves for poplar (Po), pine-poplar (PiPo) and pine (Pi) beams.

Figure 6.8 reflects a clearly elasto-plastic behaviour, with a shaped limit (30 MPa) between the elastic and plastic ranges for pure poplar beams. Similarly, the behaviour and limit are identified for the pure pine beams, although the plastic zone is characterized by a short-range with stepped fractures. Moreover, the yield stress for the poplar layout, being around 30 MPa, is smaller than for the pure pine one, which is roughly two times greater (55-60 MPa). The ultimate plastic stress is clearly higher for the pine layout, in the range of 65-75 MPa, while for the poplar beams the maximum plastic stress is up to 55 MPa. Consequently, the behaviour of poplar is ductile up to 75 mm, with a reduced maximum stress (see f_m in Table 6.4), whereas pine is mostly defined by a linear-elastic relation and higher maximum stress, with a mean around 69%.

For the pine-poplar composite layout, the stress-deflection diagram revealed an intermediate behaviour between pure poplar (Po) and pine (Pi) layouts, being closer to the pine one (see Figure 6.8). In terms of the elasto-plastic behaviour, the elastic range is 55 MPa –similar to the pine layout, but with a significant increase in the plastic range of 20% with respect to pine due to the contribution of the inner poplar layers. Thus, there is a reduction compared to the pine layout of around 23% in the maximum stress and 25% in the yield stress. The data collected in Table 6.4 confirm this tendency closer to pine, showing a significant improvement of the global and static moduli, around 54%, with respect to the pure poplar beams, and a decrease of around 13%-14% with respect to the pure pine beams. This finding is supported by the non-destructive test, where improvement in the dynamic modulus is about 50% when compared with the pure poplar layout, yet 15% less than that of pure pine.

Another important feature of the combined beam is seen in the density ρ of the specimen. The density increase between pine as opposed to poplar is around 41%, while the variation of the density between the pine-poplar composite beam and pure poplar is 17%. To highlight this aspect, the influence of the percentage of poplar on density variation is reflected in Figure 6.10 and Figure 6.12.

Analytical results-Working direction I

Following the working direction I , as described in Subsection 6.3 applied to unreinforced beams (without CFRP), the parameters that define the behaviour in tension and compression of all layouts (moduli in tension, $E_{t,poplar/pine/com,an}$, and compression $E_{c,poplar/pine/com,an}$) can be assessed with the formulation presented in Section 6.2 (Eqs. 6.6) using the global modulus of elasticity ($MoE_{m,global,ex}$) and the position of the neutral axis (Yn_{ex}) obtained from the experiments. Tables 6.5, 6.6 and 6.7 show the experimental input data ($MoE_{m,global,ex}$ and Yn_{ex}) and the corresponding analytical results ($E_{c,poplar/pine/com,an}$ and $E_{t,poplar/pine/com,an}$). The so-called “K” parameter is the ratio between the tension and compression moduli. The mean values of the previous data are presented at the bottom of the table.

A clear tendency is confirmed for all specimens in Tables 6.5 and 6.6, and 65% of the specimens in Table 6.7 for the analytical values (computed values using Eq. 6.6), defined by a higher value of the modulus of elasticity in tension than in compression for each specimen. This aspect is captured by the “K” ratio, which for the poplar layouts has an average value of 1.22, while for the pine and combined beams the mean values are respectively 1.15 and 1.21. For three pine-poplar composite beams, the opposite trend is observed, since the combination of poplar and pine layers of different strength classes can give a higher behaviour in compression than in tension (see specimens 1, 2

CHAPTER 6.

DEVELOPMENT OF AN. MODEL TO PREDICT BENDING BEHAVIOUR

Meth.	Experimental		Analytical – using working direction I		
Layout	$MoE_{m,global,ex}$ (N/mm ²)	Yn_{ex} (mm)	$E_{c,poplar,an}$ (N/mm ²)	$E_{t,poplar,an}$ (N/mm ²)	K
Poplar (Po)	9407	48.2	8466	10514	1.24
	8893	49.3	8338	9506	1.14
	7401	49.5	7957	9100	1.14
	8336	48.3	7516	9298	1.24
	8051	47.0	6928	9472	1.37
	8608	48.8	7828	9509	1.21
	9159	48.9	8306	10150	1.22
	7970	48.7	7300	8738	1.20
	$MoE_{m,global,ex,mean}$ (N/mm ²)	$Yn_{ex,mean}$ (mm)	$E_{c,poplar,an,mean}$ (N/mm ²)	$E_{t,poplar,an,mean}$ (N/mm ²)	K_{mean}
	8478 ± 7.9	48.6 ± 1.6	7830 ± 1.6	9536 ± 5.9	1.22 ± 5.9

Table 6.5: Experimental (ex) and analytical (an) results for the Po specimens (top); Mean values and covariance (%) (bottom).

Meth.	Experimental		Analytical – using working direction I		
Layout	$MoE_{m,global,ex}$ (N/mm ²)	Yn_{ex} (mm)	$E_{c,pine,an}$ (N/mm ²)	$E_{t,pine,an}$ (N/mm ²)	K
Pine (Pi)	15830	51.0	15849	15811	1.00
	16109	48.7	14743	17674	1.20
	15291	50.8	14878	15722	1.06
	13872	48.6	12418	15596	1.26
	14716	48.5	13358	16292	1.22
	15689	47.5	13749	18071	1.31
	15945	49.9	15267	16669	1.09
	14194	50.3	13801	14603	1.06
	$MoE_{m,global,ex,mean}$ (N/mm ²)	$Yn_{ex,mean}$ (mm)	$E_{c,pine,an,mean}$ (N/mm ²)	$E_{t,pine,an,mean}$ (N/mm ²)	K_{mean}
	15206 ± 5.6	49.4 ± 2.6	14258 ± 7.9	16305 ± 7.0	1.15 ± 9.7

Table 6.6: Experimental (ex) and analytical (an) results for the Pi specimens (top); Mean values and covariance (%) (bottom).

6.5. RESULTS AND DISCUSSIONS

Meth.	Experimental		Analytical – using working direction I		
Layout	$MoE_{m,global,ex}$ (N/mm ²)	Yn_{ex} (mm)	$E_{c,com,an}$ (N/mm ²)	$E_{t,com,an}$ (N/mm ²)	K
Pine + Poplar (PiPo)	12881	52.0	13389	12401	0.93
	13374	51.7	13742	13021	0.95
	13030	49.4	12032	14158	1.18
	13533	55.1	15973	11612	0.73
	12518	44.4	9673	16830	1.74
	13792	47.2	11737	16437	1.40
	13442	48.8	11918	15278	1.28
	11888	47.1	9917	14512	1.46
	$MoE_{m,global,ex,mean}$ (N/mm ²)	$Yn_{ex,mean}$ (mm)	$E_{c,com,an,mean,I}$ (N/mm ²)	$E_{t,com,an,mean,I}$ (N/mm ²)	K_{mean}
	13057 ± 4.8	49.4 ± 6.8	12298 ± 16.8	14281 ± 13.1	1.21 ± 27

Table 6.7: Experimental (ex) and analytical (an) results for the PiPo specimens (top); Mean values and covariance (%) (bottom).

and 4 with K equal to 0.93, 0.95 and 0.73, respectively, in Table 6.7).

Table 6.8 summarizes the variations of the moduli of elasticity in tension and compression of the pine-poplar composite beams with respect to the mean moduli values for poplar and pine shown in Tables 6.5 and 6.6. These computed moduli are close to those of the pine values, defined by mean variation of up to 14% with respect to the pine, while for the poplar the value reaches 57%. This aspect is also observed in the stress-deflection relations depicted in Figure 6.8.

Methodology	Variation of combined moduli computed with $MoE_{m,global,ex}$ and Yn_{ex} (%) – working direction I			
Layout	$E_{c,poplar,an,mean}$ - $E_{c,com,an,I}$	$E_{t,poplar,an,mean}$ - $E_{t,com,an,I}$	$E_{c,pine,an,mean}$ - $E_{c,com,an,I}$	$E_{t,pine,an,mean}$ - $E_{t,com,an,I}$
Pine- Poplar (PiPo)	71.0	30.0	-6.1	-23.9
	75.5	36.5	-3.6	-20.1
	53.7	48.5	-15.6	-13.2
	104.0	21.8	12.0	-28.8
	23.5	76.5	-32.2	3.2
	49.9	72.4	-17.7	0.8
	52.2	60.2	-16.4	-6.3
	26.7	52.2	-30.4	-11.0
	$E_{c,poplar,an,mean}$ -	$E_{t,poplar,an,mean}$ -	$E_{c,pine,an,mean}$ -	$E_{t,pine,an,mean}$ -
	$E_{c,com,an,mean,I}$	$E_{t,com,an,mean,I}$	$E_{c,com,an,mean,I}$	$E_{t,com,an,mean,I}$
	57.1	49.8	-13.7	-12.4

Table 6.8: Variation between the experimental and the analytical approaches for the PiPo layout.

Analytical results-Working direction II

Based on the computed moduli in tension and compression given in Tables 6.5 and 6.6 for poplar and pine, respectively, the global modulus ($MoE_{global,an,mean,II}$) and the ones in tension and compression ($E_{t,com,an,mean,II}$ and $E_{c,com,an,mean,II}$) for future manufactured combined beams (PiPo) can be assessed using the work-flow II described in Subsection 6.3. Since there are 8 sets of data available for each timber material (poplar and pine), 64 combinations of pine-poplar beams can be attained. In this case, the global modulus and the corresponding moduli in tension and compression are obtained for each particular combination. Figure 6.9 illustrates the computed results with a histogram and statistical distribution.

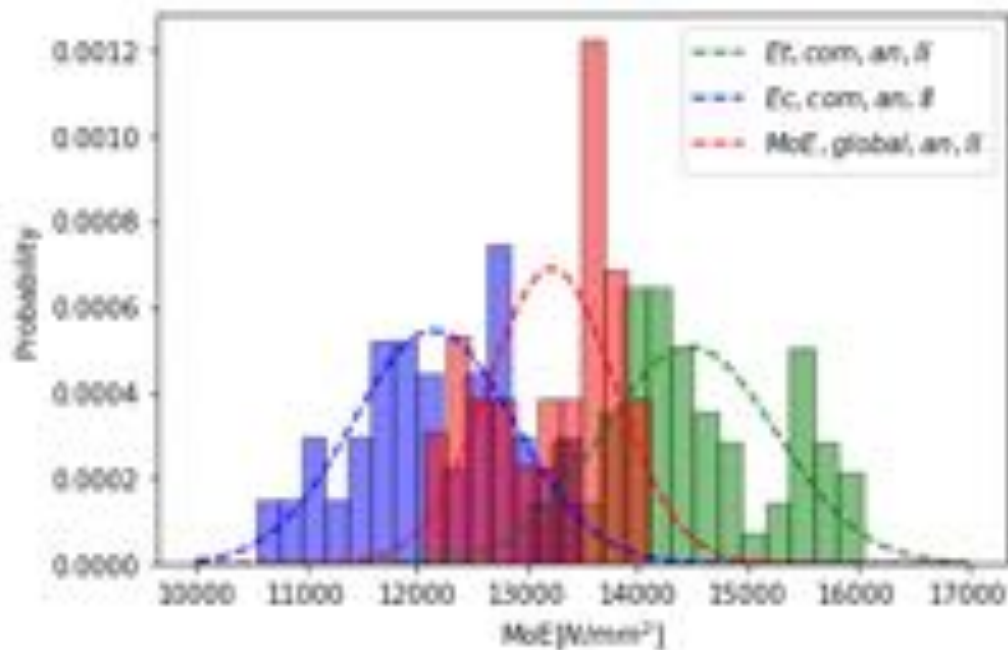


Figure 6.9: Global modulus ($MoE_{global,an,II}$) and moduli in tension ($E_{t,com,an,II}$) and compression ($E_{c,com,an,II}$). Distribution for the 64 pine poplar beams (PiPo).

As Figure 6.9 shows, the global modulus and the moduli in tension and compression lie within the range defined by the pine and poplar specimens given in Tables 6.5 and 6.6. Moreover, the global modulus reveals a concentration of values in the mid-range of $E_{c,com,an,II}$ and $E_{t,com,an,II}$ (13199 N/mm^2). The mean values are highlighted in Table 6.9; in comparison to the mean values in Tables 6.5 and 6.6, the obtained pine-poplar specimens are characterized by an intermediate behaviour with respect to pine and poplar specimens.

The variation between the mean values from the pine-poplar beams seen in Table 6.9 and those for poplar and pine given in Tables 6.6 and 6.7, respectively, are summarized in Table 6.10 to facilitate comparison. It is clear that the combined beams demonstrated the same tendency as seen in Figure 6.9.

The above results show that the combination of poplar and pine produces beams with a behaviour that lies between the individual attributes/features of these two timber species. In order to obtain the influence of the percentage of poplar or pine on the moduli of the combined beams, a parametric analysis was carried out by means of Eqs. 6.11-6.25 for the case with two different materials. Figure 6.10 highlights the clear

Method.	Analytical using working direction II (mean value over 64 beams)		
Layout	$MoE_{global,an,mean,II}$ (N/mm ²)	$E_{c,com,an,mean,II}$ (N/mm ²)	$E_{t,com,an,mean,II}$ (N/mm ²)
Pine-Poplar (PiPo)	13199 ± 4.4	12135 ± 6.1	14441 ± 5.5

Table 6.9: Analytical results for composite pine-poplar specimens, mean values and covariance (%).

Layout	Variation of mean computed moduli respect to mean experimental (%)		
Pine-Poplar (PCH)	$E_{c,com,an,II}$ respect to $E_{c,poplar,an,mean}$	$E_{t,com,an,mean,II}$ respect to $E_{t,poplar,an,mean}$	$E_{c,com,an,mean,II}$ respect to $E_{c,pine,an,mean}$
	55.0	55.7	-14.9
	$E_{t,com,an,mean,II}$ respect to $E_{t,pine,an,mean}$	$MoE_{global,an,mean,II}$ respect to $MoE_{global,ex,mean} (Po)$	$MoE_{global,an,mean,II}$ respect to $MoE_{global,ex,mean} (Pi)$
	-11.4	55.7	-13.2

Table 6.10: Variation between the mean analytical values for PiPo layout with respect to the mean values of Pi and Po specimens computed from the experiments.

influence of the percentage of poplar along the cross-section in the global modulus ($MoE_{global,an,II}$), moduli in tension ($E_{t,com,an,II}$ and $E_{c,com,an,II}$) and density ρ .

Figure 6.10 reveals that for a percentage of poplar in the range 25%-35%, the decrease of $E_{t,com,an,II}$, $E_{c,com,an,II}$, and the $MoE_{global,an,II}$ is 0.04% for $E_{t,comb,an,II}$, 1.4% for $E_{c,comb,an,II}$, and 0.08% for $MoE_{global,an,II}$, with respect to the average pine beam values. However, a remarkable 10% decrease in density ρ is obtained. The percentage of poplar used in the pine-poplar beams analyzed in this paper is 66%, since the beams are made up of four poplar layers and two pine layers of the same thickness. It can be seen in Figure 6.10 that the decrease in this case is 7.8% for $E_{t,com,an,II}$, 11.2% for $E_{c,com,an,II}$, and 9.5% for $MoE_{global,an,II}$, while for density the decrease is 16%. From the analysis of Figure 6.10, it can be concluded that an optimal sample could be achieved when the poplar percentage is 25%-35%. For this range, the reduction in the moduli of elasticity is less than 1.4%, while a 10% saving in weight may be obtained.

6.5.2 Poplar (Po) and CFRP composite beams (CLB, CLT, and CF2BT)

Experimental results

The experimental results using destructive and non-destructive tests for the three reinforced glulam beams layouts (CLB, CLT and CF2BT) and the corresponding control specimen (Po) are summarized in Table 6.11. In turn, Figure 6.11 depicts the stress-deflection curves for the composite layouts and the control layout.

The estimation of global modulus employing vertical deflection ($MoE_{m,global,ex}$) revealed improvements, defined by a variation range of 33%-39% (see Table 6.11). The highest global modulus is achieved for the CLB layouts, with an improvement around 39% upon the control layout (Po) and the steepest slope in the stress-deflection relation

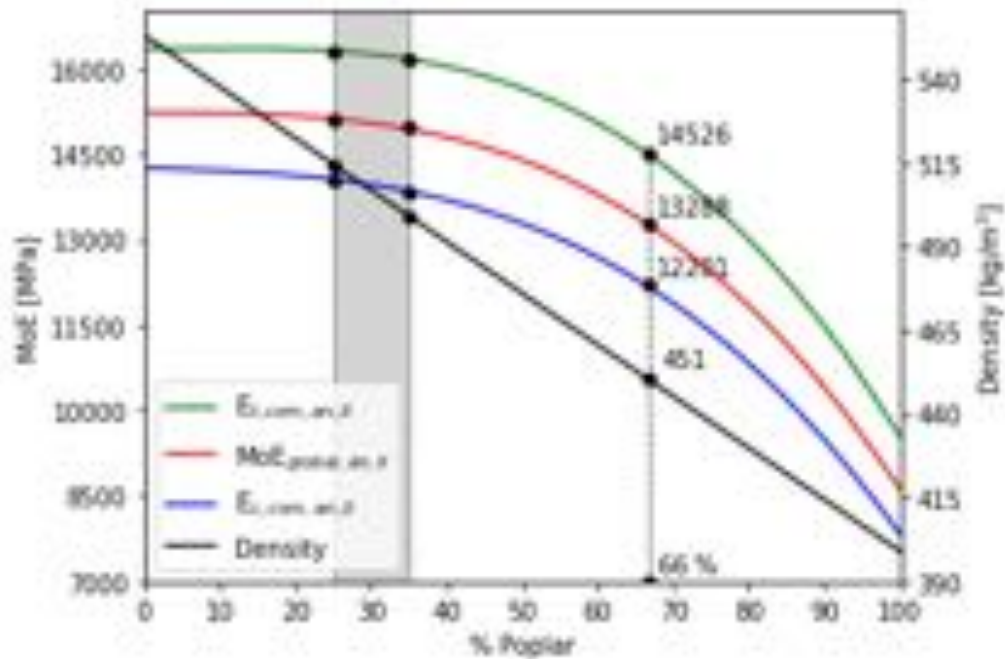


Figure 6.10: Global modulus of elasticity ($MoE_{global,an,II}$), moduli of elasticity in tension and compression ($E_{t,com,an,II}$ and $E_{c,com,an,II}$), and density ρ as a function of the percentage of poplar.

Layout / Variation	$MoE_{m,global,ex}$ (N/mm ²)	MoE_s (N/mm ²)	MoE_{dyn} (N/mm ²)	f_m (N/mm ²)	ρ (kg/m ³)
Po	8478 ± 7.9	7615 ± 17.8	7588 ± 3.5	42.9 ± 25.8	391 ± 2.8
CLB	11758 ± 2.7	11203 ± 8.1	9656 ± 3.8	57.0 ± 3.7	395 ± 1.4
Variation (%)	38.7	47.1	27.3	32.9	1.0
CLT	11629 ± 4.6	11167 ± 9.5	10086 ± 4.9	52.1 ± 12.5	417 ± 0.9
Variation (%)	37.2	46.6	32.9	21.4	6.6
CF2BT	11318 ± 5.4	10362 ± 19	9419 ± 5.3	53.9 ± 5.5	415 ± 1.5
Variation (%)	33.5	36.1	24.1	25.6	6.1

Table 6.11: Mean values (N/mm²), covariance (%) and variation with respect to control beam (Po) (%) of: Global modulus - $MoE_{m,global,ex}$; Static modulus - MoE_s ; Dynamic modulus - MoE_{dyn} ; Maximum Stress - f_m ; Density - ρ ; for poplar-CFRP composite layouts.

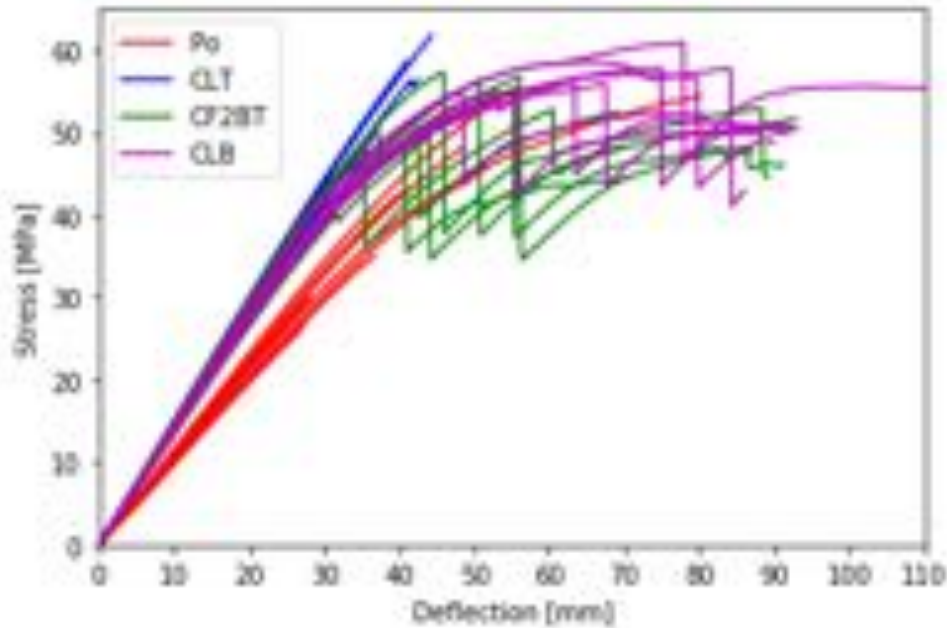


Figure 6.11: Stress-deflection relations for the control beam (poplar, Po), poplar and reinforced FRP beams (CLB, CLT and CF2BT).

in Figure 6.11. For the rest of the reinforced layouts, the slope of the stress-deflection is similar, with improvement of around 34% for CF2BT and 37% for CLT.

The highest static modulus (MoE_s) is for the CLB layouts, with an improvement around 47% compared to the Po layout. For the other layouts, CLT and CF2BT, the variation is 36%-46%. In this case, the highest improvement corresponds to CLB, since the MoE_s is determined by local measurement of the bottom strain gauge. Although the non-destructive tests estimated variations between layouts, they do not accurately predict the improvement owing to the composite material. In this case, the estimation shown in Table 11 is affected by a diverse quality of the poplar layers (strength class).

For the CLB and CF2BT layouts, two clear behaviours are identified in Figure 6.11- elastic and plastic; yet for the layout with the reinforcement placed at the top (CLT), a purely elastic relation up to failure is observed. As mentioned in Subsection 6.5.1, the control layout (Po) is characterized by the smallest slope in the stress-deflection relation and a clear limit between the elastic and plastic areas.

The influence of the CFRP in the maximum stresses and yielding points in all layouts can be deduced from Figure 6.11. For all of the reinforced layouts, except CLT, the yielding point is around 40 MPa, whereas for the unreinforced layout (Po) it varies between 27 MPa and 35 MPa. Figure 6.11 and Table 6.11 furthermore express a clear improvement in terms of the maximum stress. For the Po layout, the maximum stress ranges 35-55 MPa, while for the remaining layouts it lies between 52 MPa and 62 MPa, with a variation of 25%-33%.

Figure 6.12 presents the mean density values for all the layouts studied in this paper. It is clear that the influence of different configurations is reflected in the gross density of the specimen. As seen, the density variation due to FRP (presence) is smaller than with only-timber layouts (Pi and PiPo).

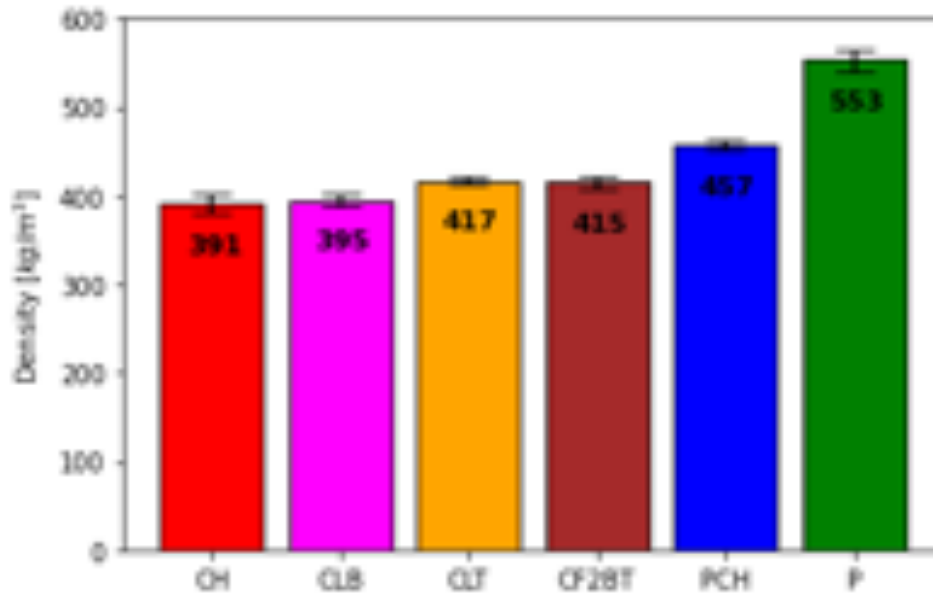


Figure 6.12: Layout density: mean and standard deviation.

Results-Working direction I

In order to evaluate the improvement of the CFRP composite material in the global modulus of elasticity MoE_{global} and the corresponding ones in tension and in compression (E_t and E_c), the analytical formulation developed in this paper for working direction I of Subsection 6.3 and Appendices 6.7.3 and 6.7.5 was applied to reinforced beams. The first and second columns in the left part of Table 6.12 indicate the global modulus of elasticity $MoE_{m,global,ex}$ and the corresponding position of the neutral axis $Y_{n_{ex}}$ acquired from the experiments for the 8 CLB beams. Applying the formulation from Table 6.3, the moduli of elasticity in tension $E_{t,com,an,I}$ and compression $E_{c,com,an,I}$ are calculated and are shown in Table 6.12. The ratio between moduli in tension and compression K_{com} is also calculated. At the bottom (left) of the table the mean values are presented.

The results on the left side of the Table show that inserting CFRP reinforcement at the bottom side increases the global modulus as well as the modulus in tension. Consequently, the “ K_{com} ” ratio is greater than 2 for all cases, with a mean value around 2.36. These increases are confirmed in Table 6.13, where the variations of the moduli in tension and in compression are compared with the mean values of the control layout (P_0). The improvements in tension are the highest, with a mean value of 89%, while the behaviour in compression showed a decrease of 2.4 %.

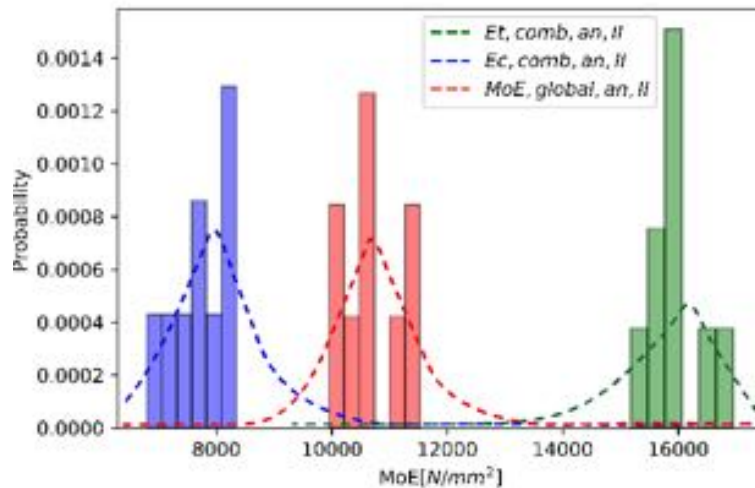
Analytical results-Working direction II

Following the working direction II as described in subsection 6.3, with Eqs. 6.10, 6.52, 6.66 the global MoE and the values of tension and compression for future manufactured reinforced beams are assessed and compared with the data in tension and compression from the pure poplar beams in Table 6.5 and the elastic modulus provided by the supplier in Section 6.3.2 for CFRP. The moduli are assessed for 8 sets of poplar-CFRP (CLB) combinations; the corresponding values are presented in the histogram on the right side of Table 6.12. As expected from the experiments, the $MoE_{global,an,II,mean}$

Meth.	Experimental		Analytical using MoE _{global,ex} (Working direction I)		
Layout	$MoE_{m,global,ex}$ (N/mm ²)	Y_{nex} (mm)	$E_{c,com,an,I}$ (N/mm ²)	$E_{t,com,an,I}$ (N/mm ²)	K_{com}
Poplar + bottom CFRP (CLB)	10992	40.4	7260	18563	2.56
	11872	41.7	8154	18864	2.31
	11031	40.5	7299	18573	2.54
	11312	41.9	7821	17794	2.28
	10947	41.5	7480	17527	2.34
	11034	41.8	7604	17439	2.29
	11268	41.5	7702	18033	2.34
	11171	42.3	7830	17216	2.20
	$MoE_{m,global,ex,mean}$ (N/mm ²)	$Y_{nex,mean}$ (mm)	$E_{c,com,an,mean,I}$ (N/mm ²)	$E_{t,com,an,mean,I}$ (N/mm ²)	$K_{com,mean}$
	11203 ± 2.7	41.4 ± 1	7644 ± 3.9	18001 ± 3.4	2.36 ± 5.4

Anal. using E_c and E_t poplar (8 poplar beams) (Working direction II)

$MoE_{global,an,II}$ (N/mm ²)	$E_{c,com,an,II}$ (N/mm ²)	$E_{t,com,an,II}$ (N/mm ²)
---	--	--



$MoE_{global,an,mean,II}$ (N/mm ²)	$E_{c,comb,an,mean,II}$ (N/mm ²)	$E_{t,com,an,mean,II}$ (N/mm ²)
10730 ± 5.3	7708 ± 7.2	15973 ± 3.5

Table 6.12: Experimental and Analytical results for the CLB layout (top); Mean values and covariance (%) (bottom).

CHAPTER 6.

DEVELOPMENT OF AN. MODEL TO PREDICT BENDING BEHAVIOUR

Method.	Variation of combined moduli computed with $MoE_{m,global,ex}$ and Y_{nex} (%) (Working direction I)	
Layout	$E_{c,poplar,an,mean} - E_{c,com,an,I}$	$E_{t,poplar,an,mean} - E_{t,com,an,I}$
Poplar + bottom CFRP (CLB)	-7.3	94.7
	4.1	97.8
	-6.8	94.8
	-0.1	86.6
	-4.5	83.8
	-2.9	82.9
	-1.6	89.1
	0.0	80.5
	$E_{c,poplar,an,mean} - E_{c,com,an,mean,I}$	$E_{t,poplar,an,mean} - E_{t,com,an,mean,I}$
	-2.4	88.8

Table 6.13: Variation between experimental and analytical approaches for CLB layout (using Working direction I).

is within the mid-range defined by moduli in tension and compression and the mean values: 10730 MPa for global, 7708 MPa for compression, and 15973 MPa for tension.

For comparative purposes, Table 6.14 shows the control layout (Po) along with the variation between mean values for working directions I (Table 6.5) and II (Table 6.12-bottom right side). The data demonstrate that improvements in the tension behaviour are near 67%, while the decrease in compression is 2% at most. Similarly, an improvement (around 27%) is achieved in terms of the global modulus with respect to the pure poplar beams (Po). That is, the global behaviour of specimens is clearly improved; note the stress-deflection relation (Figure 6.11), and the plastic behaviour indicated by plastification at the upper part of the cross-section.

Method.	Analytical variation using analytical model (%) (Working direction II)		
Layout	$E_{c,com,an,mean,II}$ respect to $E_{c,poplar,an,mean}$	$E_{t,com,an,mean,II}$ respect to $E_{t,poplar,an,mean}$	$MoE_{global,an,mean,II}$ respect to $MoE_{m,global,ex,mean(Po)}$
Poplar + bottom FRP (CLB)	-1.6	67.5	26.6

Table 6.14: Variation between experimental and analytical approaches for CLB layout using analytical data ($MoE_{m,global,ex,mean(Po)}$ represents the mean values for poplar) and Working direction II.

6.5.3 CLT layout

Analytical results-Working direction I

Similarly, Working direction I was applied for the top reinforced beams (CLT layout). Table 6.15-left shows the computed results. The insertion of the composite material at the upper part improved the elastic modulus in compression $E_{c,com,an,I}$, while the modulus in tension $E_{t,com,an,I}$ showed a minor reduction. For all of the specimens, the improvement due to top reinforcement determined a higher value for the modulus of elasticity in compression. The “ K_{com} ” ratio became sub-unitary (less than 1) in all cases. This finding is likewise expressed in Figure 11, which shows that the stress-deflection relation is completely linear, given that the modulus in compression is higher than in the rest of the layouts. Consequently, the beam fails in tension, exhibiting a brittle failure. This increase in the compression modulus is further demonstrated by the data in Table 6.16. The improvements reach a mean value of nearly 95% for compression, along with a small decrease in the tension (about 3%).

Analytical results-Working direction II

Applying working direction II as described for the CLB layout gave the results shown in Table 6.15-right. As expected from the experiments, the $MoE_{m,global,ex}$ is within the mid-range defined by the moduli (11456 MPa for global modulus, 14154 MPa for compression, and 9468 MPa for tension).

The tables evidence the variation between mean values for work-flows I (Table 6.16) and II (Table 6.17). The improvement in the tensile modulus is about 67%, while the decrease in compression amounts to 2%. Improvement of roughly 27% is achieved for the global modulus with respect to the pure poplar beams (Po). Comparison of the mean values on the right side of Table 6.15 with those of the control beam (Po) shows a clear improvement in compression (around 80%) along with a negligible decrease in tension. In addition, the global behaviour improves with the top reinforcement placed in the most susceptible part of the section. The mean improvement achieved is around 35%. This layout configuration demonstrated that plastic behaviour is avoided, as seen in Figure 6.11, due to the high modulus in compression, and an imperceptible reduction of modulus in tension is also obtained.

6.5.4 CF2BT layout

Analytical results-working direction I

The same procedure was applied for the CF2BT layout, the left part of Table 6.18 presenting the experimental and the corresponding computed results using working direction I and Eq. 6.6. The table shows the same tendency as in CLB and the control layout (Po), with moduli in tension $E_{t,com,an,I}$ greater than in compression $E_{c,com,an,I}$. The “ K_{com} ” coefficient is similar to pure poplar beams (Po). For this layout the mean improvement in compression is higher than the mean improvement in tension, respectively being around 37% and 25% (Table 6.19) due to the lower value of the modulus of poplar in compression. It is worth mentioning that CFRP layers of this specimen are considerably thinner (0.3 mm) than in the previous layouts. Hence the insertion of reinforcement provides acceptable improvement, despite the reduced thickness of the CFRP. Although this layout has a composite layer at the top (compression area), a

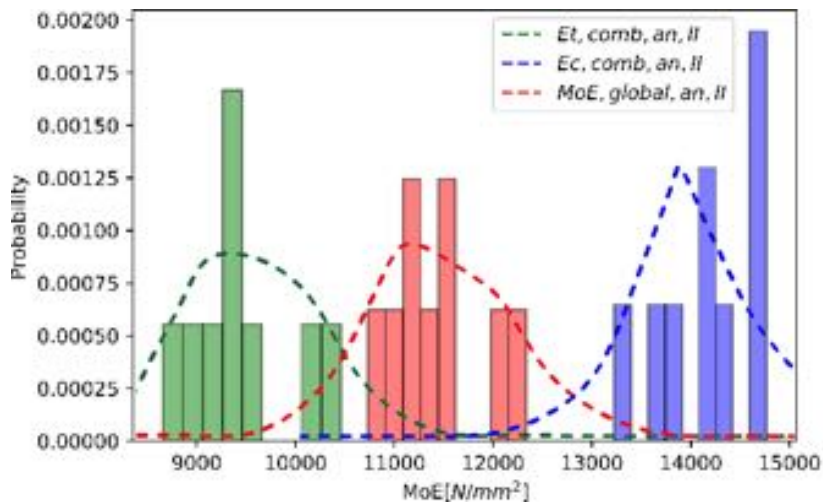
CHAPTER 6.

DEVELOPMENT OF AN. MODEL TO PREDICT BENDING BEHAVIOUR

Meth.	Experimental		Analytical using MoE _{global,ex} (Working direction I)		
Layout	MoE _{m,global,ex} (N/mm ²)	Y _{nex} (mm)	E _{c,com,an,I} (N/mm ²)	E _{t,com,an,I} (N/mm ²)	K _{com}
Poplar + top FRP (CLT)	12069	57.6	14478	10215	0.71
	10740	59.2	13768	8611	0.63
	12094	57.7	14568	10200	0.70
	11952	59.4	15815	9349	0.59
	11005	59.7	14396	8685	0.60
	11991	59.6	15658	9476	0.61
	11279	59.1	14373	9086	0.63
	11901	64.0	18942	8164	0.43
	MoE _{m,global,ex,mean} (N/mm ²)	Y _{nex,mean} (mm)	E _{c,com,an, mean,I} (N/mm ²)	E _{t,com,an, mean,I} (N/mm ²)	K _{com,mean}
	11629 ± 4.6	59.5 ± 3	15250 ± 10.8	9223 ± 8.0	0.61 ± 14

Anal. using E_c and E_t poplar (8 poplar beams) (Working direction II)

MoE _{global,an,II} (N/mm ²)	E _{c,com,an,II} (N/mm ²)	E _{t,com,an,II} (N/mm ²)
--	---	---



MoE _{global,an,mean,II} (N/mm ²)	E _{c,comb,an,mean,II} (N/mm ²)	E _{t,com,an,mean,II} (N/mm ²)
11456 ± 4.6	14154 ± 3.9	9468 ± 6.0

Table 6.15: Experimental and analytical results for the CLT layout (top); Mean values and covariance (%) (bottom).

Method.	Variation of combined moduli computed with $MoE_{m,global,ex}$ and $\gamma_{n_{ex}}$ (%) (Working direction I)	
Layout	$E_{c,poplar,an,mean} - E_{c,com,an,I}$	$E_{t,poplar,an,mean} - E_{t,com,an,I}$
Poplar + top FRP (CLT)	84.9	7.1
	75.8	-9.7
	86.1	7.0
	102.0	-2.0
	83.9	-8.9
	100.0	-0.6
	83.6	-4.7
	141.9	-14.4
	$E_{c,poplar,an,mean} - E_{c,com,an,mean,I}$	$E_{t,poplar,an,mean} - E_{t,com,an,mean,I}$
	94.8	-3.3

Table 6.16: Variation between experimental and analytical approaches for CLT layout using experimental data and Working direction I.

Method	Analytical variation using analytical model (%) (Working direction II)		
Layout	$E_{c,com,an,II}$ respect to $E_{c,poplar,an,mean}$	$E_{t,com,an,mean,II}$ respect to $E_{t,poplar,an,mean}$	$MoE_{global,an,mean,II}$ respect to $MoE_{m,global,ex,mean} (Po)$
Poplar+ top CFRP (CLT)	80.8	-0.7	35.1

Table 6.17: Variation between experimental and analytical approaches for CLT layout using analytical data with Working direction II. $MoE_{m,global,ex,mean} (Po)$ represents the mean values for poplar.

plastic behaviour is observed in the stress-deflection relationship (Figure 6.11) in contrast to CLT. Obviously, the composite material placed at the top side increased the compression behaviour, but the same amount of the CFRP is also placed at the bottom side, which withstands high tensile stress.

Analytical results-Working direction II

Applying working direction II led to the results summarized in Table 6.18-bottom. The computations for this layout configuration indicate improvement of all parameters between 20% and 25% (see Table 6.20). As the " K_{com} " ratio indicates, the differences between moduli in tension and compression are reduced, providing nearly homogeneous behaviour.

6.6 Conclusions

in this paper, an extensive analytical model is applied to compute the relations between elastic moduli for composite timber beams (without and with CFRP material). The timber materials defined within the model have different behaviour in tension and compression. While specific experimental tests to characterize the timber in tension and compression were not carried out, the analytical model is able to assess these properties.

For the beams without CFRP, the experimental tests revealed that the composite layouts made of pine and poplar (PiPo) feature high stiffness, close to that of the pine (-14% difference) than to the poplar (54% difference) layout. However, the density of the specimens underwent a reduction of 17% with respect to pine. For the composite beams with CFRP, the experimental results showed clear differences between layouts, captured by means of the analytical models.

The analytical method is able to analyze sections composed by two different timber materials (pine and poplar wood, for example) and one timber material with CFRP composite material insertion. Based on the applied models, the relation between the global modulus and the corresponding moduli in tension and compression could be assessed, and the variation between the proposed layouts could be estimated as well. Although for practitioners only the global modulus of elasticity is required, an assessment of the elastic moduli in tension and compression ensures a better understanding of the mechanical behaviour of the beam in bending. This "added value" permits one to establish the reinforcement needed to control stresses and deflections under well defined limits.

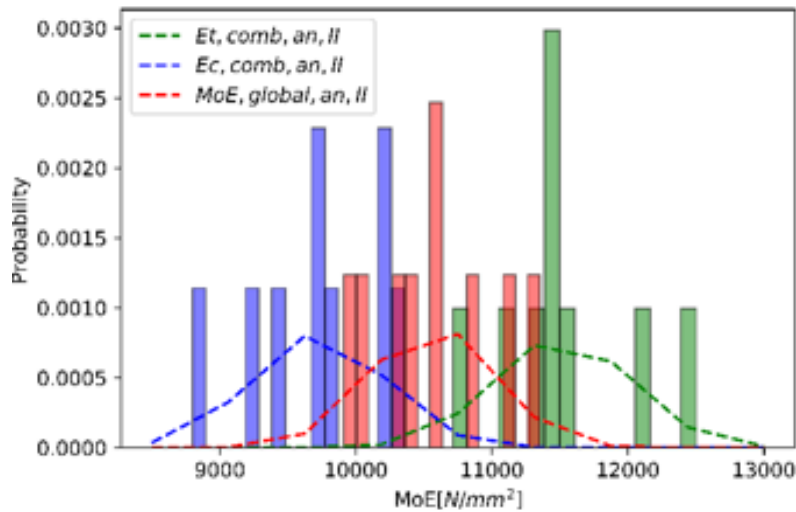
For the studied layouts, different formulations were presented considering the position of the composite material along the cross-section. As the global behaviour is obtained analytically, it confirms an improvement in view of different layout configurations involving high-class external pine layers or composite material layers. Again, the analytical formulations lend the possibility to estimate behaviour or improvement in tension and compression. For the combination of pine and poplar, improvement in the elastic moduli with respect to poplar alone is up to 50% in tension, 57% in compression and 55% global. For FRP, the improvement in the elastic moduli with respect to poplar is up to 67% in tension, 80% in compression and 35% global.

The results reported here demonstrate that the analytical method used is a powerful and versatile approach to analyze and characterize the behaviour of a cross-section

Meth.	Experimental		Analytical using MoE _{global,ex} (Working direction I)		
Layout	MoE _{m,global,ex} (N/mm ²)	Y _{n_{ex}} (mm)	E _{c,com,an,I} (N/mm ²)	E _{t,com,an,I} (N/mm ²)	K _{com}
Pop. + top and bottom FRP (CF2BT)	10766	51.7	10660	10873	1.02
	10831	51.0	10437	11248	1.08
	12411	51.5	12197	12631	1.04
	10772	50.9	10320	11255	1.09
	11055	51.6	10705	11422	1.07
	11963	51.5	11527	12424	1.08
	11516	48.9	10077	13288	1.32
	11231	49.2	9949	12777	1.28
	MoE _{m,global,ex,mean} (N/mm ²)	Y _{n_{ex,mean}} (mm)	E _{c,com,an, mean,I} (N/mm ²)	E _{t,com,an, mean,I} (N/mm ²)	K _{com,mean}
	11318 ± 5.4	50.8 ± 2	10734 ± 7.1	11990 ± 7.4	1.12 ± 10

Analytical using E_c and E_t poplar (8 poplar beams) (Working direction II)

MoE _{global,an,II} (N/mm ²)	E _{c,com,an,II} (N/mm ²)	E _{t,com,an,II} (N/mm ²)
--	---	---



MoE _{global,an,mean,II} (N/mm ²)	E _{c,com,an,mean,II} (N/mm ²)	E _{t,com,an,mean,II} (N/mm ²)
10560 ± 4.8	9724 ± 5.7	11518 ± 4.9

Table 6.18: Experimental and analytical results for the CF2BT layouts (top); Mean values and covariance (%) (bottom).

Meth.	Variation of combined moduli computed with $MoE_{m,global,ex}$ and $Y_{n_{ex}}$ (%) (Working direction I)	
Layout	$E_{c,poplar,an,mean} - E_{c,com,an,I}$	$E_{t,poplar,an,mean} - E_{t,com,an,I}$
Poplar + top and bottom FRP (CF2BT)	36.2	14.0
	33.3	18.0
	55.8	32.5
	31.8	18.0
	36.7	19.8
	47.2	30.3
	28.7	39.3
	27.1	34.0
	$E_{c,poplar,an,mean} - E_{c,com,an,mean,I}$	$E_{t,poplar,an,mean} - E_{t,com,an,mean,I}$
	37.1	25.7

Table 6.19: Variation between experimental and analytical approaches for CF2BT layout using experimental data (with work-flow I).

Meth.	Analytical variation using analytical model (%) (Working direction II)		
Layout	$E_{c,com,an,II}$ respect to $E_{c,poplar,an,mean}$	$E_{t,com,an,mean,II}$ respect to $E_{t,poplar,an,mean}$	$MoE_{global,an,mean,II}$ respect to $MoE_{m,global,ex,mean} (Po)$
Poplar + top and bottom FRP (CF2BT)	24.2	20.8	24.6

Table 6.20: Variation between experimental and analytical approaches for CF2BT layout using analytical data (with Working direction II). $MoE_{m,global,ex,mean} (Po)$ represents the mean values for poplar.

subjected to bending, in line with the possibilities stated in the standards. The analytical procedure allows one to derive the adequate poplar percentage ensuring specimens with high moduli in tension and compression, yet light in weight. This feature is clearly observed in the stiffness-poplar percentage relationship determined by means of the parametric analysis. Consequently, the assessment of the moduli in tension and compression by means of this method indicate its suitability for strengthening and retrofitting existing structures, while allowing for estimation of the degree of improvement necessary for a given structural element.

Finally, in view of the obtained results, the proposed method stands as an appropriate starting point for an optimization of the poplar percentage or amount of composite material required to obtain a timber element having homogeneous behaviour, defined by identical moduli in tension and compression.

6.7 Appendices

6.7.1 Rectangular glulam section made up of a single timber species (Pi or Po)

Relations applied to the section:

1. equilibrium of the section (moment and axial forces):

$$F_c - F_t = 0 \quad (6.27)$$

$$F_c \times (h - y_n) \times 2/3 + F_t \times y_n \times 2/3 - M_{bend} = 0 \quad (6.28)$$

2. force-stress relationships:

$$1/2 \times (h - y_n) \times b \times \sigma_c = F_c; \frac{1}{2} \times y_n \times b \times \sigma_t = F_t \quad (6.29)$$

3. stress-strain relationships :

$$E_c \times \varepsilon_c = \sigma_c; E_t \times \varepsilon_t = \sigma_t \quad (6.30)$$

4. compatibility equation:

$$\varepsilon_c \times y_n - \varepsilon_t \times (h - y_n) = 0 \quad (6.31)$$

5. geometric relation:

$$y_n + (h - y_n) = h \quad (6.32)$$

where F_c and F_t are the resultant compressive and tensile forces, respectively, M_{bend} is the applied bending moment, σ_c and σ_t are the maximum compressive and tensile stress respectively, ε_c and ε_t are the maximum compressive and tensile strains, respectively, E_c and E_t are the moduli of elasticity in compression and tension, respectively, y_n is the position of the neutral axis (measured from the bottom side), and h , b are the depth and width of the cross-section.

CHAPTER 6.

DEVELOPMENT OF AN. MODEL TO PREDICT BENDING BEHAVIOUR

6.7.2 Rectangular composite glulam section made up of a single timber species and CFRP material placed at the bottom side (CLB)

Relations applied to the section:

1. equilibrium of the section (moment and axial forces):

$$F_c - F_t - F_{tfrp} = 0 \quad (6.33)$$

$$F_c \times (h - y_n) \times \frac{2}{3} + F_t \times y_n \times \frac{2}{3} + F_{tfrp} \times (y_n - y_{frp}) - M_{bend} = 0 \quad (6.34)$$

2. force-stress relationships:

$$\frac{1}{2} \times (h - y_n) \times b \times \sigma_c = F_c; \frac{1}{2} \times y_n \times b \times \sigma_t = F_t \quad (6.35)$$

$$\frac{1}{2} \times t_{frp} \times b \times \sigma_{tfrp} = F_{tfrp} \quad (6.36)$$

3. stress-strain relationships:

$$E_c \times \varepsilon_c = \sigma_c; E_t \times \varepsilon_t = \sigma_t \quad (6.37)$$

$$E_{frp} \times \varepsilon_{tfrp} = \sigma_{tfrp} \quad (6.38)$$

4. compatibility equations:

$$\varepsilon_c \times y_n - \varepsilon_t \times (h - y_n) = 0 \quad (6.39)$$

$$\varepsilon_c \times (y_n - y_{frp}) - \varepsilon_{tfrp} \times (h - y_n) = 0 \quad (6.40)$$

5. geometric definition:

$$y_n + (h - y_n) = h \quad (6.41)$$

6.7.3 Rectangular solid section made up of a timber material and composite material at the top (CLT).

For this case, the stress-strain distribution and geometry are depicted in the following figure (Figure 6.13):

Considering the aforementioned approaches and the above layout configuration, the following relations are applied:

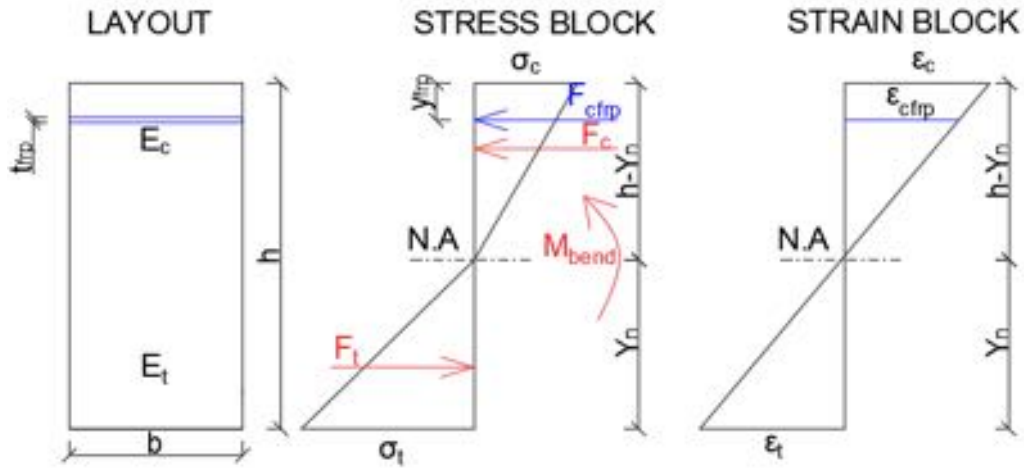


Figure 6.13: Stress-strain relations for a rectangular solid section with different behaviour in tension and compression, and composite material (CFRP) at the top side (CLT).

1. equilibrium of the section (moment and axial forces):

$$F_t - F_c - F_{cfrp} = 0 \quad (6.42)$$

$$F_c \times (h - y_n) \times \frac{2}{3} + F_t \times y_n \times \frac{2}{3} + F_{cfrp} \times (h - y_n - y_{frp}) - M_{bend} = 0 \quad (6.43)$$

2. force-stress relations:

$$\frac{1}{2} \times (h - y_n) \times b \times \sigma_c = F_c; \frac{1}{2} \times y_n \times b \times \sigma_t = F_t \quad (6.44)$$

$$\frac{1}{2} \times t_{frp} \times b \times \sigma_{cfrp} = F_{cfrp} \quad (6.45)$$

3. stress-strain relations :

$$E_c \times \epsilon_c = \sigma_c; E_t \times \epsilon_t = \sigma_t; E_{frp} \times \epsilon_{cfrp} = \sigma_{cfrp} \quad (6.46)$$

4. compatibility equations:

$$\epsilon_c \times y_n - \epsilon_t \times (h - y_n) = 0; \epsilon_c \times (h - y_n - y_{frp}) - \epsilon_{cfrp} \times (h - y_n) = 0 \quad (6.47)$$

5. geometric definitions:

$$y_n + (h - y_n) = h \quad (6.48)$$

Where F_{cfrp} is the resultant compressive force in the CFRP, σ_{cfrp} , ϵ_{cfrp} is the compressive stress/strain in the CFRP, E_{frp} is the modulus of elasticity of the CFRP, t_{frp} , y_{frp} is the FRP thickness/position (measured from the top face). Solving the above system of equations, the following expressions are obtained:

CHAPTER 6.

DEVELOPMENT OF AN. MODEL TO PREDICT BENDING BEHAVIOUR

Pos.	Stresses	Strains	Resultant forces
Top (Compression)	$\sigma_c = \frac{-6E_c M_{bend}(h-y_n)}{b\Lambda_0}$	$\varepsilon_c = \frac{\sigma_c}{E_c}$	$F_c = \frac{-3E_c M_{bend}(h-y_n)^2}{\Lambda_0}$
Bottom (Tension)	$\sigma_t = \frac{-6E_t M_{bend}y_n}{b\Lambda_0}$	$\varepsilon_t = \frac{\sigma_t}{E_t}$	$F_t = \frac{-3E_t M_{bend}y_n^2}{\Lambda_0}$
Top-FRP (Compression)	$\sigma_{cfrp} = \frac{3M_{bend}(E_c(h-y_n)^2 - E_t y_n^2)}{bt_{frp}\Lambda_0}$	$\varepsilon_{cfrp} = \frac{\sigma_{cfrp}}{E_{frp}}$	$F_{cfrp} = \frac{3M_{bend}(E_c(h-y_n)^2 - E_t y_n^2)}{\Lambda_0}$

6.7.4 Stresses, strains and resultant forces for the CLT layout.

where the above parameter is defined as:

$$\Lambda_0 = E_c(h - y_n)^2 (h - 3y_{frp} - y_n) + E_t y_n^2 (-3h + 3y_{frp} + y_n) \quad (6.49)$$

The relation for the position of the neutral axis can be expressed as a function of modulus of elasticity in tension-compression and composite material characteristics,

$$y_n = \frac{E_c h + E_{frp} t_{frp} - B}{E_c - E_t} \quad (6.50)$$

where,

$$B = \sqrt{E_{frp} t_{frp} (2E_t h + E_{frp} t_{frp} - 2E_t y_{frp}) + E_c (E_t h^2 + 2E_{frp} t_{frp} y_{frp})} \quad (6.51)$$

Similarly, the global modulus of elasticity can be expressed as for the case with the FRP at the bottom.

$$MoE_{global} = \frac{-2M_0}{h^3} \quad (6.52)$$

The procedure used for case 2, with the composite material placed at the bottom side, is applicable in this case.

6.7.5 Rectangular solid section made up of a timber material and composite material at both sides.

In this case, the stress-strain distribution and geometry are depicted in the figure below (Figure 6.14):

For this problem, several additional assumptions are considered:

1. the same composite material (CFRP) is used at both sides;
2. the composite material (CFRP) has the same thickness on both sides;
3. the composite material (CFRP) is placed symmetrical along the mid-section.

Given the above approaches and layout configuration, the following relations are applied:

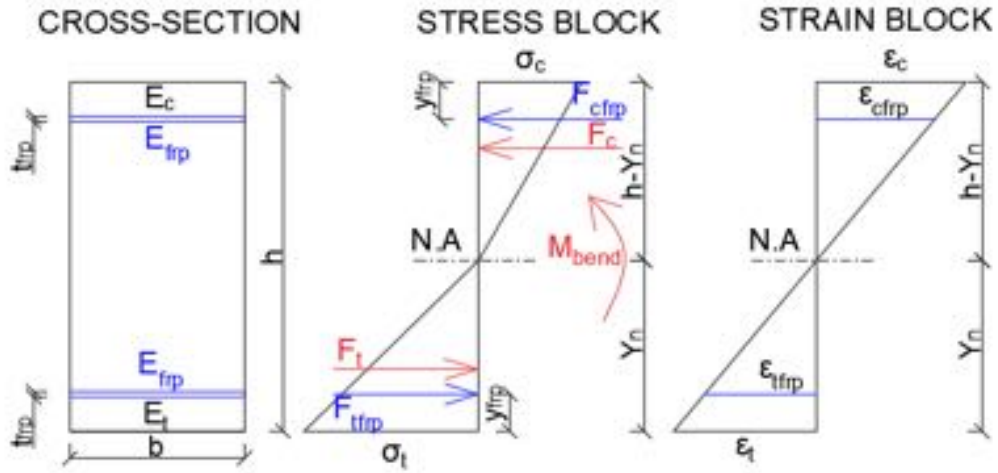


Figure 6.14: Stress-strain relations for a rectangular solid section with different behaviour in tension and compression, and composite material (FRP) at both sides.

1. equilibrium of the section (moment and axial forces):

$$F_c + F_{cfrp} - F_t - F_{tfrp} = 0 \quad (6.53)$$

$$F_c (h - y_n) \frac{2}{3} + F_t y_n \frac{2}{3} + F_{cfrp} (h - y_n - y_{frp}) + F_{cfrp} (y_n - y_{frp}) - M_{bend} = 0 \quad (6.54)$$

2. force-stress relations:

$$\frac{1}{2} \times (h - y_n) \times b \times \sigma_c = F_c; \frac{1}{2} \times y_n \times b \times \sigma_t = F_t \quad (6.55)$$

$$\frac{1}{2} \times t_{frp} \times b \times \sigma_{cfrp} = F_{cfrp}; \frac{1}{2} \times t_{frp} \times b \times \sigma_{tfrp} = F_{tfrp} \quad (6.56)$$

3. stress-strain relations :

$$E_c \times \varepsilon_c = \sigma_c; E_t \times \varepsilon_t = \sigma_t \quad (6.57)$$

$$E_{frp} \times \varepsilon_{cfrp} = \sigma_{cfrp}; E_{frp} \times \varepsilon_{tfrp} = \sigma_{tfrp} \quad (6.58)$$

4. compatibility equations:

$$\varepsilon_c \times y_n - \varepsilon_t \times (h - y_n) = 0 \quad (6.59)$$

$$\varepsilon_c \times (h - y_n - y_{frp}) - \varepsilon_{cfrp} \times (h - y_n) = 0 \quad (6.60)$$

$$\varepsilon_t \times (y_n - y_{frp}) - \varepsilon_{tfrp} \times y_n = 0 \quad (6.61)$$

CHAPTER 6.

DEVELOPMENT OF AN. MODEL TO PREDICT BENDING BEHAVIOUR

Pos.	Stresses	Strains	Resultant forces
Top (Compression)	$\sigma_c = \frac{3E_c M_{bend}(h-y_n)}{b \Psi_0}$	$\varepsilon_c = \frac{\sigma_c}{E_c}$	$F_c = \frac{3E_c M_{bend}(h-y_n)^2}{2 \Psi_0}$
Bottom (Tension)	$\sigma_t = \frac{3E_t M_{bend} y_n}{b \Psi_0}$	$\varepsilon_t = \frac{\sigma_t}{E_t}$	$F_t = \frac{3E_t M_{bend} y_n^2}{2 \Psi_0}$
Top-FRP (Compression)	$\sigma_{cfrp} = \frac{3E_{frp} M_{bend}(h-y_{frp}-y_n)}{b \Psi_0}$	$\varepsilon_{cfrp} = \frac{\sigma_{cfrp}}{E_{frp}}$	$F_{cfrp} = \frac{3E_{frp} M_{bend} t_{frp}(h-y_{frp}-y_n)}{\Psi_0}$
Bottom-FRP (Tension)	$\sigma_{tfrp} = \frac{3M_{bend} \Psi_1}{2b t_{frp} \Psi_0}$	$\varepsilon_{tfrp} = \frac{\sigma_{tfrp}}{E_{frp}}$	$F_{tfrp} = \frac{3M_{bend} \Psi_1}{2\Psi_0}$

Table 6.21: Stresses, strains and resultant forces for the CF2BT layout.

5. geometric definitions:

$$y_n + (h - y_n) = h \quad (6.62)$$

Solving the above system of equations, the following expressions are obtained: where the above parameters are defined as:

$$\Psi_0 = E_c(h + y_{frp} - 2y_n)(h - y_n)^2 + E_{frp}t_{frp}(h - 2y_n)(h - y_{frp} - y_n) + E_t y_n^2(-y_{frp} + 2y_n) \quad (6.63)$$

$$\Psi_1 = (-E_c(h - y_n)^2 + E_t y_n^2 + E_{frp}t_{frp}(-h + y_{frp} + y_n)) \quad (6.64)$$

The relation for the position of the neutral axis can again be expressed as a function of the modulus of elasticity in tension-compression and composite material characteristics.

$$y_n = \frac{E_c h - \sqrt{E_c E_t h^2 - 2E_{frp}(E_c - E_t)(h - 2y_{frp})t_{frp}}}{E_c - E_t} \quad (6.65)$$

Following the same procedure as defined in case 1, the global modulus of elasticity can be expressed as:

$$MoE_{global} = \frac{-2(\Lambda_0 + 6E_{frp}t_{frp}(h - 2y_n)(y_{frp} + y_n))}{h^3} \quad (6.66)$$

Chapter 7

Analysis of poplar timber finger joints by means of Digital Image Correlation (DIC) and Finite Element simulation subjected to tension loading

Title	Analysis of poplar timber finger joints by means of Digital Image Correlation (DIC) and Finite Element simulation subjected to tension loading
Authors	C. Timbolmas; F.J. Rescalvo; M. Portela; R. Bravo
Journal	European Journal of Wood and Wood Products
ISSN	0018-3768
Journal's performance	Journal impact factor (2020): 2.014 Q2 (Materials Science, Paper & Wood: 7/22)
Details	Accepted version: March 2022; Published online
DOI	10.1007/s00107-022-01806-6

7.1 Introduction

Wood is a natural organic, anisotropic, and renewable material with excellent ecological attributes, acting as a carbon sink, characterized by a low embodied energy. Timber is one of the most important materials used over the centuries within the construction sector [144]. Nowadays, because the timber market is continually increasing, the need for elements with special shapes and higher spans has become overwhelming. Complex connection — mechanically or adhesively bonded - is a common demand. Finger joints are currently used to produce engineered wood products like glued laminated timber beams (glulam) for different construction sectors, including buildings, bridges, or sports halls. A main benefit of implementing finger joints is the possibility to avoid certain types of flaws (e.g. grain deviation, knots, cracks, etc.) and geometrical imperfections.

Splicing two timber pieces together has been a challenging and difficult task since the early stage of finger joint applications, and the manufacturing process is highly industrialized nowadays. Finger joint parameters are therefore observed to determine

which are more closely related to the strength of a given specimen. Many compressive research works [145–149] have been carried out, employing different finger joint lengths and pitch lengths, resulting in finger joints with different slopes. Experimental results have shown that the length of the finger is one key parameter affecting finger joint strength [150]: fingers with relatively flat slopes and sharp tips could achieve a high strength finger joint, even for finger lengths shorter than the usual length in current practice. The applied end pressure is likewise a key parameter for the evaluation of a specimen's ultimate tensile strength, according to Bustos [151]; under lower-end pressure, numerous air bubbles could trigger a significant reduction of the tensile strength. It is also important to remark that higher pressure affords the greatest strength of the finger. However, Ayarkwa [150] noted that after a certain value (12 MPa) for the applied end pressure, the tensile strength of the finger joint does not significantly increase. There is moreover a risk of failure of the specimen by splitting.

In addition to these parameters, the stiffness and thickness of the adhesive would be highly relevant for finger strength. As Groom [152] stated, a stiff adhesive is recommended to reduce longitudinal and radial stress concentration at the finger base, while significantly reducing shear stress within the adhesive layer. Other important aspects regarding the behaviour of finger joints bonded with different adhesives and temperature-dependent behaviour were underlined by Frangi [153].

Numerical finite element simulations [154] were developed based on non-linear fracture mechanics to predict the behaviour of finger joints and to assess the influence of the finger joint strength when defects are located in the bond-line. Different authors [155–158] carried out further finite element models for timber members dealing with failure prediction, fracture modes, different damage definition criteria, tensile strength, and geometrical optimization of the finger joint.

The digital image correlation technique (DIC) holds great possibilities for exploring full-field displacements and strain measurements in the realm of experimental mechanics. As a non-contact, optical method, DIC has proven to be an ideal tool for the study of material behaviour for a large range of products [159]. DIC is traditionally used to analyze steel, concrete and elastic-plastic behaviour, but not wood material [160].

In recent years, however, considerable and comprehensive numerical and experimental approaches have been used to address timber fracture characterization by means of DIC and the finite element method (FEM) [161–163]. As is well known, the joints are the most critical part of most of the timber structures, being designed as mechanical or adhesively bonded joints. For that reason, joint behaviour is an interesting research area for the application of DIC [164]. Specific applications in determining the Poisson's ratio of a ductile adhesive in tension and compression have been undertaken through DIC [165].

The present study is focused on experimental and numerical investigations of the I-214 poplar cultivar behaviour in tension, with and without finger joints. The study is centered on the linear elastic part of the analysis, since the modulus of elasticity is the main variable of interest for characterization of the specimens. However, in order to take into account the influence of the contact and cohesion at the finger joints, non-linear contact and cohesive models that behave almost linearly until failure were used. The experimental campaign involved the optical evaluation of the specimen during testing by means of DIC. The main contribution of the paper is to characterize the mechanical behaviour of the poplar timber with and without finger joints through an

experimental analysis supported by DIC monitoring and FEM simulation.

7.2 Materials and Methods

7.2.1 Poplar wood and adhesive

The wood used for this work was extracted from a 9-year-old poplar plantation of the cultivar I-214 (*Populus* × *Euroamericana* [Dode] Guinier) located nearby the city of Granada, Spain. From the logs, planks of 2000 mm length and a section of 35 × 75 mm were sawn and dried for 6 months in natural conditions, always ensuring proper ventilation and avoiding direct exposure to the sun or rain. The final Moisture Content (MC) of wood was $10 \pm 2\%$. To manufacture the finger joint samples, a monocomponent polyurethane adhesive was used. The density of the adhesive was 1.12 g/cm^3 and its viscosity (Brookfield RVT) was 7000 mPa.s, spindle-6, with a rotational speed of 20 rpm and with a temperature of 20°C , measured between 16 to 36 hours after production (ISO 2555:2018 [166]).

7.2.2 Sample description and manufacturing

A set of 20 poplar specimens were prepared to be subjected to tension in the grain direction. The samples were divided into two batches of 10 specimens each, without finger joints (TT) and with finger joints (TF), respectively, without being grouped into strength classes. All the specimens were sawn to a length of 586 mm, with a general cross-section of 50 × 17 mm. So as to promote failure in the central area of the specimen and to avoid undesired breakage, the width of this central part was narrowed to 20 mm, resulting in a mid-section of the specimen of 20 × 17 mm (Figure 7.1). For the TF samples, the finger joint was located at the geometrical centre. The adhesive for the finger joint was applied at a temperature of $20 \pm 2^\circ\text{C}$, with a wood MC of $9.8 \pm 1.5\%$, complying with the requirements of the manufacturer for its application. The adhesive was applied at a rate of 250 g/m^2 . After that, the specimens were prepared and introduced in a climatic chamber at 20°C and 65% relative humidity, according to the EN 408:2010 + A1:2012 standard [19].

As Jokerst [167] stated, the geometry of the finger joint dictates the strength of a joint, and consequently the strength of the specimen. Among the research findings reported to date, the finger length is found to mostly affect the strength of the finger joint, while the pitch has a negligible effect on joint strength. In addition, tip thickness and slope of the finger bear a noticeable impact on joint strength [168]. According to the EN 14080:2013 – Annex I [21], the geometric parameters that define a joint include the finger length (l_j), finger pitch (p), finger angle (α), tip gap (l_t), and tip width (b_t) (see Figure 7.2). These parameters are interrelated, meaning that a in one parameter will change the others. This complicates research into the effect of any single parameter on strength [167]. According to studies on the performance of finger joints [169,170], good performance in terms of tensile strength and modulus of elasticity can be attained for finger lengths of 13-14 mm; hence, a length of 14 mm was selected for the specimens used here (Figure 7.2). Afterwards, the geometric parameters of the finger joint were set to fulfil the requirements stated in the Annex I from the EN 14080:2013 standard [21](see Figure 7.2). Taking into account the length of the finger joint, a final pressure of 10 N/mm^2 was applied, in view of the graph from Annex I (EN 14080:2013) [21].

CHAPTER 7.

AN. OF POPLAR TIMBER FINGER JOINTS BY MEANS OF DIC-FEM

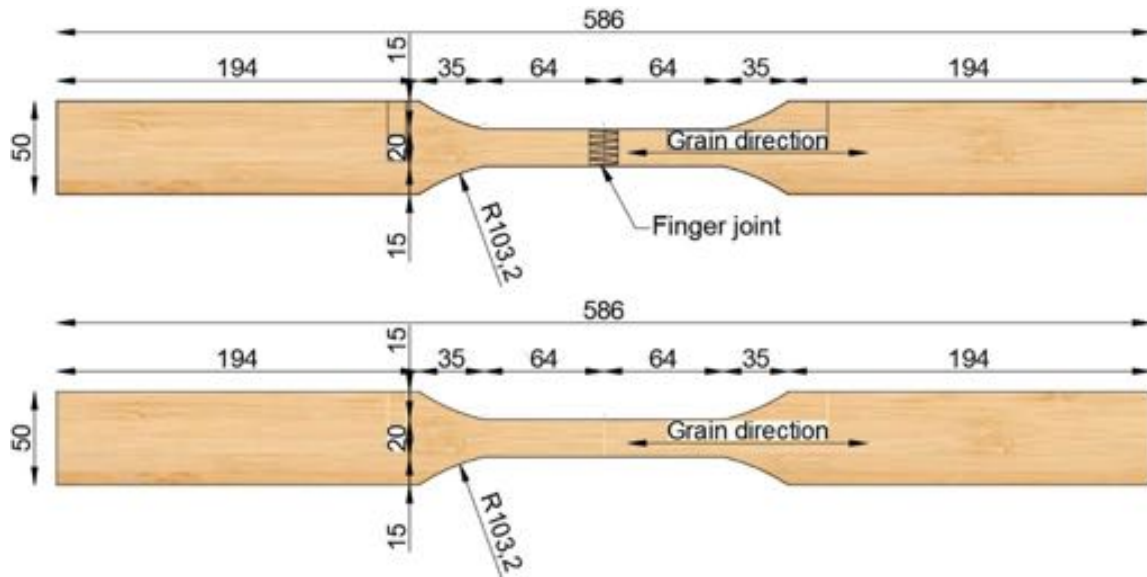


Figure 7.1: Geometry of the tensile poplar specimens with (TF) and without (TT) finger joints. Dimensions in mm.

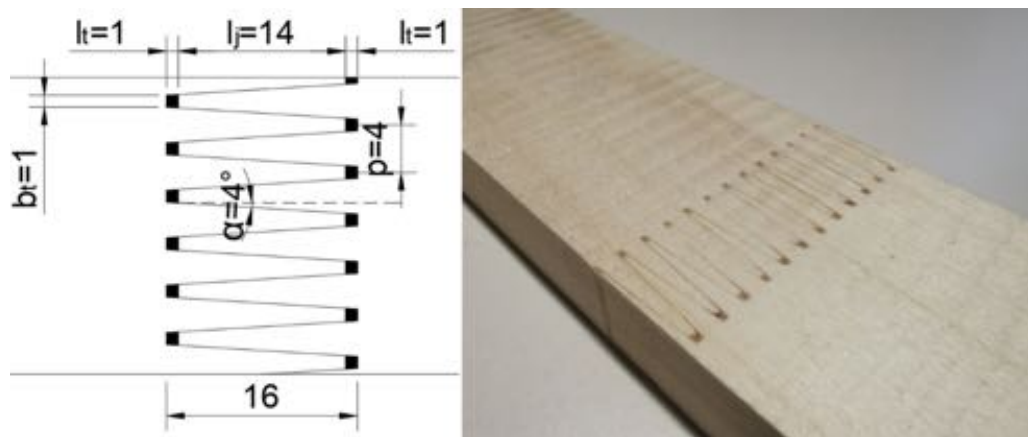


Figure 7.2: Geometrical parameters of the finger joint profile and finger joint picture. Dimensions in mm.

7.2.3 Experimental test

Tensile tests were carried out in a multi-testing machine, specially manufactured by Microtest S.A Company, with an electrical actuator having a maximum capacity of 200 kN, with an accuracy of 0.01 kN, and a speed test rate of 0.5 mm/s. In order to avoid slipping during the test, the samples were clamped 90 mm on each side. Figure 7.3 shows the set-up of the experiment with the DIC equipment during a test. The maximum tensile strength ($f_{t,0}$) was computed according to the EN408:2010 + A1:2012 standard [19] as:

$$t_{t,0} = \frac{F_{max}}{A} \quad (7.1)$$

where F_{max} is maximum axial load, and A is the cross-section of the specimen at the mid-length.

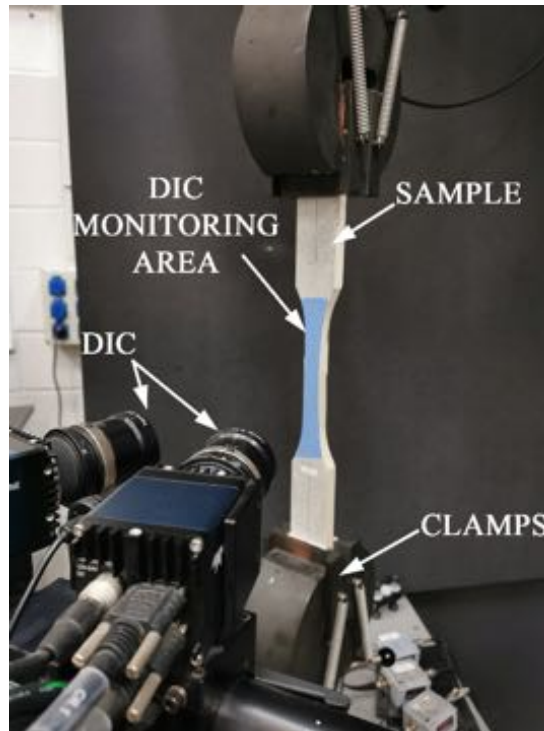


Figure 7.3: Axial tensile test set-up with DIC equipment.

7.2.4 Digital Image Correlation

For monitoring the strain field in the central part of the specimens, a three-dimensional image correlation non-contact optical measurement system was used, Aramis 3D[®] [171]. The ARAMIS 3D[®] system is a powerful non-contact measuring instrument that is suitable for assessing three-dimensional deformation and strain distributions of real components under static or dynamic loads.

The surface of the specimen should be smooth and clean. Then, a black-on-white random speckle pattern was applied as uniformly as possible, using an opaque spray paint on the face of each sample. The DIC system was calibrated using the specific Aramis 3D[®] [171] calibration protocol, which includes camera positions and lens distortion parameters. With this calibration information, the system ensures measurement accuracy. The DIC monitoring area is defined by a face size with 19 pixels, as well as 16 pixels for point distance.

The optical module of Aramis 3D[®] (made up of two 12M industrial cameras) was oriented towards the specimen surface. The placement of the Aramis 3D[®] optical module was also conditioned by the recommended calibration distance to the specimen, in this case 295 mm, with an angle of 25° between cameras. By means of this technique and the capabilities of GOM Correlate software, developed by GOM GmbH-Germany [171], the modulus of elasticity in tension was calculated using two methods: I) Based on the relationship established in the standard EN 408:2010 + A1:2012 [19]; II) Based on the average stress-strain relation, within the defined area.

CHAPTER 7.

AN. OF POPLAR TIMBER FINGER JOINTS BY MEANS OF DIC-FEM

For method I, according to standard EN 408:2010 + A1:2012 [19], the following relation was used:

$$E_{t,0} = \frac{l_1(F_2 - F_1)}{A(w_2 - w_1)} \quad (7.2)$$

where $F_2 - F_1$ are the increment of load on the straight line portion of the load deformation curve at 20-30% of the maximum load, $w_2 - w_1$ are the increment of the corresponding displacement, l_1 is the length of the extensometer and A is the cross-section of the specimen at the mid-length. In order to derive accurate and reliable results, three pairs of virtual orthogonal extensometers with different lengths were placed in three distinct locations (Figure 7.4-left). The first extensometer, Ext.1, was placed along the evaluation area (100 mm length) in accordance with EN 408:2010 + A1:2012 [19] for $E_{t,0}^{Ext.100}$ computation. The second extensometer, Ext.2, was placed at the top end of the gauge length at a length of 20 mm ($E_{t,0}^{Ext.20}$) for control of the results. In order to evaluate the influence of the finger, a third extensometer (Ext. 3) was placed within the middle of the finger joint at a length of 14 mm to calculate $E_{t,0}^{Ext.14}$. In all cases, to calculate Poisson's ratio, horizontal virtual extensometers 15 mm in length (Transversal and Transversal 1) were placed at the mid-length of the vertical ones. Thus, the relationship between transversal and longitudinal strains could be computed.

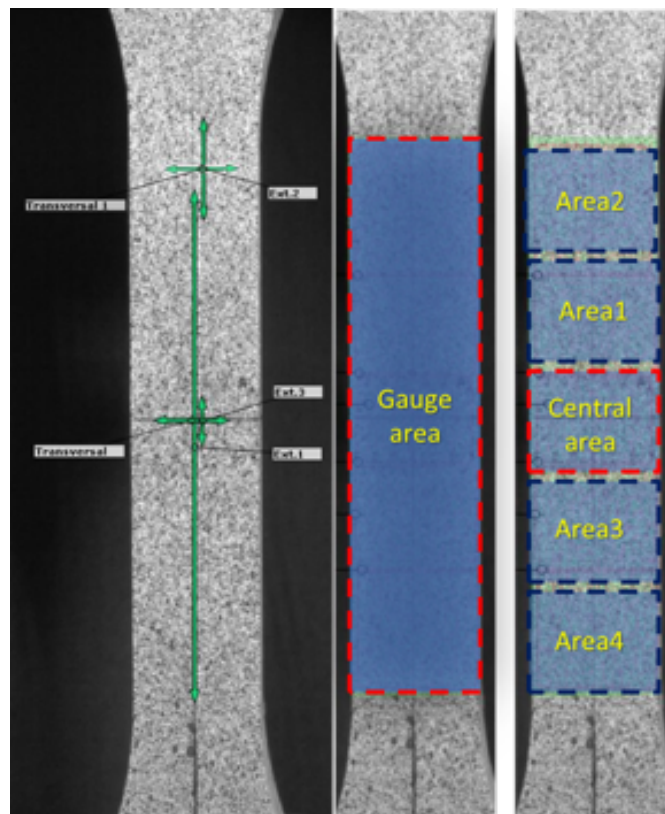


Figure 7.4: Definition of the virtual extensometer position: Ext.1, Ext.2, Ext. 3 (left), Gauge area (center); areas for strain determination (right).

In the case of method II, since the DIC technique allows one to determine the mean strains of a defined areas with different geometric sizes (Figure 7.4-center and right),

several areas were considered, starting from the mid-gauge length to the ends of the specimens. To determine the mean longitudinal strain corresponding to these areas, for the specimen with no finger joint, a gauge area corresponding to the entire gauge length was defined, allowing for computation of the corresponding modulus of elasticity ($E_{t,0}^g$) (see Figure 7.4-center).

For the specimens with finger joints, the modulus of elasticity is calculated in several distinct areas: $E_{t,0}^{ca}$ corresponding to the central area, $E_{t,0}^a$ to "Area 1", and so on (see Figure 4-right). These moduli are computed as the slope of corresponding stress-strain relation between the interval of 20%-30% of the maximum load (EN 408:2010 + A1:2012 [19]).

For both methods, Poisson's ratio of the specimen was computed. To this end, two different values of Poisson's ratio were obtained employing methods I (ν) using the extensometer, Ext. 3, and II (ν^*) using the defined central area, respectively, as follows, where, $\Delta\epsilon_{transv}$ is the transversal strain increment (method I) or the transversal average strain (method II), and $\Delta\epsilon_{axial}$ is the longitudinal strain increment (method I) or the longitudinal average strain (method II).

7.2.5 Finite element method: numerical simulations

A 3D parametric finite element model to investigate the behaviour in tension of the specimens with and without finger joints was developed employing Abaqus software [172] and the programming language Python [173]. Figure 7.5 depicts the finite element model of the sample with finger joints. This 3D solid linear material elastic anisotropic model is composed by two glued parts that interact along the finger interface by contact. The mechanical behaviour of the interface is governed by contact and damage cohesive traction laws from Abaqus [173, 174]. The failure criterion used for this study is the quadratic traction law.

The boundary conditions are defined according to the experimental test set-up; hence, they were modelled as clamped conditions applied to the all-lateral area of the bottom flange of the specimen. For the top flange, however, the boundary conditions allowed the imposed longitudinal displacement of the specimen with a constant rate of 0.4 mm/s, similar to the experimental part. In the case of the TF samples, the failure of the model is brittle due to the opening of the contacts between fingers. Owing to the sharp geometry of the fingers, a four-node tetrahedral element (C3D4) was used for the modelling of the specimen. The meshing process was refined in the surrounding finger area, with a mean element size of 0.8 mm for the fingers. For the rest of the gauge length the mean size was 2.4 mm, and the coarse size corresponds to the tapered part and clamping area with mean sizes of 6.4 mm and 7.4 mm, respectively. The size geometry of the meshing process was changed based on converge analysis until the results were stable.

The constitutive parameters as moduli of elasticity, Poisson's ratio, and the contact parameters are defined in Tables 7.1 and 7.2. The longitudinal input elastic parameter (E_1) was taken from the performed experiments, while the rest of the elastic input parameters were considered as a ratio of 1/8 for E_2/E_1 , and 1/30 for E_3/E_1 , taken close to the ratios corresponding to "Yellow Poplar" wood (Table 5-1 from Wood Handbook [130]). In turn, the input parameters for the contact interface were defined in view of previous, similar numerical simulations [157]. An iterative calibration process modifying the initial parameters from the reference was performed by trial and successive

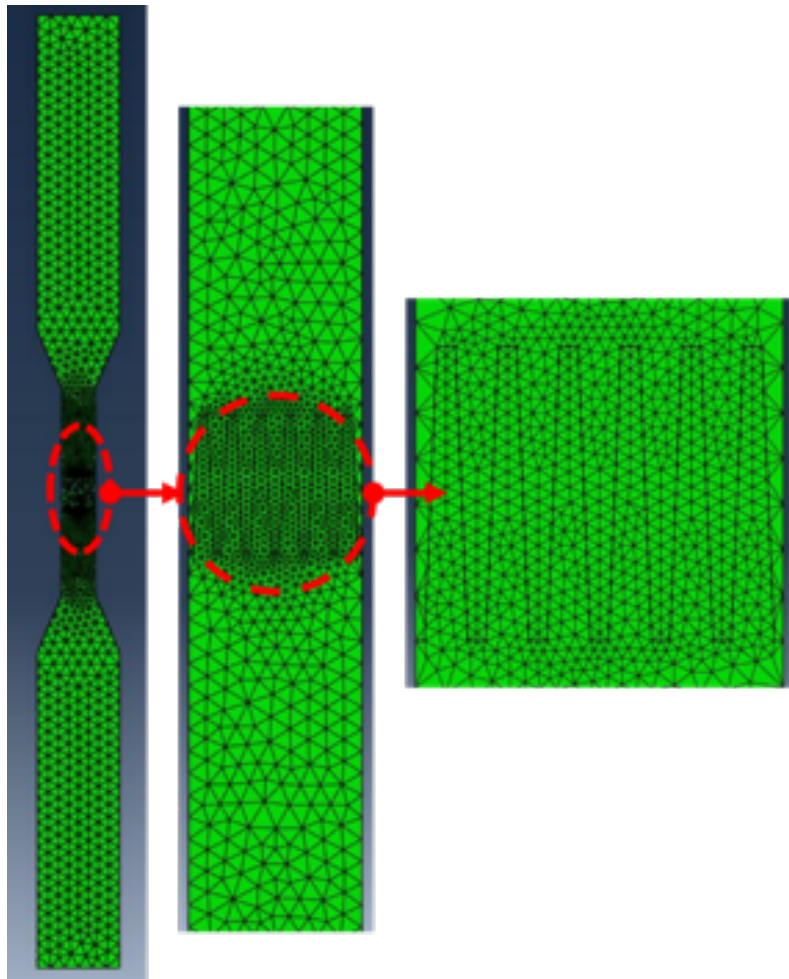


Figure 7.5: FEM mesh: general view of the specimen (left), mesh of the fingers joint (middle and right).

Specimen	E_1 (MPa)	E_2 (MPa)	E_3 (MPa)	G_{12} (MPa)	G_{13} (MPa)	G_{23} (MPa)	$\nu_{12}=\nu_{13}=\nu_{23}$
TT	9936	1244	331	759	557	278	0.40
TF	8356	1044	278	759	557	278	0.40

Table 7.1: Input elastic parameters for FEM simulations. E_1, E_2, E_3 are the moduli of elasticity in longitudinal, transversal and radial directions; G_{12}, G_{13}, G_{23} are the shear moduli in longitudinal, transversal and radial planes; $\nu_{12}, \nu_{13}, \nu_{23}$, are the Poisson's ratio.

Specimen	Friction coefficient	Normal penalty stiffness (N/mm)	Tangential penalty stiffness (N/mm)	K_{nn} (N/mm ² /mm)
TF	0.3	1E+09	1E+09	5.5
	$K_{tt} = K_{ss}$ (N/mm ² /mm)	σ_n (N/mm ²)	$\tau_{nI} = \tau_{nII}$ (N/mm ²)	δ_p (mm)
	62	4.6	8.5	0.001

Table 7.2: Input contact parameters for FEM simulations. K_{nn}, K_{tt}, K_{ss} are the normal, tangential and radial stiffness; $\sigma_n, \tau_{nI}, \tau_{nII}$ are the maximum nominal inter-facial strength in the normal and shear direction I and II; δ_p is the effective plastic displacement.

verification until the numerical model had fitted the experimental relation.

7.3 Results and Discussion

7.3.1 Experimental results

All the manufactured specimens, TT and TF, were subjected to the static axial tensile test. Figure 7.6 shows the stress-strain relations based on method I using extensometer with 100 mm length (top), based on method II, using mean longitudinal strains from the central area (bottom-left), and method I, using the extensometer of 14 mm length (bottom-right).

All the relations highlighted linear-elastic behaviour without any evidence of plastic deformation until the failure of the specimens, so that the failure is characterized by brittle failure. Clearly the TF specimens exhibit lower stiffness than the TT specimens, identified by a slight curvature within the stress-strain relation induced by the non-linear behaviour of the finger joint. For the TF specimens with an extensometer or area located at the finger joint, the relations are slightly lower due to the strain concentration captured by DIC at the base of the fingers. Therefore, this local effect produces a slight reduction in the moduli of elasticity.

Tables 3 and 4 show the longitudinal moduli of elasticity using methods I and II, for the extensometer of 100 mm length ($E_{t,0}^{Ext.100}$) according to EN 408:2010 + A1:2012 [19], the corresponding area ($E_{t,0}^{ga}$) of the extensometer located in the finger joint or mid-gauge length for the specimen without finger ($E_{t,0}^{Ext.14}$) and its corresponding central area ($E_{t,0}^{ca}$). The third extensometer is located away from the finger joint at 20 mm length ($E_{t,0}^{Ext.20}$) and a corresponding area that coincides with the extensometer location

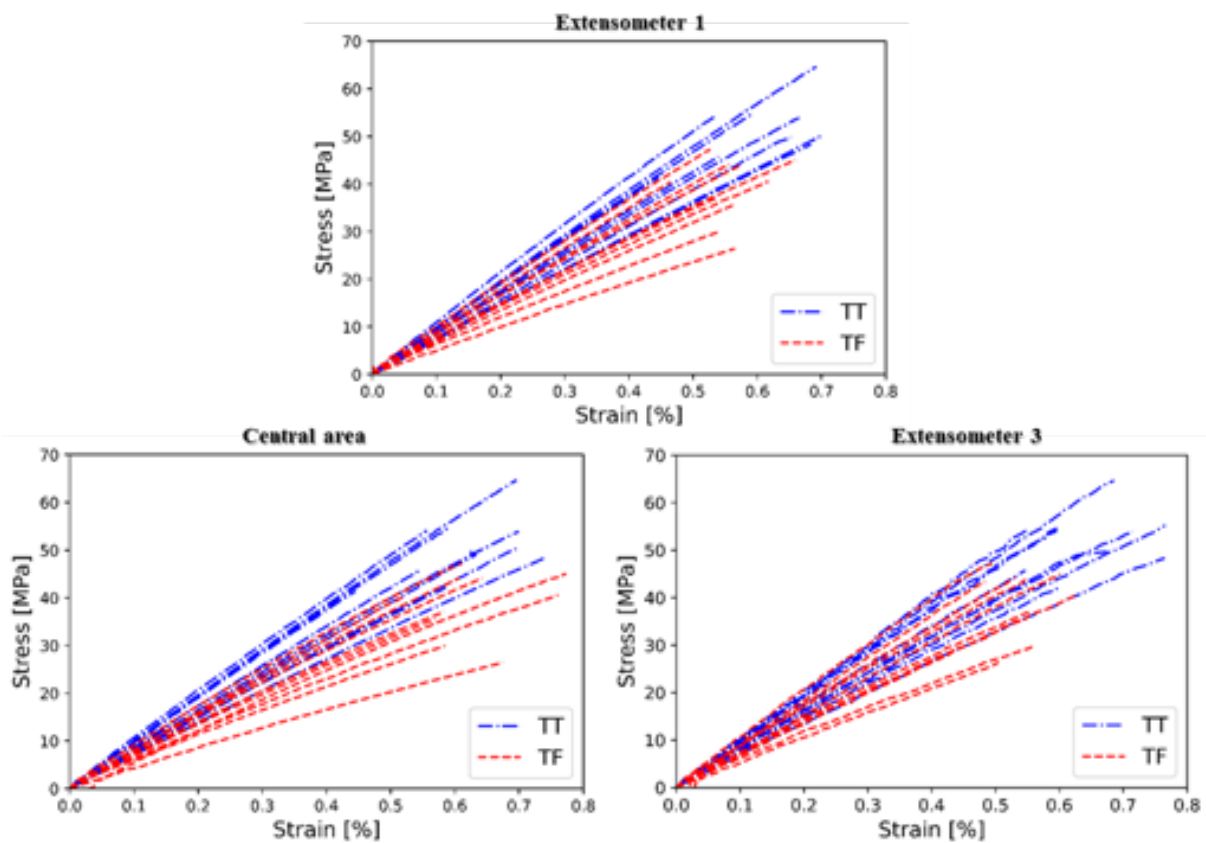


Figure 7.6: Stress-strain relations for TT and TF specimens: (top) based on Ext. 1; (bottom-left) based on defined central area; (bottom-right) based on Ext. 3.

Specimen name	$E_{t,0}^{Ext.100}$ (N/mm ²)	$E_{t,0}^{8a}$ (N/mm ²)	$E_{t,0}^{Ext.14}$ (N/mm ²)	$E_{t,0}^{ca}$ (N/mm ²)	$E_{t,0}^{Ext.20}$ (N/mm ²)	$E_{t,0}^{a2}$ (N/mm ²)
TT1	7916	9755	7529	9710	7606	9942
TT2	7611	7562	7793	7827	7247	7218
TT3	7533	7421	7926	7481	7590	7602
TT4	7531	7468	7740	7494	7396	7853
TT5	8627	8545	8124	8294	8275	8368
TT6	8661	8695	8990	8741	8844	9557
TT7	10652	10553	12128	10689	10852	11022
TT8	6527	9342	8920	9296	9610	10396
TT9	6402	9341	9225	9302	9784	10424
TT10	7487	7398	6789	7040	8675	8822
Mean (N/mm ²)	8495	8608	8516	8587	8588	9120

Table 7.3: Results for the TT specimens and the corresponding mean value.

($E_{t,0}^{a2}$). It is important to remark that in Table 7.4, the results computed based on the gauge area with method II are not meaningful, given the reduced size of the finger area (about 14 mm length) compared to the entire gauge area (area of finger joints is 11% of the gauge area). Thus, the mean longitudinal strain using the gauge area is representative only for the TT specimens, since the strain is homogeneous, giving values that match the results provided by method I using Ext.1 ($E_{t,0}^{Ext.100}$). For the TT specimens, the moduli of elasticity are considerably higher than for the TF specimens, considering that the finger joint introduces a weakness in the longitudinal behaviour of the specimen.

For the TT specimens, Table 7.3 shows that the mean values obtained by means of method I and method II are comparable, ranging 8495 N/mm² – 9120 N/mm². For the specimens with finger joints (TF), Table 7.4 shows that the mean values employing methods I and II have a wider range, 6942 N/mm² – 7736 N/mm², possibly induced by different strength classes of the top and bottom timber pieces. These higher differences related to the finger specimens are directly linked with the strain acquisition using method II, which is able to capture the high strain concentration. Consequently, the mean longitudinal strains are high, resulting in low longitudinal moduli values. Under method I, the displacements are computed by integration of the strains, for which reason the influence of the concentration of strains is averaged.

The last row in Table 7.4 shows the moduli reduction between TT and TF, which varies from 11.0% to 19.0%, indicating a relatively low dispersion of the results that is mainly induced by the finger joint and the lack of timber part classification in strength classes. The maximum reduction (19.0%) is found for the measurements located in the central area (finger joint) using Method II. In this local measurement, high strains are captured by DIC, increasing the mean longitudinal strain. Hence, the computation of the modulus of elasticity in this area provides reduced values. For the same location, the reduction is very similar to the one provided by Method I, with a variation of 0.5%. This trend is visible for all of the cases since the virtual extensometers do not take into account the local non-linear strain concentrations developed at the fingers. With regard to the obtained results using Methods I and II for the top part of the specimen (Ext. 2 and Area 2), the maximum mean reduction is 16.4% and 11.0%, which highlighted the

CHAPTER 7.

AN. OF POPLAR TIMBER FINGER JOINTS BY MEANS OF DIC-FEM

Specimen name	$E_{t,0}^{Ext.100}$ (N/mm ²)	$E_{t,0}^{8a}$ (N/mm ²)	$E_{t,0}^{Ext.14}$ (N/mm ²)	$E_{t,0}^{ca}$ (N/mm ²)	$E_{t,0}^{Ext.20}$ (N/mm ²)	$E_{t,0}^{a2}$ (N/mm ²)
TF1	8079	-	8449	7817	8082	8925
TF2	7884	-	7164	6952	9489	7455
TF3	9036	-	7882	8971	10453	8191
TF4	7182	-	7008	7015	8093	6613
TF5	7297	-	7741	6835	7088	8193
TF6	9356	-	9215	8910	9470	10840
TF7	5669	-	5302	5526	5194	7006
TF8	6468	-	5403	5982	7739	7028
TF9	4944	-	5486	4923	4246	4391
TF10	6647	-	5772	6611	6582	7612
Mean (N/mm ²)	7256	-	6942	6954	7644	7625
ΔTT-TF (%)	14.6	-	18.5	19.0	11.0	16.4

Table 7.4: Results for the TF specimens, the corresponding mean value, and the differences (Δ TF-TT %) between TT and TF specimens.

highest variation (5.4%) between methods. Consequently, the mean variation value of modulus of elasticity in tension, evaluated according to the EN 408:2010 + A1:2012 [19] standard, is around 14.6%, due to finger joint presence and class wood piece components of different strengths.

Table 7.5 summarizes the average value of the experimental results and the mean difference related to the Poisson’s ratio obtained using Methods I-II (ν and ν^*)-using the extensometer with 10 mm length (Ext. 3) and central area, tensile strength ($f_{t,0}$) and density (ρ) of the TT and TF specimens. As our results revealed, the finger joints do not have any influence on Poisson’s ratio value, because the fingers do not significantly affect the transversal strains. Yet a significant reduction (27.5%) in the tensile strength is observed for the TF specimens, because the weakness induced in the longitudinal direction triggered a failure mechanism.

Specimen name	ν	ν^*	$f_{t,0}$ (N/mm ²)	ρ (kg/m ³)
TT	0.40	0.40	51.0	385
TF	0.40	0.42	37.0	375
ΔTF-TT (%)	0.0	5.0	-27.5	-2.6

Table 7.5: Mean Poisson ratio using method I (ν) with Ext. 3, and II (ν^*) with central area, mean tensile strength parallel to the grain ($f_{t,0}$), mean density and variation in (ΔTF-TT)%.

An important aspect deserving mention is that, for both specimens, the mean Poisson ratios computed using both approaches (methods I and II) are nearly identical (0.0% and 5.0% of variation). Therefore, the proportionality between transversal and longitudinal deformation is similar for both computational methods. Subsequently, the presence of the finger joint does not exert any influence related to density (-2.6%).

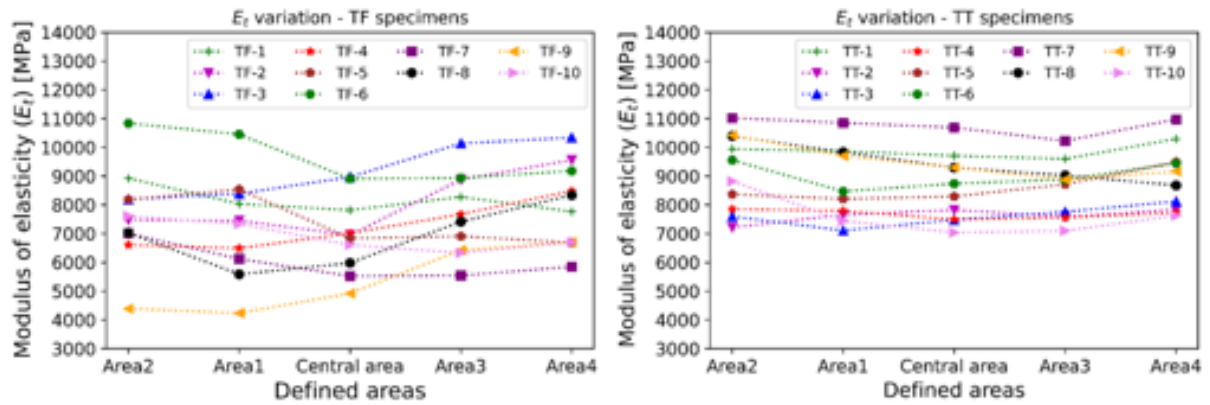


Figure 7.7: Modulus of elasticity variation of the specimens with finger joints-TF (left) and without finger joints-TT (right).

For a better understanding of the longitudinal moduli variation along the gauge length, the mean strains computed based on the defined areas (Figure 7.4)–method II, are used for the longitudinal moduli computation. The corresponding moduli distributions are shown in Figure 7.7. It is worth mentioning that for the TF specimens, a significant decrease is emphasized in the central area, corresponding to the finger joint location. However, the TT specimens revealed a homogeneous distribution of longitudinal moduli along the gauge length, mainly due to absence of the finger and therefore to the one-piece manufacturing process of the specimen. It is moreover important to remark that for the TF specimens, different moduli values are observed for the top and bottom part of the specimen, indicating different timber strength classes used in the manufacturing process.

In general, for the TT specimens, the failure is mainly caused by crack propagation along the matrix, while initiation of the failure is triggered within the tapered part (transition between gauge and top flange) (see Figure 7.8-a). Yet for the TF specimens, the failure is brittle and the crack initiation is located within the finger joint, developing in the direction perpendicular to the fingers (see Figure 7.8-b).

Figure 7.9 shows the normal distributions of the mean moduli of elasticity presented in Tables 7.3 and 7.4, based on the considered computation methods (I and II). As Figure 7.9 shows, the mean longitudinal strain distributions for specimen TT, using method I (left), are similar and identical from the pattern variation point of view, while for TF specimens, a visible decrease and a higher dispersion are revealed by the distribution (Figure 7.9-left). This heterogenic aspect of the results is likewise observed in the results based on method II (Figure 7.9-right).

Figure 7.10 shows the experimental longitudinal strain evolution for one representative TT (top) and TF (bottom) specimen with intermediate behaviour. In addition, the corresponding DIC strain map is shown at four loading stages: 25%, 50%, 75% and 100%, respectively.

As the DIC strain map shows, for low and intermediate load step levels (up to 50% of the maximum load), the strain field is homogeneous for both specimens. For the TF specimen, the force-elongation relation also captures the stiffness reduction, characterized by a reduced slope compared to the TT relation.

For higher load levels, several inhomogeneity start to appear for TF around the fingers due to the non-linear behaviour of the finger joint, while for TT the field is still



Figure 7.8: Modulus of elasticity variation of the specimens with finger joints-TF (left) and without finger joints-TT (right).

homogeneous in the mid-section of the specimen. For loads closer to the fracture point, the strain field remains homogeneous for TT, but for the TF specimen, a significant concentration of strains is reflected by the high non-linearities in the finger interface.

7.3.2 Finite element simulation and DIC results

The one representative experimental samples for each specimen and the calibrated numerical model are discussed in this subsection. Figure 7.11 presents the force-elongation relations for the TF and TT specimens obtained from the experimental and numerical simulation part. The relations from the experimental part are plotted in a representative sample with an intermediate behaviour based on the relations provided in Figure

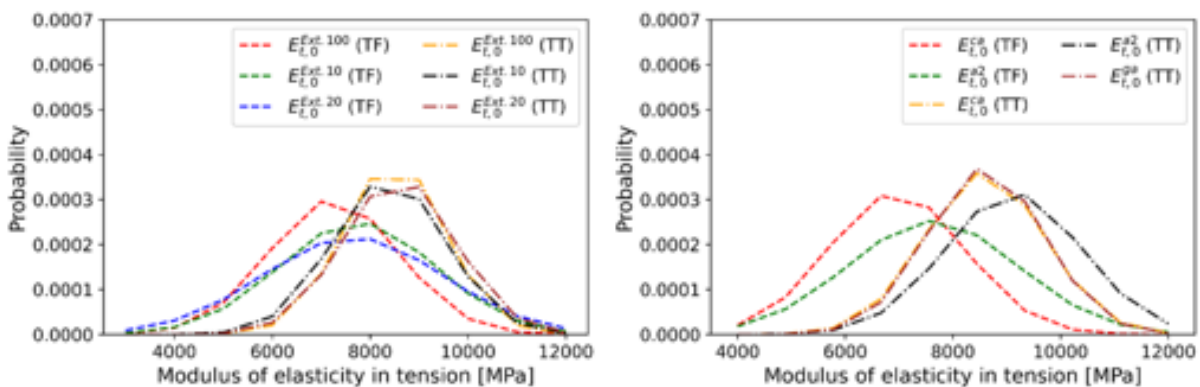


Figure 7.9: Distribution of modulus of elasticity using: extensometers - method I (left); defined areas - method II (right).

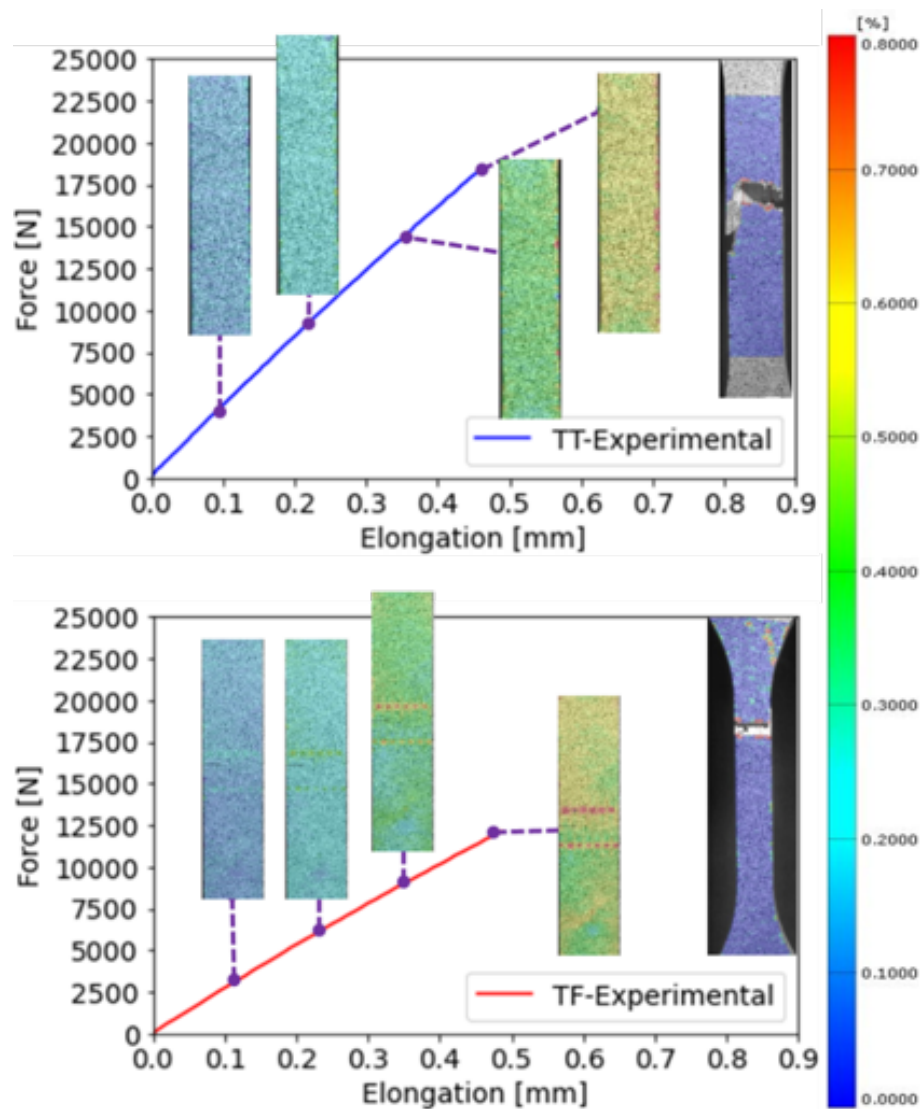


Figure 7.10: Experimental force-elongation curve and DIC vertical strains field at four different load steps for one representative TT (top) and TF (bottom) specimen.

7.6-top. The numerical simulations through the calibration process matched the experimental relation and the failure point of the specimens. The calibration process started with the experimental parameters; then, through successive steps, the final values were obtained. These parameters of the FEM calibrated models are presented in Tables 7.2 and 7.3.

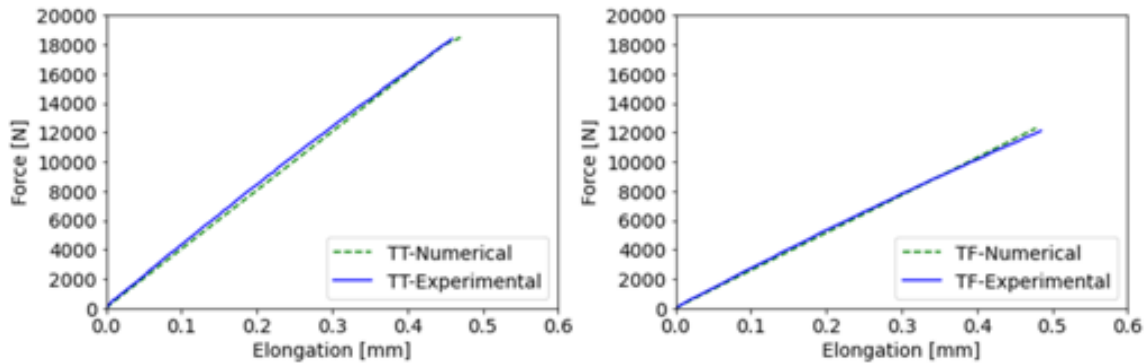


Figure 7.11: Force-elongation of numerical and experimental relationships for TF specimen (left) and TT specimen (right).

Figure 7.12 shows a comparison of the longitudinal (ϵ_x), transverse (ϵ_y) and shear (ϵ_{xy}) strain fields between DIC and FEM before failure. Both techniques capture the high strain concentration around the tip and base of the fingers due to the initiation of detachment of the fingers and the shear distortion along the lateral faces. The maximum longitudinal strain concentration occurs within the base of the fingers, giving similar values for DIC and FEM (0.8%). It is noteworthy that longitudinal strains within the tip are almost null due to the gap produced during the manufacturing process.

The maximum longitudinal strain (ϵ_x) occurs at the base owing to the action of the cohesive forces along the lateral sides of the fingers, the strain flowing through the finger base. Regarding the transversal strains and shear strains, distributions by FEM and DIC are in accordance, showing low magnitude in comparison to the longitudinal one, with a maximum transversal strain of 0.3%, and 0.12% for shear strain. For the transversal (ϵ_y), the flow is symmetric and is mainly caused by the Poisson's ratio, producing a small necking due to a high Poisson's ratio (value of 0.4 in Table 7.5). For the shear (ϵ_{xy}), the strains at the fingers are equal and opposite, and the maximum strains occur at the tips of fingers because of the reduced size of the section of the finger close to the tip. While the DIC shear strain distribution suggested small negative shear strains, which can be produced by the imperfections between the top and bottom clamps of the machine.

7.4 Conclusions

This study analyzed and characterized the mechanical behaviour of the poplar timber of I-214 cultivar for specimens with and without finger joints. Based on the obtained results, the poplar wood behaviour subjected to axial tensile stress is analyzed in parallel with the numerical simulations. The experimental results obtained employing different methodologies using DIC technique allow the possibility to analyze the samples along their entire length. As the results show, for the specimens with fingers joint,

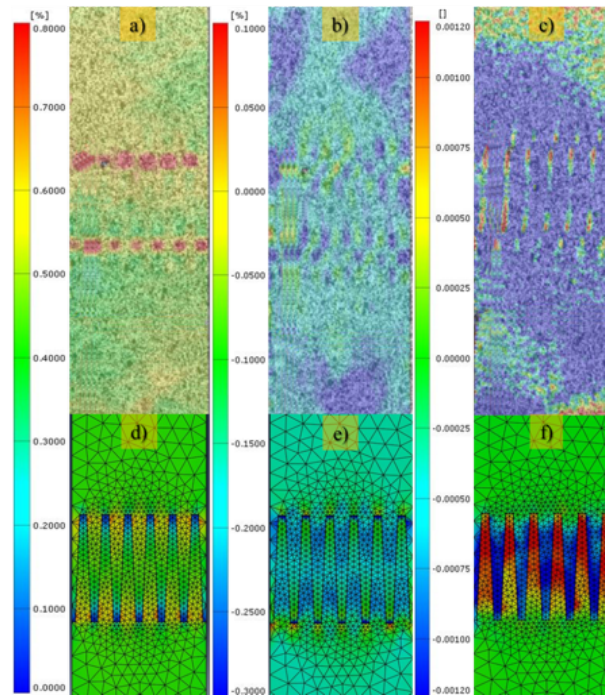


Figure 7.12: Strain field distribution for TF specimen. a) Longitudinal strain (ϵ_x); b) Transversal strain (ϵ_y); c) Shear strain (ϵ_{xy}) from DIC. d) Longitudinal strain (ϵ_x); e) Transversal strain (ϵ_y); f) Shear strain (ϵ_{xy}) from FEM.

the reduction of the stiffness and the tensile strength becomes relatively small. The results show that the presence of the fingers decreases the mechanical properties between 11.0-19.0% for moduli of elasticity, and around 27.5% of the tensile strength, respectively. However, the tensile strength remains higher than the limits specified into the EN 14080:2013 standard [21].

One of the most important experimental results obtained by means of DIC technique is the evaluation of the longitudinal modulus of elasticity in tension along the gauge length of the specimen. Consequently, two particular behaviours are identified, a homogeneous moduli of elasticity distribution along the gauge length for the TT specimens, while for the TF specimens, the results were highly dispersed, with a minimum value located within finger joint. It is worth mentioning that both methods provide similar results for the strain gauges placed within finger length and the corresponding area of the finger surface. Nevertheless, the central area is averaging the strains spread to the entire length of the finger, which revealed high parts with high strains concentration. Therefore, the low variation of the mean reduction obtained employing both methods, stated the validity of both investigation methods. Besides, the DIC technique is a powerful tool that allows evaluating the strain state at every rate load, and the strain concentrations and flow within the finger geometry.

Furthermore, numerical simulations were carried out to obtain a suitable FE model, able to capture, verify and complement the structural behaviour provided by DIC, and showing good agreement. Through these numerical simulations, the main aim was to obtain the parameters related to the contact interface, which can be extended to a further study related to the optimization of fingers joints. The results provided through this study, are useful for further research tasks, which involve glued poplar beams or other engineered wood products, where the tension behaviour of the raw material has

CHAPTER 7.

AN. OF POPLAR TIMBER FINGER JOINTS BY MEANS OF DIC-FEM

yet to be known.

Chapter 8

Multi-side Digital Image Correlation (DIC) evaluation of bonded CFRP to poplar timber

Title	Multi-side Digital Image Correlation (DIC) evaluation of bonded CFRP to poplar timber
Authors	F.J. Rescalvo; C.Timbolmas; R. Bravo; M. Portela; J. Lorenzana
Journal	Construction and Building Materials
ISSN	0950-0618
Journal's performance	Journal impact factor (2020): 6.141 D1 (Civil Engineering: 7/137)
Details	Under review process

8.1 Introduction

Timber structures are prone to degradation, especially those that are not carefully or properly maintained, therefore, rehabilitation and strengthening operations are needed to withstand the serviceability loads [175]. Over the past decades, the rehabilitation employing externally bonded Carbon Fiber Reinforced Polymer (CFRP) plates or sheets has been successfully applied to existing reinforced concrete structures [175]. Hence, the study of the bonding between CFRP and concrete has achieved progressive research interest because of its reduced weight, high mechanical properties, corrosion resistance, and relatively easy installation process [176]. In general, the CFRP strips have been bonded to base material by means of the epoxy resin, which transfers the forces to the concrete substrate. The studies of the RC members reinforced with CFRP were concerned not only in the flexural strengthening, besides this demanding parameter. Bonacci [177] investigated the interrelationships between strength, failure mode, and deflection capacity on concrete beams. Regarding this ascending trend of this strengthening method employing FRP materials, extensive and comprehensive experimental and analytical research works were developed. The main concerning aspects investigated through these studies were focused on the bond-slip models, effective bond

length, maximum critical loads, and failure mechanisms for the FRP to concrete bonding subjected to single/double shear tests [178–182]. Nowadays, finite element methods are a powerful tool to complement and to demonstrate experimental behaviour and analytical models. Hence, compressive numerical studies have been undertaken to understand these complex phenomena of debonding and to study the degradation of the bonded interface along with the constitutive interface parameters [183–186].

At this moment, for the retrofitting, strengthening of the exiting timber structures is a relatively new technique. In many areas where the plantation of poplar is very common, there are many constructions made of poplar, even historical heritages built more than 100 years ago. Poplar has low mechanical properties and durability, therefore it is necessary to retrofit and strengthen these structures. The research in this field has attracted a lot of interest and gained a high demand in both lines of investigation, experimental campaigns, and analytical models. Several research works have focused on retrofitting the old timber beams from historical buildings using different CFRP plates and layouts [116, 136, 187].

As well, the authors investigated the improvements in terms of bending strength and ductility due to the use of the CFRP in glulam beams by using low-quality timber (poplar) as a base material for different reinforcement layouts across the cross-section of the beam [125]. The improvement of the reinforcement was also quantified analytically using the transformed section technique (Parallel axis theorem) applied for multi-layered glulam beams made of poplar with different strength classes [188, 189].

Generally, in conventional testing campaigns used for FRP bonded to concrete or timber, the bond load-slip response and strain distribution can be analyzed through a single/double shear test employing closely spaced strain gauges along the FRP centerline and from the LVDTs [190–194]. A noticeable shortcoming of this method is related to the difficulties in applying many strain gauges for short bond length in order to have sufficient data collected from the specimen. In addition, the debonding process and the strain distribution through the specimens could be challenging to capture with a few strain gauges. In order to overcome these difficulties, compressive research works have been developed employing digital image correlation (DIC) technique [195], to determine the effective bond length, strain distribution, and force-slip response for concrete and timber models [196–198].

The main advantage of the DIC method is that being an optical measurement technique, the entire surface of the specimens can be analyzed in terms of strain and displacement fields. Therefore, this technique is able to capture the complex behaviour of the specimens that the strain gauges cannot acquire due to their local data acquisition capabilities. As well, the DIC allows identifying the exact locations of the maximum and minimum strain values determining in an efficient way the points of interest. Consequently, the DIC permits the complete strain evaluation from different perspectives, frontal and side view respectively [199].

In this study, the DIC technique is applied for CFRP bonded to poplar timber specimens subjected to single shear tests, with different bond lengths and types of reinforcement as explained in Sections 8.2 and 8.3. This technique is used for the determination of the longitudinal strain filed in the CFRP (frontal view) and a timber surface adjacent to the bond line (side view). Based on the acquired results, the force-slip and stiffness of the interface are analyzed for all of the specimens in Section 8.3. The experimental set-up consists of four batches with different bonding lengths, 50 mm, 100 mm, 150 mm and 200 mm. The specimens are subject to a single shear test, and the poplar

block is not restricted in the longitudinal and transversal direction of the applied force; therefore, the specimens are free to bend during the test, simulating the behaviour of members subjected to service loads as explained in Section 8.3.

The main objective of this study is to highlight the behaviour of different CFRP arrangements (carbon fabric or laminate) bonded to low-quality timber as poplar in terms of longitudinal strains distribution in CFRP and into the timber layer close to the bond line. Additionally, the main differences between specimens are presented in a comparative way considering the reference model, the specimen with the highest bond length and the lowest axial stiffness of the CFRP.

8.2 Materials and Methods

8.2.1 Poplar wood and adhesive

Local poplar cultivar I-214 (*Populus x Euroamericana* [Dode] Guinier) timber was used in this study. In order to bond the CFRP to timber and to increase the adherence between timber and the CFRP, a primer layer was applied using the resin Mapewood Primer 100[®]. Afterwards, for the bonding of the CFRP-timber interface, the two-component MapeWrapr 21[®] epoxy resin was used and both of them were supplied by the company MAPEI S.A.U. In this study, two commercial CFRP were used, unidirectional carbon fibre fabric (MapeWarp C Uni-AX 300) and pultruded carbon fibre plate (Carboplate E-170), both provided by the company MAPEI S.A.U. The mechanical parameters of the CFRP materials are depicted in Table 8.1. The fabric, which has high adaptability but a medium-low stiffness, was applied to some specimens as a single or double (superimposed) layer. While, Carboplate sheet is a laminate that provides high stiffness, and consequently, is able to carry out high stresses

CFRP (Technical name)	Total thickness [mm]	Tensile strength [MPa]	Maximum Elongation [%]	Young's Modulus [GPa]
MapeWarp C Uni-AX 300	0.164	4830	2.0	230
Carboplate E 170	1.4	3100	2.0	170

Table 8.1: Mechanical properties of the CFRP materials from [98].

8.2.2 Specimens description

The testing program consisted of 60 specimens, divided into several batches defined by the bond lengths (50, 100, 150 and 200 mm), the type of carbon reinforcement, and the acquisition location of the DIC. For each group with the same bond length (L_{bond}), three different types of specimens (CF, CF2, CL) were studied (tested), characterized by different axial stiffness of the CFRP, as summarized in Table 8.2. The first column of Table 8.2 contains the nomenclature for each batch, which is composed of three terms:

CHAPTER 8.

MULTI-SIDE DIC EVALUATION OF BONDED CFRP-POPLAR TIMBER

1) type of reinforcement (CF for one layer of fabric, CF2 for two layers of fabric, and CL for pultruded laminate sheet); 2) bonding length (L_{bond}); 3) the type of DIC analysis carried out for each particular case (F for frontal view and S for side view).

Specimen name	Number of samples	Bond length [mm]	Axial stiffness $E_{CFRP} \times t_{CFRP}$ [kN/mm]
CF-200-F / CF-200-S	2 / 3	200	37.7
CF2-200-F / CF2-200-S	2 / 3	200	75.4
CL-200-F / CL-200-S	2 / 3	200	238.0
CF-150-F / CF-150-S	2 / 3	150	37.7
CF2-150-F / CF2-150-S	2 / 3	150	75.4
CL-150-F / CL-150-S	2 / 3	150	238.0
CF-100-F / CF-100-S	2 / 3	100	37.7
CF2-100-F / CF2-100-S	2 / 3	100	75.4
CL-100-F / CL-100-S	2 / 3	100	238.0
CF-50-F / CF-50-S	2 / 3	50	37.7
CF2-50-F / CF2-50-S	2 / 3	50	75.4
CL-50-F / CL-50-S	2 / 3	50	238.0

Table 8.2: Experimental samples description and their corresponding CFRPs axial stiffness.

As can be seen in Table 8.2, for each layout, two specimens were analyzed using frontal view, corresponding to the planar surface of the CFRP, while the rest of the three specimens were analyzed using side view, which captures the interaction between CFRP to timber, and the lateral surface of the poplar block.

In all cases, the cross-section of the poplar lamella was 50 x 28 mm, with a length of 240 mm (Figure 8.1). Therefore, the bonded width was 50 mm. In order to avoid undesirable edge effects at the beginning of the timber sample, an unbonded length of 20 mm was set for all of the specimens.

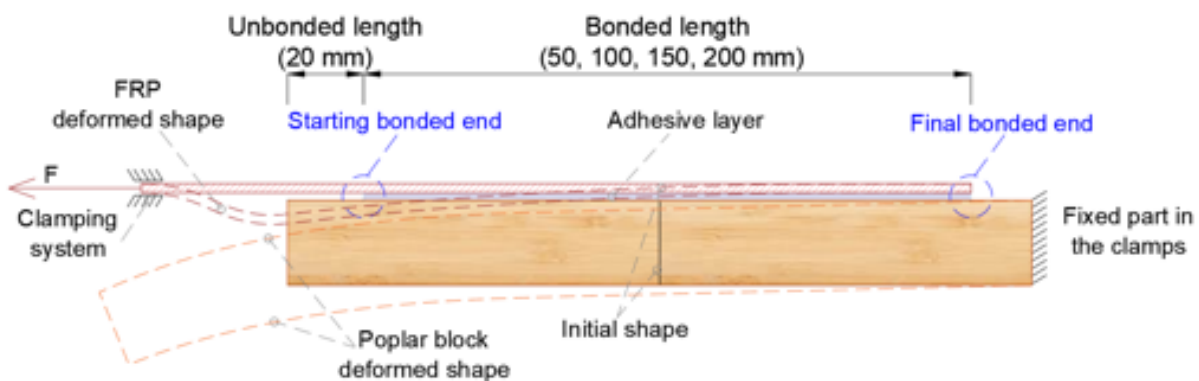


Figure 8.1: Schematic representation of the CFRP-timber sample, the boundary conditions, and the deformed shape of the specimen expected during testing.

Traditionally, adhesion tests are carried out imposing restrictions to the block in vertical and horizontal directions. In this work, to analyze the behaviour of the specimen in a situation similar to working conditions and take into account the influence of

the deformation of the timber in bending (CFRP-timber interaction), the specimen was only restricted at the clamping areas.

8.2.3 Test set-up and DIC equipment

All the samples were tested in a multi-testing machine, specially manufactured using an electrical actuator with a maximum capacity of 200 kN (accuracy of 0.01 kN) (see Figure 8.2). A load with a constant rate of 45 N/s was applied until failure occurred. The upper clamp of the testing equipment was coupled to a loading cell of 50 kN, while the lower one was fixed to a stationary metal frame so that both clamps remained the specimen completely vertical during the entire test.

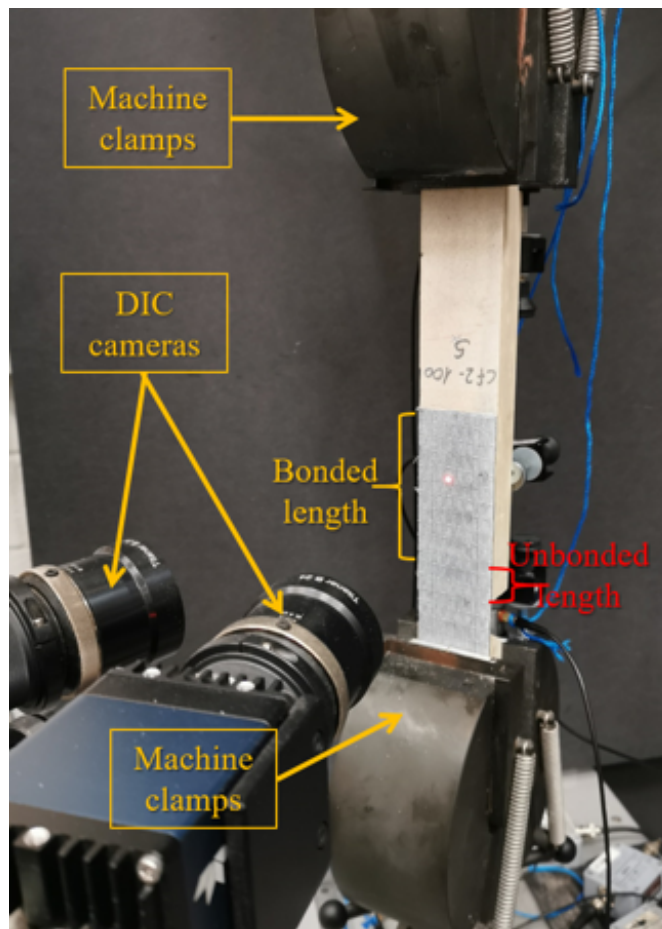


Figure 8.2: Experimental test set-up and DIC equipment.

In addition, during the single-shear test, a 3-D optical system for the strain measurements, Aramis 3D[®] [171] was used. The system applies the principles of digital image correlation (DIC) obtainment of full-field measurements widely used in all the engineering fields [200]. This technique has the advantage of being non-intrusive and requires simple sample preparation for the evaluation of surface displacements and strains by means of a stochastic pattern applied to the surface. In this case, the speckle pattern was performed via the application of a thin coating of white opaque aerosol spray paint onto two specimen faces, followed by a spot distribution of black opaque paint. The DIC system was calibrated using the specific Aramis 3D[®] calibration protocol and according to the instructions of the CP20/MV350x280 calibration object, in-

cludes camera positions and lens distortion parameters. A stereo-vision angle of 25° is set up between the two cameras before calibration. The base distance between cameras was set to 172 mm, which corresponded to a measuring distance of 455 mm. With this calibration information, the system provides measurement accuracy.

In the DIC method, the displacement field was measured by analyzing the geometrical displacements of the spots in the images of the surface of interest. The images were recorded before and after deformation by the optical module, composed of 12 MPx industrial cameras (24 mm Lens, 4096x3072 Pixels) aligned to the specimen surface. A facet size of 8 pixels x 5 pixels was chosen as the region of interest for the size and the quality of the pattern.

During the test, the cameras were triggered every four seconds, while the specimen was deforming until its final breakage. At the same time, the analogue signal of strength and machine displacements were recorded, obtaining the synchronization between the testing machine and the DIC system.

8.2.4 Experimental data-analysis methods

The behaviour of the specimen was analyzed from two different perspectives using DIC, one is the frontal one, where the strains are analyzed on the CFRP and the second one, is the lateral (side view), where the longitudinal strains field into timber are studied (see Figure 3). The reason for using two perspectives arose from the necessity to analyze the strain interactions between timber and CFRP under the same set-up and load conditions [199]. Longitudinal strains were acquired from the DIC software [171], using the frontal and side views of the specimen, whereas the selected points were defined within mid-width of the CFRP (frontal view) and along the bond line surface (side view), equally spaced from 25 mm to 25 mm, (see Figure 8.3). The complex behaviour of specimens due to the test set-up is captured in Figure 8.3-right, where the starting bonded end of the specimen is moving in the plane perpendicular to the applied load direction, which implies bending deformation as for a cantilever beam.

DIC technique besides the strain field analysis is a proper research tool for the displacement field distribution. Therefore, the relative displacement or the slip between CFRP and timber can be easily computed. The first point corresponding to the bonded area, (e.g. P2) and the last point located on the timber surface (e.g. P10) have been chosen for the computation of relative displacement calculated directly by the software. The side view analysis permits obtaining the specimen behaviour due to timber-CFRP interaction and strain distribution through the timber section. Because the composite material (CFRP) has a significantly reduced thickness compared to the timber section, the DIC technique allows acquiring information only from the lateral timber surface. To get the information influenced by the CFRP, the longitudinal strains were acquired from a set of points located closely to the bond line (Figure 8.3-right).

8.3 Results and Discussions

The experimental force-slip relations, longitudinal strain distributions, and maximum loads are analyzed for all specimens employing the digital image correlation (DIC) technique. The load slips relations and longitudinal strains fields were measured from both perspectives. All the specimens were tested until the complete debonding of the

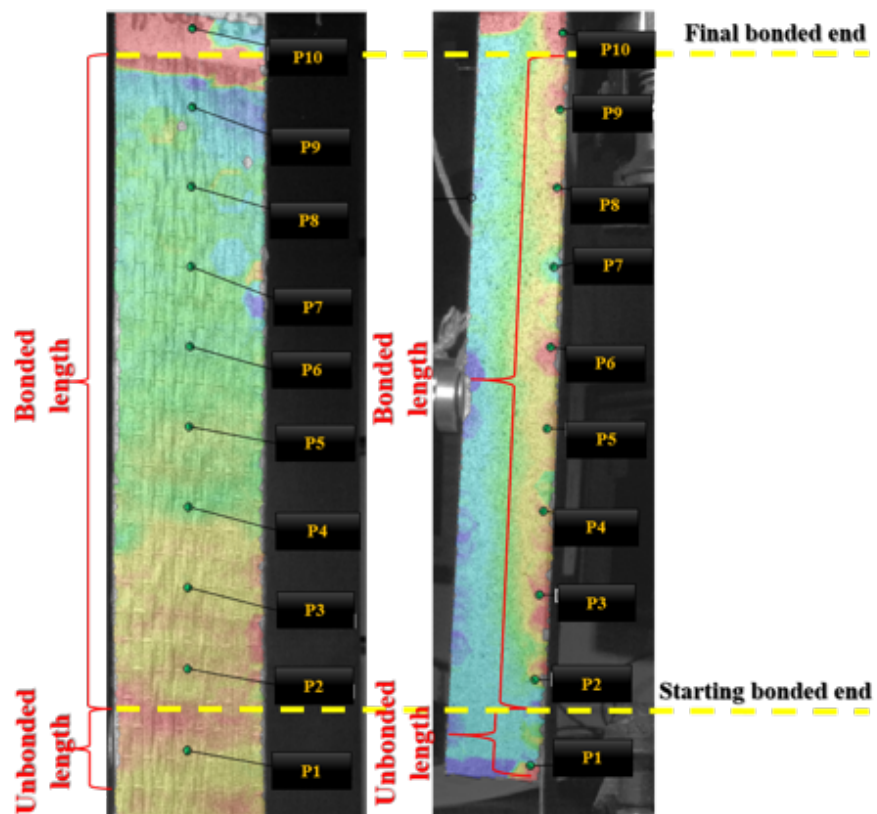


Figure 8.3: Longitudinal strain distribution in frontal view (left) and side view (right) in GOM Correlate software [171].

interface.

8.3.1 Results for 200 mm bond length

Figure 8.4 shows the DIC longitudinal strain fields for each representative specimen of CF, CF2 and CL at frontal and side views before failure. It can be seen clearly the correlation between strain and the different stiffness of the reinforcing material, noticing the homogeneous strain field in the case of the CL reinforcement.

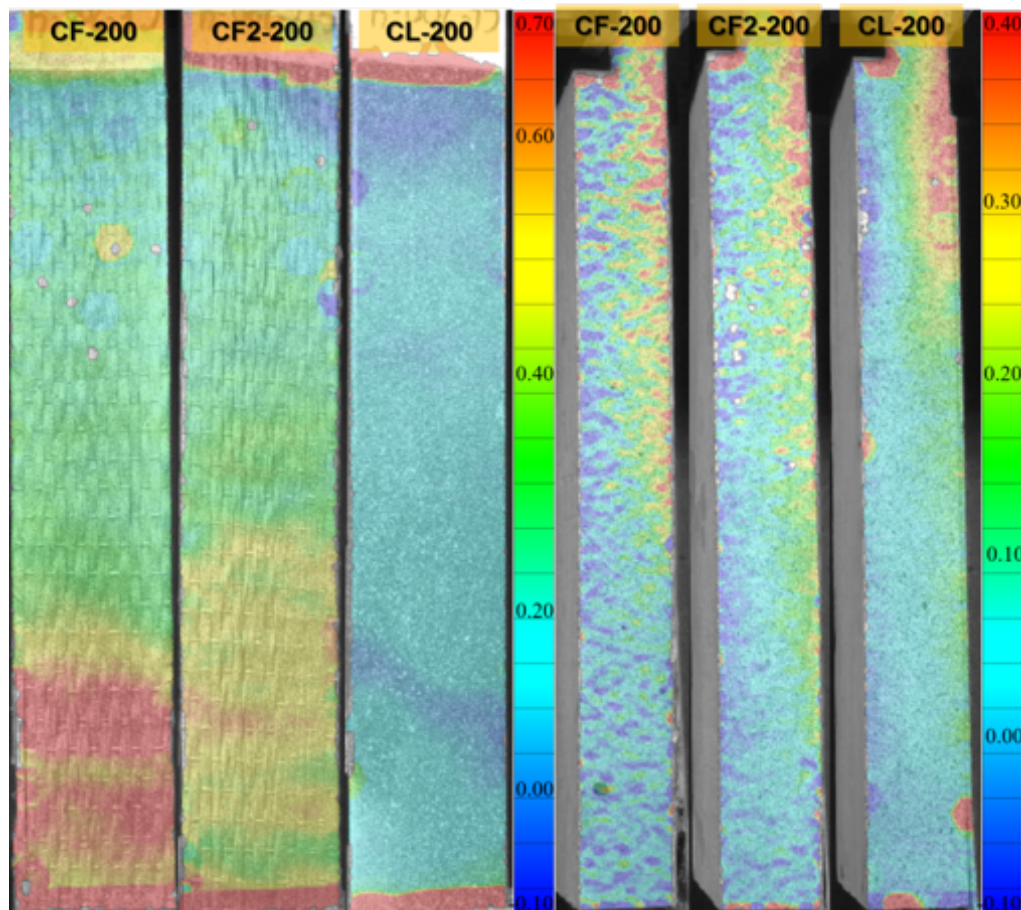


Figure 8.4: Longitudinal strain field from frontal (left) and side (right) views for the specimens with 200 mm bond length.

Due to the experimental set-up (see Figure 8.1), the starting bonded end of the timber block is free to move along the transversal direction which induces an additional bending moment in the top clamping area. This moment enforces that the tensile stresses are transferred to the stretched fibre of the specimen in the area of the composite section near the clamp. This effect is visible for the CL-200 specimens, where the local strains concentrations are captured in the side view at the final bonded zone of the composite (Figure 8.4-right) due to the sudden transition between the high stiff composite section and the timber section. The position of the neutral axis can be identified in the figure and located at the limit between positive and negative strains. The high strain at the final bonded end due to the stiffness differences between both materials produces for CL-200 high stresses and, consequently, a quick debonding towards the opposite side is developed. Counter to this behaviour is the CF-200 and CF2-200

specimens, where the debonding initiation is onset at the beginning of the bonded area. This behaviour is generated by its low stiffness and the adjustment of the fabric layer to the deformed shape of the timber block. Therefore, a low stiffness means a low-range strains transmission, generating a high strains concentration at the initial part of the bonded length. The debonding process for all three specimens is caused by the shear stress (in-plane stress) developed in different locations, as a consequence, of different stiffness of the CFRP. This different behaviour is identified in the strain distributions at both sides depicted in Figure 8.5 (top figures for frontal and bottom figures for side) for one representative specimen of each layout for different load levels.

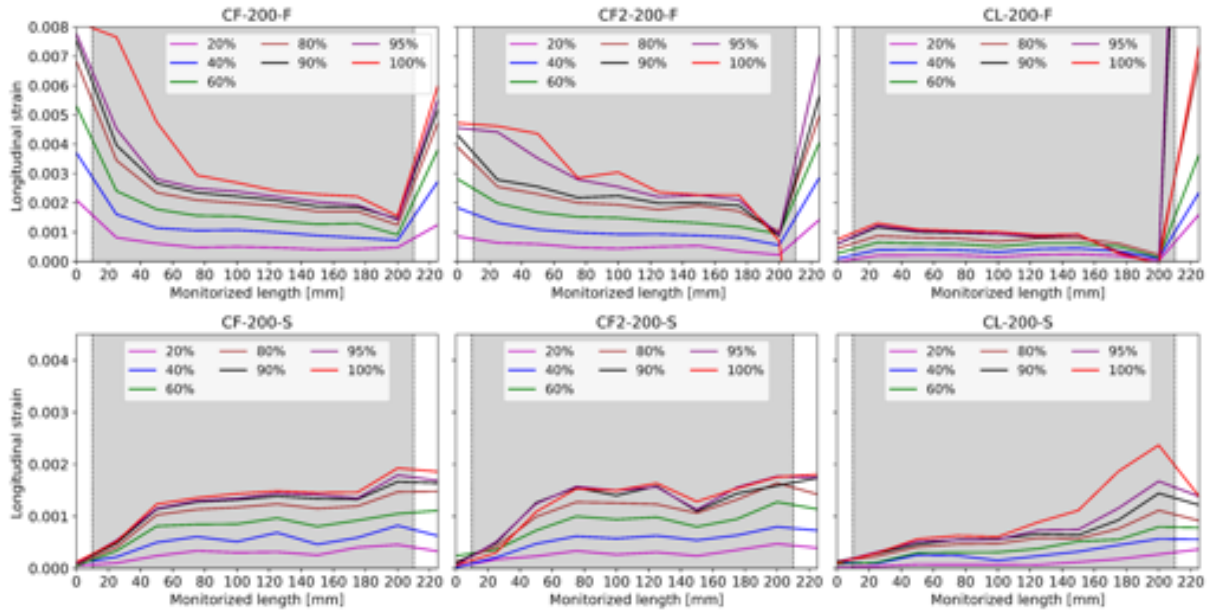


Figure 8.5: Evolution of the longitudinal strains of one representative sample with 200 mm bond length for different load levels in frontal (top) and side (bottom) views. The shaded area represents the limits of the bond length.

In Figure 8.5, the left part (starting bonded end) of the horizontal axis (10 mm) represents the limit between bonded and unbounded area, and on the opposite side (210 mm) is the final bonded end of the CFRP. The grey shaded area represents the bonded length. At the starting bonded end, a high strain concentration is visible for the CFRP (left in Figure 8.4 and top in Figure 8.5) due to the unbounded region, reaching maximum strains of 0.8% to 0.1% for CF and CL due to their lowest and highest stiffness respectively. Therefore, the strains in timber (right in Figure 8.4 and bottom in Figure 8.5) are almost negligible.

In frontal view analysis, the strains distribution in the bonded area differs for every layout. For CF-200, there is a sudden decrease in the strains, at the beginning of the bonded area, reaching an approximate plateau with a maximum strain value of around 0.3%. This decrease is also visible for the CF2-200, characterized by a smoother descending part, from 0.5% to a plateau with values similar to CF-200 specimens. For CL-200, a very homogeneous distribution is observed due to its pultruded nature.

Regarding the side view, the strains distribution in timber followed a mirror trend distribution like the ones from the frontal view analysis. It can be seen a significant increase of the longitudinal strains at the beginning of the bonded length followed by a constant strain range for the fabric layouts. While, for the CL-200 specimens, a

CHAPTER 8.

MULTI-SIDE DIC EVALUATION OF BONDED CFRP-POPLAR TIMBER

smoother steep behaviour increase is observed with an increase at the final bonded area. This effect is a clear indicator of a better transition of strains between both materials.

For the final bonded end, there is a sudden increase of the strains in the frontal view due to the transition between the composite section and the pure timber (red areas at the top of Figure 8.4). While on the side view, the strains are relatively homogeneous due to strain propagation through a pure timber section with reduced stiffness.

Figure 8.4 confirms these trends related to the strains distributions, where the strains are homogeneously distributed along the entire bonded length of CFRP to timber for the pultruded laminate specimens and for fabrics the strains are concentrated close to the starting bonded area. This behaviour is a consequence of the different axial stiffness of the CFRP layers.

The behaviour of the interface is characterized by the load-slip relations depicted in Figure 8.6 and the acquired results from frontal and side views are presented within the same plot. These relations show a clear linear and elastic part followed by sudden brittle or ductile failure. For the elastic part, the highest stiffness is observed for the CL-200 specimens and the minimum for CF-200, as expected with a difference between them of 53. As expected, the CF2-200 provides a stiffness value within the range of CF-200 and CL-200, but with a behaviour closer to the CL-200 specimens. For the plastic behaviour, the CL-200 provides the highest ductility, since their high stiffness of the CFRP produces a progressive debonding due to the homogeneous strain distribution observed in Figures 8.4 and 8.5.

For the specimens with carbon fabric strips, the plastic behaviour is almost not observable with only one sample showing this ductile pattern. However, most of the specimens show brittle behaviour due to the sudden debonding caused by the concentration of strains at the beginning of the bonded area.

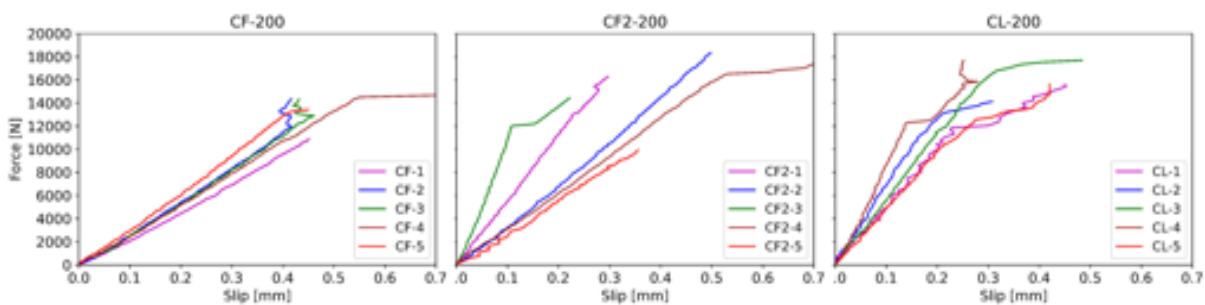


Figure 8.6: Force-slip relations for the specimens with 200 mm bond length.

Table 8.3 summarizes the most representative results related to the specimens with 200 mm bond length and their mean values. As observed also in the plots, the specimens with the laminate (CL) have reached the maximum applied force being 15% and 5% higher than CF and CF2 layouts. Consequently, CL specimens had the lowest values in terms of longitudinal strains, due to their higher stiffness. The CF-200 specimens achieve the highest longitudinal strains values with a mean value around 0.45%, being two times than CF2-200 and CL-200 specimens in accordance with their slips achieved. Regarding the interface stiffness, computed as the slope of the elastic range, the CL layout achieved a 34% and a 114% increase with respect to CF2 and CF specimens, respectively.

Specimen name	Max. longitudinal strain [%]	Max. applied force [kN]	Interface Stiffness [kN/mm]
CF-200-5 – F	0.80	13.4	32.2
CF-200-4 – F	0.89	16.7	26.3
CF-200-3 – S	0.16	14.7	28.5
CF-200-2 – S	0.21	14.5	28.3
CF-200-1 – S	0.19	10.9	24.2
MEAN	0.45	14.0	27.9
CF2-200-5 – F	0.25	9.9	27.9
CF2-200-4 – F	0.45	17.6	30.6
CF2-200-3 – S	0.05	14.4	78.7
CF2-200-2 – S	0.16	18.3	35.5
CF2-200-1 – S	0.24	16.3	50.4
MEAN	0.23	15.3	44.6
CL-200-5 – F	0.13	15.6	45.7
CL-200-4 – F	0.13	17.7	87.5
CL-200-3 – S	0.32	17.7	53.1
CL-200-2 – S	0.24	14.1	62.7
CL-200-1 – S	0.22	15.6	50.7
MEAN	0.21	16.1	59.9

Table 8.3: Maximum longitudinal strain applied force, interface stiffness and mean value based on load-slip relations for the specimens with 200 mm bond length.

8.3.2 Results for 150 mm bond length

Figure 8.7 displays the longitudinal strain distribution in frontal and side views analysis for the one representative specimen with 150 mm bond length. The longitudinal strains distributions are similar to the ones with 200 mm bond length, with strain concentration near the transition between unbounded and bonded area for CF and with a homogeneous distribution along the CFRP surface for the CL specimen (Figure 8.7-left). As well as for the specimens with a 200-bond length, the strain distribution for the side view revealed an identical behaviour along the bond line for CF and CF2. While for CL specimens, the strains are concentrated within the timber range in between clamps and the final bonded end. In this case, most of the longitudinal strains are dissipated by the timber section (Figure 8.7-right).

As well, the longitudinal strain distribution is revealed in Figure 8.8, where the strain relationships are presented at different load levels. In this case, the end of the CFRP is at a distance of 160 mm.

As Figure 8.8 shows, the general trend is similar to the ones presented for the specimen with a 200 mm bond length (Figure 8.5). Nevertheless, the maximum amplitude of strains at the starting bonded end is significantly reduced compared with the specimens with 200 mm bond length. It is worth mentioning, that for this case, the maximum amplitude is found for CF-150 and CF2-150, being around 0.45% (Figure 8.8-top). While for the CL-150, the amplitude is significantly reduced, around 0.1%, a comparable value with the one corresponding to the CL-200 specimen. In this case, for a lower maximum amplitude, the descending branch is smoother for the CF-150 and CF2-150 specimens, while for the CL-150 is a constant range variation from the starting bonded

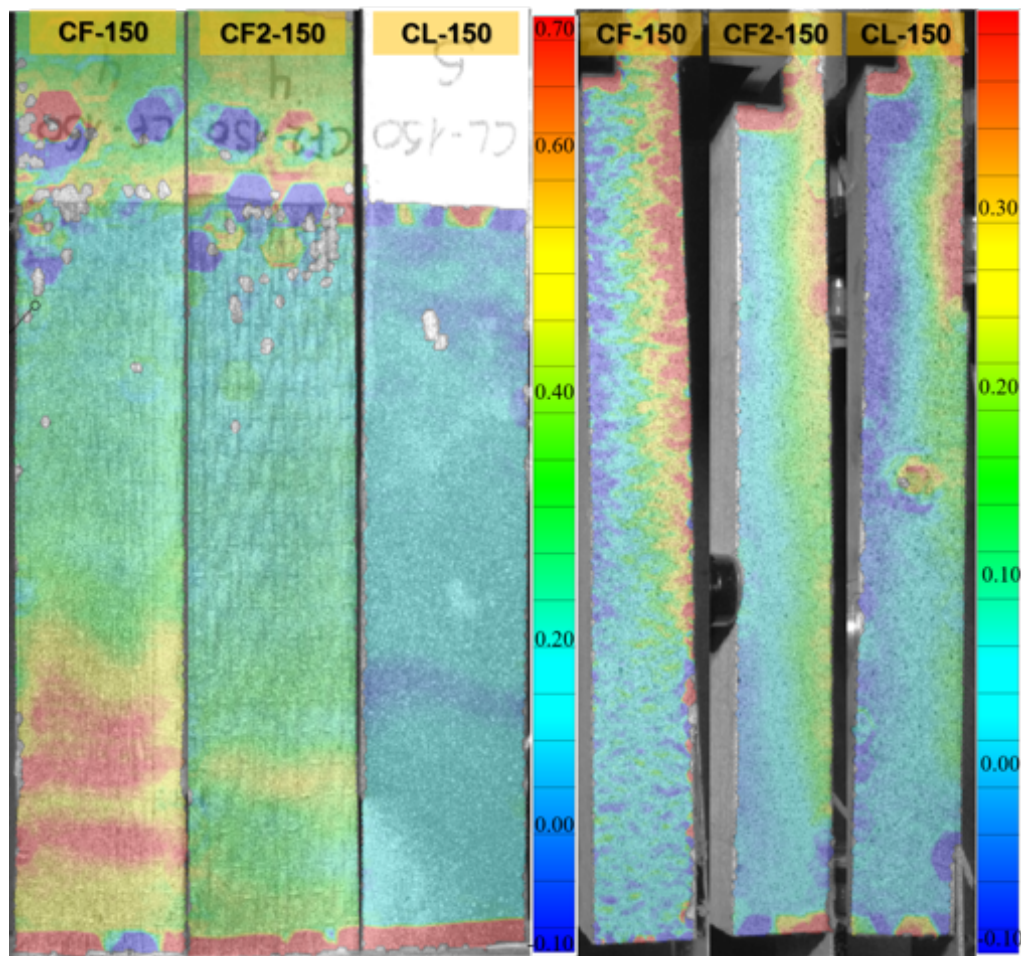


Figure 8.7: Longitudinal strain field from frontal and side views analysis for the specimens with 150 mm bond length.

area up to 100 mm length, near the final bonded end.

The longitudinal strains in timber follow the same trend as for the specimen with 200 mm bond length, with a shorter plateau range for CF-150 and CF2-150 but with a similar ratio unit of the length of plateau per bond length as for the specimens with 200 mm. For the CL-150 specimen, the strains are considerably reduced with a remarkable homogeneous behaviour even though for high loads levels, remaining under the 0.15%. As well, the longitudinal strains are dissipated through the timber section from the final bonded end up to the block edge.

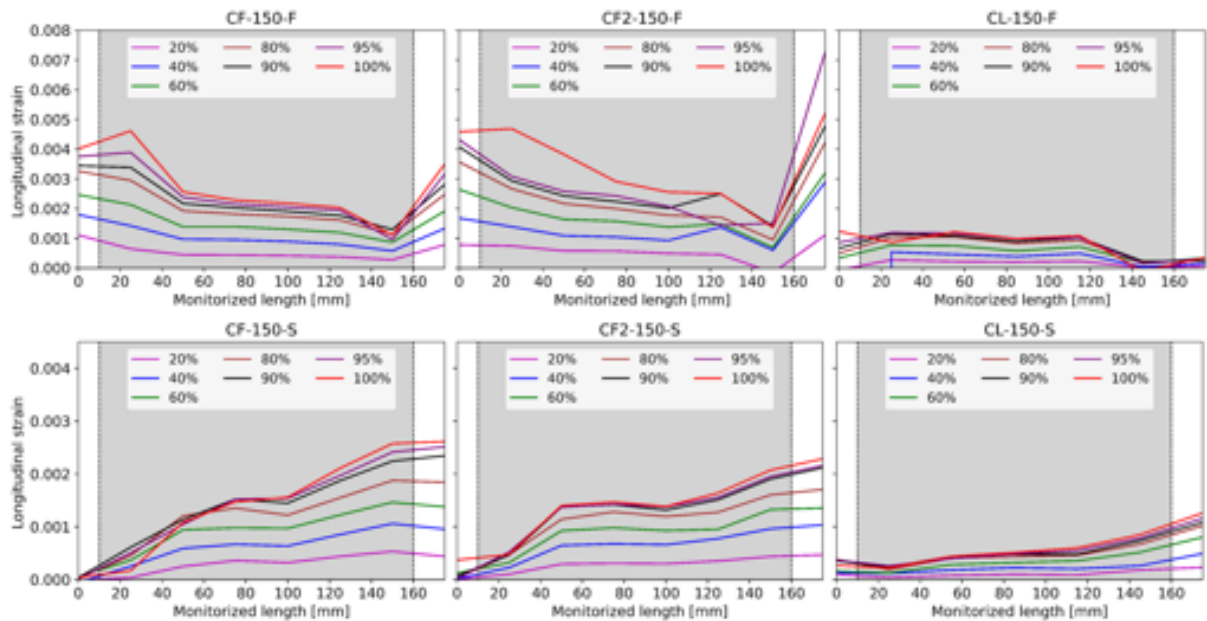


Figure 8.8: Evolution of the longitudinal strains of one representative sample with 150 mm bond length for different load levels in frontal (top) and side (bottom) views. The shaded area represents the limits of the bond length.

The load-slip relations are presented in Figure 8.9. At first sight, the lowest stiffness as expected is certainly for the CF-150 specimens, followed by the CF2-150 and the CL-150 specimens being 33% and 109% higher, respectively. These improvements are similar to those obtained for a bond length of 200 mm.

The plastic behaviour is not visible for the CF-150 specimens, while for CF2-150 and CL-150 specimens, several isolated specimens exhibited a short plastic state (Figure 8.9). Therefore, an appropriate remark related to ductility and elasto-plastic behaviour cannot be drawn.

As can be seen in Table 8.4 and Figure 8.9, in terms of maximum capacity, the CL-150 and CF2-150 specimens are very close to each other, with a difference of 0.1%.

8.3.3 Results for 100 mm bond length

For the CL-100 specimens, the longitudinal strain distribution is completely homogeneous as for the 150 mm and 200 mm bond length (Figure 8.10-left). While for the CF and CF2 specimens, the strain distributions are mostly identical, with local concentration points at the CFRP surface, on the half of the bonded surface. The upper part of the bonded area is mostly homogeneous. In the side view (Figure 8.10-right), for the CF specimen, a high strain concentration in timber is captured by the DIC along the

CHAPTER 8.

MULTI-SIDE DIC EVALUATION OF BONDED CFRP-POPLAR TIMBER

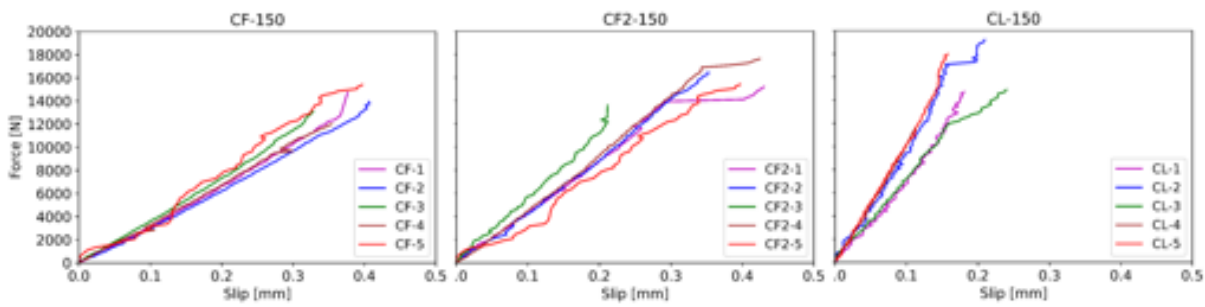


Figure 8.9: Force-slip relations for the specimens with 150 mm bond length.

Specimen name	Max. longitudinal strain [%]	Max. applied force [kN]	Interface Stiffness [kN/mm]
CF-150-5 – F	0.41	15.4	41.2
CF-150-4 – F	0.47	12.0	33.9
CF-150-3 – S	0.22	13.3	38.5
CF-150-2 – S	0.26	13.9	32.5
CF-150-1 - S	0.16	14.7	34.5
MEAN	0.30	13.9	36.2
CF2-150-5 – F	0.42	15.4	40.7
CF2-150-4 – F	0.48	17.6	48.7
CF2-150-3 – S	0.15	13.6	57.5
CF2-150-2 – S	0.21	16.5	46.9
CF2-150-1 – S	0.65	15.2	47.2
MEAN	0.38	15.7	48.2
CL-150-5 – F	0.12	18.0	82.1
CL-150-4 – F	0.08	11.7	78.2
CL-150-3 – S	0.16	14.9	70.5
CL-150-2 – S	0.12	19.2	78.5
CL-150-1 - S	0.13	14.7	69.8
MEAN	0.12	15.7	75.8

Table 8.4: Maximum longitudinal strain applied force, interface stiffness and mean value based on load-slip relations for the specimens with 150 mm bond length.

entire bond line and the entire poplar box. While, for the CF2 and CL layouts, the amplitude and the propagation length of the tensile strains are reduced. For the CL specimen, a high concentration of strains can be observed around the end of the FRP bonded area, behaviour not observed in the samples with a bond length of 150 mm.

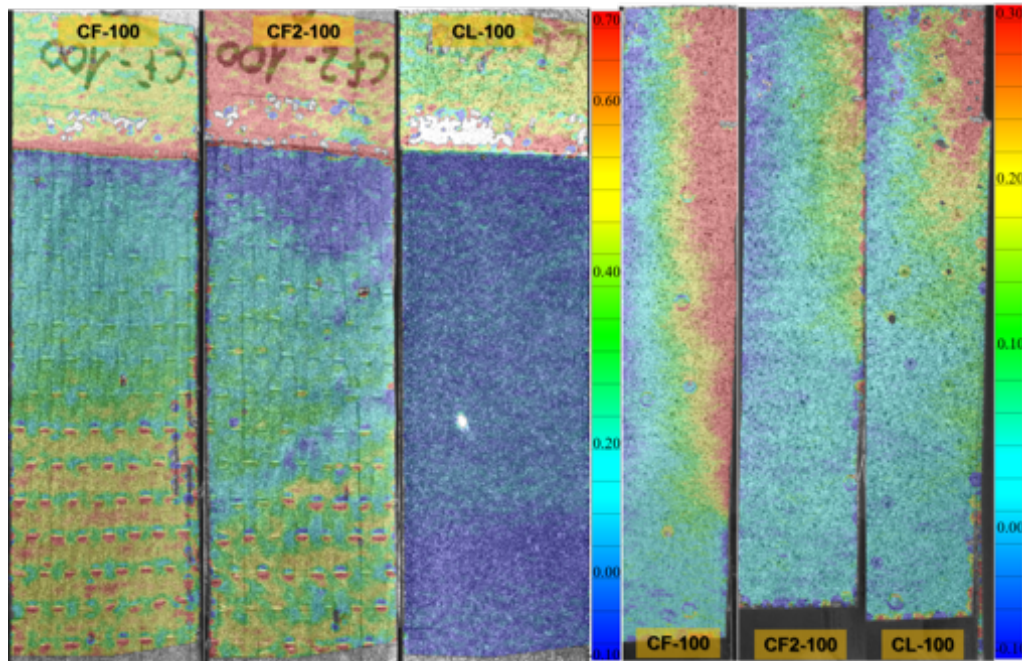


Figure 8.10: Longitudinal strain field from frontal and side views analysis for the specimens with 100 mm bond length.

The strain behaviour in the CFRP and timber is presented in Figure 8.11, in frontal and side views for all three specimens. The general longitudinal strain distributions are similar to those with 150 mm and 200 mm bond lengths. However, for these specimens, it is important to be mentioned that the strains are concentrated in a smaller area; therefore, a high strain variation is observed. The CF layout reveals a similar behaviour to specimens with a bond length of 200 mm. However, CF2-100 specimens are closer than specimens with 150 mm of bond length. For the case of the CL layout, side view (strains in wood), it is remarkable that for this case, the strains follow a continued increase, reaching values around 0.2%, double than the CL-150 specimens.

Figure 8.12, shows the force-slip relations for all of the specimens with 100 mm bond length. For most of the specimens, the behaviour is purely elastic, characterized by a brittle failure and for the specimen, with the lowest stiffness (CF) a short plastic behaviour is identified for two samples. As seen, the highest interface stiffness is observed for the specimens with the highest axial CFRP stiffness, CL-100, followed by CF2-100 and CF-100, with a difference of 38% and 91%, respectively. As Table 8.5 shows, for this bond length, the maximum applied force was very similar for the three layouts. In addition, the maximum longitudinal strains for the CL specimens were more than two times higher compared to the bond lengths of 150 and 200 mm. This may lead to the fact that for this type of FRP, a length of 100 mm may be insufficient to achieve good bonding between the two materials.

CHAPTER 8.
MULTI-SIDE DIC EVALUATION OF BONDED CFRP-POPLAR TIMBER

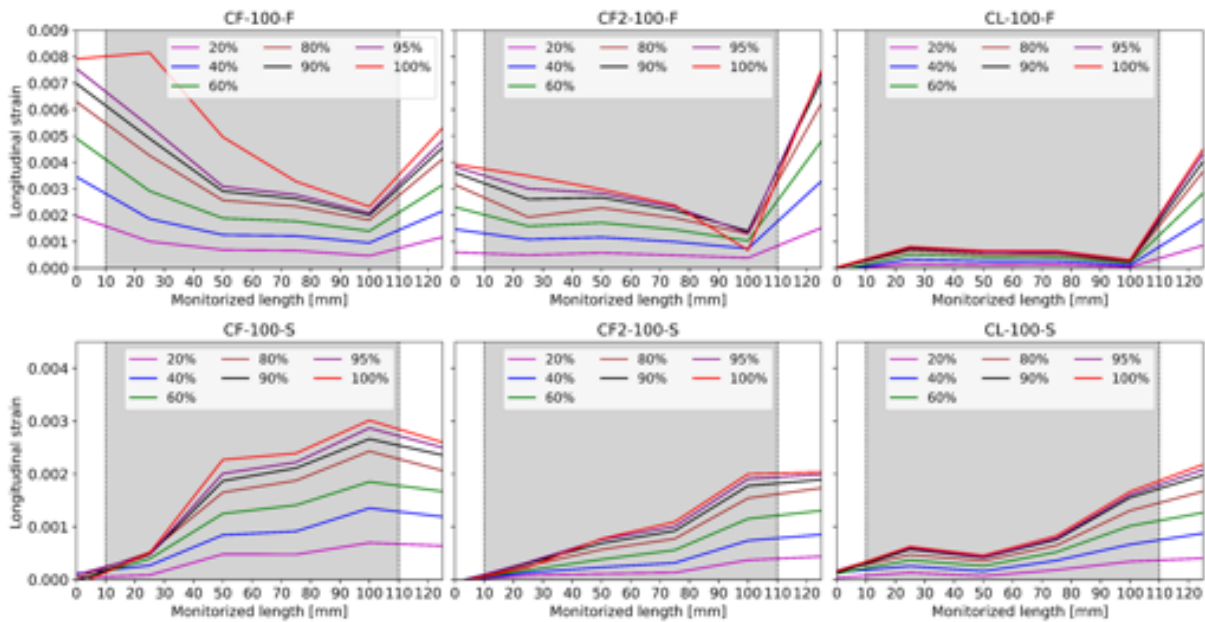


Figure 8.11: Evolution of the longitudinal strains of one representative sample with 100 mm bond length for different load levels in frontal (top) and side (bottom) views. The shaded area represents the limits of the bond length.

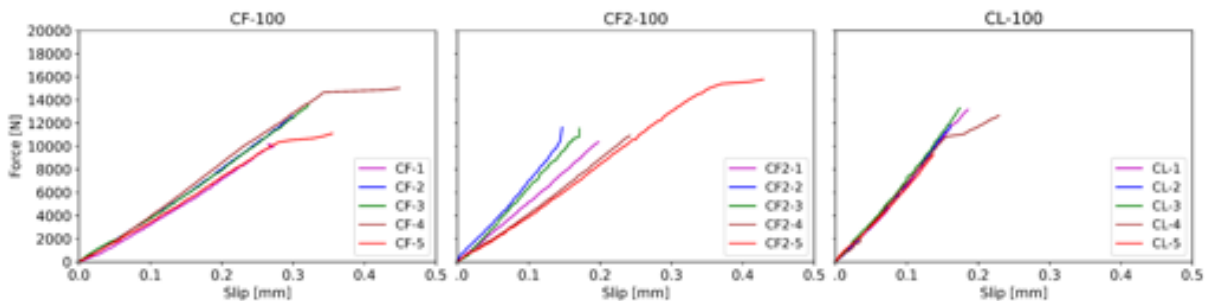


Figure 8.12: Force-slip relations for the specimens with 100 mm bond length.

Specimen name	Max. longitudinal strain [%]	Max. applied force [kN]	Interface Stiffness [kN/mm]
CF-100-5 – F	0.58	11.1	37.8
CF-100-4 – F	0.90	15.0	42.9
CF-100-3 – S	0.40	13.5	42.2
CF-100-2 – S	0.57	12.6	40.4
CF-100-1 – S	0.30	10.2	37.9
MEAN	0.55	12.5	40.2
CF2-100-5 – F	0.40	15.8	42.5
CF2-100-4 – F	0.18	10.9	45.1
CF2-100-3 – S	0.16	11.5	65.9
CF2-100-2 – S	0.17	11.6	71.5
CF2-100-1 – S	0.20	10.4	52.5
MEAN	0.22	12.0	55.5
CL-100-5 – F	0.85	9.3	67.7
CL-100-4 – F	0.83	12.6	80.9
CL-100-3 – S	0.27	13.3	77.9
CL-100-2 – S	0.19	11.8	74.2
CL-100-1 – S	0.25	13.2	83.9
MEAN	0.48	12.0	76.9

Table 8.5: Maximum longitudinal strain applied force, interface stiffness and mean value based on load-slip relations for the specimens with 100 mm bond length.

8.3.4 Results for 50 mm bond length

The frontal and side views show a high strain concentration for the fabric (CF and CF2) along the entire bond length, while for the laminate (CL) the strain is homogeneous distributed along the bonded surface (Figure 8.13). In the side view, the longitudinal strain is distributed only in the timber surface mainly after the bonding length of the CFRP, and covering all the length of the timber box. Only for the CL specimens, a tensile strain concentration is observed around the bonded end area. This continuous distribution of tensile strains can be a clear indicator of a lack of bond length, leaving the remaining wood to bear the full mechanical stress.

The strain relation distributions presented in Figure 8.14, are characterized by a similar trend as the previous ones, but with the lowest strain amplitude for the frontal perspective. For the side view, the variation is constantly increasing from the load-end to the final bonded end, as can be identified also in Figure 8.13.

As well, the behaviour of the specimens with 50 mm bond length is completely linear for almost all of the samples, with comparable performance in terms of maximum applied force (Figure 8.15). The stiffness is almost the same for the CF2 and CL specimens, while a visible reduction of 29% is observed for the CF specimens with respect to the CL ones.

Table 8.6, depicted the experimental values for the specimens with the lowest bond length. As for the bond length of 100 mm, the mean maximum applied force obtained is very similar for the three layouts. The lowest stiffness is obtained for the CF speci-

CHAPTER 8.
MULTI-SIDE DIC EVALUATION OF BONDED CFRP-POPLAR TIMBER

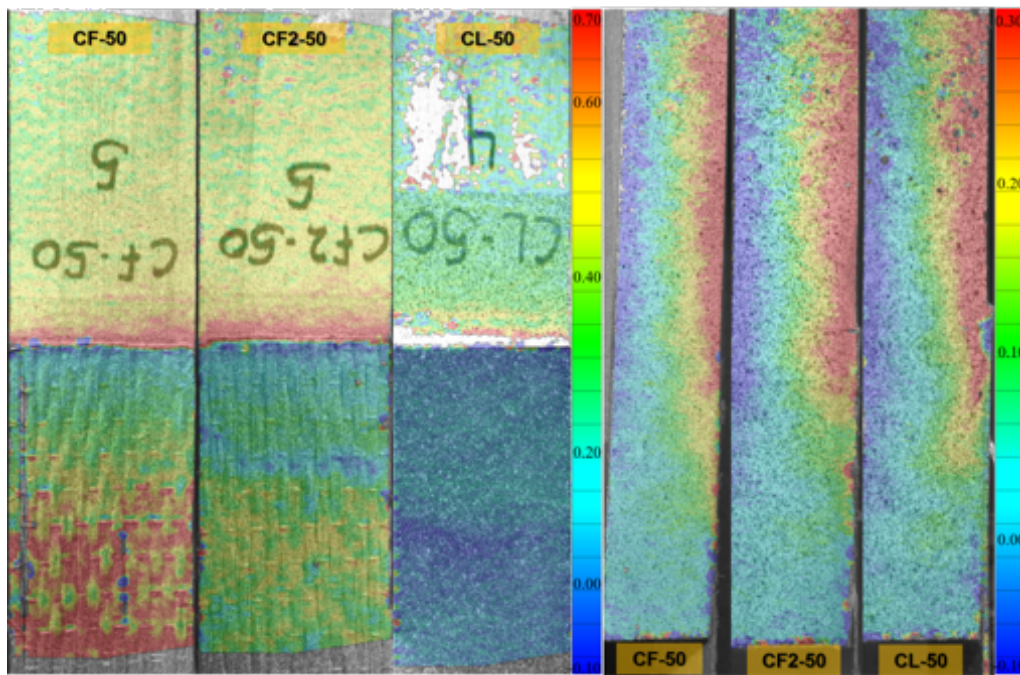


Figure 8.13: Longitudinal strain field from frontal and side views analysis for the specimens with 50 mm bond length.

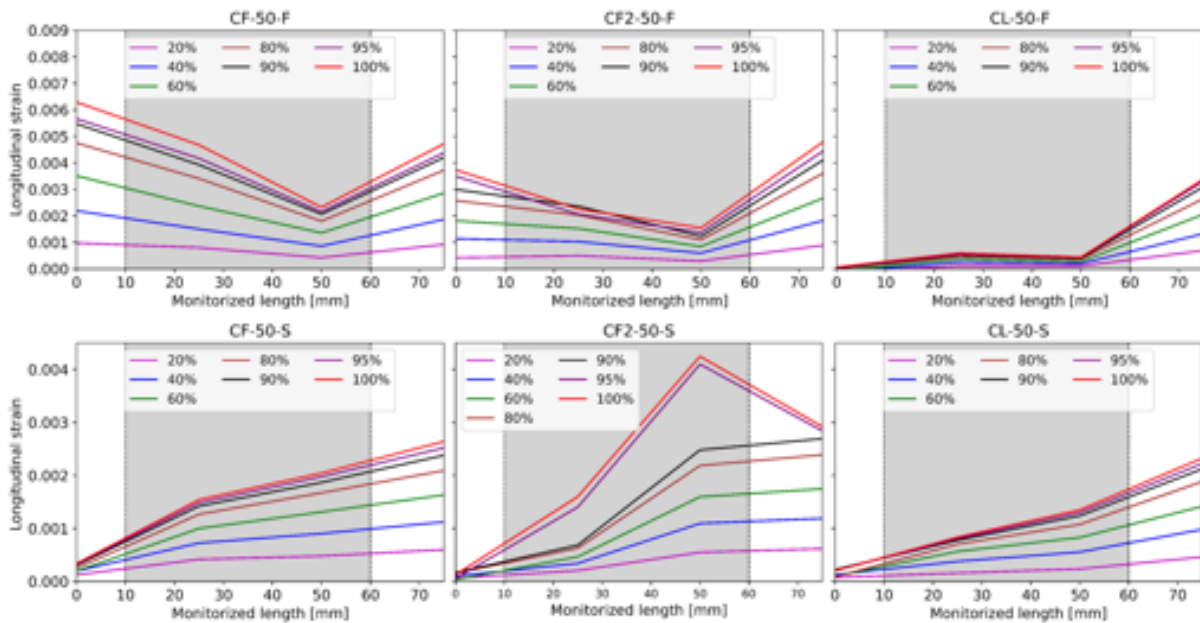


Figure 8.14: Evolution of the longitudinal strains of one representative sample with 50 mm bond length for different load levels in frontal (top) and side (bottom) views. The shaded area represents the limits of the bond length.

mens, which has also the highest mean strain amplitude.

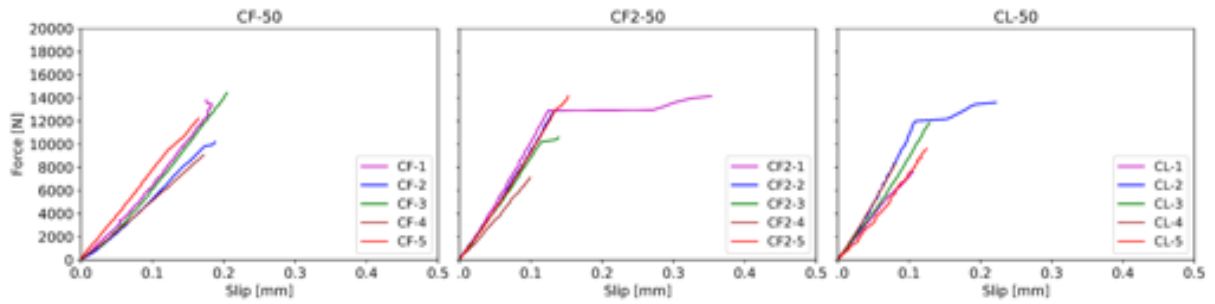


Figure 8.15: Force-slip relations for the specimens with 50 mm bond length.

Specimen name	Max. longitudinal strain [kN]	Max. applied force [kN]	Interface Stiffness [kN/mm]
CF-50-5 – F	0.42	12.2	74.9
CF-50-4 – F	0.62	9.1	52.7
CF-50-3 – S	0.23	14.4	70.6
CF-50-2 – S	0.23	10.2	56.7
CF-50-1 – S	0.20	13.8	72.2
MEAN	0.34	11.9	65.4
CF2-50-5 – F	0.38	14.3	96.3
CF2-50-4 – F	0.20	7.1	71.9
CF2-50-3 – S	0.23	10.6	88.7
CF2-50-2 – S	0.20	12.8	96.4
CF2-50-1 – S	0.35	14.2	104.7
MEAN	0.27	11.8	91.6
CL-50-5 – F	0.03	9.8	78.6
CL-50-4 – F	0.06	8.3	103.2
CL-50-3 – S	0.17	11.9	92.3
CL-50-2 – S	0.28	13.6	110.2
CL-50-1 – S	0.18	7.6	72.0
MEAN	0.15	10.2	91.3

Table 8.6: Maximum longitudinal strain applied force, interface stiffness and mean value based on load-slip relations for the specimens with 50 mm bond length.

8.3.5 General behaviour

Figure 8.16 summarizes the results for the main experimental parameters studied in this paper as a function of the bond length. It is important to remark that the ultimate load corresponds to the debonding failure.

Similar behaviour for the CF2 and CL specimens is observed in terms of maximum applied force. As expected, the maximum applied force has increased with the increase of the bonded length. It is also observed that for the shortest bonded length, 50 mm, the mean maximum applied force is higher for the CF specimen, which emphasizes the lack of bonding length. In terms of interface stiffness, the value decreases as

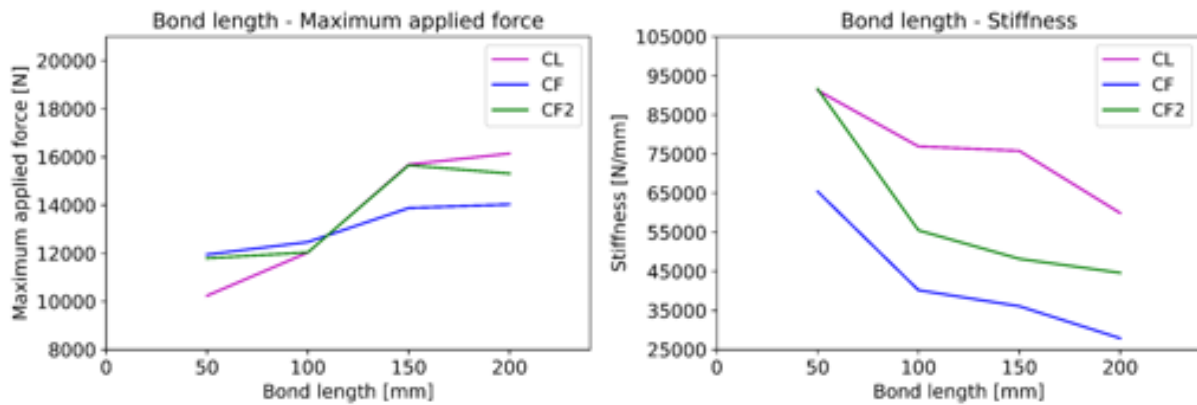


Figure 8.16: Mean maximum applied force and mean interface stiffness variation.

the bonded length increase. Therefore, there is a clear correlation between the bigger length and more flexible capacity of the specimens, something desirable for bending purposes. It is important to note that, while there is a noticeable increase in applied force between the 100 and 150 mm bond lengths, the stiffness is very similar for both cases.

Frontal view discussion

Figure 8.17 shows a general longitudinal strain pattern along the mid-width of the CFRP for the frontal view analysis and the evolution of the strains captured by DIC.

For this situation, the only aspect that can be analyzed is the behaviour of the composite (CFRP) taking into account the interactions with timber. Figure 8.17-top, depicts the important areas from the frontal view, where the left part corresponds to the unbounded area, where CFRP is being pulled. After the unbounded area, the CFRP is bonded to the timber surface; hence, the CFRP and timber are working together. Consequently, there is an increase in the stiffness of the composite section (CFRP + timber) and the stresses are transferred to CFRP through a transfer length [201,202]. Figure 8.17-bottom, shows the general longitudinal strain evolution during the experiment until initiation of the debonding. For low and medium load levels, up to 40% load rate, the longitudinal strains are constantly increasing, having a homogeneous distribution along the bond line. Since the load rate is overcoming 50%, the transfer zone (transfer length) starts to be visible. For a higher load rate (up to 90-95%), the strain relation, reveals a high non-linear behaviour along the bond line. For the last step before failure (95-100%), the relation at the left side defines a short constant plateau with a high strain value, which indicates that the CFRP was debonded, therefore the strains are carried out only by the CFRP. The second part of the relation, defined a steep descending branch, followed by a short-range with constant values. On the right side, the longitudinal strain has a high value corresponding to the timber section.

Frontal view discussion

Figure 8.18, depicts the key areas characteristic for the side analysis and its longitudinal strain distribution. Even though the specimen is working under the same loading condition as the ones from the front view analysis, the strain pattern is completely different. At the left end of the specimen, the unbounded area between CFRP and timber,

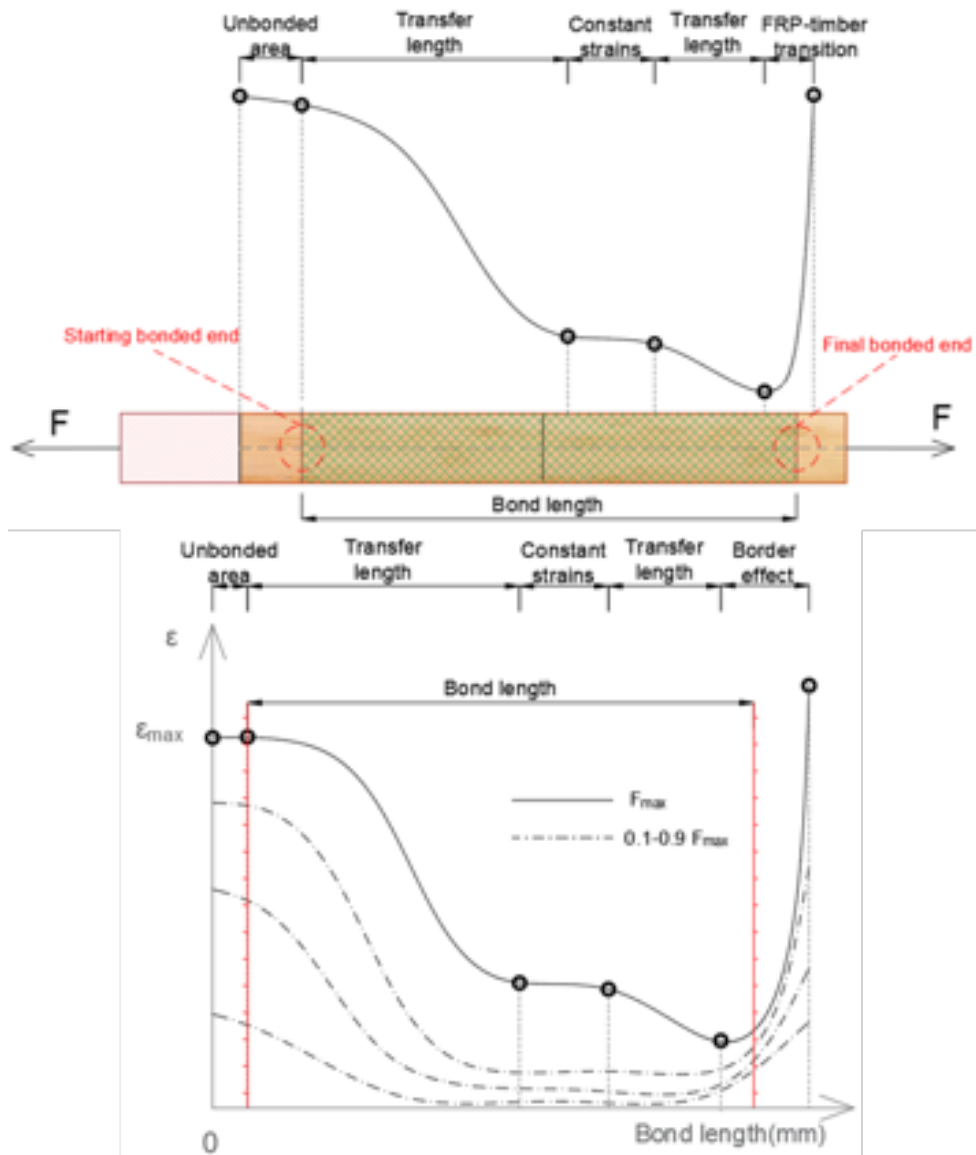


Figure 8.17: Longitudinal strain distribution within CFRP acquired frontal view analysis (top). Longitudinal strain evolution under loading conditions (bottom).

CHAPTER 8.

MULTI-SIDE DIC EVALUATION OF BONDED CFRP-POPLAR TIMBER

the load is applied directly to the CFRP layer, therefore no strain is transmitted to the timber section

Figure 8.18-bottom shows the general strain evolution during the experiment until the start of the debonding. The corresponding strain pattern for low and medium load levels is defined by a homogeneous distribution along the bond line, which strives to zero in the unbonded area (left side). While the load rate is increasing, the relation initiates a non-linear behaviour, which becomes well marked for a high load rate (80%-95%). The highest longitudinal strains in the timber surface are captured near the final bonded end of the specimen, due to the bending moment produced by the axial force. As well, in this region, the strains are only carried out by the timber section and then, the tensile strains are propagated through timber in a parallel direction with the bond-line, towards the starting bonded end, where the strain in timber is close to zero.

For short bonded lengths, 50 mm and 100 mm, the tests revealed high strains concentration within the timber located between the final bonded end and clamps of the machine, which enforce the failure of the specimens to be triggered from the final bonded end to the starting bonded end side. This behaviour is captured by the force-slip relations, outlined by a perfectly linear variation and a reduced slip value. For the specimens with 150 mm bond length, a transitional behaviour between the specimens with the shortest ones and the longest ones.

Due to the experiment set-up, complex behaviour is observed rather than in other experimental references. A particular behaviour is observed for this test set-up, where a decrease of the strains appears, which does not reach zero in any part of the CFRP. In addition, after the first descending part, the strain follows a plateau, and then a second descending branch is observed in the final bonded area location. This second descending branch corresponds to a second transfer zone of the strain located in the final bonded end of the specimen. Thus, the experimental set-up implies two-transfer zone lengths, one located in the starting bonded end and the second one developed in a subsequent step.

The variations of the maximum force and interface stiffness are presented in Table 8.7. As expected also in the above relations and plots, the highest improvement in terms of maximum force is obtained for the CL-200 specimen, while the second improvements are gained for the specimen CF2-150 and CL-150. This similar improvement is explained by the fact that the bond length has reached an effective value (effective bond length), which no longer allows a higher capacity to be achieved. Then, specimens with a lower bonded length decrease with the same trend as their maximum force.

It is worthy to be mentioned that the lowest reduction is observed for the specimen with laminate (CL-50) being in contrast with the maximum improvement obtained by the laminated specimen (CL-200), probably associated with the tensile strain concentration observed in this specimens.

Regarding the stiffness variations, two trends are depicted in Table 8.7. Hence, the interface stiffness is increasing with the reduction of the bonded length for the specimen with the same type of reinforcement. For instance, the laminate specimens (CL) are constantly increasing from 115% for 200 mm bonded length, up to 227% for 50 mm bonded length. This trend is valid also for the specimen with fabric (CF and CF2). The increase of axial stiffness of the reinforcement provides an increase of the interface of stiffness between fabrics around two times for all of the bonded lengths. Since the variation between two layers of fabric and laminate is clearly higher for the

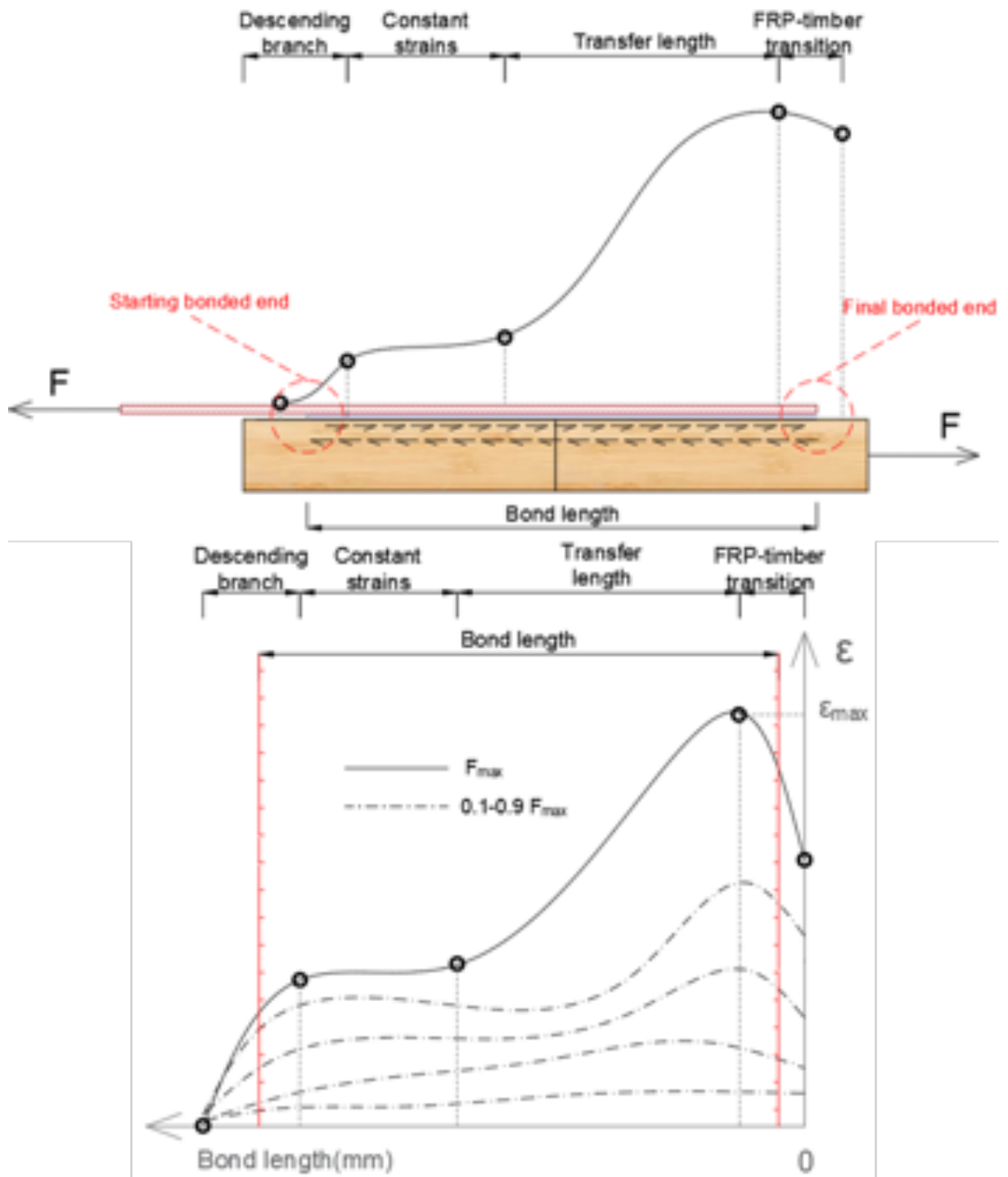


Figure 8.18: Longitudinal strain distribution within timber acquired side view analysis (top). Longitudinal strain evolution under loading conditions (bottom).

CHAPTER 8.

MULTI-SIDE DIC EVALUATION OF BONDED CFRP-POPLAR TIMBER

CL specimens, while for the shortest bonded length (50 mm) the values are almost identical.

Specimen name	Δ -Force (%)	Δ -Stiffness (%)
CF-200 - Control specimen		
CF2-200	9	60
CL-200	15	115
CF-150	-1	29
CF2-150	12	73
CL-150	12	172
CF-100	-11	44
CF2-100	-14	99
CL-100	-14	176
CF-50	-15	134
CF2-50	-16	228
CL-50	-27	227

Table 8.7: Mean maximum applied force (Δ -Force) and interface stiffness (Δ -Stiffness) differences with respect to the control specimen (CF-200) in percentage.

8.4 Conclusions

The digital image correlation (DIC) technique is a powerful tool that permits to analyze the strain distributions in solids. The behaviour of timber specimens reinforced with CFRP is complex due to its non-linear interface. In this work, the single shear test has been applied with the boundary conditions that permit the specimens to bend and deform axially similar to the members subjected to service working loads. Therefore, more complex behaviour is observed than in other experimental references due to the cantilever behaviour of the specimen. DIC allows gaining knowledge in this behaviour frontal and side views of the specimens. The strain distributions observed in both views emphasized a different strain distribution onto CFRP and timber layer. Thus, the strain relations of analyzed views are mirrored along the bond-line, with peak values corresponding to the timber section due to its reduced stiffness compared with the composite section and reinforcement.

The DIC analysis shows that the behaviour is closely related to the bonding length and type of the CFRP reinforcement. These parameters modify the stiffness of the specimen along its length. For specimens reinforced with a single layer of fabric, the improvement in the global stiffness is reduced due to the capability of the fabric to adapt to the deformations of the timber-producing high concentrations of stresses. When the thickness of the reinforcement is increased, the increase in the stiffness of the specimen is noticeable and the strain distribution in both CFRP and timber becomes homogeneous and smaller.

The bonding length also plays an important role in the stiffness. As the bonding length increases, the stiffness of the interface decreases, especially for CF due to its low contribution in the stiffness. While for CF2, the increase is intermediate between the CF and the laminate CL. The maximum load that a specimen can support is also

dependent on the type of reinforcement and bonding length. For short specimens, the specimens reinforced with fabric resist higher loads than those reinforced with laminate since the interface becomes brittle. However, for intermediate and high bonding lengths the opposite situation happens due to the homogeneous distribution of the strains produced by the high stiffness of the laminate that avoids the strain concentration and sudden failure of the interface.

Depending on the type of the reinforcement, two distinct locations of the failure have been observed, for the stiffest specimen, the failure is onset at the final bonded end and propagated to the starting bonded end. Since, for the specimens with fabric, the failure is triggered at the starting bonded end and a second debonding is started in the starting bonded end. Finally, as it was observed, the longest bonded lengths provide the lowest interface stiffness of the specimens, therefore high deformability of the specimens during the test is observed. This cantilever behaviour implies additional strain concentration in the timber fibres near the clamps, close to the final bonded end location, which enforces the detachment of the specimens at the final bonded end.

The application of DIC to boundary more complex conditions and complemented with finite element analysis is the next step that will permit to gain insights into the effective and accurate design of the reinforcement of structural members subjected to real service situations.

Chapter 9

Digital image correlation and numerical analysis of FRP-poplar timber interface subjected to single shear tests

Title	Digital Image Correlation and numerical analysis of FRP-poplar timber interface subjected to single shear tests
Authors	C. Timbolmas; R. Bravo; F.J. Rescalvo; P. Villanueva; M. Portela
Journal	Journal of Building Engineering
ISSN	2352-7102
Journal's performance	Journal impact factor (2020): 5.318 D1 (Civil Engineering: 13/137)
Details	Under review process

9.1 Introduction

Timber is a popular construction material, which has been widely used for several millennia. In the recent decade, it has also become a sustainable alternative for the structures of all building typologies (residential, hall sports, private houses, public infrastructures, etc.) because of its low carbon footprint, the environmental benefits associated with its nature characteristics and its structural efficiency [101]. Therefore, the study of the timber structures becomes an interesting research path to develop new innovative members, structural elements and hybrid joint connections, as well as strengthening and retrofitting solutions for the existing timber structures [100, 102]. In particular, the retrofitting with externally bonded (EB) fiber-reinforced polymers (FRP) composites represents a feasible and practical solution for timber structures, especially for the case of old existing ones that have reached the end of their design service life [136, 187, 203]. Additional reasons for employing externally bonded FRP materials to timber structures are related to inappropriate maintenance, fungal attack or environmental degradation which gradually result in a noticeable reduction in load capacity and subsequent safety; also, with these reinforcements, it is possible to increase the load-bearing capacity in case of new uses resulting in increased loads [119, 204]. The EB systems have their origins in reinforced concrete (RC) structures in the 1960s, and

currently, they are widely used for the retrofitting of the existing RC structures [205]. Even though at the beginning the external adhesion was used to apply steel plates, the FRP plates have been increasingly used to replace steel plates due to their remarkable mechanical properties and superior corrosion resistance. One of the most challenging aspects in the design of retrofitting solutions using external FRP plates is to determine the effective bond length and bond strength of the interface and to prevent premature debonding failure [179, 201, 206–208]. Thence, as debonding hinders the full utilization of the FRP strength, many research works have focused on these topics, implying single and double-shear tests as well as numerical modelling [107, 209, 210].

Comprehensive available literature related to the retrofitting possibilities using FRP in timber structures, especially in glulam and solid timber beams, is widely presented through large-scale research works revealing significant bending strength and stiffness improvement [113, 116, 117, 136, 211]. In the experimental work [125], the authors observed a noticeable stiffness and load capacity improvement up to 44% and 33%, respectively for different glulam beams with FRP embedded between the layers of glulam beams made with poplar lamella. In addition, the ductility and failure mode of the glulam poplar beams were analyzed for different FRP positions within the glulam section.

Recently, the study of the inter-facial performance, effective bond length and delamination have been extended from the concrete-to-FRP to timber-to-FRP specimens [180, 194, 212]. Extensive experimental works based on digital image correlation (DIC) and analytical/numerical works based on the finite element method (FEM) have been carried out using different bonded lengths and width ratios to determine the bond interface parameters, i.e. effective bond length and bond strength and debonding load [192, 207, 213].

The finite element method has been used for the analysis of bonded structures in combination with the strength of materials or with fracture mechanics-based criteria [186]. The strength of the materials approach is based on the evaluation of allowable stresses and strains by the theoretical formulations or by FEM [214, 215]. For this study, cohesive-zone models (CZMs) that model the interaction between lamellas have demonstrated to be an effective tool in recent years for modelling of damage evolution and fracture problems.

The development of non-contact optical methods has allowed researchers to employ the two-dimensional and three-dimensional digital image correlation (DIC) techniques to evaluate the inter-facial behaviour between FRP and concrete under different loading conditions and different bonded lengths [216]. DIC technique provides spatially continuous displacement fields during the evolution of damage along the bond interface. This method has been deeply applied to investigate fracture mechanisms in concrete and composites [196, 217, 218]. In order to have a clear understanding of the force transfer by the bond interface, a 3D optical displacement measurement is able to capture the full-field displacements from the front and side views for specimens subjected to shear tests [199]. To investigate the strain field on a surface, the use of strain gauges represents a traditional investigation method [191]. The gauges cannot obtain the full-strain field, providing values at single points, so the data between gages cannot be measured.

In this paper, an experimental and numerical analysis of the bonding of FRP to poplar I-214 timber specimens presented in section 9.2 is carried out using DIC for data acquisition and FEM for modelling under conditions that allow the bending and

the axial deformation as shown in subsection 9.2.3. This situation is a particular case of the experimental set-up compared to the available literature of the single shear test, in which the main timber block is always restricted in the perpendicular and longitudinal direction of the applied load. Hence, the experimental set-up considered within this study is reproducing a situation that is closer to the real working condition of the structural members. The DIC and FEM methodologies exposed in section 9.3 permit to contrast, analyse and discuss in section 9.4 the experimental and numerical behaviour of the specimens with different reinforcements at the frontal and lateral sides.

9.2 Materials and experimental set-up

9.2.1 Timber block, adhesive and composite material (FRPs)

An experimental campaign was conducted to analyse the behaviour of timber blocks reinforced with FRP. The timber used for the experimental campaign was extracted from a 9-year-old poplar plantation of the cultivar I-214 (*Populus x Euroamericana* [Dode] Guinier) located nearby the city of Granada, Spain. The sawing, milling and natural drying process lasted for 6 months, during which time proper ventilation was ensured. The final moisture content (MC) of poplar blocks was $10 \pm 2\%$ at the time of the specimen manufacturing (Figure 9.1).

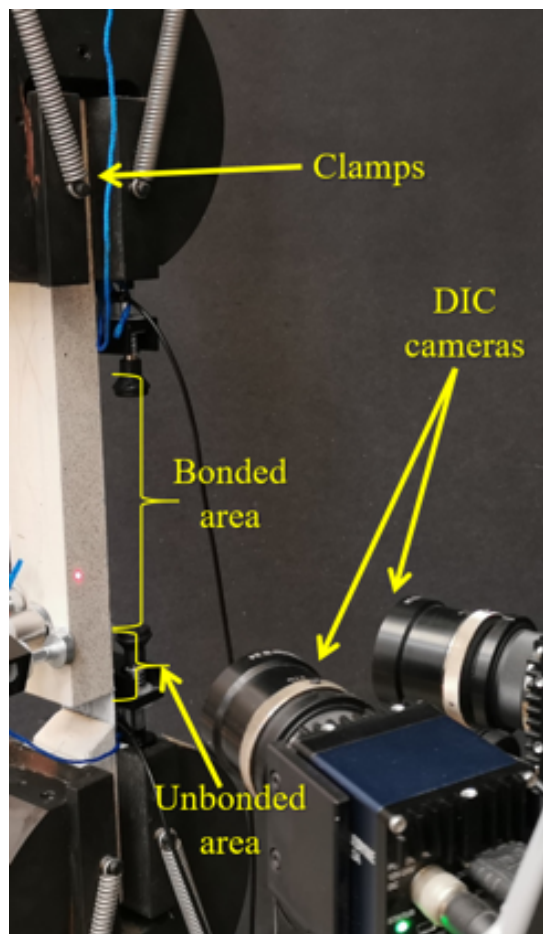


Figure 9.1: Specimen and experimental set-up.

CHAPTER 9.

DIC AND NUM. ANALYSIS OF FRP-POPLAR TIMBER INTERFACE

FRP (Technical name)	Total thickness [mm]	Tensile strength [MPa]	Maximum Elongation [%]	Young's Modulus [GPa]	Specimen nomenclature
MapeWrap C Uni-AX 300 – 1 layer	0.164	4830	2.0	230	CF
MapeWrap C Uni-AX 300 – 2 layers	0.328	4830	2.0	230	CF2
Carboplate E 170 – 1 layer	1.4	3100	2.0	170	CL

Table 9.1: Main mechanical parameters of FRP reinforcement [98].

Two different commercial composite materials were considered for this research study, unidirectional carbon fibre fabric, “MapeWrap C Uni-AX 300”, and pultruded carbon fibre plate, “Carboplate E 170”, both from Mapei Company [98]. The main mechanical parameters of the FRP employed to manufacture the samples are presented in Table 9.1.

The main elastic mechanical parameters of the poplar timber used for the manufacturing of the specimens belonged to the same trees plantation, which was studied by the authors in their previous published scientific works [63, 188, 189, 219], with a mean modulus of elasticity MOE of 9500 MPa. To increase the bond adherence between the poplar block and the reinforcement, two types of commercial resin developed by MAPEI Company [98] were applied: an epoxy primer in water dispersion, “Mape-wood Primer 100” to improve the cohesion, and a second free epoxy resin “MapeWrap 2”.

9.2.2 Timber block, adhesive and composite material (FRPs)

The testing program consisted of 15 specimens manufactured for this experimental campaign as shown in Table 9.2 and Figure 9.2. In all cases, the bonded width was 50 mm and the bonded length (L_{bond}) was 200 mm. The poplar timber blocks had a cross-section of 50 mm x 28 mm and a central length of 240 mm. A 20 mm unbonded region at the composite loaded end was reserved to eliminate the effect of block edge, see [192]. Since the DIC equipment has only two recording cameras, the specimens were divided into two analysis groups. The first group was considered to assess the longitudinal strain distribution along the FRP using the frontal view of the specimen, while the second group was designed to evaluate the strain distribution within the poplar, especially in a section along the bond line using the side view of the specimen.

Table 9.2 describes the main features of the specimens, the type of analysis performed and the corresponding samples, as well as the stiffness of the reinforcement.

9.2.3 Modified single shear test

All samples were tested in a multi-testing machine, specially manufactured for the lab by Microtest S.A Company, using an electrical actuator with a maximum capacity of 200 kN (accuracy of 0.01 kN) and speed test rate of 0.5 mm/s (see Figures 9.1 and 9.2). To increase the adherence between clamps and the specimen surfaces, a 90 mm gripping length was set. In addition, to prevent the timber block failure near the clamps,

9.2. MATERIALS AND EXPERIMENTAL SET-UP

Specimen name	Analysis type	Number of specimens	$E_{FRP} \times t_{FRP}$ [kN/mm]
CF-S	Side view	3	37.7
CF-F	Frontal view	2	37.7
CF2-S	Side view	3	75.4
CF2-F	Frontal view	2	75.4
CL-S	Side view	3	238
CL-F	Frontal view	2	238

Table 9.2: Experimental samples description and their corresponding FRPs stiffness.

a layer of composite material was glued onto the lateral face of the specimen (see the top and bottom clamping area in Figure 9.2).

The test aimed to reproduce the actual working conditions of timber elements. This was considered an important part, given that stiffness of timber beams is considerably lower than that of concrete beams, for which single shear tests with no bending have been mainly used to study the inter-facial behaviour of the FRP.

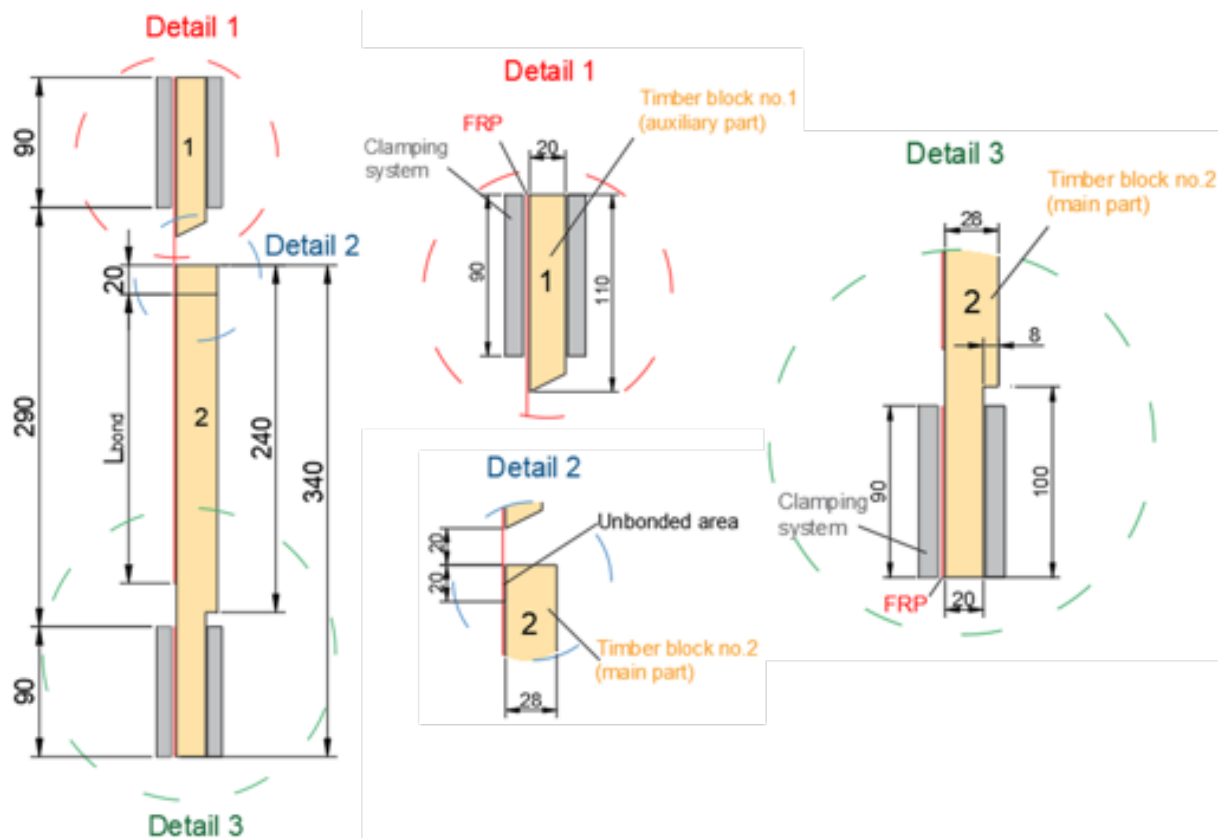


Figure 9.2: General drawing of the experimental setup and sample. Dimensions in mm.

9.3 Methods

9.3.1 DIC technique/instrumentation

For monitoring the strain field within the specimens' surfaces, at the frontal and side parts (Figure 9.3) a non-contact optical measurement system was used, Aramis 3D[®] [171].

Aramis 3D[®] system is a powerful measuring instrument that is suited for assessing three-dimensional deformation and strain distributions of real components under static or dynamic loads. Data acquisition was prepared by smoothing and cleaning the surface of the specimen, and then by applying a black-on-white random speckle pattern as uniformly as possible, using opaque spray paint on the face of each sample. The DIC system was calibrated according to the requirement calibration of Aramis 3D[®].

The DIC monitoring area is defined by a face size with 19 pixels, and 16 pixels for point distance, respectively. The optical module of Aramis 3D[®] (composed of two 12M industrial cameras) was oriented towards the specimen surface. The location of this module was also determined by the recommended calibration distance to the specimen, resulting in a 295 mm distance and an angle of 25° between cameras.



Figure 9.3: Test set-up for side and frontal views.

9.3.2 Numerical finite simulation

3D-FEM model

FEM technique was used to investigate the FRP-Poplar bond interface behaviour and longitudinal strain distributions along the FRP and poplar block, respectively, as a

function of the mechanical and geometrical properties of the FRP. Three different tested stiffness's of the FRP were transposed into different models implemented in Abaqus [172], able to reproduce the experimental behaviour of the specimens.

The boundary conditions were defined in order to simulate the real boundary condition of the experimental set-up; hence, the considered boundary conditions were modelled as clamped conditions applied to the right side of the poplar block, see Figure 9.4. To consider the movable part of the testing machine, the FRP was fixed in the transversal and radial directions (see the left side of Figure 9.4). In order to avoid element distortion and strain/stress point concentration due to reaction force (clamp) and applied force, respectively, a rigid body defined by a reference node was coupled by a kinematic coupling constrain at the right and left sides.

The numerical model was created using two different solids; the poplar block was created by an eight-node brick element C3D8, while the FRP layer was modelled by using a planar shell element with a four-node, S4 according to the Abaqus library [220]. The mesh size was kept constant for both elements, FRP and poplar block, with a size of 4 mm [221].

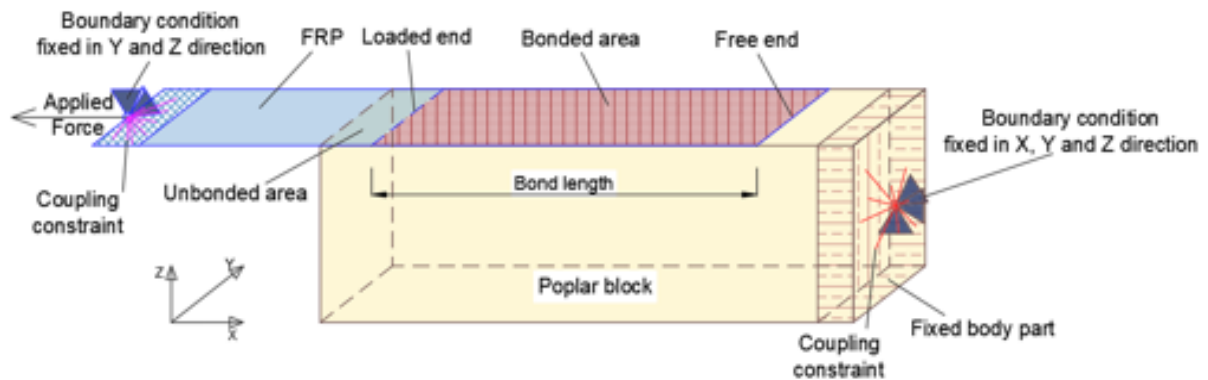


Figure 9.4: Test set-up considered in the numerical simulations.

Contact interface failure modelling (bond modelling)

To study the FRP-to-timber bond behaviour, the bonded interface between parts was introduced in the modelling with a cohesive contact approach defining damage initiation and propagation of the failure of the bond. As many studies showed, [174, 222, 223] the FRP-timber bond behaviour revealed similarities to the approach using cohesive elements [220], being generally easier to define the contact, and providing a reduced computational time than modelling the interface with thick cohesive elements [224]. This approach is valid if the thickness of the applied adhesive layer is negligibly small compared with the size of the rest of the elements and the constitutive laws/parameters of the interface are previously validated with tests.

As Figure 9.5 shows, the cohesive zone model combines two parts: an initially linear elastic behaviour (ascending branch) with a strength-based criterion to predict the damage initiation and a subsequent descending branch that models the evolution of damage according to a fracture mechanics-based criterion. The elastic behaviour is written in terms of an elastic constitutive matrix relating normal and tangential stresses (t_n , t_s and t_t) with corresponding normal and tangential strains at the interface (ϵ_n , ϵ_s , ϵ_t) by the elastic normal and tangential elastic parameters K_{nn} , K_{ss} , K_{tt} , K_{ns} , K_{nt} , K_{st}

CHAPTER 9.

DIC AND NUM. ANALYSIS OF FRP-POPLAR TIMBER INTERFACE

as shown in Equation 9.1. Hence, the elastic linear behaviour can be expressed by the nominal traction stress vector, t , as:

$$t = \begin{Bmatrix} t_n \\ t_s \\ t_t \end{Bmatrix} = \begin{bmatrix} K_{nn} & K_{ns} & K_{nt} \\ K_{ns} & K_{ss} & K_{st} \\ K_{nt} & K_{st} & K_{tt} \end{bmatrix} \times \begin{Bmatrix} \epsilon_n \\ \epsilon_s \\ \epsilon_t \end{Bmatrix} \quad (9.1)$$

where, K is the elasticity matrix and ϵ is the strain vector. The corresponding strains can be expressed as a function of the thickness of the interface T_0 , and the displacement δ_i across the interface can be expressed as:

$$\epsilon_i = \frac{\delta_i}{T_0} \quad (9.2)$$

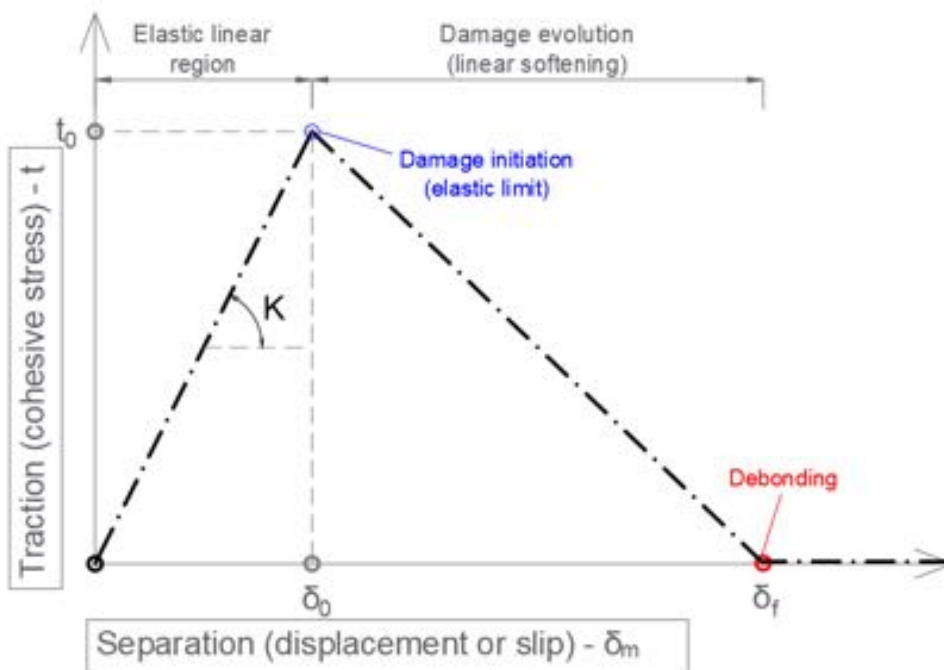


Figure 9.5: General damage process zone and corresponding bilinear traction-separation law [220].

As Figure 9.5 shows, the stress t_0 indicates the onset of the material degradation, being the peak value of the stress at the interface corresponding to a displacement δ_0 . These parameters are experimentally obtained from tests. The degradation process is triggered when the separation satisfies certain damage initiation criteria. Therefore, several damage initiation criteria are available in the literature for interfaces [220] such as maximum nominal stress and quadratic nominal stress. Due to the complex behaviour of the specimen given by the experimental set-up, both aforementioned criteria were applied to the model in order to evaluate which one is closer to the experimental behaviour. For the maximum nominal stress criterion, the initiation of the degradation is assumed to onset when the nominal stress ratio reaches a value of one. This criterion is represented in Equation 9.3 as,

$$\max = \left\{ \frac{t_n}{t_n^0}, \frac{t_s}{t_s^0}, \frac{t_t}{t_t^0} \right\} = 1, \quad (9.3)$$

where t_n, t_s and t_t are the normal and tangential stresses at the interface, and t_n^0, t_s^0 and t_t^0 are their corresponding strengths. While for the quadratic criterion the onset of the damage is assumed to initiate when a quadratic interaction function (Equation 9.4), involving the nominal stress ratio, reaches a value of one. Clearly, the pure compressive deformation or stress state does not initiate the damage.

$$\left\{ \frac{t_n}{t_n^0} \right\}^2 + \left\{ \frac{t_s}{t_s^0} \right\}^2 + \left\{ \frac{t_t}{t_t^0} \right\}^2 = 1 \quad (9.4)$$

According to the strength-based failure criterion, the damage evolution would be initiated once the damage initiation condition (equations 9.3 or 9.4) has been met. Several constitutive models have been proposed by the researchers for modelling the damage evolution at the interface. Linear softening behaviour [174] is traditionally used (see equation 9.5 and figure 9.5), where the damage evolution scheme describes the rate at which the material stiffness is degraded once the corresponding initiation criterion is reached, as can be observed in the second branch from Figure 9.5. In this model, a scalar damage variable, D , represents the overall damage in the material and captures the combined effects of all stresses. Initially, variable D has a value of 0 (no damage), and as damage is increased, D monotonically evolves from 0 to 1 (full damage) and displacement is δ_f . Therefore, the stress components of the traction-separation model are affected by the damage according to Equation 9.5.

$$t = (1 - D) \cdot \bar{t} \quad (9.5)$$

The effective displacement δ_m which describes the evolution of damage under a combination of normal δ_n and shear displacements (δ_s, δ_t) across the interface, see Figure 9.5 and [174], is defined as:

$$\delta_m = \sqrt{\delta_n^2 + \delta_s^2 + \delta_t^2} \quad (9.6)$$

Analysis procedure

For this study, two-analysis procedures are involved in the numerical simulation, linear static analysis and quasi-static simulations using explicit dynamics with mass scaling [225]. The linear static allows simulating the steps prior to detachment; however, it is unable to simulate the evolution of the detachment due to the lack of convergence of the non-linearities. The quasi-static dynamics procedure is suitable for the simulation of non-linearities that involve the detachment and subsequent evolution with a reduced computational cost. In addition, to avoid the inertial effects and to achieve computational efficiency, the mass of the entire model is artificially increased employing a mass scaling approach. Therefore, in order to get a stable computation of the model [220], a fixed mass scaling value provides a simple means to modify the mass properties of a quasi-static model at the beginning of the analysis and is computationally efficient.

Numerical parameters

Generally, the stiffness of CZM that defines ascending branch of the cohesive model, see Figure 9.5, is defined as the traction divided by the separation should be chosen as high as possible to provide a reasonable stiffness, but from a numerical perspective,

CHAPTER 9.

DIC AND NUM. ANALYSIS OF FRP-POPLAR TIMBER INTERFACE

it cannot be infinitely large because it leads to numerical ill-conditioning [221]. Many researchers have been involved in the development of various guidelines for selecting the stiffness of the interface. The experimental tests using graphite/epoxy specimens provided a stiffness parameter in normal and tangential directions of 10^6 N/mm^3 [226]. However, more sophisticated expressions for the computation of the normal and tangential stiffness's were developed by [184] to take into account the properties of the timber and FRP as follows,

$$K_{nn} = \frac{1}{\frac{t_t}{E_t} + \frac{t_{epoxy}}{E_{epoxy}}}, K_{ss}/K_{tt} = 1000 \cdot (0.16 \cdot \frac{G_{epoxy}}{t_{epoxy}} + 0.47). \quad (9.7)$$

These expressions take into account the superficial behaviour of the timber and the global behaviour of the FRP. Therefore, it is needed to estimate the thickness of timber that can be adhered to the FRP (usually taken as 1mm). The rest of the parameters are: E_t modulus of elasticity of timber 9500 MPa (see [63][38]), t_{epoxy} thickness of the resin (usually 0.5mm), E_{epoxy} modulus of elasticity of the resin 2500 MPa and G_{epoxy} the shear modulus of the resin 0.99 GPa (the last two parameters were taken from the technical specifications of the manufacturer). The rest of damage parameters δ_f and the normal strength t_n^0 were defined accordingly the manufactured technical sheets [98], while the shear strengths t_s^0 and t_t^0 were estimated based on the Von Mises criterion [227] for a stress state of pure shear stress, $t_s^0 = t_t^0 = t_n^0 / \sqrt{3}$, which can be roughly considered $0.577t_n^0$. The above parameters are used as initial values in a calibration process, where parameters are modified by trial and error until a good fitting with experimental results is obtained.

Tables 9.3, 9.4 and 9.5 present the parameters of the cohesive contact surface and its corresponding range, used in the calibration. Each table corresponds to a different FRP configuration (table 9.3 for CL specimen; table 9.4 for CF2 specimen and table 9.5 for CF specimen) and collects the damage criterion, normal strength t_n^0 , shear strengths t_s^0 and t_t^0 , displacement at debonding δ_f and stiffness parameters of the interface (K_{nn} , K_{tt} , K_{ss}) from Eq. 9.7 that have been considered in the modelling. Several numerical simulations were carried out employing the parameters from tables 9.3, 9.4 and 9.5 and the two damage criteria defined equations 3 and 4 in order to fit the experimental strain distributions.

The assigned name from "FEM1" to "FEM4" corresponds to the maximum nominal stress damage criterion, and "FEM5" to "FEM8" to the quadratic nominal stress damage criterion for CL and CF specimens. While for the CF2 specimen the six numerical simulations were considered, with three simulations for each damage criterion.

Simulation name	Damage criterion	t_n^0 (N/mm ²)	$t_s^0=t_t^0$ (N/mm ²)	δ_f (mm)	K_{nn} (N/mm ² /mm)	$K_{tt}=K_{ss}$ (N/mm ² /mm)
FEM1-FEM4	Maximum nominal stress	24.0	14.0-16.0-15.0-13.0	0.001	1398	786
FEM5-FEM8	Quadratic nominal stress	24.0	14.0-16.0-15.0-13.0	0.001	1398	786

Table 9.3: Numerical parameters used for the CL specimen. t_n^0 , t_s^0 , t_t^0 are the maximum nominal interfacial strength in the normal and shear direction I and II; δ_f is the displacement at debonding; K_{nn} , K_{tt} , K_{ss} are the normal, tangential and radial stiffness.

Simulation name	Damage criterion	t_n^0 (N/mm ²)	$t_s^0=t_t^0$ (N/mm ²)	δ_f (mm)	K_{nn} (N/mm ² /mm)	$K_{tt}=K_{ss}$ (N/mm ² /mm)
FEM1-FEM3	Maximum nominal stress	24.0	12.5-13.0 -13.5	0.001	1938	786
FEM4-FEM7	Quadratic nominal stress	24.0	12.5-13.0 -13.5	0.001	1938	786

Table 9.4: Numerical parameters used for the CF2 specimen. t_n^0 , t_s^0 , t_t^0 are the maximum nominal interfacial strength in the normal and shear direction I and II; δ_f is the displacement at debonding; K_{nn} , K_{tt} , K_{ss} are the normal, tangential and radial stiffness.

Simulation name	Damage criterion	t_n^0 (N/mm ²)	$t_s^0=t_t^0$ (N/mm ²)	δ_f (mm)	K_{nn} (N/mm ² /mm)	$K_{tt}=K_{ss}$ (N/mm ² /mm)
FEM1-FEM4	Maximum nominal stress	24.0	18.0-20.0 19.0-18.5	0.001	1938	786
FEM5-FEM8	Quadratic nominal stress	24.0	18.0-20.0 19.0-18.5	0.001	1938	786

Table 9.5: Numerical parameters used for the CF specimen. t_n^0 , t_s^0 , t_t^0 are the maximum nominal interfacial strength in the normal and shear direction I and II; δ_f is the displacement at debonding; K_{nn} , K_{tt} , K_{ss} are the normal, tangential and radial stiffness.

9.4 Results and Discussions

DIC technique permits obtaining the longitudinal strain field on the surface of the FRP during loading and debonding processes. Figure 9.6 shows the strain fields for three representative specimens with carbon laminate (CL), two layers of carbon fabric (CF2) and one layer of carbon fabric (CF) at the last load step before initiation of debonding. Table 9.6 shows the mean experimental failure loads and the corresponding numerical (FEM) loads at debonding for all specimens with the parameters defined in Tables 9.3, 9.4 and 9.5.

Specimen name	Mean Experimental maximum load (kN)	Mean FEM Debonding load (kN)	Error (%)
CL	16.1 ± 1.5	16.9 ± 0.2	4.97
CF2	15.3 ± 3.3	15.6 ± 0.2	1.96
CF	14.0 ± 2.1	14.8 ± 0.5	5.71

Table 9.6: Mean experimental and numerical failure loads, the corresponding error and standard deviation. Mean values over five specimens of each specimen typology.

For all specimens, the longitudinal strain distributions shown in Figure 9.6 reveal different patterns as a consequence of the stiffness of the reinforcement, which is directly linked with the failure loads, and which are discussed below. However, a general behaviour is shown for all of the specimens, when the applied load increased before reaching the debonding load, the FRP longitudinal strain also increased and redistributed within the bond length. The higher maximum load is found for the specimens reinforced with the carbon laminate (CL) due to their high stiffness and homogeneous distributions of the longitudinal strains, while the minimum corresponds to the specimens with one layer of fabric (CF) due to the local concentration of longitudinal strains

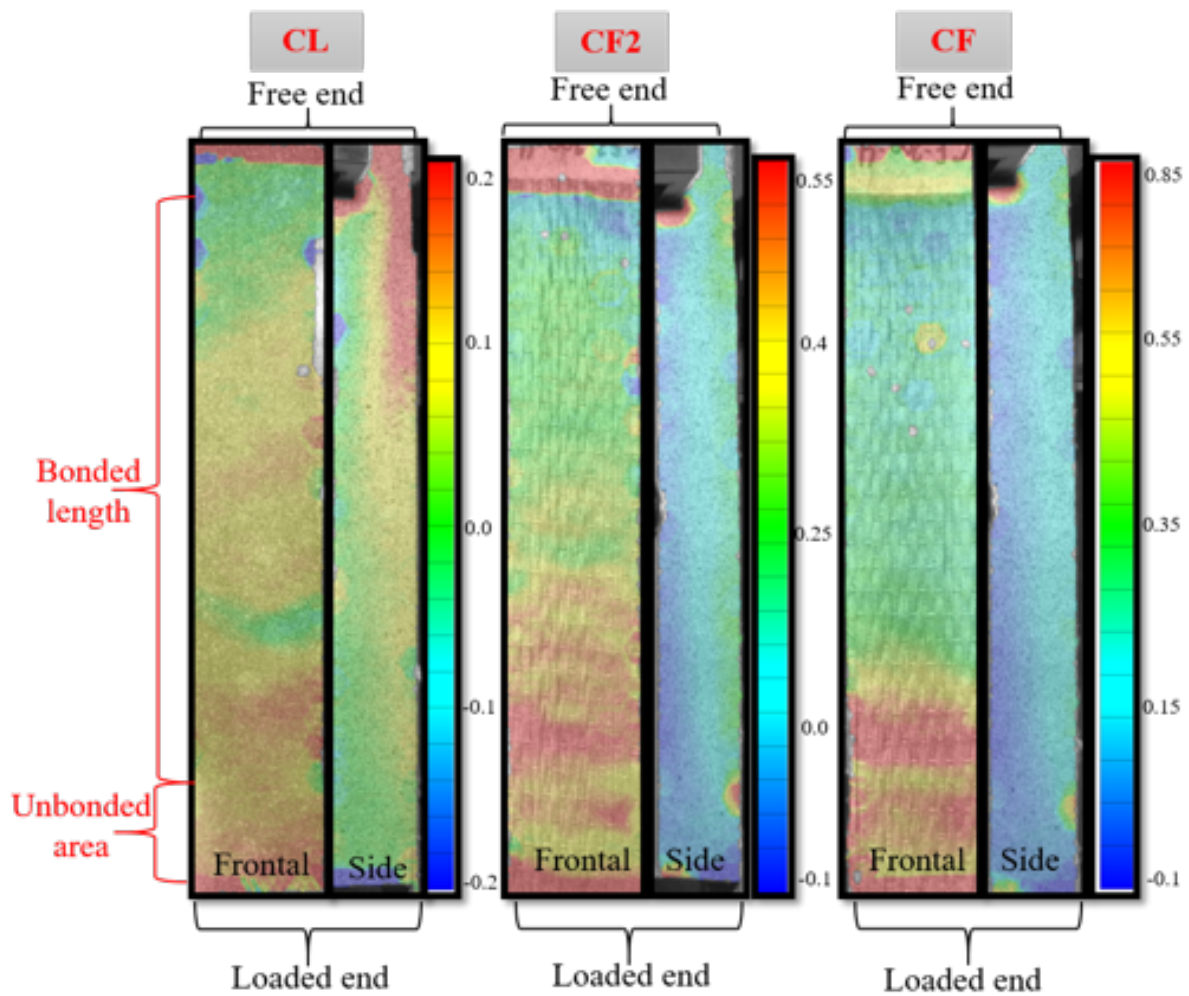


Figure 9.6: Digital Image Correlation of the longitudinal strain field in frontal view of FRP (left) and side view of timber (right) of three representative specimens of CL (left), CF2 (middle) and CF (right), respectively prior initiation of debonding.

close to the loaded end. Figure 9.7 shows in a lateral view the location of the debonding onset and progression until the complete detachment for the representative three-layout configuration acquired by means of the DIC technique.

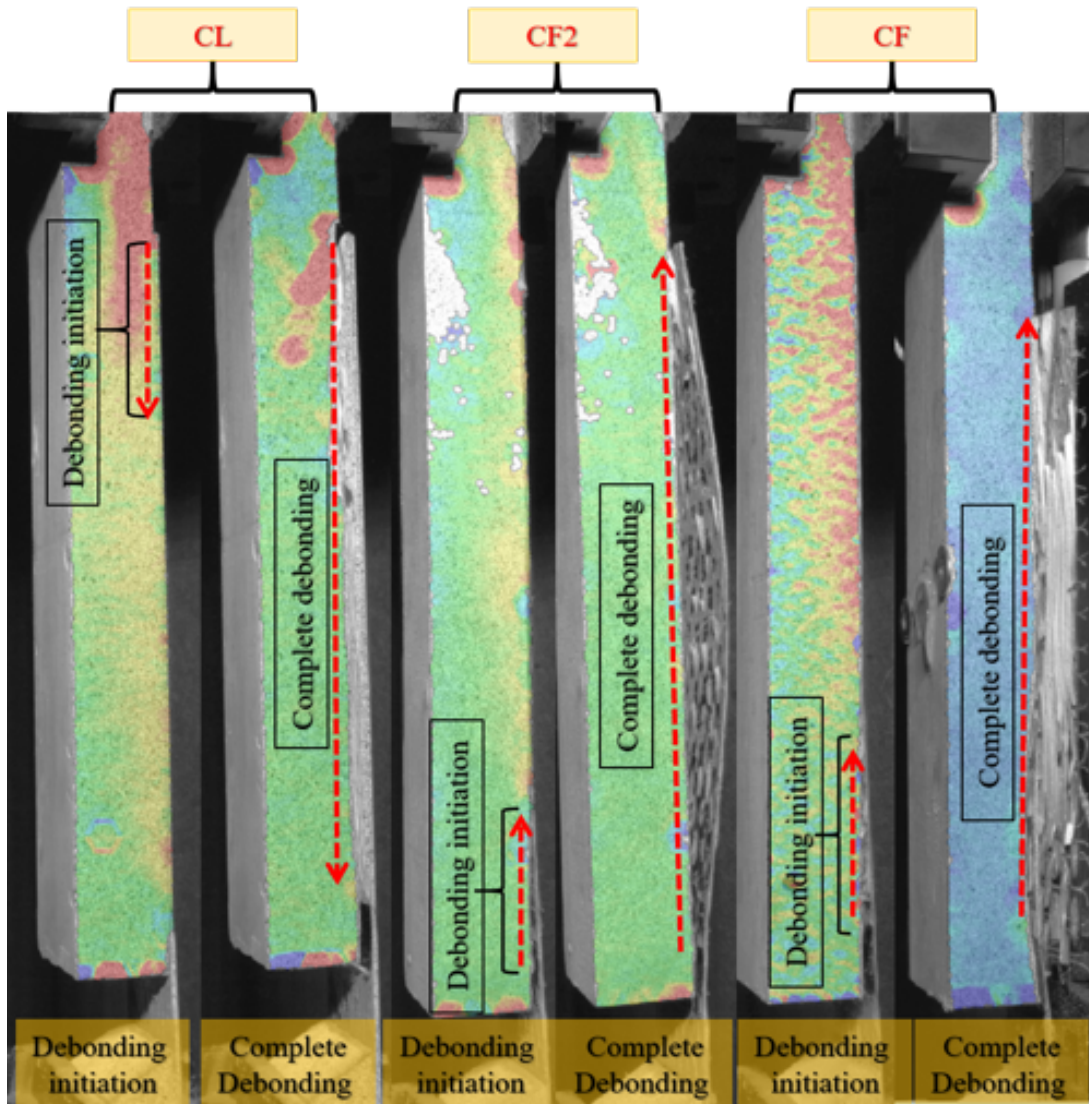


Figure 9.7: Lateral DIC view of strain flow, debonding and progression for CL (left), CF2 (central) and CF (right) specimens.

9.4.1 CL specimen behaviour

In particular, the specimen with carbon laminate CL has the highest FRP stiffness due to its highest thickness of 1.4 mm. The longitudinal strain distribution along the FRP (see Figure 9.6-left), shows a homogeneous distribution of the strain field, consequently, the laminate transmits an approximately constant strain to the interface. This fact is also demonstrated by the strain amplitude, showing lower strain values, up to 0.0010%, along the laminate and up to 0.0025% in timber compared to the CF2 and CF specimens (Figure 9.6-left for frontal and side view). These trends and values are confirmed by the experimental (Exp1-2) and numerical (FEM1-8) strain distributions for the load step prior to debonding represented in Figure 9.8. In both CL specimens,

CHAPTER 9.

DIC AND NUM. ANALYSIS OF FRP-POPLAR TIMBER INTERFACE

the longitudinal strains at the frontal and side views located in the mid-area of the specimen are almost a plateau with a slight decrease due to strains' dissipation along the specimen. As the load increases, due to the experiment set-up (see Figure 9.2), the specimen works as a cantilever beam and a bending moment appears near the clamp. Consequently, the strains and stresses in this area increase, and are transferred towards the end of the FRP near the clamp. The transfer results in high stresses at the interface, thus appearing the detachment, see Figure 9.7-left. This behaviour is clearly visible in the strain distributions of Figure 9.8 (both numerical and experimental) where at the right side (between 180-220 mm) a sudden reduction of the strains in the FRP can be observed (Figure 9.8-left) due to detachment and the increase of the strain in the timber (Figure 9.8-right). Also, both experimental longitudinal strains acquired by means of the DIC technique and numerical results revealed a homogeneous distribution of the strains along the FRP and timber interface (Figure 8), providing similar results. The only difference is related to the second descending slope, corresponding to the right end of the specimen (Figure 9.8-left) or ascending slope in (Figure 9.8-right), where all FEM simulations (except "FEM-8") provide a good fitting. Therefore, the parameters in Table 9.3 are valid for numerical simulation except those for "FEM-8".

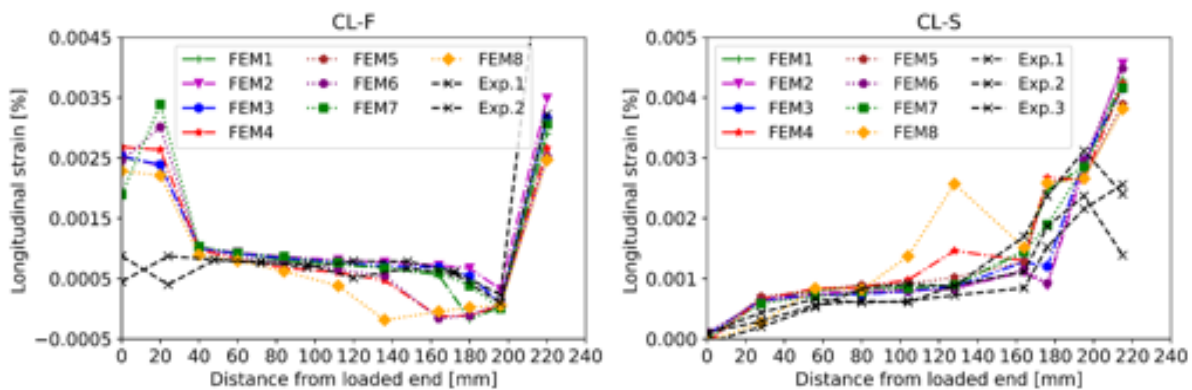


Figure 9.8: Experimental and FEM longitudinal strain for CL, frontal (left) and side (right).

The finite element simulations confirm the general behaviour of the specimen. The simulations allow to compare the strains distribution provided by DIC and to compute the strains/stresses at FRP and the interface. The numerical strain distributions given in figure 9.8-9.9 fit those given by the experiments, and confirm that the detachment firstly appears at the free end of the specimen near the clamp due to the increase of strains at the FRP and the corresponding decrease at timber (see Figure 9.9 for FEM and Figure 9.7 (left) for the experiment). The detachment progressively reduces the stiffness of the timber and, consequently, the concentration of strains are increasing and moving to the loaded end, enforcing the detachment of this area. Figure 9.10, shows the deformed shapes of the specimen and the evolution of the detachment during the test.

Therefore, two areas can be distinguished: the detached area where the stiffness is relatively low and the bonded area, where the stiffness is high due to the composite sectional behaviour (FRP and timber). For this specimen (CL), the debonding onsets at an area close to the clamp and propagates to the opposite end until the complete detachment of the bond surface.

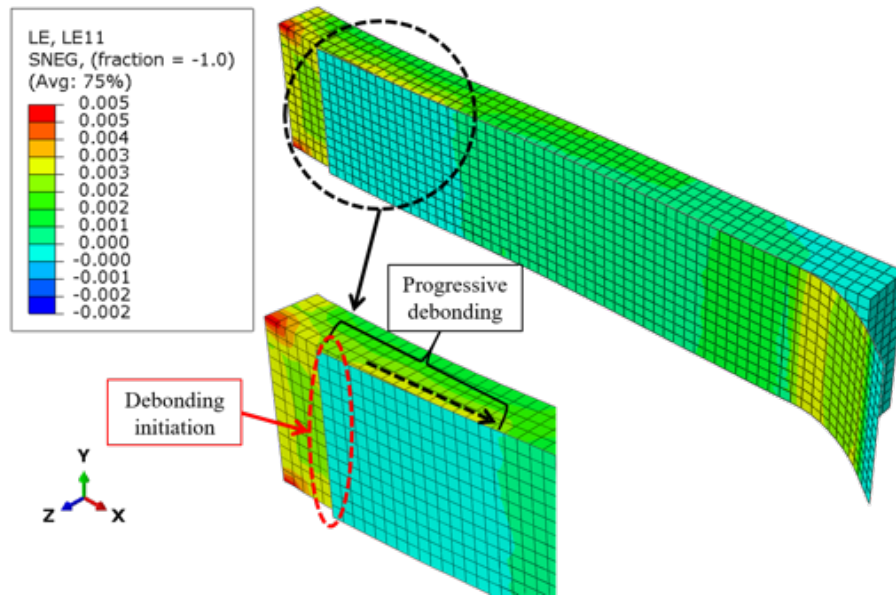


Figure 9.9: Longitudinal strain distribution from the FEM model for the CL specimen corresponding to the initiation of detachment at the free end.

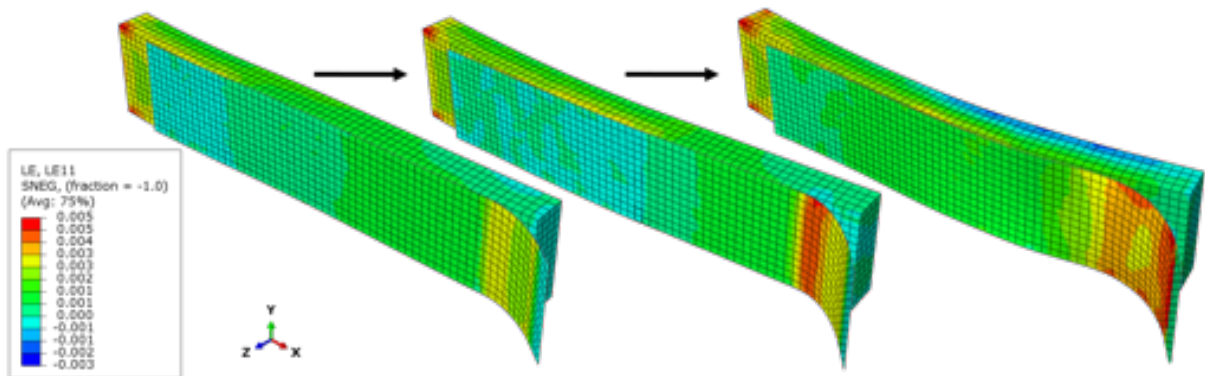


Figure 9.10: Longitudinal strain field at damage initiation (left), damage evolution (middle) and final debonding (right) of the CL specimen. FEM simulation.

9.4.2 CF2 specimen behaviour

For the specimens with two layers of carbon fabric (CF2), the longitudinal DIC strain field at the frontal view of the FRP (see Figure 9.6-center) shows a less homogeneous field than in the previous case. This can be attributed to the considerably reduced thickness of the FRP and the consequent stiffness reduction. For these specimens, the maximum longitudinal strain achieved in the FRP is up to 0.005%, while the maximum strain developed in timber is up to 0.004% (Figure 9.6-center). These strains are concentrated near the end due to reduced stiffness of the FRP and therefore, the high flexibility of the fabric, which adapts to the deformed shape of the timber block. In this case, the experiments show that the strains initiate the detachment at the loaded end; therefore, the detachment now progresses oppositely, from the loaded end to the opposite end of the specimen.

Now, the experimental results in FRP, (Figure 9.11-left) and timber lateral side (Figure 9.11-right) are getting dispersed compared with the results from CL, therefore the numerical results (FEM1-FEM6) provide intermediate results as shown in Figure 9.11. In this case, the closest numerical results to the experimental ones are provided by simulations "FEM3" and "FEM4" with corresponding calibrated parameters shown in Table 9.4 for both failure criteria.

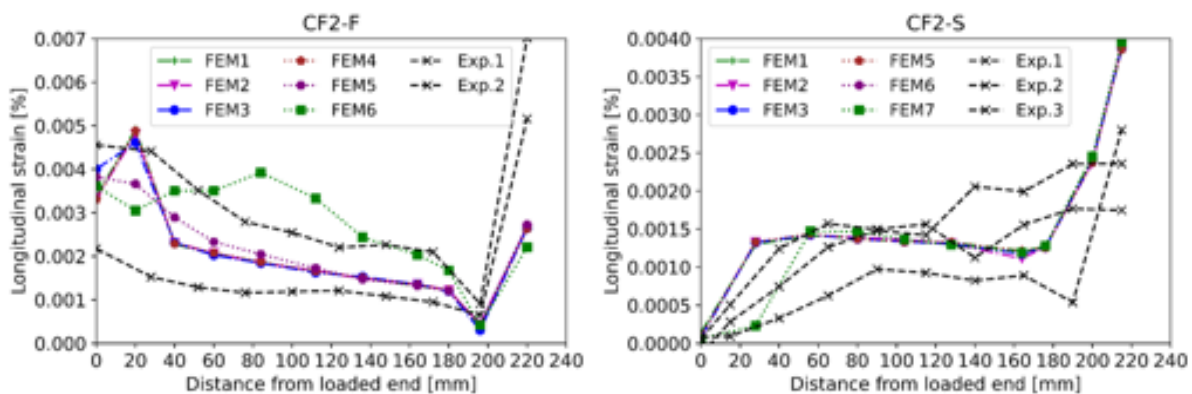


Figure 9.11: Experimental and FEM longitudinal strain for CF2, frontal (left) and side (right).

The progressive detachment enforces the reduction of the longitudinal strains in timber, which implies the stiffness reduction of the poplar timber block and, therefore, an increase of its vertical displacement as shown in Figure 9.12.

As bending moment increases and the reduction of stiffness due to progressive debonding along the FRP occurs, the second area of high strains concentration appeared near the end close to the clamp, now in a situation similar to CL, which produced a second detachment onset at this side that determined the failure of the bonded surface. This is captured by the numerical simulation in Figure 9.13 and by the experiments (see bent FRP in Figure 9.7-central).

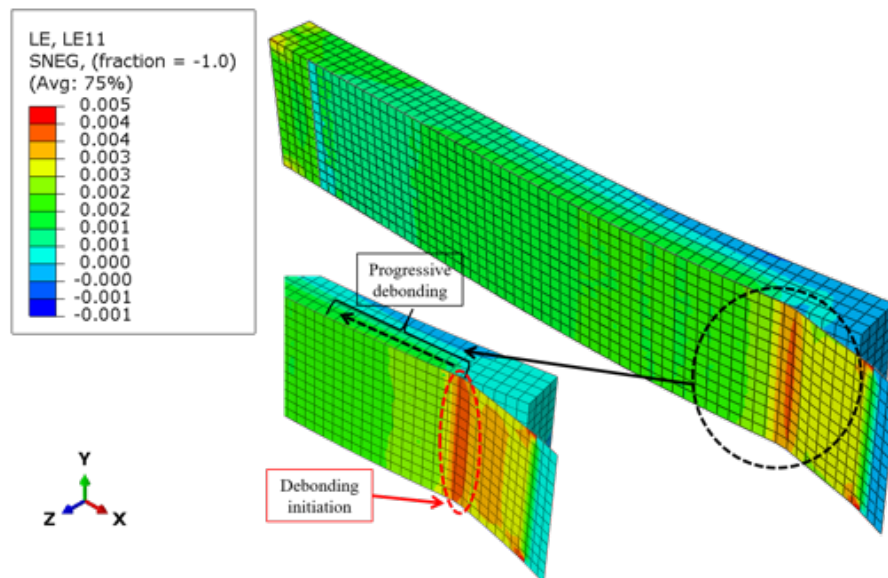


Figure 9.12: Longitudinal strain distribution from the FEM model for the CF2 specimen corresponding to the initiation of detachment at the free end.

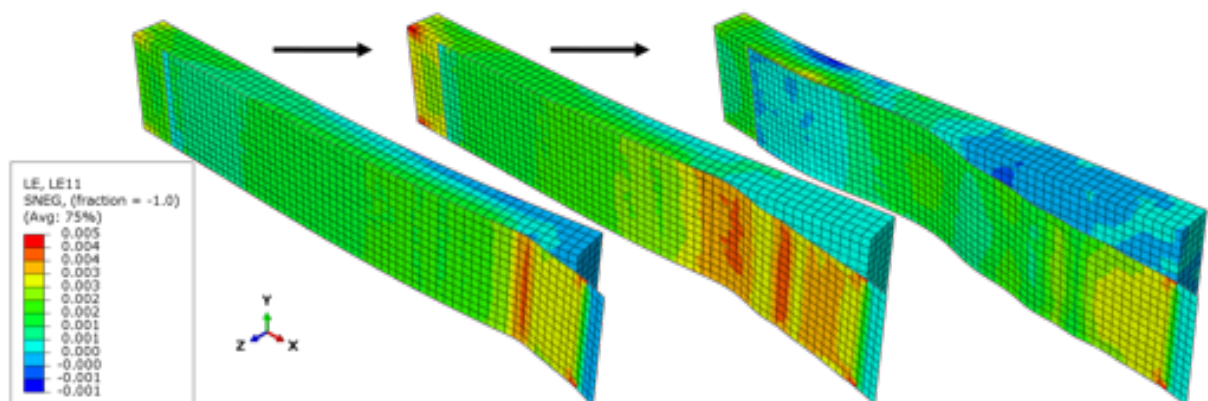


Figure 9.13: Longitudinal strain field at damage initiation (left), damage evolution (middle) and final debonding (right) of the CF2 specimen. FEM simulation.

9.4.3 CF specimen behaviour

For the specimen with only one layer of carbon fabric (CF), the DIC longitudinal strain field (see Figure 9.6-right) shows a concentration of strains near the loaded end due to the flexibility of the FRP that accommodates the deformation of timber. In this area, the maximum amplitude of the longitudinal strain is roughly two times higher (up to 0.009% in Figure 9.14-left) than for the CF2 specimen.

Figure 9.14-right shows the longitudinal strains in timber and confirms the situation where a progressive increase of the strains is produced at the loaded end due to the stress transfer from FRP to timber. The strains reach a plateau (between 60-160 mm) in timber and finally, a decrease in FRP and an increase in timber is produced due to the transition between the bonded section of FRP and timber to the section of pure timber.

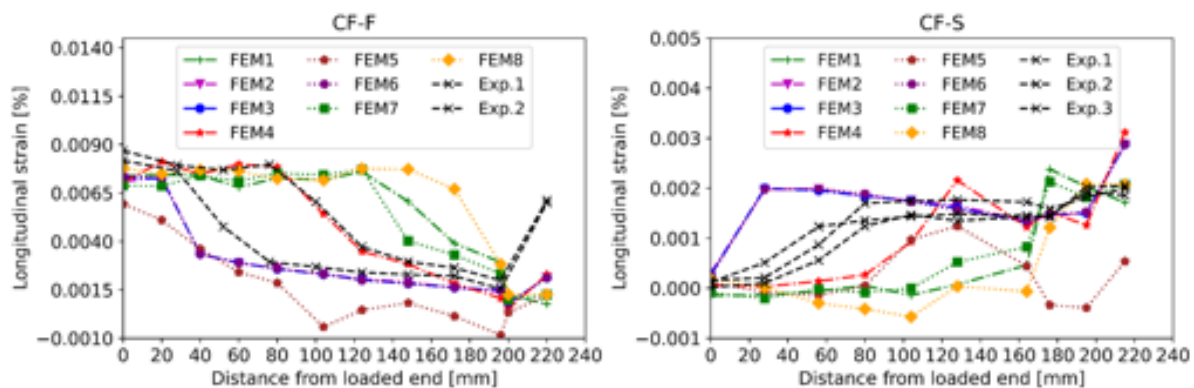


Figure 9.14: Experimental and FEM longitudinal strain for CF, frontal (left) and side (right).

The numerical simulation captures this behaviour (Figure 9.15), resulting in a high strain near the loaded end, a plateau and a final descending part in the longitudinal strain evolution of the FRP (Figure 9.14-left) with a corresponding increase in timber (Figure 9.14-right). As the experimental results showed, the results have high scatter in both FRP and timber. This dispersion is attributed to the low stiffness introduced by the FRP. Generally, these experimental results fall, for most of the cases, in the variation range for the numerical ones. The most accurate numerical results are provided by the simulation “FEM 4” with parameters defined in Table 9.5.

The numerical simulation (Figure 9.15) shows the adaptation of the layer of fabric to the timber deformed shape at the loaded end until the initiation of the debonding. When the axial force becomes significant, a high strain concentration is observed at the interface near the loaded end. Therefore, when the shear stress at the interface overcomes the maximum shear strength of the interface, a progressive debonding from the loaded end to the free end is triggered.

Consequently, the timber block starts to bend due to an increase of applied forces and the progressive reduction of stiffness across the debonding line (Figure 9.16). In this situation, a second debonding is not produced due to the low stiffness of the FRP.

9.5 Conclusions

The analysis of the behaviour of the bonded FRP to poplar timber interface is essential to obtain the maximum load and the failure modes of poplar timber specimens rein-

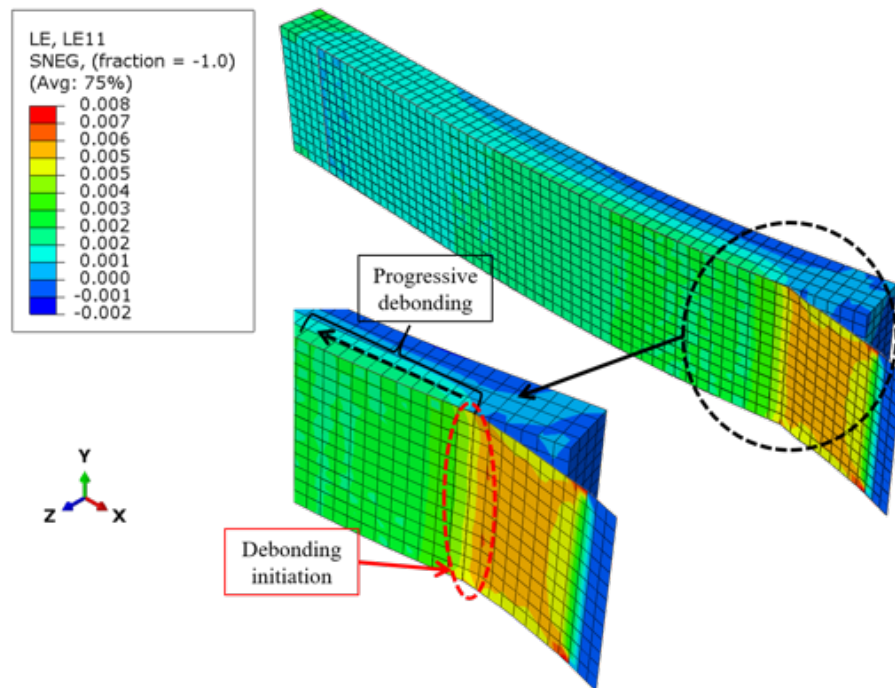


Figure 9.15: Longitudinal strain distribution from the FEM model for the CF specimen corresponding to the initiation of detachment at the free end.

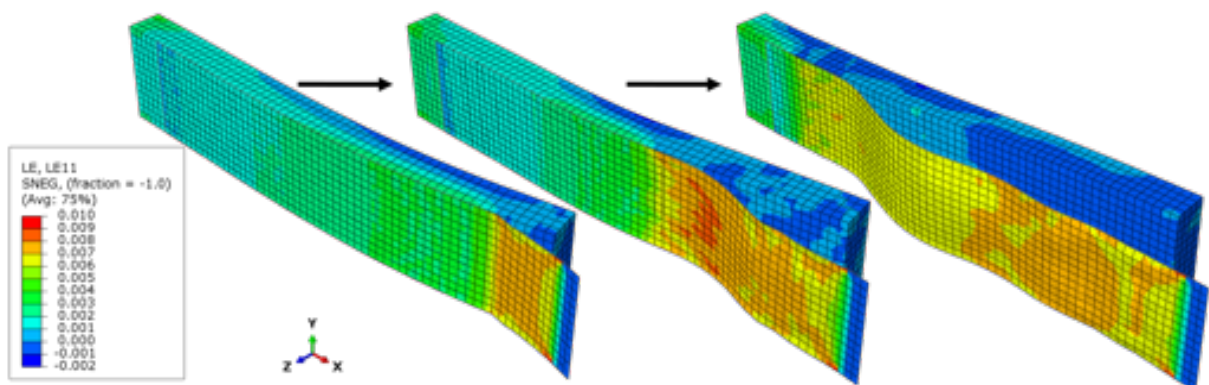


Figure 9.16: Longitudinal strain field at damage initiation (left), damage evolution (middle) and final debonding (right) of the CF specimen. FEM simulation.

CHAPTER 9.

DIC AND NUM. ANALYSIS OF FRP-POPLAR TIMBER INTERFACE

forced with externally bonded composites. The DIC and FEM techniques are adequate tools to examine and foresee the behaviour of the specimens.

The DIC permits obtaining the strain fields at the FRP and lateral sides of the specimen. It also captures the different modes of failure due to the strain concentration, which is related to the different composite stiffness of the layouts of the specimens. The FEM allows detecting phenomena that are not completely captured by DIC. Consequently, it is a suitable and complementary tool to analyse and predict the behaviour of specimens. The sets of experimental data permit to obtain the model parameters with few experimental adjustments.

The experimental set-up used in this work considered the bending and axial deformation of the specimens, simulating the real working conditions where reinforcement and timber are working together. For stiff reinforcements, as the FRP pultruded laminate (CL), the maximum load was achieved due to the quasi-homogeneous strain distribution along the bonded area. In this case, the bending at the clamped end produces high stresses that are transferred to the laminate and triggered debonding initiation at one side.

However, when the thickness of the reinforcement is reduced (CF2 and CF specimens) and consequently, the global stiffness is also reduced, the load capacity is decreased. In these cases, the strains are not homogeneously distributed, enforcing the debonding at relatively early loading stages. In these cases, the FRP adapts to the deformed shape of the poplar timber block and, consequently, high stresses are produced in the loaded end area resulting in the premature debonding of this area.

The DIC technique evidenced these behaviours while FEM was able to predict them with relatively low computation time. The experimental data and knowledge acquired from DIC convert FEM in a valuable tool for the design and optimization of reinforced timber specimens.

Chapter 10

General conclusions of the thesis

This thesis is a compilation of works that contains the experimental part focused on the characterization of the standing trees, logs and boards selections, and manufacturing process of the final products; therefore, the drawn conclusions are treated in comparison with the results obtained through analytical and/or numerical methods.

Experimental comparisons employing different CFRP layout configurations or timber species combinations have been studied and analyzed in terms of bending resistance, modulus of elasticity, ductility and failure pattern. Later on, the behaviour of the poplar timber subjected to pure tension and shear stress is deeply studied through experimental campaigns in parallel with the digital image correlation (DIC) technique and finite element analysis (FEA).

In relation with the obtained experimental results in standing trees, logs, boards and beams, the mechanical properties, such as bending resistance, compression strength, and modulus of elasticity are highly influenced by the age of the plantations, while the stand density does not influence these parameters. Additionally, the non-destructive evaluation has demonstrated a high level of fidelity for the assessment of the elastic modulus in the standing trees, logs, and beams providing a homogeneous variation of the data.

Furthermore, the behaviour of the poplar within the glulam beams has been deeply studied through experimental and numerical simulations carried out for pine, pine-poplar and poplar glulam beams. Experimental results showed that hybrid combined pine-poplar beams can achieve comparable results with the pure pine ones, which emphasize that the quality of the inner boards has a small-scale influence in terms of the mechanical performance of the entire cross-section. In addition, the non-destructive tests, such as Acoustic Resonance Test (ART) performed on pure (mono-species) specimens are in good correlation with the experimental ones, characterized by a low variation of the results. The developed finite element models were able to capture the local strains concentration near supports and load cells since a calibration process has been applied to the constitutive parameters, which resulted in a numerical model in good agreement with the experimental behaviour.

The experimental studies were extended to the cases of the glulam beams made of poplar employing finger joints. Concerning the possibilities and capabilities to apply CFRP materials to the glulam poplar section to achieve higher mechanical performance, several layout configurations employing different CFRP layers have been experimentally investigated. Therefore, in this work, it was observed that the highest improvement in terms of modulus of elasticity, bending strength and ductility, has

CHAPTER 10.

GENERAL CONCLUSIONS OF THE THESIS

been achieved for the beam with one layer of pultruded carbon laminate placed at the bottom side (between first and second lamellas), since at the top part of the beam, top lamella, exhibited significant plasticization and deformation at the mid-span. For the specimen with 2-layers of fabric placed at both sides, top and bottom, the plastic behaviour is observed near the failure point. It is worth mentioning that with CFRP placed only in the compression part, the local deformation and plasticization of the section are completely avoided. Therefore, the CFRP placed at the top part plays an important role in the definition of the linear-elastic range. It is important to remark, that even the specimen with CFRP placed only in the compression area, provided notable improvements in terms of bending strength and modulus of elasticity, although a significant reduction of the ductility was been observed, up to 11%, characterized by a straight linear-elastic relation. Consequently, the specimen with CFRP placed at both sides revealed an optimal structural behaviour through all of the studied parameters.

The experimental campaign has been also oriented towards a comparable, low-medium quality, timber species with poplar, namely *Platanus*. In this work, three cross-sections were analyzed experimentally and analytically based on the Parallel Axis theorem (Steiner Theorem) and the transformed section method. Identically, the *Platanus* lamellas have been placed within the inner part of the cross-section, while the pine has been assigned to the external lamellas. The experimental results revealed that the combined cross-section, Pine-*Platanus*, showed comparable results with pure Pine ones, in terms of stress-deflection relation. The analytical method was able to determine the moduli in tension and compression for the pure beams, and with these results, it was possible forecasting the global modulus of the combined Pine-*Platanus* beams with a variation below 1% with respect to the experimental ones. Moreover, the proposed analytical models are able to establish the influence of the percentage of inner layers of the moduli in tension and compression and the global modulus, in furtherance of the sustainable and economical combined cross-section with superior stiffness (mechanical properties).

The study of the previous analytical method has been extended towards the aforementioned glulam section with CFRP layers. Thus, an extensive analytical model, which is able to calculate the main strength parameters (stresses, strains, resultant forces), and elastic parameters for different layout configurations assuming the linear elastic behaviour, has been also applied for composite beams Pine-Poplar. Based on these formulations and experimental results from the bending test, through a parametric analysis, the optimum percentage of the poplar lamellas was ranging between 25-40%, in order to obtain a beam with comparable mechanical properties with the pure Pine one, but with significant reduction of the raw density of the specimen. The proposed models allow computing the performance of the glulam beam with the CFRP if the moduli of each material are available, with a variation between experimental and analytical results up to 1.5%. In addition, through this method is possible to compute the improvement of moduli in compression and tension for the beam with CFRP with respect to the moduli in tension and compression of the base timber material (Poplar). The proposed analytical procedure can be used for the optimization procedure of the combined glulam beams using poplar and obtaining glulam beams with homogeneous behaviour in tension and compression. It is worth mentioning that, this analytical formulation can be applied to different timber species and section shapes, without being limited by the numbers of lamellas or percentage of one material.

The poplar behaviour subjected to tension forces has been investigated through ex-

perimental and numerical approaches for the case with finger and without finger joint. The reduction of modulus of elasticity in tension has decreased up to 24% and up to 28% related to tensile strength for the specimen with the finger joint. Employing the DIC technique, it was able to capture and to compute the distribution of the moduli in tension along the gauge length of the specimen, where high variation have been obtained for the specimens with finger joint, being in contrast with the specimen without finger joint, which exhibited a homogeneous variation of the moduli. The strain distribution near the finger joint and the force-elongation relationship have been studied in parallel with the numerical simulation, and through the calibration process of the constitutive and interface parameters, a numerical model in agreement with the experimental behaviour has been obtained. Hence, the study, demonstrated that the existence of the finger joint subjected to pure tensile forces is a susceptible failure point, which induces uncertainties that must be taken into account. An agreeable correlation between the DIC and FEM simulation is obtained in the evaluation of the longitudinal, transversal and shear strain in the surrounding area of the finger joint. The FEM model permits to study and to check the strains nearby the finger joint in order to find the proper finger joint geometry, which can lead to the highest mechanical performance.

The capabilities of the DIC has been involved also in studying the bond behaviour of the FRP to poplar timber for four different bonded lengths, analyzing the longitudinal strain distribution from two viewpoints. This multi-side view analysis allows investigating the longitudinal strain distribution onto the CFRP surface and in timber surface adjacent to the bond line. Different behaviour has been observed where the specimen bonded to a CFRP with high axial stiffness undergoes higher capacity and a homogeneous distribution of the longitudinal strains along the bond line. While for the specimen with a lower stiffness (one layer of fabric), the CFRP layer has accommodated/readjusted to the deformed shape of the specimen, generating high stress and strain concentration at the borders of the bond line. It is clear, that the bonding performance is related to the bond length and type of the CFRP, through its stiffness, although for the specimen with the shortest bond length, 50 mm, the maximum force capacity is achieved for the fabric, because for this case, the other specimens revealed a decidedly brittle behaviour that led to premature failure.

Through multi-side view analysis, is allowing to get the longitudinal strain evolution onto CFRP, where a significant strain peak is observed at the border of the loaded end, which descends to the free end of the bond line. At the same time, the strain variation in the timber layer, alongside the bond line, is the highest near the free end and is dissipated through the timber section towards the loaded end. Therefore, the longitudinal strain relation in timber is mirrored compared with the ones onto CFRP. Consequently, the composite section, timber and CFRP, having a higher stiffness leads to lower longitudinal stiffness in the timber section.

The numerical simulations carried out for each type of CFRP allow gaining insights into the onset of the bond line failure, which are not entirely captured by the DIC. Simulating the boundary condition of the test set-up, it was observed that for the longest bonded length, the specimens are behaving as a cantilever beam, which involves additional strains at the top timber block. Through these simulations, two distinct failure modes have been identified, being closely related to the axial stiffness of the CFRP. For the case with the lowest stiffness, one layer of fabric, the debonding of the interface is onset at medium load levels located at the loaded end, which is propagated towards the opposite side, free end. Since for the specimen with the highest axial stiffness,

CHAPTER 10.

GENERAL CONCLUSIONS OF THE THESIS

one layer of laminate, the failure is initiated in the opposite side, at the free end for high load levels, and is progressively developing to the load end. While for the case with two layers of fabric, the failure is onset at the loaded end propagates to the free end. Subsequently, a second failure has started developing from the free end, until the complete debonding of the interface.

A relevant point to be emphasized is that the entire bond line is active from the loaded end to the free end, being a specific behaviour due to the test set-up of the specimen, which is close to the behaviour of the structural members subjected to service loads.

This thesis through the obtained results, open the lines for new and challenging research possibilities employing poplar. The market is currently switching its attention to fast-growing trees, such as poplar, which shortly will become a highly used timber for the manufacturing of structural elements. Most of the structural elements (glulam members) will be as combined sections, where the poplar is placed at the inner part. Through the presented results, the influence of the poplar percentage on mechanical performance can be estimated. Therefore, sustainable structural elements, with a lower density and high or comparable mechanical properties can be achieved through judicious use of poplar timber.

In conclusion, the proposed analytical methods, together with the finite element analysis and the experimental results, can be extended in the optimization of the hybrid glulam poplar beams to offer a sustainable and economical alternative to today's timber market.

Bibliography

- [1] R. O. Foschi and B. J.D, "Glued-laminated beam strength: a model," *J. Struct Div*, vol. 106, no. 8, pp. 1735–1754, 1980.
- [2] Bodig, J.; Jayne, B.A., *Mechanics of wood and wood composites*. Michigan: Van Nostrand Reinhold, 1982.
- [3] H. Thelandersson, S.; Larsen, *Timber engineering*. West Sussex: John wiley & Sons Ltd, 2003.
- [4] R. L. J. Moody, "Glued structural members," in *Wood Handbook: Wood as an Engineering material*, Madison: USDA Forest Servies FPL, 1999.
- [5] R. J. Isebrands I, *Poplar and willows: Trees for society and the environment*. Rome: CAB International and FAO (Food and Agriculture Organization of the United Nations), 2014.
- [6] A. Koller, W.; Lebedys, "Poplar cultivation in Europa and Spain," in *II Poplar Symposium*, (Valladolid), 2019.
- [7] E. Biblis, "Analysis of wood-fiberglass composite beams within and beyond the elastic region," *FPJ*, vol. 15, pp. 81–88, 1965.
- [8] R. Moody, "Design criteria for large structural glued-laminated timber beams using mixed species of visually graded lumber," *FPL*, vol. 236, p. 42, 1974.
- [9] M. M. Lepper and F. J. Keenan, "Development of poplar glued-laminated timber. I: Tensile strength and stiffness of poplar laminating stock," *Canadian Journal of Civil Engineering*, vol. 13, pp. 445–459, aug 1986.
- [10] C. Martins, A. M. Dias, and H. Cruz, "Using non-destructive testing to predict the mechanical properties of glued laminated poplar," *Proceedings of the Institution of Civil Engineers - Structures and Buildings*, vol. 172, pp. 661–670, sep 2019.
- [11] G. Castro and F. Paganini, "Mixed glued laminated timber of poplar and Eucalyptus grandis clones," *Holz als Roh- und Werkstoff*, vol. 61, pp. 291–298, sep 2003.
- [12] R. Tomasi, M. A. Parisi, and M. Piazza, "Ductile Design of Glued-Laminated Timber Beams," *Practice Periodical on Structural Design and Construction*, vol. 14, pp. 113–122, aug 2009.
- [13] R. Hernandez, R.; Davalos, J.F.; Sonti, S.S.; Kim, Y.; Moody, "Strength and stiffness of reinforced yellow-poplar glued-laminated beams," *FPL*, vol. 236, p. 28, 1997.

- [14] Kusnindar, S. Murni Dewi, A. Soehardjono, and Wisnumurti, "Performance of glue laminated timber beams composed of sengon wood (*Albizia falcatara*) and coconut wood (*Cocos nucifera*) with nylon-threads reinforcement," *MATEC Web of Conferences*, vol. 195, pp. 20–29, aug 2018.
- [15] W. H. Wan Mohamad, N. Mohamad Bhkari, and Z. Ahmad, "Bending and bonding properties of mixed-spices glued laminated timber from Merpauh, Jelutong and Sesendok," *Jurnal Teknologi*, vol. 81, jun 2019.
- [16] Shim, KB, Kim, KM, Park, and JS, "Improvement of prediction accuracy of glulam modulus of elasticity by considering neutral axis shift in bending," *Wood and Fiber Science*, vol. 41, no. 1, pp. 90–96, 2009.
- [17] L. Brancheriau and H. Bailleres, "Natural vibration analysis of clear wooden beams: a theoretical review," *Wood Science and Technology*, vol. 36, no. 4, pp. 347–365, 2002.
- [18] Cirad, "Non-destructive testing of wood," 2020.
- [19] Standard, "EN 408:2010 + A1:2012 Timber structures. Structural timber and glued laminated timber. Determination of some physical and mechanical properties," tech. rep., CEN, 2012.
- [20] Standard, "EN 384:2016 + A1:2019. Structural timber - Determination of characteristic values of mechanical properties and density," tech. rep., CEN, 2019.
- [21] Standard, "EN 14080:2013 Timber structures. Glued laminated timber and glued solid timber. Requirements," tech. rep., CEN, 2013.
- [22] EN338, "EN 338:2010. Structural timber - Strength classes," tech. rep., CEN, 2010.
- [23] Code2020, "Code-Aster," 2020.
- [24] P. Mallick, *Composites Engineering Handbook*. Boca Raton: CRC Press, mar 1997.
- [25] T. A. Laursen, *Computational Contact and Impact Mechanics*. Berlin, Heidelberg: Springer Berlin Heidelberg, 2003.
- [26] R. Bravo, J. Pérez-Aparicio, and T. Laursen, "An energy consistent frictional dissipating algorithm for particle contact problems," *International Journal for Numerical Methods in Engineering*, vol. 92, pp. 753–781, nov 2012.
- [27] F. J. Rescalvo, L. Morillas, I. Valverde-Palacios, and A. Gallego, "Acoustic emission in I-214 poplar wood under compressive loading," *European Journal of Wood and Wood Products*, vol. 78, pp. 723–732, jul 2020.
- [28] L. A. Kollert W, "Poplar cultivation in Europa and Spain," in *III Poplar Symposium*, (Valladolid), 2018.
- [29] Z.-H. Jiang, X.-Q. Wang, B.-H. Fei, H.-Q. Ren, and X.-E. Liu, "Effect of stand and tree attributes on growth and wood quality characteristics from a spacing trial with *Populus xiaohei*," *Annals of Forest Science*, vol. 64, pp. 807–814, jan 2007.

- [30] B. Zobel and J. Buijtenen, *Wood variation, its cause and control*. Berlin, Heidelberg: Springer-Verlag, 1989.
- [31] D. R. Zhang SY, Chauret G, Ren HQ, "Impact of plantation black spruce initial spacing on lumber grade yield, bending properties and MSR yield," *Wood Fiber Science*, vol. 34, pp. 460–475, 2002.
- [32] M. J. Carson SD, Cown DJ, McKinley RB, "Effects of site, silviculture and seed lot on wood density and estimated wood stiffness in radiata pine at mid-rotation," *NZ j of For Science*, vol. 44, no. 1, p. 26, 2014.
- [33] F. Rescalvo, M. Ripoll, E. Suarez, and A. Gallego, "Effect of Location, Clone, and Measurement Season on the Propagation Velocity of Poplar Trees Using the Akaike Information Criterion for Arrival Time Determination," *Materials*, vol. 12, p. 356, jan 2019.
- [34] R. K. Aydin S, Yardimci MY, "Mechanical properties of four timber species commonly used in Turkey," *Turkish J Eng Env Sci*, vol. 31, pp. 19–27, 2007.
- [35] F. Y. Huda ASMA, Koubaa A, Cloutier A, Hernández RE, "Variation of the physical and mechanical properties of hybrid poplar clones," *Bioresources*, vol. 9, no. 1, pp. 1456–1471, 2014.
- [36] P. P. Yu Q, Zhang SY, Pliura A, MacKay J, Bousquet J, "Variation in Mechanical Properties of Selected Young Poplar Hybrid Crosses," *Forest Science*, vol. 54, no. 3, pp. 255–259, 2008.
- [37] M. Casado, L. Acuña, L.-A. Basterra, G. Ramón-Cueto, and D. Vecilla, "Grading of structural timber of *Populus × euramericana* clone I-214," *Holzforschung*, vol. 66, pp. 633–638, jul 2012.
- [38] V. d. B. J. Van Acker J, Defoirdt N, "Enhanced potential of poplar and willow for engineered wood products," in *2nd Conference on Engineered Wood Products based on Poplar/Willow Wood (CEPPW2)*, 2016.
- [39] M. Legg and S. Bradley, "Measurement of stiffness of standing trees and felled logs using acoustics: A review," *The Journal of the Acoustical Society of America*, vol. 139, pp. 588–604, feb 2016.
- [40] M. E. Santaclara O, "Acoustic segregation of *Pinus pinaster* logs for structural lumber production according to strength classes," in *17th International Nondestructive Testing and Evaluation of Wood Symposium*, (Sopron), p. 775, 2011.
- [41] D. Ridley-Ellis, P. Stapel, and V. Baño, "Strength grading of sawn timber in Europe: an explanation for engineers and researchers," *European Journal of Wood and Wood Products*, vol. 74, pp. 291–306, may 2016.
- [42] D. F. Llana, G. Íñiguez-González, M. R. Díez, and F. Arriaga, "Nondestructive testing used on timber in Spain: A literature review," *Maderas. Ciencia y tecnología*, vol. 22, no. ahead, pp. 133–156, 2020.
- [43] X. Wang, "Acoustic measurements on trees and logs: a review and analysis," *Wood Science and Technology*, vol. 47, pp. 965–975, sep 2013.

BIBLIOGRAPHY

- [44] E. Merlo, J. G. Alvarez, O. Santaclara, and G. Riesco, "Modelling modulus of elasticity of *Pinus pinaster* Ait. in northwestern Spain with standing tree acoustic measurements, tree, stand and site variables," *Forest Systems*, vol. 23, p. 153, apr 2014.
- [45] M. Madhoushi and S. Daneshvar, "Predicting the static modulus of elasticity in eastern cottonwood (*Populus deltoides*) using stress wave non-destructive testing in standing trees," *European Journal of Wood and Wood Products*, vol. 74, pp. 885–892, nov 2016.
- [46] B. H. Amateis RL, "Use of the Fakopp Treesonacoustic device to estimate wood quality characteristics in loblolly pine trees planted at different densities," in *Proceedings of the 17th Biennial Southern Silvicultural Research Conference* (U.S. Department of Agriculture, ed.), (Asheville, NC, USA), p. 5, Forest Service, Southern Research Station, 2015.
- [47] R.-E. D. Moore J, Lyon A, Searles G, Lehneke S, "Within- and between-stand variation in selected properties of Sitka spruce sawn timber in the UK: implications for segregation and grade recovery," *Ann For Science*, vol. 70, pp. 403–415, 2013.
- [48] M. Madhoushi and Z. Boskabadi, "Relationship between the dynamic and static modulus of elasticity in standing trees and sawn lumbers of *Paulownia fortune* planted in Iran," *Maderas. Ciencia y tecnología*, vol. 21, no. ahead, pp. 35–44, 2019.
- [49] A. Rais, H. Pretzsch, and J.-W. G. van de Kuilen, "Roundwood pre-grading with longitudinal acoustic waves for production of structural boards," *European Journal of Wood and Wood Products*, vol. 72, pp. 87–98, jan 2014.
- [50] K. Simic, V. Gendvilas, C. O'Reilly, and A. M. Harte, "Predicting structural timber grade-determining properties using acoustic and density measurements on young Sitka spruce trees and logs," *Holzforschung*, vol. 73, pp. 139–149, feb 2019.
- [51] X. Wang, R. J. Ross, D. W. Green, B. Brashaw, K. Englund, and M. Wolcott, "Stress wave sorting of red maple logs for structural quality," *Wood Science and Technology*, vol. 37, pp. 531–537, apr 2004.
- [52] G. Pavić, "Analysis of Vibration Reduction by Damping Using Simple Analytical Modelling," *Shock and Vibration*, vol. 2018, pp. 1–13, jun 2018.
- [53] I. Fundova, T. Funda, and H. X. Wu, "Non-Destructive Assessment of Wood Stiffness in Scots Pine (*Pinus sylvestris* L.) and its Use in Forest Tree Improvement," *Forests*, vol. 10, p. 491, jun 2019.
- [54] M. Grabianowski, B. Manley, and J. C. F. Walker, "Acoustic measurements on standing trees, logs and green lumber," *Wood Science and Technology*, vol. 40, pp. 205–216, mar 2006.
- [55] R. Ross, R. F. Pellerin, N. Volny, W. W. Salsig, and R. H. Falk, "Stress wave timing nondestructive evaluation tools for inspecting historic structures : a guide for use and interpretation.," tech. rep., Forest Service - U.S. Department of Agriculture, 2000.

- [56] U. Dackermann, K. Crews, B. Kasal, J. Li, M. Riggio, F. Rinn, and T. Tannert, "In situ assessment of structural timber using stress-wave measurements," *Materials and Structures*, vol. 47, pp. 787–803, may 2014.
- [57] C. R. Mora, L. R. Schimleck, F. Isik, J. M. Mahon, A. Clark, and R. F. Daniels, "Relationships between acoustic variables and different measures of stiffness in standing *Pinus taeda* trees," *Canadian Journal of Forest Research*, vol. 39, pp. 1421–1429, aug 2009.
- [58] I. Alemdag, "An analytical look at the log volume formulas," tech. rep., Forest Management Institute, 1978.
- [59] H. V. Wiant, G. B. Wood, and M. Williams, "Comparison of three modern methods for estimating volume of sample trees using one or two diameter measurements," *Forest Ecology and Management*, vol. 83, pp. 13–16, jun 1996.
- [60] B. B. Wang X, Carter P, Ross RJ, "No Title Acoustic assessment of wood quality of raw forest materials - A path to increased profitability," *Forest Products Journal*, vol. 57, no. 5, pp. 6–14, 2007.
- [61] P. E. Berthelot A, Reuling D, Robert G, Bouvet A, Lanvin JD, Legrand G, Moreau J, Denaud L, "Qualités du bois des nouveaux cultivars de peuplier," tech. rep., FCBA Institut Technologique, Arts et Métiers ParisTech, 2013.
- [62] Bucur, V., *Acoustics of Wood*. Springer Berlin Heidelberg, 2006.
- [63] F. J. Rescalvo, C. Timbolmas, R. Bravo, and A. Gallego, "Experimental and Numerical Analysis of Mixed I-214 Poplar/*Pinus Sylvestris* Laminated Timber Subjected to Bending Loadings," *Materials*, vol. 13, p. 3134, jul 2020.
- [64] EN13183, "EN 13183-1:2002/AC:2003 - Moisture content of a piece of sawn timber - Part 1: Determination by oven dry method," tech. rep., European Committee for Standardization CEN, 2008.
- [65] L. Boever, D. Vansteenkiste, J. Acker, and M. Stevens, "End-use related physical and mechanical properties of selected fast-growing poplar hybrids (*Populus trichocarpa* × *P. deltoides*)," *Annals of Forest Science*, vol. 64, pp. 621–630, jan 2007.
- [66] F. Y. Hernández RE, Koubaa A, Beaudoin M, "Selected mechanical properties of fast-growing poplar hybrid clones," *Wood Fiber Science*, vol. 30, no. 2, pp. 138–147, 1998.
- [67] P. J. Beaudoin M, Hernández RE, Koubaa A, "Interclonal, intraclonal and within-tree variation in wood density of poplar hybrid clones," *Wood Fiber Science*, pp. 147–153, 1992.
- [68] S. J. Bendtsen BA, "Mechanical and anatomical properties in individual growth rings of plantation-grown eastern cottonwood and loblolly pine," *Wood Fiber Science*, vol. 18, no. 1, pp. 23–38, 1986.
- [69] I. Ištok, T. Sedlar, B. Šefc, T. Sinković, and T. Perković, "Physical Properties of Wood in Poplar Clones 'I-214' and 'S1-8'," *Drvna industrija*, vol. 67, no. 2, pp. 163–170, 2016.

BIBLIOGRAPHY

- [70] F. G. Wessels BC, "The potential for improving the stiffness of young South African grown *Pinus radiata* lumber by using high planting densities," *Pro Lingo*, vol. 11, pp. 58–64, 2015.
- [71] Forêt Privée Française, "Wood qualities of new poplar cultivars," *Forêt-entreprise* 212, 2013.
- [72] Smulski SJ, "Relationship of stress wave- and static bending- determined properties of four northeastern hardwoods," *Wood and Fiber Science*, vol. 23, pp. 44–57, 1991.
- [73] Ilic J, "Relationship among the dynamic and static elastic properties of air-dry *Eucalyptus delegatensis* R. Baker," *Holz als Roh- und Werkstoff*, vol. 59, pp. 169–175, 2001.
- [74] L. G. Casado M, Acuña L, Vecilla D, Relea E, Basterra A, Ramon G, "The influence of size in predicting the elastic modulus of *Populus x euramericana* timber using vibration techniques," in *Structures and Architecture – Cruz*, pp. 2025–2032, London: Taylor & Francis Group, 2010.
- [75] F. Cheng and Y. Hu, "Nondestructive test and prediction of MOE of FRP reinforced fast-growing poplar glulam," *Composites Science and Technology*, vol. 71, pp. 1163–1170, may 2011.
- [76] W. T. Yang JL, Ilic J, "Relationships between static and dynamic modulus of elasticity for a mixture of clear and decayed eucalypt wood," *Australian Forestry*, vol. 66, no. 3, pp. 193–196, 2002.
- [77] S. Chauhan and A. Sethy, "Differences in dynamic modulus of elasticity determined by three vibration methods and their relationship with static modulus of elasticity," *Maderas. Ciencia y tecnología*, vol. 18, no. ahead, pp. 373–382, 2016.
- [78] P. F. Newton, "Acoustic-Based Prediction of End-Product-Based Fibre Determinates within Standing Jack Pine Trees," *Forests*, vol. 10, p. 605, jul 2019.
- [79] Bertoldo C, *Propriedades de resistência e de rigidez da madeira obtidas a partir da avaliação acústica na árvore [Predicting of strength and stiffness of wood using acoustic measurement in trees]*. PhD thesis, Universidade Estadual de Campinas , SP, Brazil, 2014.
- [80] W. J. Chauhan SS, "Variations in acoustic velocity and density with age, and their interrelationships in radiata pine," *Forest Ecol Management*, vol. 229, pp. 388–394, 2006.
- [81] F. Liu, X. Wang, H. Zhang, F. Jiang, W. Yu, S. Liang, F. Fu, and R. J. Ross, "Acoustic Wave Propagation in Standing Trees – Part 1. Numerical Simulation," *Wood and Fiber Science*, vol. 52, pp. 53–72, jan 2020.
- [82] S. S. Araújo, G. N. Guimarães, and A. L. B. Geyer, "Influence of the type of measuring device in determining the static modulus of elasticity of concrete," *Revista IBRACON de Estruturas e Materiais*, vol. 5, pp. 555–575, oct 2012.

- [83] M. H. Ramage, H. Burrridge, M. Busse-Wicher, G. Fereday, T. Reynolds, D. U. Shah, G. Wu, L. Yu, P. Fleming, D. Densley-Tingley, J. Allwood, P. Dupree, P. F. Linden, and O. Scherman, "The wood from the trees: The use of timber in construction," *Renewable and Sustainable Energy Reviews*, vol. 68, pp. 333–359, 2017.
- [84] F. H. Theakston, "A feasibility study for strengthening timber beams with fiberglass," *Can. Agric. Eng.*, vol. 7, no. 1, pp. 17–19, 1965.
- [85] R. Rowlands, R. V. Deweghe, T. Laufenberg, and G. Krueger, "Fiber-reinforced wood composites," *Wood and Fiber Science*, vol. 18, no. 1, pp. 39–57, 1986.
- [86] D. Martin, Z.A.; Tingley, "Fire resistance of FRP reinforced glulam beams," in *Proceedings of World Conference on Timber Engineering*, (Whistler), 2000.
- [87] T. Williamson, "Fire performance of fiber reinforced polymer glued laminated timber," in *Proceedings 9th World Conference on Timber Engineering*, (Portland, Oregon), 2006.
- [88] K. Luggin, W.; Bergmeister, "Carbon fiber reinforced and prestressed timber beams," in *Proceedings 2nd Int. PhD Symposium in Civil Engineering*, (Budapest), 1998.
- [89] Y. J. Kim and K. A. Harries, "Modeling of timber beams strengthened with various CFRP composites," *Engineering Structures*, vol. 32, no. 10, pp. 3225–3234, 2010.
- [90] W. Lu, Z. Ling, Q. Geng, W. Liu, H. Yang, and K. Yue, "Study on flexural behaviour of glulam beams reinforced by Near Surface Mounted (NSM) CFRP laminates," *Construction and Building Materials*, vol. 91, pp. 23–31, 2015.
- [91] A. S. Ribeiro, A. M. de Jesus, A. M. Lima, and J. L. Lousada, "Study of strengthening solutions for glued-laminated wood beams of maritime pine wood," *Construction and Building Materials*, vol. 23, no. 8, pp. 2738–2745, 2009.
- [92] S. Osmannezhad, M. Faezipour, and G. Ebrahimi, "Effects of GFRP on bending strength of glulam made of poplar (*Populus deltoids*) and beech (*Fagus orientalis*)," *Construction and Building Materials*, vol. 51, pp. 34–39, jan 2014.
- [93] H. Yang, W. Liu, W. Lu, S. Zhu, and Q. Geng, "Flexural behavior of FRP and steel reinforced glulam beams: Experimental and theoretical evaluation," *Construction and Building Materials*, vol. 106, pp. 550–563, mar 2016.
- [94] G. M. Raftery and A. M. Harte, "Low-grade glued laminated timber reinforced with FRP plate," *Composites Part B: Engineering*, vol. 42, pp. 724–735, jun 2011.
- [95] G. M. Raftery and C. Whelan, "Low-grade glued laminated timber beams reinforced using improved arrangements of bonded-in GFRP rods," *Construction and Building Materials*, vol. 52, pp. 209–220, feb 2014.
- [96] A. Jorissen and M. Fragiaco, "General notes on ductility in timber structures," *Engineering Structures*, vol. 33, pp. 2987–2997, nov 2011.

BIBLIOGRAPHY

- [97] F. J. Rescalvo, A. Aguilar-Aguilera, E. Suarez, I. Valverde-Palacios, and A. Gallego, "Acoustic emission during wood-CFRP adhesion tests," *International Journal of Adhesion and Adhesives*, vol. 87, pp. 79–90, dec 2018.
- [98] M. Spain, "Mapewood Primer 100; MapeWarp 21; Mape Wrap C Uni-Ax 300; Carbonplate E 170," 2021.
- [99] Standard, "SR EN 1995-1-1:2016, Eurocode 5: Design of timber structures – Part 1-1: General-Common rules and rules for buildings," tech. rep., CEN, 2016.
- [100] C. Ong, "Glue-laminated timber (Glulam)," in *Wood Composites* (M. Ansell and P. W. Composites, eds.), pp. 123–140, Elsevier, 2015.
- [101] J. Porteous, "Composite section I-beams," in *Wood Composites* (M. Ansell and P. W. Composites, eds.), pp. 169–193, Elsevier, 2015.
- [102] W. A. Chugg, *Glulam: The Theory and Practice of the Manufacture of Glued Laminated Timber Structures ...* Benn, 1964.
- [103] O. A. Hassan and C. Johansson, "Glued laminated timber and steel beams," *Journal of Engineering, Design and Technology*, vol. 16, pp. 398–417, jun 2018.
- [104] V. Baño, F. Arriaga, A. Soilán, and M. Guaita, "Prediction of bending load capacity of timber beams using a finite element method simulation of knots and grain deviation," *Biosystems Engineering*, vol. 109, pp. 241–249, aug 2011.
- [105] B. Iraola and J. M. Cabrero, "An algorithm to model wood accounting for different tension and compression elastic and failure behaviors," *Engineering Structures*, vol. 117, pp. 332–343, 2016.
- [106] S. Timoshenko, *Strength of Materials*. New York: Lancaster Press, Inc, 1 ed., 1940.
- [107] W. Li, P. Huang, Z. Chen, X. Zheng, Y. Yang, and X. Guo, "Bond behavior of fully bonded CFRP-concrete interface with improved double shear tests," *Journal of Building Engineering*, vol. 43, p. 102866, nov 2021.
- [108] S. Tesfaye Deresa, J. Xu, B. Shan, H. Ren, and Y. Xiao, "Experimental investigation on flexural behavior of full-scale glued laminated bamboo (glubam)-concrete composite beams: A case study of using recycled concrete aggregates," *Engineering Structures*, vol. 233, p. 111896, apr 2021.
- [109] A. C. Ugural and S. K. Fenster, *Advanced Mechanics of Materials and Applied Elasticity*. International Series in the Physical and Chemical Engineering Sciences Series, Prentice Hall, 2011.
- [110] T. Wu, Y. Sun, X. Liu, and Y. Cao, "Comparative study of the flexural behavior of steel fiber-reinforced lightweight aggregate concrete beams reinforced and prestressed with CFRP tendons," *Engineering Structures*, vol. 233, p. 111901, apr 2021.
- [111] B. Shi, W. Zhu, H. Yang, W. Liu, H. Tao, and Z. Ling, "Experimental and theoretical investigation of prefabricated timber-concrete composite beams with and without prestress," *Engineering Structures*, vol. 204, p. 109901, feb 2020.

- [112] K. Buka-Vaivade, D. Serdjuks, V. Goremikins, A. Vilguts, and L. Pakrastins, "Experimental Verification of Design Procedure for Elements from Cross-laminated Timber," *Procedia Engineering*, vol. 172, pp. 1212–1219, 2017.
- [113] T. P. Nowak, J. Jasieńko, and D. Czepiżak, "Experimental tests and numerical analysis of historic bent timber elements reinforced with CFRP strips," *Construction and Building Materials*, vol. 40, pp. 197–206, mar 2013.
- [114] M. Fossetti, G. Minafò, and M. Papia, "Flexural behaviour of glulam timber beams reinforced with FRP cords," *Construction and Building Materials*, vol. 95, pp. 54–64, oct 2015.
- [115] J. J. Lee, J. S. Park, K. M. Kim, and J. K. Oh, "Prediction of bending properties for structural glulam using optimized distributions of knot characteristics and laminar MOE," *Journal of Wood Science*, vol. 51, pp. 640–647, dec 2005.
- [116] A. D'Ambrisi, F. Focacci, and R. Luciano, "Experimental investigation on flexural behavior of timber beams repaired with CFRP plates," *Composite Structures*, vol. 108, pp. 720–728, feb 2014.
- [117] P. de la Rosa García, A. C. Escamilla, and M. Nieves González García, "Bending reinforcement of timber beams with composite carbon fiber and basalt fiber materials," *Composites Part B: Engineering*, vol. 55, pp. 528–536, dec 2013.
- [118] J. Fiorelli and A. A. Dias, "Glulam beams reinforced with FRP externally-bonded: theoretical and experimental evaluation," *Materials and Structures*, vol. 44, pp. 1431–1440, oct 2011.
- [119] Y.-F. Li, M.-J. Tsai, T.-F. Wei, and W.-C. Wang, "A study on wood beams strengthened by FRP composite materials," *Construction and Building Materials*, vol. 62, pp. 118–125, jul 2014.
- [120] E. Lukaszewska, H. Johnsson, and M. Fragiaco, "Performance of connections for prefabricated timber-concrete composite floors," *Materials and Structures*, vol. 41, pp. 1533–1550, nov 2008.
- [121] E. McConnell, D. McPolin, and S. Taylor, "Post-tensioning of glulam timber with steel tendons," *Construction and Building Materials*, vol. 73, pp. 426–433, dec 2014.
- [122] F. Rescalvo, I. Valverde-Palacios, E. Suarez, A. Roldán, and A. Gallego, "Monitoring of Carbon Fiber-Reinforced Old Timber Beams via Strain and Multiresonant Acoustic Emission Sensors," *Sensors*, vol. 18, p. 1224, apr 2018.
- [123] F. J. Rescalvo, I. Valverde-Palacios, E. Suarez, and A. Gallego, "Experimental and analytical analysis for bending load capacity of old timber beams with defects when reinforced with carbon fiber strips," *Composite Structures*, vol. 186, pp. 29–38, 2018.
- [124] Y.-l. Yang, J.-w. Liu, and G.-j. Xiong, "Flexural behavior of wood beams strengthened with HFRP," *Construction and Building Materials*, vol. 43, pp. 118–124, jun 2013.

BIBLIOGRAPHY

- [125] F. J. Rescalvo, C. Timbolmas, R. Bravo, I. Valverde-Palacios, and A. Gallego, "Improving ductility and bending features of poplar glued laminated beams by means of embedded carbon material," *Construction and Building Materials*, vol. 304, p. 124469, oct 2021.
- [126] J. Oscarsson, A. O. E. Serrano, and B. Enquist, "Identification of weak sections in glulam beams using calculated stiffness profiles based on lamination surface scanning," in *World Conference on Timber Engineering*, (Quebec), pp. 10–14, 2014.
- [127] J. Viguier, C. Bourgeay, A. Rohumaa, G. Pot, and L. Denaud, "An innovative method based on grain angle measurement to sort veneer and predict mechanical properties of beech laminated veneer lumber," *Construction and Building Materials*, vol. 181, pp. 146–155, aug 2018.
- [128] I. Glišović, M. Pavlović, B. Stevanović, and M. Todorović, "Numerical analysis of glulam beams reinforced with CFRP plates," *Journal of Civil Engineering and Management*, vol. 23, pp. 868–879, jul 2017.
- [129] I. Rahayu, L. Denaud, R. Marchal, and W. Darmawa, "Ten new poplar cultivars provide laminated veneer lumber for structural application.," *Annals of Forest Science*, vol. 72, no. 6 SRC - BaiduScholar FG - 0, pp. 705–715, 2015.
- [130] U. S. D. of Agriculture, *Wood handbook : Wood as an engineering material*. Madison Wisconsin (USA): U.S. Dept. of Agriculture, Forest Service, Forest Products Laboratory, [2010] ©2010, centennial ed., 2010.
- [131] M. Nocetti, L. Brancheriau, M. Bacher, M. Brunetti, and A. Crivellaro, "Relationship between local and global modulus of elasticity in bending and its consequence on structural timber grading," *European Journal of Wood and Wood Products*, vol. 71, pp. 297–308, may 2013.
- [132] M. Bacher and S. Krzosek, "Modulus of elasticity tension/bending ratio of polish grown pine (*pinus sylvestris* l.) and spruce (*picea abies* karst.) timber," *Forestry and Wood Technology*, vol. 82, pp. 31–38, 2013.
- [133] E. P. Gómez, M. N. González, K. Hosokawa, and A. Cobo, "Experimental study of the flexural behavior of timber beams reinforced with different kinds of FRP and metallic fibers," *Composite Structures*, vol. 213, pp. 308–316, 2019.
- [134] B. Xue and Y. Hu, "Mechanical properties analysis and reliability assessment of laminated veneer lumber (LVL) having different patterns of assembly," *BioResources*, vol. 7, feb 2012.
- [135] S. Gao, M. Xu, N. Guo, and Y. Zhang, "Mechanical Properties of Glued-Laminated Timber with Different Assembly Patterns," *Advances in Civil Engineering*, vol. 2019, pp. 1–13, jul 2019.
- [136] A. Borri, M. Corradi, and A. Grazini, "A method for flexural reinforcement of old wood beams with CFRP materials," *Composites Part B: Engineering*, vol. 36, pp. 143–153, mar 2005.

- [137] B. P. Gilbert, H. Bailleres, H. Zhang, and R. L. McGavin, "Strength modelling of Laminated Veneer Lumber (LVL) beams," *Construction and Building Materials*, vol. 149, pp. 763–777, sep 2017.
- [138] Y. Shen, D. Huang, A. Zhou, and D. Hui, "An inelastic model for ultimate state analysis of CFRP reinforced PSB beams," *Composites Part B: Engineering*, vol. 115, pp. 266–274, apr 2017.
- [139] V. A. Nguyen Trung, R. Le Roy, and J.-F. Caron, "Multi-reinforcement of timber beams with composite materials: Experiments and fracture modeling," *Composite Structures*, vol. 123, pp. 233–245, may 2015.
- [140] J. Š. L. Melzerová, T. Janda, M. Šejnoha, "FEM Models of Glued Laminated Timber Beams Enhanced by Bayesian Updating of Elastic Moduli," *International Journal of Civil and Environmental Engineering*, vol. 9, no. 5, pp. 692 – 698, 2015.
- [141] S. R. S. Monteiro, C. E. J. Martins, A. Dias, and H. Cruz, "Mechanical characterization of clear wood from Portuguese poplar," *BioResources*, vol. 14, no. 4 SRC - BaiduScholar FG - 0, pp. 9677–9685, 2019.
- [142] K. Kin, K. Shim, and C. Lum, "Predicting tensile and compressive moduli of structural lumber.," *Wood and Fiber Science*, vol. 43, no. 1 SRC - BaiduScholar FG - 0, pp. 83–89, 2011.
- [143] C. Wang, J. Reddy, and K. Lee, "Bending of Beams," in *Shear Deformable Beams and Plates*, ch. 2. Bending, pp. 11–38, Elsevier, 2000.
- [144] A. Harte, *Chapter 60: Timber engineering: an introduction*. Institution of Civil Engineer's, 2016.
- [145] A. Özçifçi and F. Yapıcı, "Structural performance of the finger-jointed strength of some wood species with different joint configurations," *Construction and Building Materials*, vol. 22, pp. 1543–1550, jul 2008.
- [146] R. L. Hernández, Roger; Coman, Razvan; Beauregard, "Influence of machining parameters on the tensile strength of finger-jointed high-density black spruce lumber," *Wood and fiber science: journal of the Society of Wood Science and Technology*, vol. 43, no. 1, pp. 2–10, 2011.
- [147] M. Shuzhan, Rao; Meng, Gong; Ying, Chui; Mohammad, "Effect of geometric parameters of finger joint profile on ultimate tensile strength of single finger-jointed boards," *Wood and fiber science: journal of the Society of Wood Science and Technology*, vol. 44, no. 3, pp. 263–270, 2012.
- [148] M. Yeh and Y. Lin, "Finger joint performance of structural laminated bamboo member," *Journal of Wood Science*, vol. 58, pp. 120–127, apr 2012.
- [149] A. Morin-Bernard, P. Blanchet, C. Dagenais, and A. Achim, "Glued-laminated timber from northern hardwoods: Effect of finger-joint profile on lamellae tensile strength," *Construction and Building Materials*, vol. 271, p. 121591, feb 2021.

- [150] J. Ayarkwa, Y. Hirashima, Y. Sasaki, and M. Yamasaki, "Influence of finger-joint geometry and end pressure on tensile properties of three finger-jointed Tropical African Hardwoods," *The Southern African Forestry Journal*, vol. 188, pp. 37–49, jul 2000.
- [151] C. Bustos, R. E. Hernández, R. Beauregard, and M. Mohammad, "Effects of end-pressure on the finger-joint quality of black spruce lumber: a microscopic analysis," *Maderas. Ciencia y tecnología*, vol. 13, no. 3, pp. 319–328, 2011.
- [152] L. H. Groom and R. J. Leichti, "Effect of Adhesive Stiffness and Thickness on Stress Distributions in Structural Finger Joints," *The Journal of Adhesion*, vol. 44, pp. 69–83, jan 1994.
- [153] A. Frangi, M. Bertocchi, S. Clauß, and P. Niemz, "Mechanical behaviour of finger joints at elevated temperatures," *Wood Science and Technology*, vol. 46, pp. 793–812, sep 2012.
- [154] E. Serrano and P. J. Gustafsson, "Influence of bondline brittleness and defects on the strength of timber finger-joints," *International Journal of Adhesion and Adhesives*, vol. 19, pp. 9–17, feb 1999.
- [155] M. Oudjene and M. Khelifa, "Finite element modelling of wooden structures at large deformations and brittle failure prediction," *Materials & Design*, vol. 30, pp. 4081–4087, dec 2009.
- [156] A. Khennane, M. Khelifa, L. Bleron, and J. Viguier, "Numerical modelling of ductile damage evolution in tensile and bending tests of timber structures," *Mechanics of Materials*, vol. 68, pp. 228–236, jan 2014.
- [157] V. Tran, M. Oudjene, and P. Méausoone, "FE analysis and geometrical optimization of timber beech finger-joint under bending test," *International Journal of Adhesion and Adhesives*, vol. 52, pp. 40–47, jul 2014.
- [158] M. Khelifa, A. Celzard, M. Oudjene, and J. Ruelle, "Experimental and numerical analysis of CFRP-strengthened finger-jointed timber beams," *International Journal of Adhesion and Adhesives*, vol. 68, pp. 283–297, jul 2016.
- [159] P. Lava, S. Cooreman, S. Coppieters, M. De Strycker, and D. Debruyne, "Assessment of measuring errors in DIC using deformation fields generated by plastic FEA," *Optics and Lasers in Engineering*, vol. 47, pp. 747–753, jul 2009.
- [160] M. Quanjin, M. Rejab, Q. Halim, M. Merzuki, and M. Darus, "Experimental investigation of the tensile test using digital image correlation (DIC) method," *Materials Today: Proceedings*, vol. 27, pp. 757–763, 2020.
- [161] F. Dubois, M. Méité, O. Pop, and J. Absi, "Characterization of timber fracture using the Digital Image Correlation technique and Finite Element Method," *Engineering Fracture Mechanics*, vol. 96, pp. 107–121, dec 2012.
- [162] J. Milch, M. Brabec, V. Sebera, and J. Tippner, "Verification of the elastic material characteristics of Norway spruce and European beech in the field of shear behaviour by means of digital image correlation (DIC) for finite element analysis (FEA)," *Holzforschung*, vol. 71, pp. 405–414, may 2017.

- [163] K. Ostapska and K. A. Malo, "Crack path tracking using DIC and XFEM modelling of mixed-mode fracture in wood," *Theoretical and Applied Fracture Mechanics*, vol. 112, p. 102896, apr 2021.
- [164] M. Angelidi, A. P. Vassilopoulos, and T. Keller, "Ductile adhesively-bonded timber joints – Part 1: Experimental investigation," *Construction and Building Materials*, vol. 179, pp. 692–703, aug 2018.
- [165] M. Angelidi, A. P. Vassilopoulos, and T. Keller, "Displacement rate and structural effects on Poisson ratio of a ductile structural adhesive in tension and compression," *International Journal of Adhesion and Adhesives*, vol. 78, pp. 13–22, oct 2017.
- [166] Standard, "ISO 2555:2018. Plastics-Resins in the Liquid State or As Emulsions or Dispersions—Determination of Apparent Viscosity by the Brookfield Test Method," tech. rep., ISO, Geneva, 2018.
- [167] R. W. Jokerst, "Finger-Jointed Wood Products," in *RP-FPL*, vol. 382, (Madison Wisconsin (USA)), Forest Products Laboratory, 1981.
- [168] Strickler M.D., "Finger-jointed dimension lumber: past, present, and future," *Forest Products Journal*, vol. 30, no. 9, pp. 51–56, 1980.
- [169] N. Hu, X. Li, Y. Wu, and X. Zhou, "Effects of finger length on finger joint process of glued laminated timber," in *Proceedings of 2012 International Conference on Biobase Material Science and Engineering*, pp. 288–291, IEEE, oct 2012.
- [170] B. Habipi and D. Ajdinaj, "Wood Finger-Joint Strength as Function of Finger Length and Slope Positioning of Tips," *International Journal of Engineering and Applied Sciences*, vol. 2, no. 12, 2015.
- [171] G. GmbH, "GOM Correlate Professional Software," 2020.
- [172] A. CAE, "ABAQUS/Standard User's Manual, Version 2020," 2020.
- [173] Python Core Team, "Python: A dynamic, open source programming language," 2015.
- [174] P. P. Camanho, C. G. Davila, and M. F. de Moura, "Numerical Simulation of Mixed-Mode Progressive Delamination in Composite Materials," *Journal of Composite Materials*, vol. 37, pp. 1415–1438, aug 2003.
- [175] L. Hollaway and J. Teng, *Strengthening and Rehabilitation of Civil Infrastructures Using Fibre-Reinforced Polymer (FRP) Composites*. Cambridge: Woodhead Publishing CRC Press, 1st editio ed., 2008.
- [176] W. Sun and W. Ghannoum, "Modeling of anchored CFRP strips bonded to concrete," *Construction and Building Materials*, vol. 85, pp. 144–156, jun 2015.
- [177] J. F. Bonacci and M. Maalej, "Behavioral Trends of RC Beams Strengthened with Externally Bonded FRP," *Journal of Composites for Construction*, vol. 5, pp. 102–113, may 2001.
- [178] X. Lu, J. Teng, L. Ye, and J. Jiang, "Bond-slip models for FRP sheets/plates bonded to concrete," *Engineering Structures*, vol. 27, pp. 920–937, may 2005.

BIBLIOGRAPHY

- [179] Y. Sato, Y. Asabo, and T. Ueda, "Fundamental study on bond mechanism of carbon fiber sheet," *Doboku Gakkai Ronbunshu*, vol. 47, pp. 71–87, may 2000.
- [180] C. Mazzotti, M. Savoia, and B. Ferracuti, "An experimental study on delamination of FRP plates bonded to concrete," *Construction and Building Materials*, vol. 22, pp. 1409–1421, jul 2008.
- [181] J. Dai, T. Ueda, and Y. Sato, "Development of the Nonlinear Bond Stress–Slip Model of Fiber Reinforced Plastics Sheet–Concrete Interfaces with a Simple Method," *Journal of Composites for Construction*, vol. 9, pp. 52–62, feb 2005.
- [182] W. Sun, X. Peng, and Y. Yu, "Development of a simplified bond model used for simulating FRP strips bonded to concrete," *Composite Structures*, vol. 171, pp. 462–472, jul 2017.
- [183] T. Ueda and J. Dai, "Interface bond between FRP sheets and concrete substrates: properties, numerical modeling and roles in member behaviour," *Progress in Structural Engineering and Materials*, vol. 7, pp. 27–43, jan 2005.
- [184] Y. T. Obaidat, S. Heyden, and O. Dahlblom, "Evaluation of Parameters of Bond Action between FRP and Concrete," *Journal of Composites for Construction*, vol. 17, pp. 626–635, oct 2013.
- [185] T. Mohammadi, B. Wan, K. A. Harries, and M. E. Sweriduk, "Bond Behavior of FRP–Concrete in Presence of Intermediate Crack Debonding Failure," *Journal of Composites for Construction*, vol. 21, p. 04017018, oct 2017.
- [186] I. A. Cortez Flores, J. Fernández Gómez, P. Villanueva Llauradó, A. Ferreira, and M. Parente, "Evaluation through a finite element simulation of the performance of FRP anchors for externally bonded reinforcements," *Composite Structures*, vol. 267, p. 113919, jul 2021.
- [187] F. Rescalvo, I. Valverde-Palacios, E. Suarez, and A. Gallego, "Experimental Comparison of Different Carbon Fiber Composites in Reinforcement Layouts for Wooden Beams of Historical Buildings," *Materials*, vol. 10, p. 1113, sep 2017.
- [188] C. Timbolmas, R. Bravo, F. J. Rescalvo, and M. Portela, "Transformed-section method applied to multispecies glulam timber beams subjected to pure bending," *Mechanics of Advanced Materials and Structures*, pp. 1–10, oct 2021.
- [189] C. Timbolmas, R. Bravo, F. J. Rescalvo, and A. Gallego, "Development of an analytical model to predict the bending behavior of composite glulam beams in tension and compression," *Journal of Building Engineering*, vol. 45, p. 103471, jan 2022.
- [190] X. Guo, S. Shu, Y. Wang, P. Huang, J. Lin, and Y. Guo, "Effect of Subtropical Natural Exposure on the Bond Behavior of FRP–Concrete Interface," *Polymers*, vol. 12, p. 967, apr 2020.
- [191] J. Wan, S. T. Smith, P. Qiao, and F. Chen, "Experimental Investigation on FRP-to-Timber Bonded Interfaces," *Journal of Composites for Construction*, vol. 18, jun 2014.

- [192] A. Vahedian, R. Shrestha, and K. Crews, "Effective bond length and bond behaviour of FRP externally bonded to timber," *Construction and Building Materials*, vol. 151, pp. 742–754, oct 2017.
- [193] A. Vahedian, R. Shrestha, and K. Crews, "Analysis of externally bonded Carbon Fibre Reinforced Polymers sheet to timber interface," *Composite Structures*, vol. 191, pp. 239–250, may 2018.
- [194] H. C. Biscaia, C. Chastre, D. Cruz, and A. Viegas, "Prediction of the interfacial performance of CFRP laminates and old timber bonded joints with different strengthening techniques," *Composites Part B: Engineering*, vol. 108, pp. 1–17, jan 2017.
- [195] H. C. Biscaia, R. Almeida, S. Zhang, and J. Canejo, "Experimental calibration of the bond-slip relationship of different CFRP-to-timber joints through digital image correlation measurements," *Composites Part C: Open Access*, vol. 4, p. 100099, mar 2021.
- [196] A. Hosseini and D. Mostofinejad, "Effective bond length of FRP-to-concrete adhesively-bonded joints: Experimental evaluation of existing models," *International Journal of Adhesion and Adhesives*, vol. 48, pp. 150–158, jan 2014.
- [197] C. Yuan, W. Chen, T. M. Pham, and H. Hao, "Bond behaviour between hybrid fiber reinforced polymer sheets and concrete," *Construction and Building Materials*, vol. 210, pp. 93–110, jun 2019.
- [198] M. Ali-Ahmad, K. Subramaniam, and M. Ghosn, "Experimental Investigation and Fracture Analysis of Debonding between Concrete and FRP Sheets," *Journal of Engineering Mechanics*, vol. 132, pp. 914–923, sep 2006.
- [199] C. Czaderski, K. Soudki, and M. Motavalli, "Front and Side View Image Correlation Measurements on FRP to Concrete Pull-Off Bond Tests," *Journal of Composites for Construction*, vol. 14, pp. 451–463, aug 2010.
- [200] K. Walotek, J. Bzówka, and A. Ciołczyk, "Examples of the Use of the ARAMIS 3D Measurement System for the Susceptibility to Deformation Tests for the Selected Mixtures of Coal Mining Wastes," *Sensors*, vol. 21, p. 4600, jul 2021.
- [201] M. Ben Ouezdou, A. Belarbi, and S.-W. Bae, "Effective Bond Length of FRP Sheets Externally Bonded to Concrete," *International Journal of Concrete Structures and Materials*, vol. 3, pp. 127–131, dec 2009.
- [202] K. V. Subramaniam, C. Carloni, and L. Nobile, "Width effect in the interface fracture during shear debonding of FRP sheets from concrete," *Engineering Fracture Mechanics*, vol. 74, pp. 578–594, mar 2007.
- [203] D. Radford, D. Van Goethem, R. Gutkowski, and M. Peterson, "Composite repair of timber structures," *Construction and Building Materials*, vol. 16, pp. 417–425, oct 2002.
- [204] T. W. Buell and H. Saadatmanesh, "Strengthening Timber Bridge Beams Using Carbon Fiber," *Journal of Structural Engineering*, vol. 131, pp. 173–187, jan 2005.

BIBLIOGRAPHY

- [205] J. G. Teng, J. F. Chen, S. T. Smith, and L. Lam, "Behaviour and strength of FRP-strengthened RC structures: a state-of-the-art review," *Proceedings of the Institution of Civil Engineers - Structures and Buildings*, vol. 156, pp. 51–62, feb 2003.
- [206] A. Khalifa, W. J. Gold, A. Nanni, and A. A. M.I., "Contribution of Externally Bonded FRP to Shear Capacity of RC Flexural Members," *Journal of Composites for Construction*, vol. 2, pp. 195–202, nov 1998.
- [207] A. Franco and G. Royer-Carfagni, "Effective bond length of FRP stiffeners," *International Journal of Non-Linear Mechanics*, vol. 60, pp. 46–57, apr 2014.
- [208] I. A. Cortez Flores, J. Fernández Gómez, P. Villanueva Llauro, and A. Ferreira, "An empirical model to estimate FRP anchored joint strength using spike anchors," *Composite Structures*, vol. 254, p. 112789, dec 2020.
- [209] J. R. Gilfillan, S. G. Gilbert, and G. R. H. Patrick, "The Use of FRP Composites in Enhancing the Structural Behavior of Timber Beams," *Journal of Reinforced Plastics and Composites*, vol. 22, pp. 1373–1388, oct 2003.
- [210] H. C. Biscaia, C. Chastre, and M. A. Silva, "Nonlinear numerical analysis of the debonding failure process of FRP-to-concrete interfaces," *Composites Part B: Engineering*, vol. 50, pp. 210–223, jul 2013.
- [211] M. R. Valluzzi, E. Garbin, and C. Modena, "Flexural strengthening of timber beams by traditional and innovative techniques," *Journal of Building Appraisal*, vol. 3, pp. 125–143, aug 2007.
- [212] Y. Lei, S. Liu, J. Zhao, J. Zhang, and C. Bai, "Experimental and analytical analyses of the bonding performance of CFRP–wood interface," *Journal of Building Engineering*, vol. 46, p. 103687, apr 2022.
- [213] H. Yuan, J. Teng, R. Seracino, Z. Wu, and J. Yao, "Full-range behavior of FRP-to-concrete bonded joints," *Engineering Structures*, vol. 26, pp. 553–565, apr 2004.
- [214] J. Harris and R. Adams, "Strength prediction of bonded single lap joints by non-linear finite element methods," *International Journal of Adhesion and Adhesives*, vol. 4, pp. 65–78, apr 1984.
- [215] S. J. Lee and D. G. Lee, "Development of a Failure Model for the Adhesively Bonded Tubular Single Lap Joint," *The Journal of Adhesion*, vol. 40, pp. 1–14, dec 1992.
- [216] S. Kurtz, P. Balaguru, and J. Helm, "Experimental Study of Interfacial Shear Stresses in FRP-Strengthened RC Beams," *Journal of Composites for Construction*, vol. 12, pp. 312–322, jun 2008.
- [217] S. Choi and S. P. Shah, "Measurement of deformations on concrete subjected to compression using image correlation," *Experimental Mechanics*, vol. 37, pp. 307–313, sep 1997.
- [218] B. Wan, M. A. Sutton, M. F. Petrou, K. A. Harries, and N. Li, "Investigation of Bond between Fiber Reinforced Polymer and Concrete Undergoing Global Mixed Mode I/II Loading," *Journal of Engineering Mechanics*, vol. 130, pp. 1467–1475, dec 2004.

- [219] A. Gallego, M. A. Ripoll, C. Timbolmas, F. Rescalvo, E. Suarez, I. Valverde, M. Rodríguez, F. B. Navarro, and E. Merlo, "Modulus of elasticity of I-214 young poplar wood from standing trees to sawn timber: influence of the age and stand density," *European Journal of Wood and Wood Products*, vol. 79, pp. 1225–1239, sep 2021.
- [220] M. Smith, "Abaqus/standard user's manual, version 6.9," 2009.
- [221] A. Turon, C. Dávila, P. Camanho, and J. Costa, "An engineering solution for mesh size effects in the simulation of delamination using cohesive zone models," *Engineering Fracture Mechanics*, vol. 74, pp. 1665–1682, jul 2007.
- [222] N. Dourado, F. Pereira, M. de Moura, and J. Morais, "Repairing wood beams under bending using carbon–epoxy composites," *Engineering Structures*, vol. 34, pp. 342–350, jan 2012.
- [223] L. M. Bustamante-Góez, E. Chica-Arrieta, and J. A. Villarraga-Ossa, "Assessment of cohesive traction-separation relationship according stiffness variation," *Revista UIS Ingenierías*, vol. 18, pp. 67–76, feb 2019.
- [224] K. Park, H. Choi, and G. H. Paulino, "Assessment of cohesive traction-separation relationships in ABAQUS: A comparative study," *Mechanics Research Communications*, vol. 78, pp. 71–78, dec 2016.
- [225] G. Cocchetti, M. Pagani, and U. Perego, "Selective mass scaling for distorted solid-shell elements in explicit dynamics: optimal scaling factor and stable time step estimate," *International Journal for Numerical Methods in Engineering*, vol. 101, pp. 700–731, mar 2015.
- [226] P. P. Camanho and F. L. Matthews, "Delamination Onset Prediction in Mechanically Fastened Joints in Composite Laminates," *Journal of Composite Materials*, vol. 33, pp. 906–927, may 1999.
- [227] T. Mase, R. Smelser, and G. Mase, *Continuum Mechanics for Engineers*. Boca Raton: CRC Press, 3rd editio ed., 2010.